A Thesis Submitted for the Degree of PhD at the University of Warwick

http://go.warwick.ac.uk/wrap/71009

Characterisation and identification of brown adipose tissue on positron-emission tomography and magnetic resonance imaging

Terence Alan Jones
BDS, MBChB, MFDSRCPS(Glasg),
MFGDP(UK), CertMIRCS(Ed), FRCR, FRGS

A thesis submitted in partial fulfilment of the
requirements for the degree of Doctor of Philosophy
(PhD) at the University of Warwick, Department of
Health Sciences.

March 2015

Acknowledgements

First and foremost my sincere thanks go to my supervisors Professor Charles Hutchinson and Dr Sarah Wayte for their unwavering support and guidance. It is no exaggeration to say that this thesis would not have been possible without them. Additional thanks are also due to Dr Sarah Wayte for teaching me MR physics for the FRCR examination, in fact I enjoyed it so much I returned for more.

Much of the work in this thesis was performed in conjunction with Dr Tom Barber and Dr Narendra Reddy of the Human Metabolism Research Unit at University Hospitals Coventry & Warwickshire, both of whom provided an endless supply of good ideas.

Thanks to Ric Crossman at the Department of Statistics, University of Warwick Medical School for statistical advice and performing the Tobit analysis in chapter 4.

Thank you to Mr Barry Hall, Climate Enquiry Officer and the Central Climate Unit of the Met Office who kindly supplied copious quantities of weather data which proved invaluable in chapters 3 and 4.

Thank you to Mr Timor Kadir of Mirada Medical Limited for help with Mirada XD 3.4. Work performed with the aid of this software laid the foundations for much of this thesis.

Thanks also to the CT and MR radiographers who taught me to operate the MR scanners, including assisting me in spending hours practising on the MR scanner in the dead of night.

For Hattie.

Declaration

I declare that this thesis represents my own work, except where due acknowledgement is made, and that it has not been previously included in a thesis, dissertation or report submitted to this University or to any other institution for a degree, diploma or other qualification.

The work presented (including data generated and data analysis) was carried out by the author except in the cases outlined below:

For chapters 3 and 4, data collection was performed in conjunction with Dr Narendra Reddy, who included data on determinants of brown fat prevalence and mass in his MD thesis.

For chapters 5 and 6, I identified suitable subjects and controls, and Dr Narendra Reddy as a clinical endocrinologist, liaised with the patients themselves. Image analysis was my own work. Dr Reddy included data from one patient (BAT13) in his MD thesis. Similarly the *ex vivo* murine study in chapters 8 and 9 was a collaborative effort, and included in both theses.

Parts of this thesis have been published by the author: the case report in section 9.3. Published and other material arising from this thesis is listed in Appendix B.

Terence Alan Jones

March 2015

Abstract

Characterisation and identification of brown adipose tissue on positron-emission tomography and magnetic resonance imaging

Since the first published description of brown adipose tissue (BAT) in 1551 its reputation has changed from that of a mere curiosity of little physiological significance in adult humans, to meriting reclassification as a metabolic organ in its own right.

Obesity is a major global public health problem. Modulation of non-shivering thermogenesis through BAT manipulation presents an attractive therapeutic target for inducing weight loss. Testing the efficacy of such pharmacological agents requires the development of a reliable imaging biomarker to enable BAT quantification.

In this thesis we have evaluated the effectiveness of positron-emission tomography (PET) and magnetic resonance (MR) imaging in quantifying BAT.

Retrospective analysis of 3,295 consecutive PET scans performed at University Hospitals Coventry & Warwickshire NHS Trust (Coventry, UK) in 2007-2012 showed ^{18}F-FDG uptake consistent with BAT in 5.3% of scans. Gender (female), age (younger), BMI (lower), serum glucose (lower), time of day (earlier), and temperature (lower) were all significant predictors of BAT prevalence. Regression analysis showed patients' age and preceding day's minimum temperature to correlate most strongly with BAT volume, while the impact of other factors is less clear.

We also showed the pattern of BAT uptake within individuals to be consistent across serial PET scans. Quantitative colocalisation techniques showed this degree of colocalisation to be significant in 14/15 patients, implying fixed BAT deposits in adult humans.

Concerns over the high ionising radiation dose of PET scans has stimulated research into MR as an alternative means of detecting BAT, with the potential to identify BAT irrespective of its activation state.

Using IDEAL FSE sequences acquired on a 3 Tesla clinical MR scanner, we found BAT to have a significantly lower fat fraction than white adipose tissue in rats *post mortem* and adult humans *in vivo*. Our efforts to identify BAT prospectively using fat fraction yielded inconsistent results.

Terence Alan Jones
For the degree of Doctor of Philosophy (PhD), the University of Warwick,
March 2015

Abbreviations

^{18}F	Flourine-18
^{18}F-FDG	^{18}F-fluorodeoxyglucose
^{18}F-FDG BAT	^{18}F-fluorodeoxyglucose uptake within areas of putative brown adipose tissue (on positron-emission tomography)
^{133}Xe	Xenon-133
ADP	Adenosine diphosphate
ATP	Adenosine triphosphate
AUC	Area under curve
BAT	Brown adipose tissue
$\text{BAT}_{\text{prosp}}$	Prospectively identified brown adipose tissue
BDS	Bachelor of Dental Surgery
BMI	Body mass index
BMP	Bone morphogenetic protein
BMR	Basal metabolic rate
BOLD	Blood oxygenation level dependent[a]
cAMP	Cyclic adenosine monophosphate
CertMIRCS(Ed)	Certificate in Medical Informatics of the Royal College of Surgeons of Edinburgh
CK	Creatine kinase
CNR	Contrast-to-noise ratio
CT	Computed tomography
FLAIR	Fluid attenuation inversion recovery[a]
FRCR	Fellow of the Royal College of Radiologists
FSE	Fast spin echo
GLUT	Glucose transporter
GRE	Gradient echo
HU	Hounsfield units, a measure of attenuation in computed tomography
IDEAL	Iterative decomposition with echo asymmetry and least squares estimation[a]
IFG	Impaired fasting glucose
IU	International units
iZQC	Intermolecular zero-quantum coherence transitions
kBq	Kilobecquerels, an SI-derived unit for radioactivity (where 1 Becquerel = 1 nuclear disintegration per second)
LBM	Lean body mass
MBChB	Bachelor of Medicine and Bachelor of Surgery
MBq	Megabecquerels
MFDSRCPS(Glasg)	Membership of the Faculty of Dental Surgery of the Royal College of Physicians and Surgeons of Glasgow
MFGDP(UK)	Membership of the Faculty of General Dental Practitioners (UK) of the Royal College of Surgeons of England
MIP	Maximum intensity projection
MR(I)	Magnetic resonance (imaging)
mRNA	Messenger ribonucleic acid
mSv	millisieverts

---

[a] A magnetic resonance imaging sequence

M_{xy}	Transverse magnetisation
Mya	Million years ago
M_z	Longitudinal magnetisation
NADH	Nicotinamide adenine dinucleotide
NADPH	Nicotinamide adenine dinucleotide phosphate
PACS	Picture archiving and communications system
PCR	Polymerase chain reaction
PET	Positron emission tomography
PPAR-γ	Peroxisome proliferator-activated receptor-γ
PRDM16	PR domain containing 16
RF	Radiofrequency
ROI	Region of interest
SCF	Supraclavicular fossa
SE	Spin echo
STIR	Short tau inversion (or time to inversion) recovery[a]
SUV	Standardised uptake value
SUV_{max}	Maximum standardised uptake value
SUV_{mean}	Mean standardised uptake value
T	Tesla
T1w	T1 weighted longitudinal (spine-lattice) recovery[a]
T2w	T2 weighted transverse (spin-spin) relaxation[a]
T3	Tri-iodothyronine
TNF	Tumour necrosis factor
UHCW	University Hospitals Coventry and Warwickshire NHS Trust
UCP1	Uncoupling protein 1
WAT	White adipose tissue

Table of contents

Acknowledgements .... **i**

Declaration .... **ii**

Abstract .... **iii**

Abbreviations .... **iv**

Table of contents .... **vi**

List of figures .... **xiii**

List of tables .... **xxii**

List of supplementary tables .... **xxv**

List of equations .... **xxvi**

Chapter 1 : Introduction **27**

- 1.1 Biological significance of BAT 28
- 1.2 Origins of BAT 30
  - 1.2.1 Evolutionary origins 30
  - 1.2.2 Embryological origins 31
- 1.3 Anatomical distribution and histology of BAT 33
  - 1.3.1 Histology 33
- 1.4 Physiology including non-shivering thermogenesis 35
- 1.5 The dynamic nature of BAT 37
  - 1.5.1 Cold and BAT activity 37
  - 1.5.2 Age and BAT activity 39
  - 1.5.3 Obesity and BAT activity 39

1.6 Therapeutic importance of BAT 40

1.7 Overview of the thesis 41

Chapter 2 : Identification and quantification of brown adipose tissue (BAT) on positron emission tomography with computed tomography (PET/CT) 43

2.1 Basic principles of ^{18}F-FDG PET/CT 43

2.2 Integration of PET with CT 46

2.3 Scanning protocol 48

2.4 Clinical applications of PET/CT 49

2.5 Identification of BAT on ^{18}F-FDG PET/CT 53

2.5.1 Incidental discovery and prevalence of BAT on ^{18}F-FDG PET and PET/CT 53

2.5.2 Evidence that ^{18}F-FDG uptake within fat represents BAT 55

2.5.3 Prevalence of ^{18}F-FDG BAT based on retrospective studies 57

2.5.4 Dedicated studies to evaluate prevalence of BAT 60

2.6 Aims 63

Chapter 3 : Predictors of ^{18}F-FDG BAT prevalence on PET/CT 64

3.1 Aims 64

3.2 Subjects and methods 64

3.2.1 Subject selection 64

3.2.2 Collection of data 65

3.2.3 PET/CT protocol 66

3.2.4 Image analysis 67

3.2.5 Statistical analysis 67

3.3 Ethics 69

3.4 Results.. 70

3.4.1 Demographic differences between ^{18}F-FDG BAT positive and negative PET/CT scans 70

3.4.2 Binomial logistic regression 81

3.4.3 Regression analysis of ^{18}F-FDG prevalence on first PET/CT scans 85

3.4.4 Multicollinearity testing... 86

3.4.5 Comparison of differences between ^{18}F-FDG BAT prevalence on first and second PET/CT scans 89

3.4.6 Sensitivity and specificity of PET/CT in detecting ^{18}F-FDG BAT 89

3.4.7 Cumulative prevalence of ^{18}F-FDG BAT on serial PET/CT scans 90

3.5 Summary.. 92

Chapter 4 : Predictors of ^{18}F-FDG BAT volume and activity on PET/CT 93

4.1 Aims.. 93

4.2 Subjects and methods 93

4.2.1 Subject selection 93

4.2.2 Data collection 93

4.2.3 Image analysis 93

4.2.4 Statistical analysis.. 95

4.3 Results.. 97

4.3.1 Factors associated with ^{18}F-FDG BAT volume.. 98

4.3.2 Factors associated with ^{18}F-FDG BAT activity (SUVmax) 107

4.3.3 Linear regression analysis.. 112

4.4 Summary 115

Chapter 5 : Occurrence of ^{18}F-FDG BAT uptake within anatomical compartments on serial PET/CT scans 116

5.1 Aims 116

5.2 Subjects and methods 116

5.2.1 Image analysis 116

5.2.2 Statistical analysis 117

5.3 Results 118

5.3.1 Patterns of ^{18}F-FDG BAT uptake 118

5.3.2 ^{18}F-FDG BAT distribution patterns on serial ^{18}F-FDG BAT positive scans 119

5.4 Summary 125

Chapter 6 : Colocalisation analysis of ^{18}F-FDG BAT uptake on serial PET/CT scans 126

6.1.1 Aims 130

6.1.2 Subjects and method 130

6.1.3 Results 134

6.1.4 Summary 142

Chapter 7 : Identification and quantification of BAT on magnetic resonance imaging 143

7.1 Basic principles of MR imaging 143

7.1.1 MR physics 143

7.1.2 Generating an MR signal 145

7.1.3 Free induction decay 145

7.1.4 Spin-lattice relaxation (T_1 recovery) 146

7.1.5 Spin-spin relaxation (T_2 decay) 147

7.1.6 MR sequences 150

7.2 BAT identification on MR 153

Chapter 8 : Retrospective identification and characterisation of BAT on MR in rats and humans 162

8.1 Aims 162

8.2 Validation of an MR foodstuff phantom to test fat fraction 163

8.2.1 Subjects and methods 163

8.2.2 Results 164

8.3 *Ex vivo* and *in situ* BAT characterisation in rats using MR 165

8.3.1 Subjects and methods 165

8.3.2 Results 168

8.4 *In vivo* BAT characterisation in adult humans using MR 175

8.4.1 Subjects and methods 175

8.4.2 Results 179

8.5 Summary 192

Chapter 9 : Prospective identification of BAT in rats and adult humans on MR imaging 194

9.1 Introduction 194

9.2 Aims 194

Study I: Visual identification of BAT on fat-only IDEAL MR images 195

9.2.1 Subjects and methods 195

9.2.2 Results.. 198

9.3 Identification of BAT using MR and ^{18}F-FDG PET/CT in an human adult with histological and immunohistochemical confirmation [188] 210

9.4 Study II: prospective identification of BAT using fat fraction images........... 212

9.4.1 Subjects and methods 213

9.4.2 Results.. 214

9.5 Summary.. 222

Chapter 10 : Discussion.. 224

10.1 Summary of the thesis 224

10.2 Determinants of BAT prevalence on ^{18}F-FDG PET/CT.............................. 226

10.2.1 Demographic factors... 227

10.2.2 Glycaemic status 230

10.2.3 Circadian fluctuation... 231

10.2.4 Effect of temperature upon ^{18}F-FDG BAT 233

10.2.5 Determinants of ^{18}F-FDG BAT volume and activity............................. 236

10.3 Colocalisation of ^{18}F-FDG BAT on serial PET/CT scans 241

10.3.1 ^{18}F-FDG BAT distribution is fairly constant within individuals 241

10.3.2 High degree of ^{18}F-FDG BAT colocalisation on serial PET/CT scans .. 242

10.4 Limitations of PET/CT in the identification of ^{18}F-FDG BAT 245

10.5 MR studies 249

10.5.1 Phantom validation of fat fractions derived from IDEAL MR.............. 250

10.5.2 Studies of fat fraction and T2* relaxation time in rats ... 251

10.5.3 Studies of fat fraction and T2* relaxation time in adult humans ... 256

Chapter 11 : Future directions ... 265

11.1 The future of PET/CT in BAT detection and quantification ... 265

11.2 Alternative imaging techniques in BAT detection and quantification ... 266

11.3 The future of MR in BAT detection and quantification ... 267

Appendix A : Supplementary tables ... 270

Appendix B : Articles, abstracts and presentations arising from this work ... 273

References ... 275

List of figures

Figure 2-1: Chemical structure of D-glucose and ^{18}F-FDG. 43

Figure 2-2: Facilitated transport and metabolism of ^{18}F-FDG. The dephosphorylation reaction involving glucose-6-phosphatase occurs slowly within malignant cells, resulting in intracellular accumulation of ^{18}F-FDG (Glut-1 = glucose transporter). Adapted from Kapoor *et al.* [140] and Kelloff *et al.* [141]. 44

Figure 2-3: The basic principle of PET: a positron interacts with an electron resulting in their mutual annihilation, which emits two 511 keV photons in opposite directions..... 45

Figure 2-4: Diagram of a PET detector ring array showing two photons from a single annihilation event interacting simultaneously with opposing scintillation crystals along a single 'line of response'. By convention axial images are displayed as if standing at the patient's feet.. 46

Figure 2-5: Maximum intensity projection (MIP) PET image performed on a 71-year old male showing physiological ^{18}F-FDG uptake within brain, myocardium, liver, urinary tract and liver.. 50

Figure 2-6: MIP PET image (left) and coronal fused PET/CT image (right) of a 71-year old male, showing avid ^{18}F-FDG uptake within a bronchogenic carcinoma within the right lung (red arrow). A metastatic deposit within a mediastinal lymph node (yellow arrow) evident on the MIP image is not evident on the fused PET/CT image. 51

Figure 2-7: MIP PET performed in a 26-year old female showing physiological ^{18}F-FDG uptake within the neck and supraclavicular fossae consistent with BAT. 53

Figure 2-8: (a) Maximum intensity projection PET, (b) fused coronal and (c) axial PET/CT images in a 17-year old male with a testicular germ cell tumour metastasis in the right lung showing the typical symmetrical pattern of ^{18}F-FDG BAT uptake within the supraclavicular fossa and paravertebral regions. 55

Figure 3-1: Flow chart showing recruitment of the sample. 65

Figure 3-2: ^{18}F-FDG prevalence decreases with age for both males and females. 72

Figure 3-3: Number of PET/CT scans performed according to age. 73

Figure 3-4: Box and whisker plot with Tukey’s hinges showing significant differences between the mean ages of those with and without ^{18}F-FDG BAT ($p < 0.001$). 73

Figure 3-5: Breakdown of BMI categories by sex. 74

Figure 3-6: Scatterplot of age against BMI, showing no significant correlation. The dotted line at 25 kg/m^2 indicates the upper limit of the ‘ideal’ BMI. 75

Figure 3-7: Mean BMI for ^{18}F-FDG BAT negative and positive scans. Lines at 25 and 30 kg/m^2 indicate the boundaries between ideal, overweight and obese BMI values. 76

Figure 3-8: Prevalence of ^{18}F-FDG BAT according to BMI and gender. 76

Figure 3-9: Prevalence of ^{18}F-FDG BAT with glycaemic status according to sex. 78

Figure 3-10: Mean monthly temperature and ^{18}F-FDG BAT prevalence. 79

Figure 3-11: Variation in ^{18}F-FDG BAT prevalence with time of day. 80

Figure 3-12: Seasonal variation in monthly temperature, and mean monthly sunshine. 86

Figure 3-13: Cumulative prevalence of ^{18}F-FDG BAT with increasing numbers of scans. 91

Figure 4-1: Semi-automatic selection of ^{18}F-FDG regions of interest by defining an isocontour set at SUV of 2.5 g/ml (a). Isocontours set at 2.0g/ml overestimate the extent of ^{18}F-FDG BAT uptake (b). 94

Figure 4-2: Coronal PET MIP image, showing isocontours around BAT from which volumes were derived. 95

Figure 4-3: Frequency histogram showing distribution of ^{18}F-FDG BAT volumes. 95

Figure 4-4: Normal Q-Q plot showing almost normal distribution of $\log_{10}[^{18}$F-FDG BAT volume$]$ except for those at the extremes. 96

Figure 4-5: Scatterplot of ^{18}F-FDG BAT volume against SUVmax. 97

Figure 4-6: Box and whisker plot showing no significant differences between mean ^{18}F-FDG BAT volume between sexes. 98

Figure 4-7: Scatterplot showing inverse correlation between age and ^{18}F-FDG BAT volume for both genders. 100

Figure 4-8: Box and whisker plot (with Tukey's hinges) showing no significant difference in ^{18}F-FDG BAT volume between BMI categories. 101

Figure 4-9: Scatterplot of ^{18}F-FDG BAT volume against BMI category (according to gender). 101

Figure 4-10: Mean ^{18}F-FDG BAT volumes according to glycaemic groups. 102

Figure 4-11: Scatterplot showing a weak positive correlation between mean temperature on the day of scanning and ^{18}F-FDG BAT volume. 103

Figure 4-12: Mean ^{18}F-FDG BAT volume by month. 104

Figure 4-13: Bubble plot showing monthly variation in ^{18}F-FDG BAT volume for 15 subjects with multiple positive scans. A: index scans (highest volume PET/CT scans for each subject); B: All scans (including subordinate and negative scans). 106

Figure 4-14: Box and whisker plot showing no significant differences between mean ^{18}F-FDG BAT SUVmax between sexes (n=175). 107

Figure 4-15: Scatterplot showing inverse correlation between age and ^{18}F-FDG BAT SUVmax for both sexes (n=175). 108

Figure 4-16: Scatterplot of mean ^{18}F-FDG BAT SUVmax against BMI category (by gender). 109

Figure 4-17: Mean SUVmax against fasting glycaemic status (by gender). 110

Figure 4-18: Scatterplot showing of mean temperature on the day of scanning against ^{18}F-FDG BAT activity (SUVmax) according to gender. 111

Figure 4-19: Mean ^{18}F-FDG BAT SUVmax according to time of day. 111

Figure 5-1: Bar chart showing the number of anatomical depots on serial scans for 15 patients (orange = index scan, blue = subordinate scan). 122

Figure 5-2: Box and whisker plot showing super-linear relationship between the number of compartments showing ^{18}F-FDG BAT uptake and mean BAT volume.......... 125

Figure 6-1: Object-based colocalisation analysis using centre/particle coincidence (from Bolte *et al.* [218]).......... 127

Figure 6-2: Probability distribution function from randomised images (from Bolte and Cordelières [218]).......... 129

Figure 6-3: Subordinate CT superimposed over the index CT prior to image registration. 131

Figure 6-4: Graphical user interface of the visualisation tool within Mirada XD 3.4.. 131

Figure 6-5: The same case shown in Figure 6-3 following automatic rigid registration. 132

Figure 6-6: Visual representation of colocalisation analysis on serial PET/CT scans. 133

Figure 6-7: Production of an ‘envelope of interaction’ through segmentation of a CT image.......... 134

Figure 6-8: Axial PET/CT of the upper thorax showing colocalised ^{18}F-FDG BAT ROIs between index (yellow) and subordinate (green) scans.......... 134

Figure 6-9: Stacked bar chart showing the proportion of colocalised ^{18}F-FDG BAT ROIs for each subordinate scan with respect to the index scan.......... 135

Figure 6-10: Serial PET/CT scans showing colocalised ^{18}F-FDG BAT ROIs for 2 subjects (I & J).......... 136

Figure 6-11: Scatterplot showing strong correlation between number of ^{18}F-FDG BAT ROIs and volume. 137

Figure 6-12: Correlation between number of ROIs on subordinate scan, and percentage colocalised ROIs.......... 137

Figure 6-13: Proportion of ^{18}F-FDG BAT ROIs on subordinate scans colocalising with index scan (subordinate ∩ index). 138

Figure 6-14: Probability distribution curve of the randomised M2 coefficients. 139

Figure 6-15: Manders' M2 colocalisation coefficients for each subordinate scan (red), with randomised M2 coefficients (grey boxes denotes 95% CI). 140

Figure 6-16: Scatterplot showing a strong correlation between the proportion of colocalised ^{18}F-FDG BAT ROIs and M2 colocalisation coefficient. 141

Figure 6-17: Bland-Altman plot comparing proportions of colocalised ^{18}F-FDG BAT ROIs and M2 coefficients. 141

Figure 7-1: The magnetic vectors associated with a precessing proton (a) resolved into transverse (m_{xy}) and longitudinal (m_z) components (b) (adapted from Pooley *et al.* [228]). 144

Figure 7-2: An RF pulse at the correct Larmor frequency displaces net magnetisation from being in a net longitudinal (z) direction (a) into the transverse (xy) plane (b) (adapted from Pooley *et al.* [228].) 145

Figure 7-3: T_1 recovery curve of longitudinal magnetisation M_z (adapted from Pooley *et al.* [228]). 146

Figure 7-4: T1 recovery curves for two tissues demonstrating maximum tissue contrast at time point A (adapted from Pooley *et al.* [228]). 147

Figure 7-5: De-phasing of net M_{xy} magnetisation (a) results in a loss of net transverse magnetisation as shown on the T2 decay curve (b) (adapted from Pooley *et al.* [228]). 148

Figure 7-6: T2 decay curves for two tissues showing effects of tissue contrast (adapted from Pooley *et al.* [228]). 149

Figure 7-7: Dixon imaging with derived fat fraction image of a pork chop. 152

Figure 7-8: Fat fraction image derived from Dixon images. 152

Figure 8-1: Calculated fat fraction images of various foodstuffs with known fat content. 164

Figure 8-2: Dissected BAT and WAT specimens from male Wistar rates kept in the cold (4°C) and warm (30°C). 168

Figure 8-3: Calculated fat fraction maps showing (from left to right) interscapular BAT, omental WAT and subcutaneous WAT specimens, from rats kept at (a) 4°C, and (b) 30°C. 169

Figure 8-4: Box and whisker plot (showing 1-99 percentiles) showing fat fractions within dissected interscapular BAT, omental WAT and subcutaneous WAT. 170

Figure 8-5: T2* map of (from left to right) interscapular BAT, omental WAT and subcutaneous WAT specimens, from rats kept at (a) 4°C, and (b) 30°C. 171

Figure 8-6: Box and whisker plot (showing 1-99 percentiles) showing T2* values within dissected interscapular BAT, omental WAT and subcutaneous WAT. 171

Figure 8-7: Scatterplot of fat fraction and T2* value for the *ex vivo* specimens at 4°C. 172

Figure 8-8: Axial fat-only IDEAL MR sequence through the upper thorax at the level of the interscapular fat pad (yellow arrow) at (a) 4°C and (b) 30°C, showing low fat fraction within the interscapular BAT (c) and (d). 173

Figure 8-9: Box and whisker plot (with Tukey's hinges) showing fat fraction of *in situ* BAT and WAT within rat carcasses at 4°C and 30°C. 174

Figure 8-10: T2* map through the upper thorax showing shorter T2* relaxation time within the interscapular fat pad (yellow arrow) at (a) 4°C and (b) 30°C. 174

Figure 8-11: Crude supraclavicular ROIs superimposed over thresholded fat fraction images. 177

Figure 8-12: Verification of PET/CT and MR co-registration. 178

Figure 8-13: Position of ^{18}F-FDG BAT and subcutaneous WAT ROIs. 178

Figure 8-14: Pairwise comparison of magnitude of image deformation required to register PET/CT and MR according to arm position. ... 180

Figure 8-15: Scatter dot plot showing mean WAT and BAT fat fractions. ... 183

Figure 8-16: Fat fraction within crude supraclavicular fossa ROIs in ^{18}F-FDG BAT positive and negative individuals. ... 183

Figure 8-17: Variation in WAT and ^{18}F-FDG BAT fat fraction with BMI. ... 184

Figure 8-18: Variation in WAT and ^{18}F-FDG BAT fat fraction according to MR slice thickness ... 186

Figure 8-19: T2* relaxation times within crude supraclavicular fossa ROIs in ^{18}F-FDG BAT positive and negative individuals. ... 188

Figure 8-20: Scatter dot plot showing mean WAT and BAT T2* relaxation time for each MR scan. ... 188

Figure 8-21: Variation in fat fraction within supraclavicular fossa ROIs on serial MR scans. ... 189

Figure 8-22: Variation in fat fraction within subcutaneous WAT on serial MR scans. 190

Figure 8-23: Variation in fat fraction within ^{18}F-FDG BAT on serial MR scans. ... 191

Figure 8-24: Seasonal variation in fat fraction within transposed ^{18}F-FDG BAT ROIs. Red lines correspond to BAT06, 11 and 13 in whom the fat fraction varied significantly. ... 192

Figure 9-1: Surface-rendered image showing truncated ^{18}F-FDG BAT within the supraclavicular fossae (BAT06). ... 197

Figure 9-2: Variation in signal intensity within BAT and WAT along the B_0 axis in a single patient (BAT13). ... 199

Figure 9-3: BAT:WAT signal ratio for ^{18}F-FDG BAT ROIs and matched WAT ROIs in a single patient (BAT13) ... 199

Figure 9-4: Box and whisker plot showing variation in contrast to noise ratio between patients. 200

Figure 9-5: Bland-Altman plot of BAT$_{prosp}$ and truncated ^{18}F-FDG BAT volumes for rater 1 (red) and rater 2 (blue). 203

Figure 9-6: Colocalised BAT$_{prosp}$ and ^{18}F-FDG BAT ROIs in a single patient (BAT06). 203

Figure 9-7: Stacked bar chart showing the proportion of colocalised BAT$_{prosp}$ and truncated ^{18}F-FDG BAT ROIs for each rater. 204

Figure 9-8: Pearson's colocalisation coefficients (red bar) with randomised values (grey bars with 95% CI) of BAT$_{prosp}$ ROIs against ^{18}F-FDG BAT ROIs for each rater. 207

Figure 9-9: Scatterplot of ^{18}F-FDG BAT volume against M1 colocalisation coefficients for rater 1 (red) and rater 2 (blue). 208

Figure 9-10: Fused (a) ^{18}F-FDG PET/CT and (b) fat-only IDEAL MR images of the upper thorax. 212

Figure 9-11: Histopathological specimens from the suprasternal adipose tissue stained with (a) H&E and (b) UCP1 confirming BAT. 212

Figure 9-12: ROC curve for excised murine interscapular BAT samples. 214

Figure 9-13: Fat fraction images of (from left to right) *ex vivo* interscapular BAT, omental WAT and omental WAT (thresholded at 40-75%) from rats kept at (a) 4ºC and (b) 30ºC. 215

Figure 9-14: Fat fraction images following edge erosion of the samples in Figure 9-13 215

Figure 9-15: ROC curve for *in situ* interscapular BAT for the rat housed at 30ºC. 216

Figure 9-16: (a) Axial fat fraction images through the upper thorax of the rat housed at 30ºC (thresholded at 50-70% fat fraction); (b) mask and (c) following edge erosion. 217

Figure 9-17: Typical ROC curves for BAT and WAT discrimination in human adults, showing examples of good (a), moderate (b) and poor (c) BAT discrimination.......... 219

Figure 9-18: Merged colocalised ^{18}F-FDG BAT and edge-eroded BAT$_{prosp}$ ROIs (BAT06).. 220

Figure 9-19: Bland-Altman plot of BAT$_{prosp}$ and ^{18}F-FDG BAT ROIs........................ 222

List of tables

Table 2-1: Range of CT attenuation values for various tissues [147]. 48

Table 2-2: Retrospective studies of BAT prevalence on PET/CT. 58

Table 2-3: Dedicated prospective studies of BAT prevalence. 62

Table 3-1: Demographic, clinical and meteorological profile for PET/CT scans with and without ^{18}F-FDG BAT uptake. 71

Table 3-2: ^{18}F-FDG BAT prevalence by age octile for males and females. 72

Table 3-3: Frequency of ^{18}F-FDG BAT positive scans according to BMI category. 77

Table 3-4: Mean monthly temperature and ^{18}F-FDG BAT prevalence. 79

Table 3-5: Variation in ^{18}F-FDG BAT prevalence with time of day. 80

Table 3-6: Univariate binomial logistic regression performed on all PET/CT scans (n=3,295). 82

Table 3-7: Binomial multivariate logistic regression (forced entry technique) performed on all scans (n=3,295) showing determinants of ^{18}F-FDG BAT. 84

Table 3-8: Stepwise forwards and backwards binomial logistic regression for all scans (n=3,295) showing significant predictors of ^{18}F-FDG BAT for each regression model. 85

Table 3-9: Multicollinearity calculations for predictors of ^{18}F-FDG BAT prevalence. . 87

Table 3-10: Multivariate binomial logistic regression of predictors of ^{18}F-FDG BAT prevalence following removal of covariates. 88

Table 3-11: Stepwise forwards and backwards binomial logistic regression for all scans (n=3,295) following removal of covariates, showing significant predictors of ^{18}F-FDG BAT prevalence for each regression model. 88

Table 3-12: 2x2 contingency table showing concordance in ^{18}F-FDG BAT uptake between first and second PET/CT scans. 89

Table 3-13: Contingency table showing proportion of patients with ^{18}F-FDG BAT activity correctly identified on their first PET/CT. 90

Table 3-14: Cumulative prevalence of ^{18}F-FDG BAT on serial PET/CT scans. 91

Table 4-1: Spearman's correlations with ^{18}F-FDG BAT volume and SUVmax (** = $p<0.01$, * = $p<0.05$). 99

Table 4-2: Mean ^{18}F-FDG BAT volume for each BMI category according to sex. 102

Table 4-3: Correlations between ^{18}F-FDG BAT volume and temperature by sex. 104

Table 4-4: Likelihood of an index scan being performed according to season. 107

Table 4-5: Correlations between ^{18}F-FDG BAT SUVmax and mean temperature by gender. 110

Table 4-6: Predictors of ^{18}F-FDG BAT mass on Tobit model univariate and multivariate regression analyses. 113

Table 4-7: Predictors of $\log_{10}[^{18}$F-FDG BAT volume$]$ on parametric univariate and multivariate linear regression. 114

Table 4-8: Predictors of ^{18}F-FDG BAT activity (SUVmax) on Tobit model univariate and multivariate regression analysis. 115

Table 5-1: Distribution patterns of ^{18}F-FDG BAT on serial PET/CT scans. 119

Table 5-2: Patient demographics of individuals with multiple positive PET/CT scans. 120

Table 5-3: Anatomical compartments showing ^{18}F-FDG BAT on serial PET/CT scans. 121

Table 5-4: Inter-rater reliability calculations for serial ^{18}F-FDG BAT positive PET/CT scans. 123

Table 5-5: Landis and Koch's criteria for interpreting kappa statistics [213]. 124

Table 7-1: Fat fraction and T2* differences between BAT and WAT. 157

Table 8-1: Advertised and calculated fat fractions of foodstuff phantoms. 165

Table 8-2: MR scanning parameters for the *ex vivo* and *in situ* rat studies. 166

Table 8-3: Fat fraction and T2* values within excised BAT and WAT samples. 170

Table 8-4: Fat fraction and T2* values within *in situ* BAT and WAT 173

Table 8-5: Opportunistic sample of patients (n=13) recruited to the first phase of the study. 181

Table 8-6: Recruited patients with high ^{18}F-FDG BAT uptake (n=6), and age- and sex-matched controls (n=6). 182

Table 8-7: BAT and WAT fat fraction (on first MR scan) according to patient. 185

Table 8-8: T2* relaxation times within BAT and WAT. 187

Table 8-9: Serial fat fraction measurements in the supraclavicular fossae. 189

Table 8-10: WAT fat fraction measurements on serial MR scans. 190

Table 8-11: Serial fat fraction for ^{18}F-FDG BAT regions of interest. 191

Table 9-1: BAT$_{prosp}$ ROIs and volumes identified by raters. 202

Table 9-2: Coincidence statistics for BAT$_{prosp}$ and ^{18}F-FDG BAT ROIs for each rater. 205

Table 9-3: Manders' colocalisation coefficients for each rater against ^{18}F-FDG BAT.208

Table 9-4: Inter-rater variability statistics for raters 1 and 2. 210

Table 9-5: Receiver operator statistics for BAT and WAT discrimination within ^{18}F-FDG BAT positive human adults (n=16). 218

Table 9-6: Colocalisation statistics for BAT$_{prosp}$ and ^{18}F-FDG BAT ROIs (following edge erosion). 221

List of supplementary tables

Supplementary table 1: Binomial univariate logistic regression analysis of patients' first scans (n=2,685), showing predictors of ^{18}F-FDG BAT. 270

Supplementary table 2: Binomial multivariate logistic regression analysis (forced entry method) of patients' first scans (n=2,685), showing predictors of ^{18}F-FDG BAT. 271

Supplementary table 3: Correlation matrix of ^{18}F-FDG BAT determinants. 271

List of equations

Equation 2-1: Equation for calculating CT number (CT_n); μ_t = linear attenuation coefficient of tissues, μ_W = linear attenuation coefficient of water [147]. 48

Equation 2-2: Calculation of standardised uptake value. 'ROI' = region of interest, 'injected dose' = decay-adjusted injected dose of radiotracer, 'body weight' is used as a surrogate for the volume of distribution of radiotracer... 51

Equation 7-1: The Larmor equation.. 144

Equation 7-2: T1 longitudinal recovery curve equation. 147

Equation 7-3: T2 transverse magnetisation decay curve equation. 148

Equation 7-4: Calculation of fat fraction from Dixon images. 152

Equation 8-1: Formula describing the mono-exponential decay for T2* relaxation.... 167

Equation 9-1: Contrast to noise formula.. 196

Equation 9-2: Youden's J statistic for calculating the optimal cut-off point for ROC analysis. 214

Equation 10-1: Equations for calculating lean body mass... 229

Chapter 1: Introduction

This thesis is based on some aspects of physiology and the imaging of brown adipose tissue (BAT). In this introductory chapter I shall explain what BAT is and why it is important to image it.

BAT is a discrete type of fat found exclusively in mammals [1] which is anatomically, biochemically, embryologically and functionally distinct from its more prevalent counterpart white adipose tissue (WAT) [2]. Brown and white adipose tissue have essentially antagonistic functions, which have evolved in response to external threats [3]. WAT acts as a reservoir to store excess energy (in the form of triglycerides) to protect against starvation, as well as being an insulator, and a source of cytokines and hormones that modulate metabolic activity and insulin resistance. BAT, in contrast, is a specialised thermogenic tissue which metabolises fatty acids and dissipates the energy as heat [2, 4, 5].

BAT was first described in 1551 by the Swiss physician and naturalist Konrad Gessner [6] who observed that hibernating European marmots (*Muris alpines*) "… have a lot of fat on their back, although the other parts of the body are lean. In truth it can be called neither fat nor flesh, but similar to the bovine mammary gland, it is something in between" (*Dorsum præpingue habent, quũ ceteræ corporis partes sint macræ. Quandꝫ hæc vere nec pinguitudo nec caro dici potest: sed ut mamillarũ caro in bubus, inter eas est medium quidda*) [7].

Enerbäck [5] credits the first description of BAT in humans to Shinkishi Hatai in 1905 when he wrote that embryos contained "…a gland which corresponded closely in position, general appearances and to some extent in structure, to the hibernating gland of lower mammals" [8]. As Bonnot [9] pointed out, Hatai was preceded by Merkel [10] who described a structure called "*Fettpolster*", and Charpy [11] who called it "*coussinet* *adipeux*" (fat pad). Nevertheless its metabolic significance as a thermogenic organ was not elucidated until 1961 [12].

BAT has been considered distinct from WAT in other cultures; in Mongolian folk medicine BAT (хүний мах translating loosely as 'human meat') has been used as remedy for pancreatitis (washed down with vodka), and to assist in the healing of wounds and fractures [13].

1.1 Biological significance of BAT

In temperate environments, heat generated by basal metabolism is generally sufficient to maintain body temperature. At lower temperatures, additional mechanisms are required to maintain thermal homeostasis and avoid hypothermia. These mechanisms include shivering and non-shivering thermogenesis. Shivering thermogenesis generates heat through sustained episodic contractions of antagonistic muscles, increasing ATP turnover and dissipating heat [14]. Non-shivering thermogenesis maintains core body temperature during periods of sustained cold [5] when thermal homeostasis cannot be maintained by shivering thermogenesis alone, and is exemplified by hibernation. The primary effector organ for non-shivering thermogenesis is BAT [15]. BAT tends to be abundant in small mammals including human neonates, who are predisposed to heat loss due to their high surface area to volume ratio, and in whom shivering thermogenesis and insulation by WAT are insufficient to maintain core body temperature [3].

At resting metabolic rate, non-shivering thermogenesis is thought to account for an average of 11.8% of total energy expenditure, albeit with high individual variation [16], but may be as high as 50% in small mammals when exposed to cold. Following cold exposure BAT is able to adaptively increase its capacity for thermogenesis such that if maximally stimulated (*e.g.* following administration of noradrenaline to cold-acclimatised rodents), can generate 300 times more heat per unit mass than any other tissue [17]. The rate of heat dissipation by BAT is approximately 160-190 mW and 330-480 mW per gram of BAT for warm and cold conditions respectively [18, 19]. It has been postulated that as little as 50g of brown adipose tissue, if maximally stimulated, could account for up to 20% of daily energy expenditure in an adult humans, equivalent to 20 kg of body weight per annum [20].

BAT may also have a role in dissipating excess chemical energy to maintain energy balance (*i.e.* diet-induced thermogenesis) and thereby help humans deal with a dangerously hypercaloric environment and still remain in good health, effectively acting as an energy buffer [5, 21]. In addition to metabolising glucose, activated BAT also has a role in lipoprotein homeostasis, and therapeutic manipulation of BAT may serve to reduce elevated serum triglycerides to combat obesity [22]. It has been suggested that BAT dysfunction may have a role in obesity [21, 23, 24] and predisposition to metabolic syndrome [25]. In humans, however, it is not clear whether decreased BAT activity causes obesity or vice versa [26]. The suggestion that BAT lowers susceptibility to obesity has, however, been criticised as being unphysiological [27-29].

Although BAT persists throughout life in rodents, in humans it was thought to be largely confined to neonates in whom it provided non-shivering thermogenesis to maintain core body temperature in the tumultuous immediate postnatal period [30-32].

BAT development commences in the 5th month *in utero* [33] reaching its peak at birth, before largely involuting in the first 9 months *post partum* [34]. In contrast WAT develops later and typically continues throughout life [35]. A histological study of adipose tissue excised from the neck of 35 patients undergoing thyroid surgery identified distinct islands of BAT in a third (typically those who were younger and leaner), indicating that BAT does involute with age [36]. Various mechanisms for the involution of BAT have been suggested [36] including infiltration of BAT depots by

WAT, transdifferentiation of brown adipocytes into white (but retaining the ability to revert to the BAT phenotype), or brown adipocytes merely disguising themselves as white.

Post mortem anatomical studies identified BAT in human adults in a similar distribution as in human neonates, *i.e.* supraclavicular fossa, axillae, neck and lesser quantities in the mediastinum and peritoneal cavity [37, 38]. BAT has also been reported in individuals exposed to low temperatures for prolonged periods [39], or those with hyper-adrenergic stimulation due to phaeochromocytoma [40, 41]. For the most part BAT was considered to be largely non-existent in adult humans under normal circumstances, and of little or no physiological relevance [2, 27]. It is now known, largely thanks to integrated positron-emission tomography with computed tomography (PET/CT), that BAT in humans is much more prevalent than previously thought [36, 42-44].

Therefore, modulation of adaptive thermogenesis through the manipulation of BAT presents a potential pharmacological target which may reduce elevated triglyceride levels and combat obesity [22, 45]. To test the efficacy of such pharmacological agents would require the development of a reliable biomarker to enable quantification of BAT. As a result there has been a resurgence in interest in brown adipose tissue in recent years.

1.2 Origins of BAT

1.2.1 Evolutionary origins

BAT is largely confined to endothermic placental (Eutherian) mammals, and was therefore believed to have originated approximately 140 million years ago (mya). More recently BAT has been identified in species of South American and Australian marsupials including the fat-tailed dunnart (*Sminthopsis crassicaudata*) implying the existence of a common primitive BAT organ by at least 150 mya [46].

1.2.2 Embryological origins

The embryological origin of BAT is a subject of on-going debate, though the consensus is that classical BAT and WAT are separate entities. Although brown adipocytes, together with white adipocytes, myocytes and chondrocytes, are of mesodermal origin [47], BAT and skeletal muscle precursors both express *Engrailed-1* (*En1*). This implies that both are derived from the central dermomyotome (derived from paraxial mesoderm) [48], while WAT is derived from lateral plate mesoderm [49]. Similarly brown adipocytes and myocytes also express the marker *Myogenic factor 5* (*Myf5*) while white adipocytes do not, implying a shared lineage for BAT and skeletal muscle with both being derived from a bi-potent precursor cell [47, 50, 51], although two separate lineages of *Myf5* positive cells is a possibility [3]. The Zn-finger transcriptional regulator *PRD1-BF1-RIZ1* homologous domain containing 16 (*PRDM16*) is thought to control a bidirectional cell fate switch that determines whether the *Myf5*+ progenitor cells differentiate into skeletal muscle myoblasts or brown adipocytes [50, 52]. *PRDM16* stimulates differentiation of brown adipocytes by binding to PPAR-γ (peroxisome proliferator-activated receptor-γ) receptors. Loss of *PRDM16* from brown adipocyte precursors results in them differentiating into skeletal muscle myocytes, while ectopic production of *PRDM16* has been shown to induce de-differentiation of skeletal muscle myocytes into brown adipocytes [50].

Bone morphogenetic protein 7 (*BMP7*) has also been shown to be a potent activator of brown adipocyte differentiation [53], and appears to regulate the *PRDM16* master switch [52].

A third class of adipocyte has also been described [52, 54, 55], which show a mixed morphology intermediate to that of BAT and WAT, scattered throughout areas of WAT These 'paucicellular adipocytes' have an mRNA signature which partly overlaps with that of classical BAT in humans [56]. They resemble white adipocytes insofar as they express low levels of the proton UCP1 (discussed below) which hitherto was considered characteristic of BAT, but do not express *Myf5*, implying that they are derived from a different cell lineage than the myoblast precursors [50], and are probably derived from pericytes surrounding blood vessels traversing WAT [47, 49] but not the vasculature of other tissues. Stimulation with cAMP results in high UCP1 levels, however, which is a characteristic of brown adipocytes [57].

Several mechanisms for the occurrence of these 'brown-like' adipocytes have been postulated [58, 59], including a dedicated lineage of brown adipocyte precursors derived from the WAT lineage, differentiation of white preadipocytes, and transdifferentiation of terminally differentiated mature white adipocytes to produce recruitable adipocytes. The consensus is that these recruitable 'brite' [60] or 'beige' [61] adipocytes are derived from transdifferentiated mature white adipocytes [62], and the process by which this occurs as 'browning'. Indeed it has been proposed that (in mice at least) most brown adipocytes scattered within WAT are in fact transdifferentiated beige adipocytes [62]. Supraclavicular BAT deposits in adult humans show some genetic similarities to murine beige adipose tissue, therefore it has been suggested that human adult BAT predominantly consists of beige rather than classical brown adipose tissue [57, 63], although it is now clear that they in fact co-exist [64]. Whether all white adipocytes possess the ability to undergo browning, or whether this is confined to a small sub-population remains unclear [65].

1.3 Anatomical distribution and histology of BAT

For the most part BAT is found in distinct anatomical sites [5, 37]; in children BAT occurs as a kite-shaped layer between the scapulae, axillae, supraclavicular fossae extending into the neck and beneath the clavicles. Smaller deposits also occur within the thorax deposits (in close proximity to the heart, trachea and mediastinal vessels) and upper abdomen including peri-renal and peri-adrenal regions [38, 66]. This distribution has been likened to a ‘heating jacket’ [14] which acts as a warming mechanism for blood supplying the vital organs [3]. In addition peri-renal and suprarenal BAT deposits are recognised. The distribution of BAT in human adults is largely derived from ^{18}F-FDG PET/CT studies, and tends to occurs within supraclavicular fossae, neck, paravertebral and suprarenal regions [38, 43, 44].

As described above, in addition to classical BAT depots, brown adipocyte-like cells have been identified scattered throughout larger areas of WAT. These comprise a distinct group of adipose tissue which share some of the histological characteristics of BAT, but appear to be derived from WAT. These beige adipocytes appear to be derived from the pericytes surrounding blood vessels in WAT [36] and may therefore occur in atypical sites unlike classical BAT.

1.3.1 Histology

There are macroscopic and microscopic differences between BAT and WAT. White adipocytes are typically large (25-200 μm) unilocular spherical cells featuring a single large vacuole containing triglycerides which comprises more than 90% of the cell volume. Brown adipocytes are comparatively smaller (15-60 μm) multilocular polygonal cells which contain multiple small lipid vacuoles, and characteristically contain numerous large mitochondria [67], which give rise to the eponymous brown colouration of BAT [68]. In addition the mitochondria show a high density of laminar cristae, increasing the available surface area on the inner membrane [69], implying high metabolic activity. Mitochondria in white adipocytes tend to be thin, elongated and variable in number.

Brown adipocytes typically occur in clusters forming islands interspersed within WAT in both rodents [70] and humans [36], but do not necessarily occupy an entire fat lobule, which may explain why BAT may not always be visible macroscopically. In addition BAT was thought to involute with increasing age, eventually becoming largely indistinguishable from WAT [30].

BAT has a rich matrix of capillaries, up to 4-6 times denser than in WAT [36, 71]. This likely reflects the increased demand for oxygen and substrates necessary for non-shivering thermogenesis, and to redistribute and dissipate heat [72]. When thermogenesis is activated, blood flow through interscapular BAT increases more than ten-fold, which together with other BAT deposits can take up 25% of cardiac output [18]. In rodents, activated BAT can account for up to 50% of total oxygen consumption in the cold [73].

BAT characteristically has dense sympathetic innervation, at least 10-fold higher than in WAT [36]. β_1-, β_2- and β_3-adrenoceptors have been identified, of which β_3 are the most significant [2, 74], which enable BAT to respond to fluctuations in temperature. The exception to this is pericardial and mediastinal BAT which also has parasympathetic innervation [75].

In addition, cells characterised by a distinct basal membrane, glycogen particles, and mitochondria devoid of cristae have been identified within BAT islands in human adults, which could potentially represent brown adipocyte precursors in adult humans [36].

1.4 Physiology including non-shivering thermogenesis

In eukaryotic cells mitochondria store energy in the form of a proton gradient across the inner mitochondrial membrane. The energy released when protons flow along this gradient (proton motive force) is used to synthesise adenosine triphosphate (ATP) and is mediated by the enzyme ATP synthase which forms the basis of oxidative phosphorylation. The proton gradient is maintained by electron-driven proton pumps, leading to oxygen consumption. Inevitably some protons leak through the mitochondrial membrane, following the proton gradient by-passing ATP synthesis (uncoupling), instead being dissipated as heat [2]. This is a normal phenomenon in all mitochondria and accounts for approximately 15% of oxygen consumption in mammals *in vivo* [76].

BAT is unique in that it is able to totally uncouple oxidative phosphorylation and dissipate all proton motive force generated from fatty acid metabolism as heat [77]. This is mediated by uncoupling protein 1 (UCP1 or 'thermogenin'), a 32 kDa transmembrane protein which increases permeability of the mitochondrial inner membrane thereby dissipating the proton gradient [2, 78, 79]. This process is very inefficient, and requires uptake of substrate from the surrounding tissues and circulation, in particular free fatty acids and glucose.

UCP1 is activated by noradrenaline release from sympathetic nerve endings which activate β_3-adrenergic receptors on the plasma membranes of brown adipocytes. This triggers an intracellular cascade in which adenylyl cyclase catalyses conversion of ATP to cyclic AMP (cAMP), which in turn activates protein kinase A. Protein kinase A phosphorylates triacylglycerol lipase, which catalyses the conversion of triacylglycerols into free fatty acids, which in turn activates UCP1 in the mitochondrial membrane [2]. The mechanism by which fatty acids activate UCP1 is unclear, but they may act as allosteric regulators, co-factors or proton shuttles [2].

Catecholamines and thyroid hormones have also been implicated in BAT activation. Activated protein kinase A phosphorylates deiodinases, resulting in local conversion of thyroxine (T4) into its active form tri-iodothyronine (T3) [80]. T3 binds to intracellular thyroid hormone-sensitive receptors in brown adipocytes to further amplify catecholamine-induced UCP1 transcription [81]. Stimulation of β_3-adrenergic receptors on the cell membrane further increases the intracellular concentration of T3 by means of type 2 5’ deiodinase [82]. The importance of sympathetic innervation in BAT function is highlighted by the discovery that surgical sympathetic denervation abolishes glucose uptake within BAT [83, 84]. Sympathetic innervation to BAT is regulated by the lateral hypothalamus, through melanocortin signalling [85]. Consequently central nervous system depressants including volatile anaesthetic agents suppress BAT [86].

UCP1 was once considered to be the unique immunohistochemical protein marker for BAT [87], with other genetic markers showing only relative quantitative differences between BAT and WAT, for example the homeobox genes *HoxC8* and *HoxC9* are more highly expressed in WAT (and beige) fat than BAT [51, 64]. *HoxC9* is much more abundant in beige fat than WAT.

Differences in the genetic expression profiles between human adult and neonatal BAT have also been reported, with *HoxA1* and *HoxC4* being preferentially expressed in human foetal BAT, and *HoxA4* and *HoxC8* being more abundant in human adult BAT [35]. Furthermore, UCP1 differs between mammals, with the human protein being 1 kdalton smaller than that of the rat [79].

Increasingly the reliability of UCP1 as a marker of BAT activity has been called into question. In several species of domestic pigs and wild boars, for example, the UCP1 gene is non-functional [88]. Furthermore UCP1 is not specific to BAT, as it is also expressed in beige adipocytes [56]. Novel genetic makers, specifically *Zic1* show greater specificity for classical BAT than does UCP1 [64].

1.5 The dynamic nature of BAT

The plasticity of adipose tissue in response to external stress is recognised. In this instance the term plasticity refers to the variable phenotype and fluctuating metabolic activity of BAT. In mice, retroperitoneal adipose tissue changes from a white phenotype, to brown, and then back to white during the first few weeks *post partum* [89]. Administration of the β_3-adrenoceptor agonist CL316,243 has been shown to induce transdifferentiation of terminally differentiated mature white adipocytes into brown in mice [62]. Administration of PPAR-γ (peroxisome proliferator-activated receptor-γ) agonists (*e.g.* rosiglitazone) has also been shown to induce UCP1 expression in human white adipocytes, leading to the 'browning' of white adipocytes [90, 91]. Transdifferentiation of white adipocytes to brown has also been shown *in vivo* in phaeochromocytoma [92].

As described above, both BAT and the newly discovered beige fat are not fixed depots, but are highly dynamic and plastic which greatly affects the total capacity for non-shivering thermogenesis. Apoptosis plays a major role of BAT degeneration, and is induced by tumour necrosis factor α (TNFα) [93]. It is noteworthy that TNFα levels are elevated in obese humans, and that resulting BAT dysfunction may be causative in obesity and metabolic syndrome [94, 95]. Conversely obese rats, when exposed to prolonged cold, showed a reduced level of apoptotic brown adipocytes than at thermoneutrality [93]. To date no direct evidence of BAT apoptosis in human adults has been reported.

1.5.1 Cold and BAT activity

The amount of BAT is dependent on tissue recruitment which may require days or weeks and requires chronic sympathetic stimulation, whereas activity is regulated by acute sympathetic stimulation [2]. Acute cold exposure has been shown to induce UCP1 mRNA expression [96, 97]. Meyer *et al.* [98] showed that a 23g wild type B6 mouse increased its maximal heat production to 750 mW at thermoneutrality, which when housed at 18°C for 3 weeks this increased to 1,000 mW, and increased further to 1,200 mW when housed at 5°C. This suggests that, at least in mice, BAT undergoes adaptive hyperplasia in response to sustained cold [99].

The same pattern has been identified in beige adipocytes. The appearance of UCP1-immunoreactive brown adipocytes has been reported within WAT after sustained cold exposure (6°C for 10 days) without a corresponding increase in the number of adipocyte precursors. This implies that beige adipocytes are derived from terminally differentiated white adipocytes, and like classical brown adipocytes, are also stimulated by cold exposure mediated by β_3-adrenoceptor stimulation [62].

Conversely loss of UCP1 in mice has been shown to result in an increase in cold sensitivity and an inability to maintain body temperature during 24 hours of cold exposure [100].

Cold-exposure has been shown to mediate BAT throughout β-adrenergic activation [2, 101, 102]; sustained cold exposure over the course of days or weeks increases the total capacity for thermogenesis [95, 103]. In hamsters, ATPase activity in BAT mitochondria increases within brown adipocytes in response to cold [104].

The mechanism of BAT activation is likely a combination of transdifferentiation of WAT and recruitment of latent brown adipocytes. The speed with which BAT can be activated following short periods of cold exposure implies latent BAT deposits, as it is unlikely that BAT (or brown fat) can proliferate in such a short period of time [105].

Other stimuli which stimulate sympathetic outflow to BAT (*e.g.* baclofen) have also been shown to lead to increased metabolic rate and thermogenesis [106].

1.5.2 Age and BAT activity

Thermoregulation diminishes with age in both humans [107] and rodents [108, 109], which may manifest as decreased cold tolerance [110]. Reduced expression of UCP1 mRNA has been reported with increasing age [111, 112], implying a decrease in BAT thermogenic capacity [113]. This has been attributed to age-related BAT atrophy, which appears, at least in part, to be due to abnormalities in adrenergic signalling [114]. The age-related decline in BAT functionality is less pronounced in females than males [115].

Gene profiling studies suggest that UCP1 mRNA expression is an unreliable marker of BAT activity [116].

1.5.3 Obesity and BAT activity

There is compelling evidence of a link between obesity and BAT status. Individuals with low BMI are more prone to feeling cold, and as a result more likely to induce non-shivering thermogenesis by sympathetic nervous system stimulation [117]. *Post mortem* studies have shown larger accumulations in BAT in individuals with low BMIs [118].

BAT dysfunction or absence has not only been shown to lead to impaired non-shivering thermogenesis but also an increased propensity to obesity in rodents [119], which may persist into adulthood [120]. BAT ablation in mice has been shown to induce obesity [121] and abolish diet-induced thermogenesis [119].

There is also evidence of a blunted cold-induced non-shivering thermogenesis in obesity implying differences in BAT activity [16].

1.6 Therapeutic importance of BAT

Obesity is major global public health problem [122]. The prevalence of obesity has doubled since 1980, with approximately 1.4 billion adults being overweight (*i.e.* body mass index >25 kg/m^2) in 2008, of whom 500 million were obese (body mass index >30 kg/m^2) [123]. The problem is increasingly common in low- and middle-income countries, such that 65% of the world's population now live in countries where being overweight or obese kill more people than malnutrition. Furthermore, 44% of diabetes cases, 23% of ischaemic heart disease and 7-41% of cancers are attributable to being overweight or obese [123].

Obesity occurs as a result of chronic imbalance between energy intake and expenditure. It has been suggested that humans are evolutionarily maladapted to the modern obesogenic and thermo-regulated environment. This has lead to an abundance of food and the adoption of a sedentary lifestyle resulting in accumulation of excess WAT [124].

It has been suggested that BAT evolved to safely dissipate large amounts of chemical energy from excess food intake (a process known as diet-induced thermogenesis) [5], including clearance of glucose [125] and triglycerides [22]. This role for BAT as an energy sink affording protection against obesity has been criticised as being unphysiological [27-29].

This phenomenon might be harnessed to help humans deal with a dangerously hypercaloric environment and still remain in good health [5]. Recruitment and activation of BAT may be used as a means of protecting the animal against obesity [23, 117].

Although some studies have suggested that the impact of BAT mediated non-shivering thermogenesis is small in adult humans [126], the increasing prevalence of obesity throughout the world, and the possibility that BAT is much more prevalent than was previously thought, may be sufficient to contribute to weight loss over time. This has triggered a resurgence of interest in BAT modulation as a potential anti-obesity strategy. Much of the work evaluating BAT prevalence on imaging has involved PET/CT, and more recently magnetic resonance (MR) imaging. These imaging techniques will be discussed in more detail in their respective chapters.

Multiple retrospective observational studies of BAT prevalence on ^{18}F-FDG PET/CT scans suggest a point prevalence under 10% [38, 127-136], while dedicated prospective studies indicate a much higher prevalence of between 36% and 96% [42, 43, 113, 125]. Age, sex, BMI and temperature have been shown to be significant determinants of BAT prevalence of ^{18}F-FDG PET/CT. These will be explored in further detail later in this thesis.

Some patients may have a genetic predisposition to BAT thermogenesis, which would explain why some individuals maintain a lean body habitus with minimal effort [117]. Following the recent discovery of beige fat, and the discovery of brown adipocyte precursors in adult humans there is the potential for stimulating non-shivering thermogenesis in individuals lacking classical BAT.

1.7 Overview of the thesis

In this thesis we shall explore the role of two imaging modalities: ^{18}F-FDG PET/CT and MR imaging.

After introducing the basic principles of positron emission tomography in chapter 2, we shall analyse retrospective PET/CT data to determine the demographics of the patient group, predictors that influence the prevalence, volume and activity of BAT. Following on from this, we shall analyse patterns of BAT uptake on sequential PET/CT scans to determine whether BAT occurs in fixed depots. These will comprise chapters 2-6.

The basic principles of MR imaging, and their application in BAT imaging will be introduced in chapter 7. In chapter 8 we shall attempt to characterise the appearances of BAT on MR, and in chapter 9 we shall explore whether these characteristics can be used to prospectively identify BAT on MR.

Each chapter will be followed by a brief summary of the results, but more detailed discussion will take place in chapter 10.

Chapter 2: Identification and quantification of brown adipose tissue (BAT) on positron emission tomography with computed tomography (PET/CT)

2.1 Basic principles of ^{18}F-FDG PET/CT

Positron emission tomography (PET) is a functional imaging modality that measures metabolic activity within the body following injection of a radionuclide-labelled tracer molecule. The commonest tracer is 2-deoxy-2-[^{18}F]fluoro-D-glucose (^{18}F-FDG), comprising the glucose analogue deoxyglucose attached to a radioactive positron-emitter (^{18}F) substituted for a hydroxyl group at the 2' position (Figure 2-1). Like glucose, ^{18}F-FDG is taken up by mitochondria, within all metabolically active tissues. where it becomes phosphorylated by hexokinase as part of the glycolytic metabolism pathway. Unlike glucose, which undergoes further glycolysis by phosphohexokinase isomerase, ^{18}F-FDG becomes trapped intracellularly as FDG-6-PO_4 (Figure 2-2) as it lacks the requisite hydroxyl group at position 2' [137].

Figure 2-1: Chemical structure of D-glucose and ^{18}F-FDG.

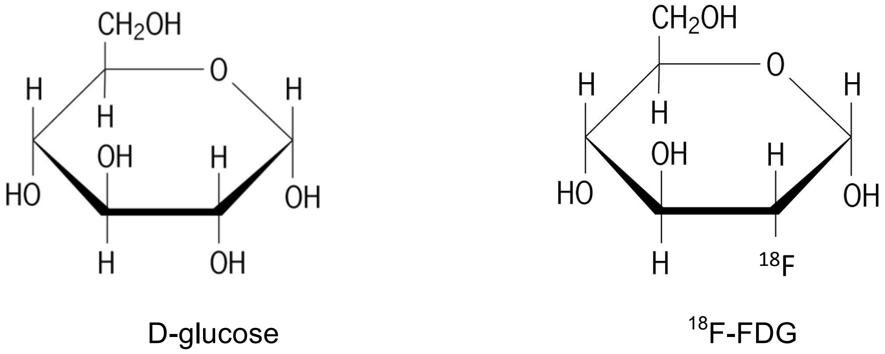

Malignant tumours typically have normal to low levels of glucose-6-phosphatase activity [138]. Glucose-6-phosphatase activity is higher in BAT than in WAT, particularly following cold exposure [139]. If high levels of glucose-6-phosphatase are present, the phosphate group may be cleaved off from the molecule to regenerate ^{18}F-FDG which then diffuses back out of the cell to be taken up by the bloodstream for uptake elsewhere.

Figure 2-2: Facilitated transport and metabolism of ^{18}F-FDG. The dephosphorylation reaction involving glucose-6-phosphatase occurs slowly within malignant cells, resulting in intracellular accumulation of ^{18}F-FDG (Glut-1 = glucose transporter). Adapted from Kapoor *et al.* [140] and Kelloff *et al.* [141].

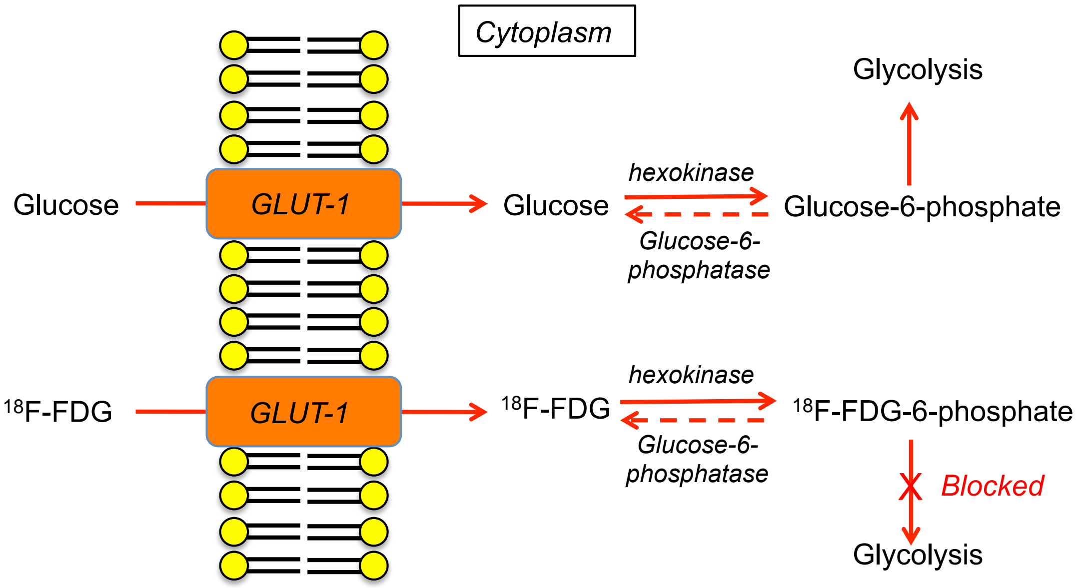

^{18}F is the preferred radioisotope due to its relatively long half-life of 110 minutes, which allows adequate time for preparation, testing and transport, although ^{11}C, ^{13}N, ^{15}O and ^{82}Rb have been also used. Being radioactive, ^{18}F is unstable and decays by emitting positrons (positively charged electrons, β+) from the nucleus. The positrons travel a short distance through tissue before interacting with their antiparticle (an electron), resulting in the annihilation of both. Their combined mass is converted into two 511 keV photons (according to Einstein's mass-energy equivalence formula $E = mc^2$) at 180° (± 0.5° depending on the speed of the positrons) to each other [142] (Figure 2-3).

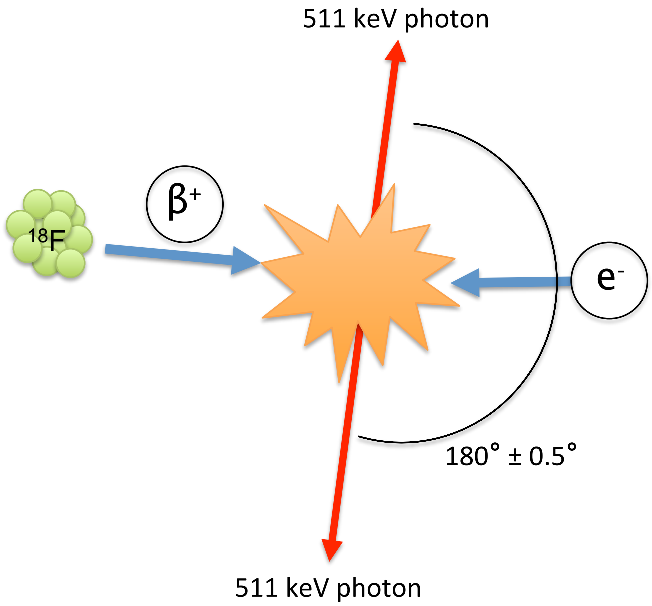

Figure 2-3: The basic principle of PET: a positron interacts with an electron resulting in their mutual annihilation, which emits two 511 keV photons in opposite directions.

The simultaneous detection of two coincident photons in opposite detectors along the line of response (a straight line connecting two photons and the detectors) allows the source of the positron emission to be triangulated (Figure 2-4). The necessity for simultaneous detection (within a window of approximately 10 x 10^{-9} seconds) of two photons in opposite detectors for a signal to be registered is termed 'electronic collimation', and affords a much greater spatial resolution than the traditional mechanical collimation provided by lead filters used in SPECT (single-photon emission computed tomography) scanners for example.

The gamma rays interact with a circular array of detectors comprising multiple (10,000 – 20,000) scintillation detectors (which convert the gamma rays to visible light) and photomultiplier tubes. The scintillation crystals are most commonly bismuth germinate (BGO), but lutetium oxyorthosilicate (LSO), gadolinium orthosilicate (GSO) are also used. The visible light is then converted to electrons by photomultiplier tubes (the number of electrons produced being proportional to the energy of the incident photons), which are processed digitally to form the image.

The spatial resolution of PET is therefore determined by three factors: the distance travelled by the positron prior to annihilation (typically 0.5 – 2 mm depending on energy), the variation in angle of incidence of the two 511 keV photons generated following annihilation, and the size of the detectors (1 – 3 mm). As a result, modern PET scanners have a resolution of approximately 4 – 7 mm, resulting in slightly blurred images [143].

Figure 2-4: Diagram of a PET detector ring array showing two photons from a single annihilation event interacting simultaneously with opposing scintillation crystals along a single 'line of response'. By convention axial images are displayed as if standing at the patient's feet.

2.2 Integration of PET with CT

To enable more accurate anatomical localisation of ^{18}F-FDG uptake, PET scanners are now combined with a multi-detector computed tomography (CT) scanner mounted on a single gantry. This enables the functional PET data an anatomical CT data to be acquired in rapid succession thereby minimising patient movement, allowing image co-registration and fusion to be performed.

Furthermore, the integration of CT enables attenuation correction to be performed upon the PET data [144]. This corrects for the fact that photons produced in the centre of the body are attenuated or scattered to a greater degree than those produced superficially, resulting in a spuriously low measurement of radioactivity.

Although the concept of tomography was conceived in 1826, the first CT examination and the development of the first functional CT scanner are credited to Sir Godfrey Hounsfield in 1971 and 1973 respectively [145, 146]. The term 'tomography' is derived from the Greek adjective *tomos* (τομώτερος, slice) and the verb *graphein* (γράφω, to write). CT provides high-resolution structural imaging by acquiring multiple x-ray projections of cross-sectional slices through an object.

The scanner comprises an x-ray tube mounted on a rotating gantry and an arc housing hundreds of x-ray detectors (or multiple arcs in the case of multiple slice scanners). The x-rays are produced by applying a high voltage across the cathode, is mounted within the evacuated x-ray tube, which in turn emits electrons. These bombard an anode composed of tungsten, rhenium or molybdenum to produce x-rays. The x-ray tube and detector bank rotates around the subject, emitting x-rays throughout from multiple angles - approximately 1,000 projections in every 360° rotation [147]. The x-rays are differentially attenuated by tissues according to the atomic mass of their constituent atoms, and transmitted x-rays are then detected by photosensitive diodes in the detectors.

Images are digitally reconstructed, typically using a form of filtered back projection, in which the x-ray attenuation for each voxel ('linear attenuation coefficient') is averaged and calibrated with respect to the attenuation of water (Equation 2-1). The resulting averaged CT attenuation values (eponymously called 'Hounsfield units' in honour of the CT pioneer Sir Godfrey Hounsfield) for each voxel are presented graphically as an image. This technique almost abolishes the effects of x-ray scatter, which would otherwise cause blurring of the image. As a result, even the earliest commercially available CT scanners had a contrast resolution (the ability to distinguish between objects of similar densities) approximately 100 times greater than plain x-rays [145]. Consequently tissues may oftentimes be differentiated on the basis of their CT attenuation (Table 2-1).

Equation 2-1: Equation for calculating CT number (CT_n); μ_t = linear attenuation coefficient of tissues, μ_W = linear attenuation coefficient of water [147].

$$CT_n = 1000 \times \frac{\mu_t - \mu_w}{\mu_w}$$

Table 2-1: Range of CT attenuation values for various tissues [147].

Tissue	Range of CT numbers (Hounsfield units)
Bone	500-1,500
Muscle	40-60
Brain (grey matter)	35-45
Brain (white matter)	20-30
Water	0
Adipose tissue	-60 to -150
Lung	-300 to -800
Air	-1,000

2.3 Scanning protocol

Adequate preparation is required to maximise the diagnostic yield of PET scanning [137]. Serum glucose should be within normal range, as high levels of free glucose compete with ^{18}F-FDG, resulting in lower radiotracer uptake and image degradation. To this end patients are fasted for a minimum of four hours prior to scanning [140]. Hyperglycaemia may be treated with administration of 2-5 units of insulin, and the serum glucose level rechecked prior to ^{18}F-FDG administration. There is some disagreement over this, as insulin drives glucose transport into muscle, adipose tissue and myocardium, which may exaggerate physiological uptake [140].

Abstinence from caffeine, nicotine and alcohol in the 24 hours before the scan is recommended to minimise physiological myocardial uptake [140]. Some centres advocate a low carbohydrate/high protein/high fat diet on the preceding day to the same end [148].

To minimise physiological muscle uptake exercise is kept to a minimum on the day of scanning, and the patient instructed to rest following ^{18}F-FDG administration. Patients are also kept warm to minimise physiological uptake within BAT [129].

The scan is obtained 50-70 minutes following intravenous injection of the radio-labelled tracer ^{18}F-FDG. This allows sufficient time for trapping of the radiotracer within metabolically active tissue, whilst minimising the amount of residual radioactivity within the plasma and extracellular fluid [149].

2.4 Clinical applications of PET/CT

Most tumour cells are highly metabolically active, exhibiting higher mitotic rates [150, 151]. Over-expression of GLUT glucose transporters and hexokinase [151-153], and therefore higher rates of glucose metabolism than normal tissue making ^{18}F-FDG PET/CT useful in the detection and staging of cancer and its metastases, and in the monitoring of treatment response [141]. The sensitivity and specificity of PET (without integrated CT) in cancer are approximately 84% and 88% respectively [154]. ^{18}F-FDG is not specific and also accumulates in any metabolically active tissue including inflammation and infection. Consequently, ^{18}F-FDG PET/CT has also been used successfully in the assessment of myocardial viability [155], Alzheimer disease [156], pyrexia of unknown origin [157], granulomatous and vasculitic diseases [158-160], and Crohn’s disease [161] to name but a few. Normal physiological ^{18}F-FDG uptake occurs within the brain, myocardium, liver, bowel and urinary tract [162], typified by Figure 2-5.

Figure 2-5: Maximum intensity projection (MIP) PET image performed on a 71-year old male showing physiological ^{18}F-FDG uptake within brain, myocardium, liver, urinary tract and liver.

Most tumours and their metastases manifest as areas of increased ^{18}F-FDG uptake on PET (Figure 2-6). The degree of radiotracer uptake may be quantified and expressed in terms of the amount of radioactivity per unit volume. This 'standardised uptake value' (SUV), which is corrected for body weight and the injected dose of ^{18}F-FDG (Equation 2-2:), is a practical semi-quantitative index for ^{18}F-FDG uptake [163] which may be used as a biomarker to assess treatment response [164, 165]. SUV is also useful in differentiating between malignant and benign tumours [163]. An SUV of 2.5 g/ml is typically taken as the threshold, above which uptake is considered suspicious for malignancy, although this threshold may not be applicable in all cases [166].

Equation 2-2: Calculation of standardised uptake value. ‘ROI’ = region of interest, ‘injected dose’ = decay-adjusted injected dose of radiotracer, ‘body weight’ is used as a surrogate for the volume of distribution of radiotracer.

$$SUV\ (g/ml) = \frac{average\ activity\ in\ ROI\ (MBql/ml)}{injected\ dose\ (MBq)} \times body\ weight\ (g)$$

Figure 2-6: MIP PET image (left) and coronal fused PET/CT image (right) of a 71-year old male, showing avid ^{18}F-FDG uptake within a bronchogenic carcinoma within the right lung (red arrow). A metastatic deposit within a mediastinal lymph node (yellow arrow) evident on the MIP image is not evident on the fused PET/CT image.

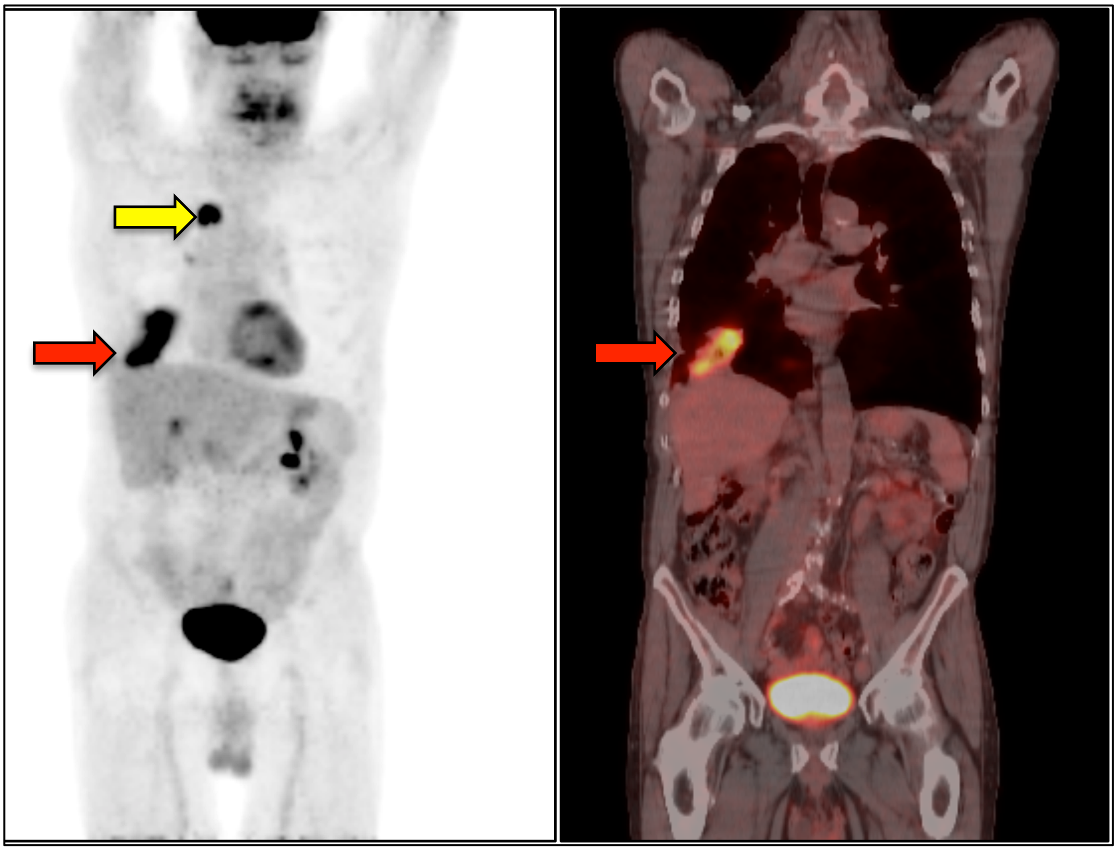

As a result of the correction for body weight, SUV measurements are semi-quantitative, but are subject to certain limitations. The SUV has a strong positive correlation with weight [167] as the SUV equation assumes that all the weight corresponds to glucose metabolising mass, when in fact this additional tissue is mostly adipose tissue which accumulates minimal ^{18}F-FDG in the resting state [168]. Lean body mass (LBM) has been suggested as an alternative, but may be limited by the fact that LBM varies with age, which SUV calculations do not take into account [167].

The delay between ^{18}F-FDG administration and scanning is an important determinant of SUV. It takes 1-2 hours for ^{18}F-FDG to become phosphorylated and trapped intracellularly, after which ^{18}F-FDG uptake plateaus [169]. To scan too early would generate artificially low SUV measurements; conversely delayed scans will yield high SUVs.

SUV measurements may be spuriously low in small lesions due to them being below the spatial resolution of the detectors resulting in ‘volume averaging’ or ‘partial volume’ effects [170, 171], but any lesion below 3 cm may be too small to measure accurately [137]. Furthermore, in areas of mis-registration between PET and CT images, for example in areas of respiratory motion, incorrect attenuation correction may cause SUV to vary by as much as 30% [172].

The high ionising radiation dose of PET/CT can be justified when performed for the diagnosis, staging and monitoring of cancer and its metastases. The utility of PET/CT in other situations is limited by its substantial effective radiation dose; a multicentre study of PET/CT doses in Germany reported an effective dose of 23-26 mSv for a 70 kg person [173], and the dose is similar in the UK [174]. The 2005 review of the Ionising Radiation Exposure of the UK Population [175] identified that the PET component contributes approximately 8 mSv, while the dose from the CT is dependent on the extent of the body scanned, but is in the order of 5 mSv for a CT thorax, 8.7 mSv for a CT abdomen, 4.9 mSv for a low dose CT of the abdomen and 16.6 mSv for a CT of the neck, chest and abdomen [176]. To put this into perspective the mean annual UK ionising radiation dose is approximately 2.7 mSv, of which 84% is derived from natural background radiation [175].

2.5 Identification of BAT on ^{18}F-FDG PET/CT

2.5.1 Incidental discovery and prevalence of BAT on ^{18}F-FDG PET and PET/CT

In 1996, shortly after the commercial introduction of PET, Barrington *et al.* described avid symmetrical ^{18}F-FDG uptake occurred within the neck, thorax and paravertebral regions [177], as demonstrated in Figure 2-7. Without the benefit of anatomical localisation afforded by concomitant CT this was interpreted as muscle uptake, as it disappeared following administration of diazepam (a benzodiazepine muscle relaxant) on repeat PET scanning. Other authors reported that diazepam had no effect on ^{18}F-FDG BAT uptake, but instead found that propranolol was more effective [178].

Figure 2-7: MIP PET performed in a 26-year old female showing physiological ^{18}F-FDG uptake within the neck and supraclavicular fossae consistent with BAT.

Although this novel pattern of ^{18}F-FDG uptake was observed to be typically symmetrical in predictable locations, asymmetrical distributions were also reported in unusual locations [179, 180] which could mimic pathological uptake. Furthermore large quantities of BAT may also reduce the sensitivity of PET in assessing cancer by decreasing the available pool of ^{18}F-FDG [181]. Consequently PET protocols evolved to minimise this potential source of false positives (see section 2.3), including keeping subjects warm, high fat and low carbohydrate diets prior to fasting [182] and administering pharmacological agents to suppress BAT activity including propranolol [183].

With the commercial introduction of integrated co-registered PET/CT in 2001, it became possible to localise this uptake thereby reducing the likelihood of erroneous false positive diagnoses being made [184]. Hany *et al.* [131], Cohade *et al.* [185] and Yeung *et al.* [186] soon identified that this uptake occurred largely within areas of adipose tissue attenuation (Figure 2-8) on CT, and postulated that what later became known as 'USA-fat' (uptake in the supraclavicular area fat) may in fact represent BAT as the distribution of USA-fat on PET/CT was similar to that of BAT already described in *post mortem* human studies [37]. In 2007 Nedergaard *et al.* [101] analysed the radiological literature from a physiological perspective and concluded that there was overwhelming evidence that this this tissue did represent BAT.

Figure 2-8: (a) Maximum intensity projection PET, (b) fused coronal and (c) axial PET/CT images in a 17-year old male with a testicular germ cell tumour metastasis in the right lung showing the typical symmetrical pattern of ^{18}F-FDG BAT uptake within the supraclavicular fossa and paravertebral regions.

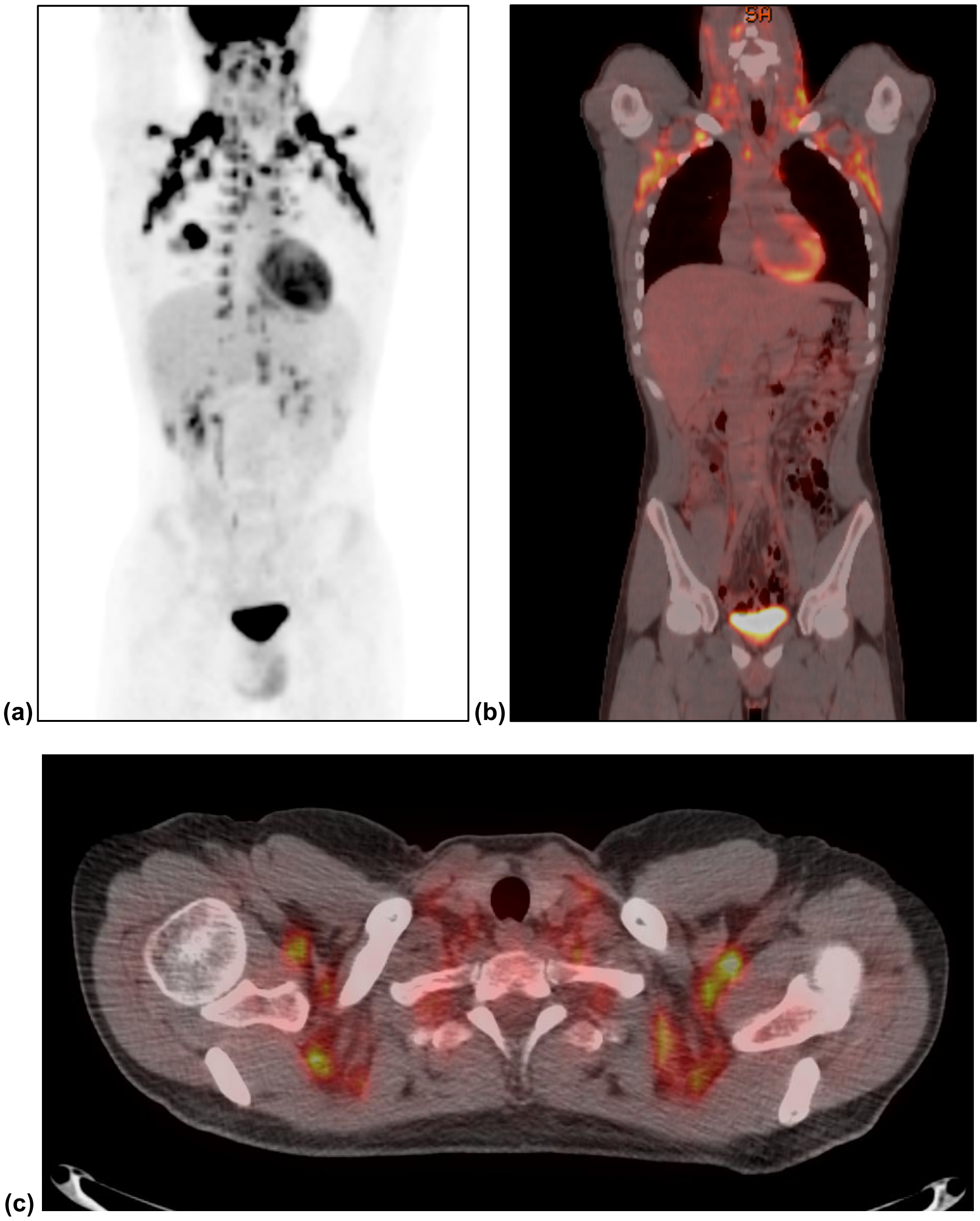

2.5.2 Evidence that ^{18}F-FDG uptake within fat represents BAT

Pathological studies had shown that BAT was prevalent in adult humans; a post-mortem study of 31 adults identified histological evidence of BAT in 26 (84%) [37].

The first immunohistochemical proof that this avid ^{18}F-FDG uptake did indeed represent BAT came in 2007, when Virtanen *et al.* [44] obtained tissue samples from areas of supraclavicular ^{18}F-FDG BAT uptake in three adult human volunteers. The samples were subjected to immunohistochemical staining using the anti-UCP1 antibody, which confirmed BAT. Further studies have demonstrated UCP1 in human tissue specimens taken from the neck [36, 38, 187], supraclavicular fossae [42-44, 105], mediastinum [188] and suprarenal [34] regions. In only four of these [44, 105, 187, 188] were the samples taken from areas of ^{18}F-FDG BAT uptake on PET/CT, of which one was authored by our own team [188]. Lee *et al.* [105] performed immunohistochemical and quantitative polymerase chain reaction (PCR) analyses on samples of fat taken from the supraclavicular fossae and subcutaneous tissue in 17 patients with head and neck cancer: Three ^{18}F-FDG BAT positive patients and 14 negative patients. All 17 subjects showed characteristic histological features of BAT within the supraclavicular fat and expressed the UCP1, PRDRM1, NDUFS3 (NADH dehydrogenase (ubiquinone) iron-sulphur protein 3) and β_3-adrenoceptor transcripts characteristic of BAT. UCP1 levels in subcutaneous fat on the other hand were barely detectable. Similar findings were reported by Lee *et al.* [187] and Van Marken Lichtenbelt *et al.* [43] who also identified strong UCP1 expression in samples of putative BAT but not in WAT.

Zingaretti *et al.* [36] performed immunohistochemical analysis on fat samples from the neck of 35 patients undergoing surgery for thyroid diseases. Distinct islands of BAT were identified 10 patients (28.6%), on the basis of characteristic histological appearances and positive UCP1 staining. No correlation with PET/CT was performed however.

These studies provide compelling evidence that areas of ^{18}F-FDG uptake within fat do represent BAT based on UCP1 expression, while areas of non-^{18}F-FDG avid fat (*i.e.* WAT) do not. As discussed in chapter 1, following the discovery of a separate population of beige adipocytes, which are derived from a separate lineage, but also express UCP1 [60], the classical definition of BAT on the basis of UCP1 expression may be an oversimplification. Furthermore, the transcription factor PRDM16 which was previously associated with classical BAT [50], has also been identified in beige adipocytes. Nonetheless Nedergaard *et al.* [189] are of the opinion that BAT identified in humans most likely represents classical BAT.

2.5.3 Prevalence of ^{18}F-FDG BAT based on retrospective studies

There is enormous variation in the reported prevalence of ^{18}F-FDG BAT (summarised in Table 2-2), ranging from an overall prevalence of 1.1% in a large retrospective study of 6,005 PET/CT scans in South Korea [190], to 45% in a small French study analysing serial PET/CT scans in 33 women undergoing treatment for breast cancer [191]. A large retrospective study of 8,640 patients' PET scans by Garcia *et al.* [192] reported a prevalence of 0.34%, but their inclusion criteria were extremely strict and all patients with proven or suspected head and neck cancer were excluded (as they did not have integrated PET/CT scanners to assist in anatomical localisation), as were those who had received treatment between scans (presumably for cancer). Therefore this value is undoubtedly a conservative estimate.

^{18}F-FDG BAT prevalence varies according to the cohort was being studied. Typically retrospective studies evaluating heterogeneous adult samples report ^{18}F-FDG BAT prevalence below 10% [38, 127-136, 182, 186, 187, 190, 193-199]. A higher prevalence has been reported in certain homogenous groups, including women [191], young adults and children [200], and patients with phaeochromocytoma [201] all of whom are known to have a higher prevalence than average.

Table 2-2: Retrospective studies of BAT prevalence on PET/CT.

Year	Authors	City	No of BAT+ subjects	No of subjects	Prevalence
2002	Hany *et al.* [131]	Zurich, Switzerland	17	638	2.5%
2003	Yeung *et al.* [186]	New York, USA	20	863	2.3%
2003	Cohade *et al.* [129]	Baltimore USA	68	1,017	6.7%
2004	Truong *et al.* [135]	Houston, USA	15	845	1.8%
2006	Rousseau *et al.* [191]	Nantes, France	(74)	33 (163[a])	45%
2007	Hadi *et al.* [201]	New York, USA	16	83[b]	19.3%
2007	Kim *et al.* [194]	New York, USA	35	1,159	3.0%
2008	Fang *et al.* [193]	Qingdao, China	12	457	2.6%
2008	Williams and Kolodny [182]	Boston, USA		1972	5%
2009	Au-Yong *et al.* [127]	Nottingham, UK	167	3614	4.6%
2009	Cypess *et al.* [38]	Boston, USA	106	1,972	5.4%
2009	Cheng *et al.* [128]	Beijing, China	41	1,080	3.8%
2010	Garcia *et al.* [202]	Washington, DC, USA	30[c]	8,640	0.34%
2010	Jacene *et al.* [132]	Baltimore, USA	56	908	6.2%
2010	Lee *et al.* [187]	Sydney, Australia	250	2,934	8.5%[d]
2010	Park *et al.* [190]	Seoul, South Korea	63	5115	1.1%
2010	Pfannenberg *et al.* [199]	Tübingen, Germany	110	3,604	3.1%[e]
2010	Zukotynski *et al.* [200]	Boston, USA	45	99	26.8%[f]
2011	Akkas *et al.* [196]	Ankara, Turkey	31	1032	3.0%
2011	Pace *et al.* [134]	Naples, Italy	73	848	8.6%
2011	Ouellet *et al.* [133]	Sherbrooke, Québec, Canada	328	4842	6.8%
2012	Cronin *et al.* [130]	Boston, USA	298	6,867	4.3%

---

[a] In this study each patient underwent 5 PET/CT scans, which should equate to 165 scans, although the paper only reports a total of 163 scans

[b] Patients with suspected or proven phaeochromocytoma. Of those subsequently shown not to have phaeochromocytoma, 9.5% had evidence of ^{18}F-FDG BAT

[c] Based on strict exclusion criteria; all those with head and neck cancer, or who received treatment between scans were excluded

[d] 145 patients were scanned more than once; ^{18}F-FDG BAT prevalence increased to 65% in those who underwent more than 4 PET/CT scans

[e] Comparison made against 198 age and sex matched controls

[f] ^{18}F-FDG BAT seen in 16/185 scans (8.6%) in the retrospective control group who were warmed to 24°C prior to scanning

2012	Huang *et al.* [197, 203]	Kaohsiung, Taiwan	30	1,740	1.7%
2012	Mei *et al.* [136]	Hong Kong, China	66	1442	4.6%
2013	Persichetti et al. [204]	Rome, Italy	217	6454	3.4%
2013	Perkins *et al.* [198]	Pretoria, South Africa	38	386	9.8%

In these retrospective studies, analyses have either been confined to the first PET scan (to avoid clustering), or have only evaluated sequential scans for the purposes of identifying changes in the pattern or activity of ^{18}F-FDG BAT. BAT is facultative and therefore only metabolically active when it is required as part of non-shivering thermogenesis [2], therefore inactive BAT will not be visible on PET. Furthermore BAT is highly dynamic and its activity may fluctuate over a matter of minutes [43], therefore any retrospective study is subject to the opportunistic nature of BAT detection. Essentially, the absence of evidence of BAT (in retrospective PET studies) cannot be taken as evidence of its absence, consequently it has even been suggested that prevalence data from these retrospective studies are so unreliable that they should be disregarded [189].

To address this limitation, some studies have evaluated the prevalence of ^{18}F-FDG BAT based on serial scans. Lee *et al.* [187] reviewed the PET/CT scans of 145 patients scanned on multiple occasions and identified that the likelihood of detecting ^{18}F-FDG BAT increased the more scans a patient underwent: 8% in those scanned twice, 18% in those scanned three times, 50% in those scanned four times, and plateauing at 65% for those undergoing more than 4 scans. In effect each additional PET/CT scan increased the likelihood of detecting ^{18}F-FDG BAT by approximately 13%. This indicates that the true prevalence of BAT is far higher than most retrospective studies suggest. Similarly, Rousseau *et al.* [191], in their cohort study of 33 women with breast cancer, all of whom underwent 5 PET/CT scans, found that ^{18}F-FDG BAT prevalence increased from 36.4% if only the first PET/CT scan was assessed, to 84.8% if all 5 scans were assessed.

2.5.4 Dedicated studies to evaluate prevalence of BAT

A potential limitation of retrospective studies is that been that they have been performed on patients with proven or suspected malignancy, which may be a confounder. There is controversy over whether BAT plays a role in cancer cachexia, with some post-mortem studies showing that BAT is more prevalent in patients with cancer cachexia (80%) than in age-matched controls [205] although it is not clear whether this association is clinically relevant. No convincing correlation between ^{18}F-FDG BAT prevalence and neoplastic status has been demonstrated. Nonetheless these studies still rely on the opportunistic identification of ^{18}F-FDG BAT. As described above (section 2.3) the scanning protocol has been devised to suppress physiological uptake (including within BAT), therefore even serial PET/CT imaging performed in ambient conditions is poorly reproducible, insensitive and may underestimate the true prevalence of BAT [187].

A small number of dedicated studies have explored the effect of temperature manipulation on BAT prevalence (Table 2-3), which have reported a BAT prevalence of between 15.3% and 100%. Skillen *et al.* [206] reported that following a change in scanning protocol in which patients were warmed with space blankets, the prevalence of ^{18}F-FDG BAT fell from 15.3% to 3.3%. The baseline prevalence of 15.3% is still rather low, reflecting the fact that patients were scanned at thermoneutrality (although the exact value is not reported) rather than being deliberately cooled, and is unlikely to have maximally stimulated ^{18}F-FDG BAT.

Few studies have sought to induce ^{18}F-FDG BAT uptake on PET [42, 43, 113]. A small prospective study by Saito *et al.* [42] in Sapporo, Japan, reported a prevalence of approximately 33% in healthy volunteers exposed to cold (19°C) prior to PET scanning.

Of these, 8 underwent repeat scanning 2 weeks later following a period of warming (27°C), all of whom showed total abolition of ^{18}F-FDG BAT uptake. In an extension to this study, Yoneshiro *et al.* [113] identified ^{18}F-FDG BAT in 41.4% in a sample of 162 healthy volunteers scanned prospectively (which included the 56 volunteers included in the study by Saito *et al.*) all of whom were exposed to cold (19°C) prior to PET scanning.

Van Marken Lichtenbelt *et al.* [43] prospectively scanned 24 young health male volunteers using a standardised validated PET protocol in which subjects were exposed to cold (16°C) for 2 hours prior to scanning. ^{18}F-FDG BAT was identified in 23/24 (95.8%); the only subject to not demonstrate ^{18}F-FDG BAT uptake had the highest BMI (38.7 kg/m^2) and body fat percentage (41.8%). After an unspecified wash-out period, three volunteers were rescanned at thermoneutrality (22°C) all of whom showed no detectable ^{18}F-FDG BAT uptake.

Lee et al. [105] highlighted the extent to which PET/CT underestimates the true prevalence of BAT. They identified ^{18}F-FDG BAT in 3/17 pre-operative PET/CT scans performed for staging of head and neck cancer (17.6%), but found immunohistochemical evidence of BAT in 100%. The proportion of UCP1-positive BAT cells was higher in those who were PET-positive (95-100%) than those who were PET-negative (3-28%). Similarly, Virtanen *et al.* [44], in a prospective study of 5 healthy adult volunteers in Finland, reported ^{18}F-FDG BAT in all subjects when exposed to cold (ambient temperature 17-19°C, whilst intermittently immersing the subjects' feet in cold water for 5 minute periods) for 2 hours prior to scanning. Guided by the PET/CT biopsy specimens were obtained in 3 subjects, which showed the characteristic histological features of BAT, and stained for UCP1, whereas samples obtained from WAT did not.

Table 2-3: Dedicated prospective studies of BAT prevalence.

Year	Authors	City	No of BAT+ subjects	No of subjects	Intervention	Prevalence
2009	Virtanen *et al.* [44]	Turku, Finland	5	5	Cold (17-19°C)	100%
2009	Saito *et al.* [42]	Sapporo, Japan	19	56	Cold (19°C)	33.9%
2009	van Marken Lichtenbelt *et al.* [43]	Maastricht, the Netherlands	23	24	Cold (16°C)	95.8%
2011	Lee *et al.* [105]	Sydney, Australia	3	17	UCP1	17.6%[a]
2009	Zingaretti *et al.* [36]	Ancona, Italy	10	35	UCP1	28.6%
2012	Skillen *et al.* [206]	Wagga Wagga, Australia	23 4	150 150	Thermoneutrality Warming	15.3%[b] 3.3%
2011	Yoneshiro *et al.* [113]	Sapporo, Japan	67	162	Cold (19°C)	41.4%[c]

Despite the considerable variable in ^{18}F-FDG BAT uptake on PET with its inherent limitations, PET/CT remains the standard against which other imaging modalities are compared. As described above, ^{18}F-FDG BAT uptake on PET/CT is highly variable in terms of volume and activity, therefore whether its distribution on PET/CT reflects its true distribution is uncertain. In the next four chapters we shall explore both factors influencing ^{18}F-FDG uptake, and how its pattern of distribution changes over time.

---

[a] 100% expressed gene transcripts seen in BAT including UCP1 and PRDM16

[b] Two groups: group A (n=150) was scanned using normal protocol at thermoneutrality; group B (n=150) following warming measures. Prevalence in group A = 15.3%, group B = 3.3%; overall prevalence 9.3%.

[c] includes the 56 volunteers reported by Saito et al

2.6 Aims

In chapters 3 and 4 we shall present work with the aim of determining the prevalence of ^{18}F-BAT non-invasively on PET/CT (*i.e.* ^{18}F-FDG BAT) and assessing the correlation between various demographic, biological and environmental factors, upon the prevalence, volume and activity of ^{18}F-FDG BAT. As studies of point prevalence underestimate the true prevalence of BAT in adult humans, we shall also evaluate the cumulative prevalence of ^{18}F-FDG BAT on serial PET/CT scans.

As discussed above, dedicated studies indicate that BAT is far more prevalent than analysis of *ad hoc* PET/CT scans would suggest. This calls into question the usefulness of PET/CT as a standard against which other imaging modalities can be compared. Therefore in chapters 5 and 6 we shall evaluate the reliability of ^{18}F-FDG BAT uptake further by analysing the pattern and consistency of ^{18}F-FDG BAT distribution on serial PET/CT scans to determine whether it occurs in a reproducible pattern, or in a more piecemeal fashion. This will enable the consistency of ^{18}F-FDG BAT uptake on PET/CT to be tested.

Chapter 3: Predictors of ^{18}F-FDG BAT prevalence on PET/CT

3.1 Aims

It is thought that multiple environmental and demographic variables (including temperature, gender and age) influence ^{18}F-FDG BAT prevalence. In this chapter we shall determine the correlation between a variety of meteorological and biological variables on ^{18}F-FDG BAT prevalence.

3.2 Subjects and methods

3.2.1 Subject selection

The reports of 3,317 consecutive ^{18}F-FDG PET/CT scans performed between June 2007 and August 2012 at University Hospitals Coventry and Warwickshire NHS Trust (Coventry, UK; latitude 52.42°N, longitude 1.44°W) were searched using the keywords "brown adipose tissue" and "brown fat", as normal practice at our institution is to comment on BAT if present. The vast majority of scans were performed for the purposes of cancer assessment. Twenty two scans were excluded from further analysis as they did not include all areas in which ^{18}F-FDG BAT could occur (*e.g.* scans restricted to the head, neck and upper thorax), or were abandoned prematurely (Figure 3-1).

Figure 3-1: Flow chart showing recruitment of the sample.

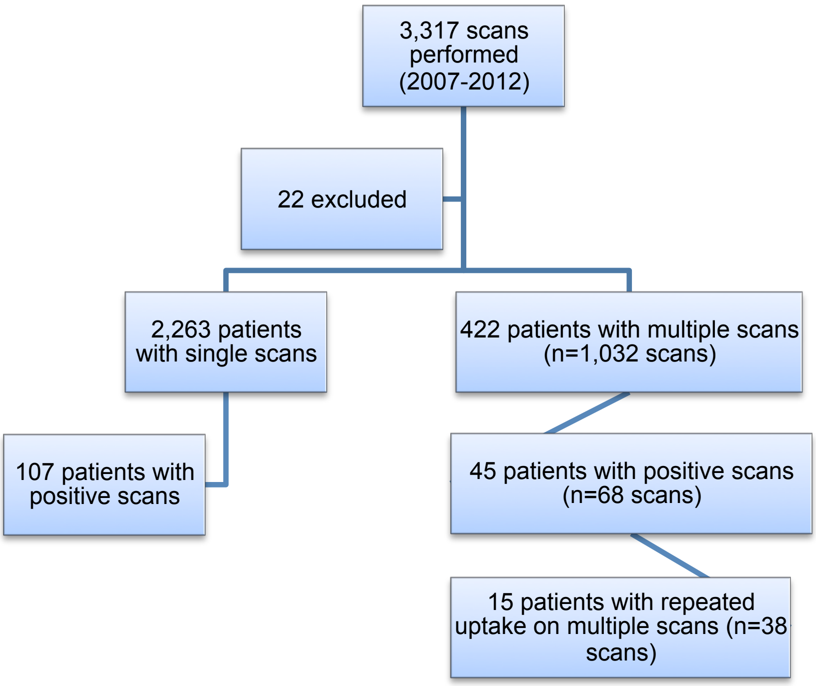

3.2.2 Collection of data

All eligible PET/CT scans performed between 1/6/2007 and 31/8/2012 which showed ^{18}F-FDG uptake consistent with BAT (henceforth referred to as ^{18}F-FDG BAT) were retrospectively evaluated to confirm that ^{18}F-FDG BAT was present, including cases where multiple PET/CT scans had been performed.

Demographic data were collected including age, sex, height and weight. Body mass index (BMI) was calculated and categorised according to the World Health Organization classification [207], namely underweight (BMI <18.5 kg/m^2), normal (18.5 – 24.99 kg/m^2), overweight (25 – 30 kg/m^2) and obese (≥ 30 kg/m^2).

Diabetic status was recorded inconsistently and may not therefore reflect the true prevalence. Furthermore binary categorisation into ‘diabetic’ and ‘not diabetic’ may not accurately reflect the quality of glycaemic control. Serum glucose levels following a period of fasting are, however, routinely checked and recorded prior to PET/CT examinations at our institution, which may better reflect the quality of glycaemic control as well as capturing those who may be undiagnosed. We retrospectively assigned patients to one of three groups according to the World Health Organization 2006 criteria [208], namely normoglycaemia (serum blood glucose ≤6.1mmol/l), impaired fasting glucose (6.1 - 6.9 mmol/l) and diabetes (≥7.0 mmol/l).

Meteorological data (temperatures and sunlight data for the day of scanning, preceding day, three days, week and month) were obtained for the nearby Coundon weather station (latitude 52.42°N, longitude 01.53°W) from the Central Climate Unit, Meteorological Office and the website of Bablake School[a] (Coventry, UK; latitude 52.41°N, longitude 1.52°W), both within the urban confines of Coventry, 5 miles (8 km) and 4 miles (6.4 km) respectively from our institution.

3.2.3 PET/CT protocol

Scanning was performed on a combined GE Discovery STE PET/CT scanner (General Electric Medical Systems, Milwaukee, USA). In accordance with standard administration and acquisition protocol patients were fasted for 6 hours prior to scanning. After administration of ^{18}F-FDG, patients sat for 60 minutes within the PET/CT suite, where ambient temperature was maintained at approximately 24°C.

Prior to administration of ^{18}F-FDG, serum glucose was checked, and 2 international units (IU) of insulin administered subcutaneously in cases of hyperglycaemia. Mean serum glucose was 5.7 mmol/l (standard deviation 1.6 mmol/l, range 1.0 – 26.8 mmol/l). ^{18}F-FDG was administered intravenously one hour prior to the scan (mean injected dose 362.1 MBq, standard deviation 33.2 MBq; range 103 – 505 MBq).

Static emission data were obtained from the skull base to mid thigh with the arms elevated whenever possible. In cases of head and neck cancer a second set of emission data were obtained of the head and neck with the arms by the patients' side. Emission

---

[a] http://bws.users.netlink.co.uk/

data were obtained for 3 minutes in each bed position (each covering 20 cm) with 3-dimensional acquisition. PET images were reconstructed using a model-based iterative reconstruction algorithm.

Unenhanced spiral CT scans were acquired from the skull base to the mid-thighs using 3.3 mm slice thickness. All oncology patients with the exception of those being scanned for the purposes of head and neck cancer were given water-soluble iodinated contrast media (Gastrografin®, Bayer plc, Newbury, UK) for bowel opacification. Images were reconstructed using the filtered back-protection algorithm.

3.2.4 Image analysis

All PET/CT scans were initially reported by a consultant radiologist with expertise in nuclear imaging[a] as part of the patients' routine clinical care using a Centricity PACS workstation (GE Healthcare, USA), and ^{18}F-FDG BAT recorded in the report if present. For the purposes of this study each PET/CT scan was re-evaluated by second radiologist[b] using a GE ADW Advantage Workstation 4.3 (GE Healthcare, Milwaukee, USA) to confirm the presence of ^{18}F-FDG BAT. ^{18}F-FDG BAT was considered present when there was avid ^{18}F-FDG uptake at a greater-than-background level (*i.e.* SUV > 1.0 g/ml) in areas corresponding to the attenuation of adipose tissue on CT (*i.e.* an attenuation of between -100 and -10 Hounsfield units).

3.2.5 Statistical analysis

Statistical analyses were performed using SPSS version 21.0 (SPSS IBM Corp., New York, USA) and GraphPad Prism version 5.0 for Windows (GraphPad Software, San Diego, USA). Continuous data were initially tested for normality using the Kolmogorov-Smirnoff test. To assess differences between patients with and without

---

[a] Dr Oludolapo Adesanya

[b] Dr Terence Jones

^{18}F-FDG BAT, Student's *t* test or the Wilcoxon-Mann Whitney U test were performed for normally and non-normally distributed continuous variables respectively (*e.g.* age, temperature, BMI, serum glucose). The Chi-square test (or Fisher's exact test if appropriate) was used for categorical data (*e.g.* gender).

As the dependent variable is dichotomous (*i.e.* ^{18}F-FDG BAT present or absent) binomial logistic regression was performed to identify the effect of variables on the prevalence of ^{18}F-FDG BAT. Both univariate and multivariate analyses were employed, namely: univariate analysis to determine the effect of each variable in isolation, and multivariate to determine the effect when other variables are taken into account. Three techniques for multivariate binomial logistic regression were used in an attempt to address the problem of multicollinearity between variables: forced entry, forwards and backwards regressions. The forced entry technique, in which all variables are entered into the regression model, is the best known. Forwards regression seeks to construct a model that predicts the presence or absence of ^{18}F-FDG BAT iteratively by incrementally adding single variables on the basis of likelihood, and continues until none of the remaining variables contribute significantly to the model. Conversely, backwards regression begins with a model containing all variables, and iteratively excludes those that contribute least to the model. The backwards method is generally preferred over forwards regression due to the potential for suppressor effects (*i.e.* when a predictor is only significant when another variable is held constant). Forward stepwise regression is more likely to erroneously exclude these predictors, thereby introducing a type II error (*i.e.* erroneously excluding a variable that is in fact significant). Multicollinearity was tested for using SPSS 21. Sex was defined as a categorical variable within the regression analysis. Missing values were substituted with means. A *p*-value <0.05 was considered to be statistically significant.

Logistic regression was performed on scan data (including where multiple scans were performed for the same patient). To address the potential risk of clustering, logistic regression was also performed for scan data for each patients' first PET/CT scans (irrespective of whether it was positive or negative), and also for the scan showing the largest BAT volume.

To compare the prevalence of ^{18}F-FDG BAT between the first and second scans, McNemar's test was performed[a] on the recommendation Dr Ric Crossman of the department of Statistics at Warwick Medical School. This is a variant of the Chi-squared test for paired categorical data that takes into account the fact that the cells are not independent, and is appropriate when comparing the presence or absence of a dichotomous variable (*i.e.* the presence or absence of ^{18}F-FDG BAT) in the same individual at two time points.

3.3 Ethics

Ethical approval had previously been obtained from the National Research Ethics Service of Birmingham East, North and Solihull Research Ethics Committee (NHS REC reference 11/H/1206/3) on 31 January 2011 for a study entitled 'Investigation of metabolism in human participants', as was NHS trust approval from the Research and Development office of University Hospitals Coventry and Warwickshire NHS Trust.

---

[a] VassarStats: Website for Statistical Computation, http://vassarstats.net/propcorr.html, accessed 10 January 2014.

3.4 Results

3.4.1 Demographic differences between ^{18}F-FDG BAT positive and negative PET/CT scans

Retrospective evaluation of 3,295 eligible PET/CT scans in 2,685 individuals (1,188 women, 1,497 men; mean age 61, standard deviation 15 years; range 10 – 91 years) between June 2007 and August 2012 revealed ^{18}F-FDG BAT in 175 scans (5.3%) in 152 individuals (5.7%). 422 patients underwent multiple PET/CT scans (1,032 scans; mean scanning interval 9.1 ± 8.7 months), in whom 15 individuals (38 scans) showed ^{18}F-FDG BAT activity on more than one scan.

A comparison of the demographic and environmental metrics for PET/CT scans with (n=175) and without ^{18}F-FDG BAT uptake (n=3,120) is shown in Figure 3-1.

3.4.1.1 Gender

Although males comprised the greater proportion of the study group (55.8%), they only accounted for 26.3% of the ^{18}F-FDG BAT positive scans (Table 3-1). There was a higher prevalence of ^{18}F-FDG BAT on women's scans (129/1,485; 8.7%) than for men (46/1,810; 2.5%), which was statistically significant ($\chi^2 = 60.043$; odds ratio 3.6, 95% CI 2.6 to 5.1 using the approximation of Woolf; $p < 0.0001$), and persisted with increasing age (Figure 3-2). Comparison of ^{18}F-FDG BAT prevalence between the sexes using Chi-square (or Fisher's exact test as appropriate) analysis for each age octile, showed that the difference was only significant between the 30-40 and 70-80 year octiles (Figure 3-2 and Table 3-2).

Table 3-1: Demographic, clinical and meteorological profile for PET/CT scans with and without ^{18}F-FDG BAT uptake.

Characteristic	**No ^{18}F-FDG PET uptake**	**^{18}F-FDG BAT uptake**	***p-value***
Number of scans	3,120	175	-
Sex; M:F ratio (% male)	1,356:1,764 (43.5%)	46:129 (26.3%)	< 0.001
Age (years)	62.0 ± 14.2	48.4 ± 19.6	< 0.001
BMI (kg/m^2)	26.6 ± 5.4	24.3 ± 4.5	< 0.001
Fasting serum glucose (mmol/l)	5.7 ± 1.7	5.2 ± 0.8	< 0.001
Dose of ^{18}F-FDG administered (MBq)	362.3 ± 32.7	357.5 ± 41.2	0.374
Daily temperature (°C)			
Min	6.1 ± 5.2	4.3 ± 5.4	<0.001
Mean	10.0 ± 5.4	8.0 ± 5.4	< 0.001
Max	14.2 ± 6.3	11.8 ± 6.1	< 0.001
Preceding day’s temperature (°C)			
Min	6.0 ± 5.3	4.3 ± 5.3	<0.001
Mean	10.0 ± 5.5	7.9 ± 5.4	< 0.001
Max	14.2 ± 6.5	11.9 ± 6.1	< 0.001
Preceding 3 days temperature (°C)			
Min	4.0 ± 5.3	2.3 ± 5.3	<0.001
Mean	9.9 ± 5.3	7.8 ± 5.2	< 0.001
Max	15.8 ± 6.4	13.3 ± 6.0	< 0.001
Preceding Weekly temperature (°C)			
Min	2.5 ± 5.1	0.7 ± 4.9	<0.001
Mean	9.9 ± 5.1	8.1 ± 4.8	< 0.001
Max	17.2 ± 6.2	15.0 ± 5.7	< 0.001
Mean monthly temp	10.5 ± 4.9	9.0 ± 4.6	0.472
Hours of daylight (hours)	4.1 ± 2.8	3.6 ± 2.5	0.095
Preceding day’s sunshine	4.1 ± 2.9	3.6 ± 2.4	0.051
Mean monthly sunshine	4.0 ± 1.9	3.7 ± 1.9	0.016
Total monthly sunshine	130.3 ± 50.1	119.0 ± 51.8	0.006
Difference between mean temps (day of scan – preceding day)	-0.0 ± 2.1	-0.1 ± 2.2	0.342

Figure 3-2: ^{18}F-FDG prevalence decreases with age for both males and females[a].

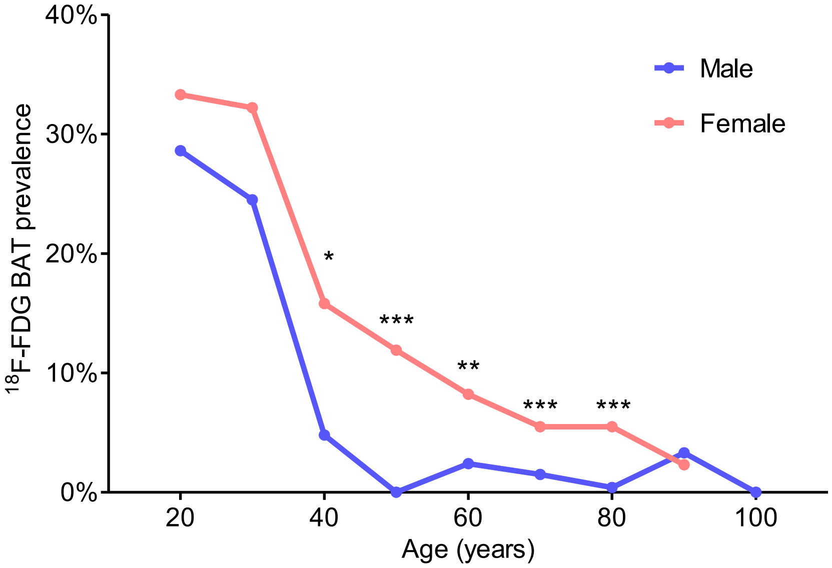

Table 3-2: ^{18}F-FDG BAT prevalence by age octile for males and females.

Age octile (years)	^{18}F-FDG positive scans in females (%)	^{18}F-FDG positive scans in males (%)	Odds ratio (95% confidence intervals) and *p-value*
10-20	6/18 (33.3%)	6/21 (28.6%)	1.250 (0.320-4.855), *p* = 1.000
20-30	19/59 (32.2%)	12/49 (24.5%)	1.465 (0.6260-3.427); *p* = 0.4017
30-40	16/101 (15.8%)	4/84 (4.8%)	3.765 (1.207-11.744); *p* = 0.0175
40-50	21/176 (11.9%)	0/144 (0.0%)	39.958 (2.397-666.15); *p* <0.0001
50-60	23/282 (8.2%)	8/340 (2.4%)	3.685 (1.622-8.375); *p* = 0.0013
60-70	24/436 (5.5%)	9/582 (1.5%)	3.709 (1.706-8.064); *p* = 0.0005
70-80	18/326 (5.5%)	2/464 (0.4%)	13.500 (3.109 – 58.617); *p* <0.0001
80-90	2/87 (2.3%)	4/123 (3.3%)	0.933 (0.1526 – 5.710); *p* = 1.000

3.4.1.2 Age

The age distribution of the sample is skewed towards older adults, with the greatest proportion of scans being performed in the 60-70 year age groups for both males and females (Figure 3-3). Individuals in whom scans showed ^{18}F-FDG BAT uptake were on average younger (mean ± SD 48.4 ± 19.6 years) than those in whom scans were negative (62.0 ± 14.2 years; $p < 0.001$; Table 3-1 and Figure 3-4).

---

[a] * = *p*-value <0.05, ** < 0.01, *** <0.001

Figure 3-3: Number of PET/CT scans performed according to age.

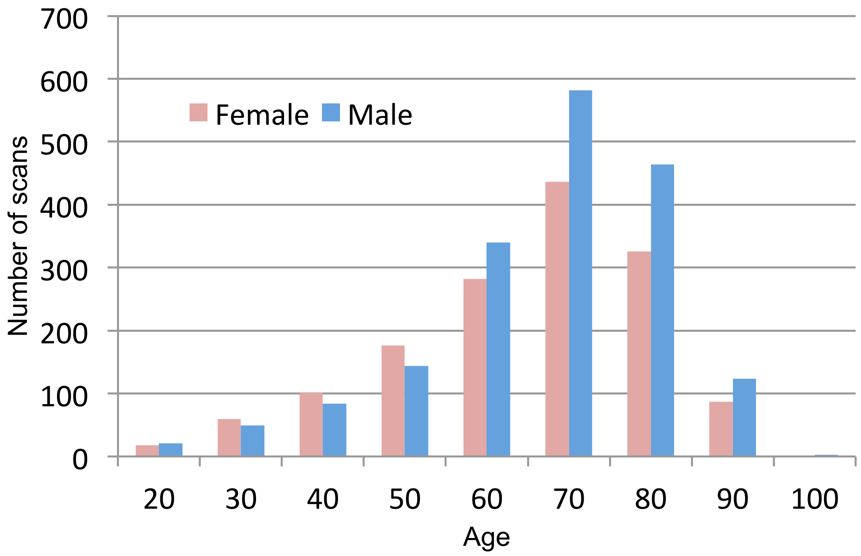

Figure 3-4: Box and whisker plot with Tukey's hinges[a] showing significant differences between the mean ages of those with and without ^{18}F-FDG BAT (p < 0.001).

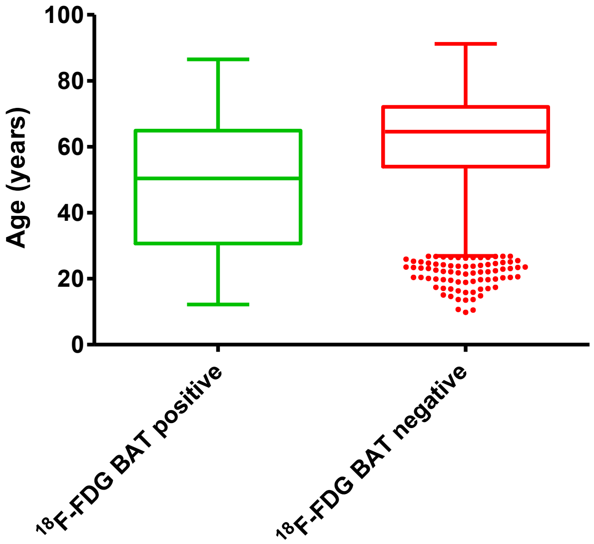

3.4.1.3 BMI

The prevalence of patients who were overweight or obese was slightly lower than the English average, with 783/1,463 females (53.5%) and 1,085/1,792 males (60.5%) having a BMI in ≥ 25 kg/m^2 (Figure 3-5), compared the English average of 58% for females and 65% for males; 360/1,463 females (24.6%) and 348/1,792 males (19.4%)

---

[a] The boxes demonstrate the 75th and 25th centiles, with the line in the centre indicating the mean. The whiskers represent the maximum and minimum values, while the dots represent outliers whose values are more than 1.5 times the interquartile range (the difference between the 25th and 75th quartile) above the 75th centile

were obese (BMI ≥ 30 kg/m^2), compared with the English average of 26% of women and 24% for men [209].

There was no significant difference in mean BMI between the females and males at baseline (26.5 kg/m^2 and 26.4 kg/m^2 respectively). No significant correlation between age and BMI was observed overall ($r = 0.02$, $p = 0.28$), nor between sexes ($r = 0.05$, $p = 0.06$ for females; $r = -0.02$, $p = 0.46$ for males).

Figure 3-5: Breakdown of BMI categories by sex.

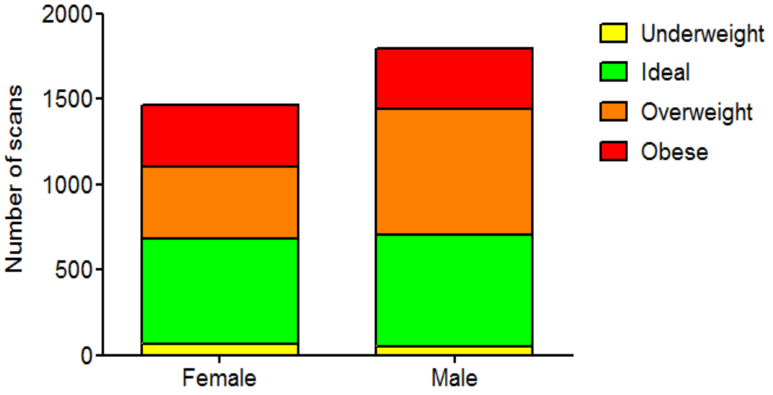

^{18}F-FDG BAT was observed in all BMI categories. There is a weak positive correlation between age and BMI for those scans demonstrating ^{18}F-FDG BAT ($r = 0.22$, $p = 0.0045$), but not for those without evidence of ^{18}F-FDG BAT ($r = -0.001$, $p = 0.59$; Figure 3-6).

Figure 3-6: Scatterplot of age against BMI, showing no significant correlation. The dotted line at 25 kg/m^2 indicates the upper limit of the 'ideal' BMI.

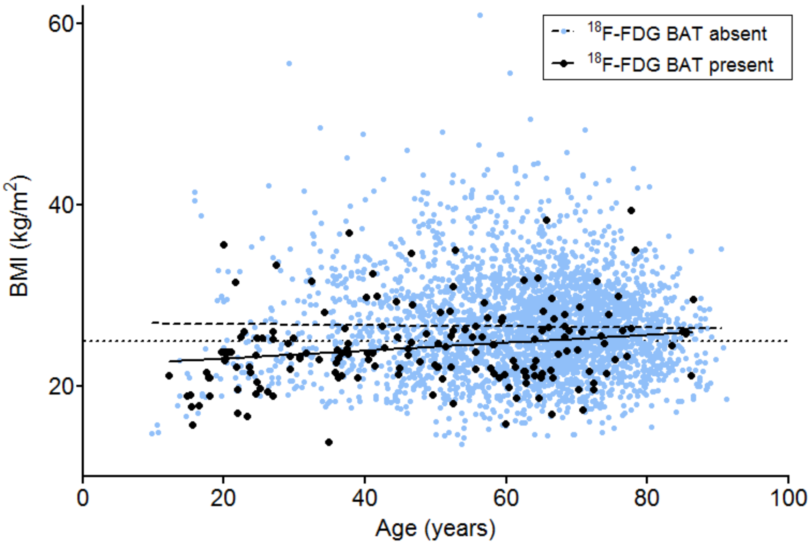

The mean BMI of those who exhibited ^{18}F-FDG BAT was slightly lower (24.3 ± 4.5 kg/m^2) than those who did not (26.6 ± 5.4 kg/m^2), which was statistically significant ($p < 0.001$; Figure 3-7). In males the highest prevalence of ^{18}F-FDG BAT occurred in those who were underweight (7.3%) while in females the highest prevalence was in those with an ideal BMI (11.0%). ^{18}F-FDG BAT uptake was evident in all BMI categories, although for both males and females, the prevalence progressively decreased in those who were overweight and obese (Figure 3-8 andTable 3-3), although the trend was most marked in males, in whom ^{18}F-FDG BAT prevalence fell to 0.9% in those who were either overweight or obese. The gender difference in ^{18}F-FDG BAT prevalence was significant for all BMI categories except for those who were underweight.

Figure 3-7: Mean BMI for ^{18}F-FDG BAT negative and positive scans. Lines at 25 and 30 kg/m^2 indicate the boundaries between ideal, overweight and obese BMI values.

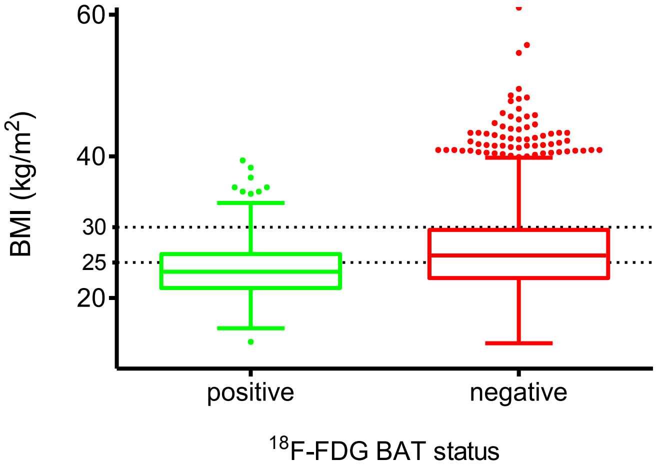

Figure 3-8: Prevalence of ^{18}F-FDG BAT according to BMI and gender[a].

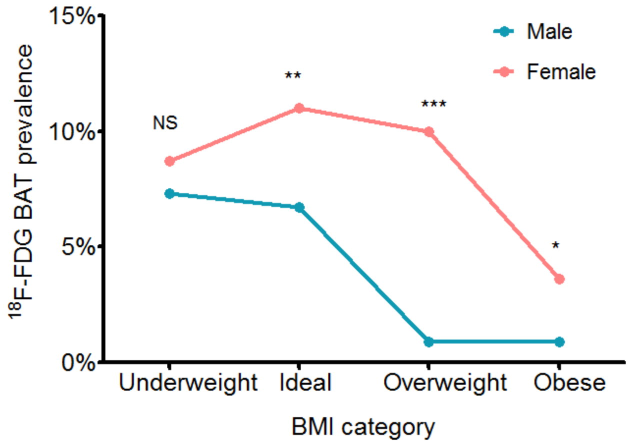

---

[a] * = *p*-value <0.05, ** < 0.01, *** <0.001

Table 3-3: Frequency of ^{18}F-FDG BAT positive scans according to BMI category[a].

BMI (kg/m^2)	^{18}F-FDG positive scans in females (%)	^{18}F-FDG positive scans in males (%)	OR (95% CI) and significance
Underweight (<18.5)	6/69 (8.7%)	4/55 (7.3%)	1.21 (9.32-4.54); *p* = 1.000
Ideal (18.5-24.99)	67/611 (11.0%)	43/652 (6.7%)	1.74 (1.17-2.60), *p* = 0.0069
Overweight (25-29.99)	42/423 (10.0%)	7/737 (0.9%)	10.92 (4.86-24.54); *p* <0.0001
Obese (≥30)	13/360 (3.6%)	3/348 (0.9%)	4.31 (1.22-15.26), *p* = 0.0202
BMI data not recorded	1/22 (4.5%)	0/18 (0%)	-

3.4.1.4 Fasting glycaemic status and injected ^{18}F-FDG dose

Mean fasting serum glucose was lower in individuals showing ^{18}F-FDG PET (5.3 ± 0.8 mmol/l) than those who did not (5.7 ± 1.7 mmol/l), which was also statistically significant ($p < 0.0001$).

There was a higher prevalence of ^{18}F-FDG BAT in normoglycaemic subjects (fasting serum glucose ≤ 5.5 mmol/L; 6.5%), becoming progressively smaller in those with impaired fasting glucose (‘IFG’; 5.6 – 6.9 mmol/L; 4.4%) or diabetes mellitus (≥ 7.0 mmol/L; 1.9%). This trend was statistically significant ($p = 0.0002$). Although males showed a consistently lower prevalence for all glycaemic categories (Figure 3-9), the difference between sexes did not quite reach statistical significance ($p = 0.88$).

There was no significant difference in the dose of ^{18}F-FDG radiopharmaceutical administered between individuals with (357.5 ± 41.2 MBq) and without ^{18}F-FDG BAT uptake (362.3 ± 32.7 MBq) on PET/CT.

---

[a] BMI data not available for 22 females and 18 males

Figure 3-9: Prevalence of ^{18}F-FDG BAT with glycaemic status according to sex.

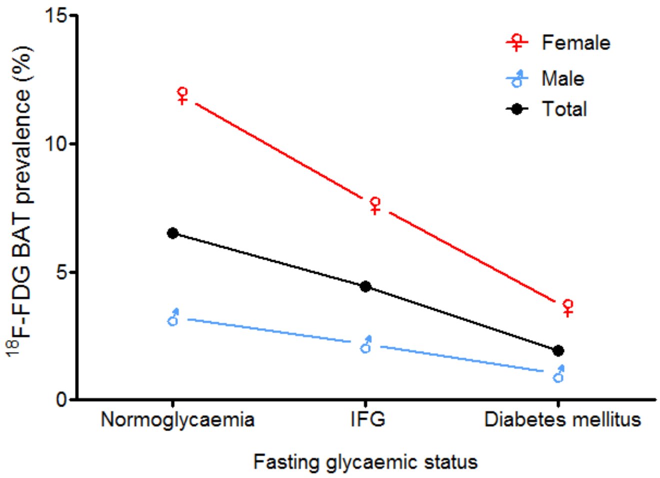

3.4.1.5 Environmental variables

A strong inverse correlation was identified between mean monthly temperature and the prevalence of ^{18}F-FDG BAT (r = -0.74; Figure 3-10 and Table 3-4), although there was no statistically significant difference in the mean monthly temperature between ^{18}F-FDG BAT positive and negative scans (Table 3-1). The probability of detecting ^{18}F-FDG BAT on PET/CT was highest in February, and lowest in July (Table 3-4 and Figure 3-10).

The mean daily temperature was slightly lower in ^{18}F-FDG positive scans (8.0 ± 5.4°C) than negative scans (10.0 ± 5.4°C), which was statistically significant ($p < 0.0001$). The same pattern was seen for the remaining temperature metrics (Table 3-1).

Table 3-4: Mean monthly temperature and ^{18}F-FDG BAT prevalence.

Month	Mean monthly temperature (°C)	Number of ^{18}F-FDG BAT positive scans (%)
January	1.2	16 / 294 (5.4%)
February	1.5	30 / 279 (10.8%)
March	3.0	18 / 291 (6.2%)
April	4.9	11/265 (4.2%)
May	7.1	16/284 (5.6%)
June	10.6	11/297 (3.7%)
July	12.2	5/309 (1.6%)
August	12.4	11/297 (3.7%)
September	10.2	10/239 (4.2%)
October	7.2	14/227 (6.2%)
November	4.6	17/272 (6.3%)
December	0.4	16/241 (6.6%)

Figure 3-10: Mean monthly temperature and ^{18}F-FDG BAT prevalence.

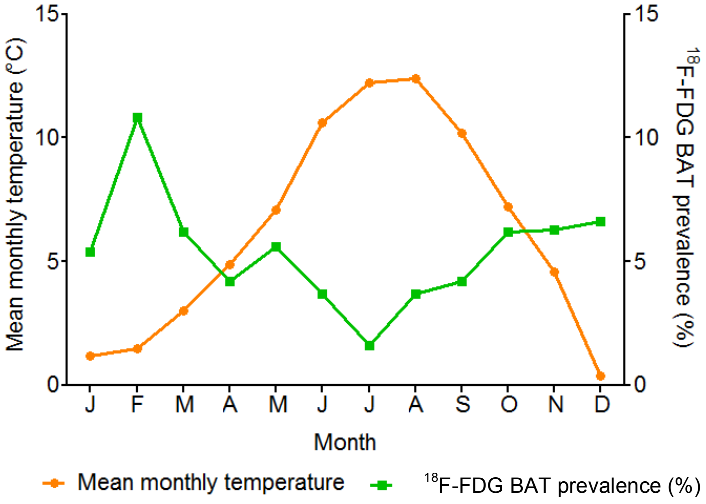

There is a significant negative correlation (r = -0.89, p = 0.001) between the time when the scan was acquired, and ^{18}F-FDG BAT prevalence (Table 3-5 and Figure 3-11); the highest prevalence being 7.0% at 09:00, and the lowest prevalence of 3.2% at 14:00.

Only 6 scans were performed after 17:00, all of which were negative – a potentially aberrant result that may skew the correlation. Nonetheless, even if these data are excluded, a significant correlation persists (*r* = -0.85, *p* = 0.006). Chi-squared test for trend showed this trend to be significant ($p = 0.015$, $\chi^2 = 5.95$).

Table 3-5: Variation in ^{18}F-FDG BAT prevalence with time of day.

Time of day	Number of ^{18}F-FDG BAT positive scans	Total number of scans	% of ^{18}F-FDG BAT positive scans
08:00	12	175	6.9%
09:00	38	542	7.0%
10:00	18	302	6.0%
11:00	29	562	5.2%
12:00	24	438	5.5%
13:00	30	632	4.7%
14:00	9	284	3.2%
15:00	11	245	4.5%
16:00	4	83	4.8%
17:00	0	6	0%

Figure 3-11: Variation in ^{18}F-FDG BAT prevalence with time of day.

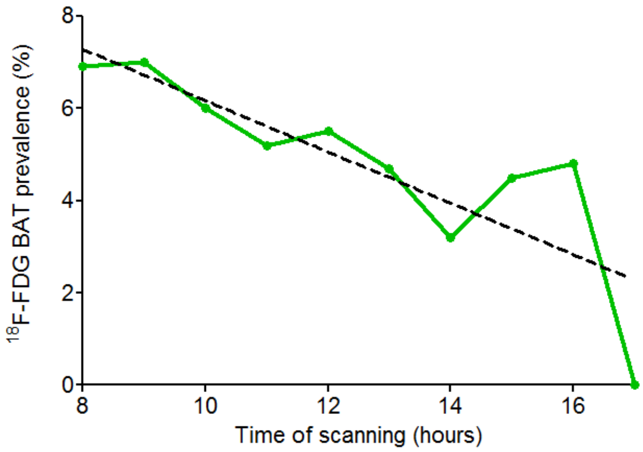

3.4.2 Binomial logistic regression

3.4.2.1 Univariate regression analysis of ^{18}F-FDG BAT prevalence

Univariate analysis revealed that lower age, female sex, lower BMI and lean body mass, basal metabolic rate, and lower fasting serum glucose level were all predictive of higher ^{18}F-FDG BAT prevalence (Table 3-6). Lower temperature (be it on the day of scanning, preceding day, preceding 3 days, preceding month and mean monthly temperature), time of day (earlier), shorter duration of sunlight (on the day of scanning, preceding day, and total monthly sunlight) were also predictive of higher ^{18}F-FDG BAT prevalence.

Table 3-6: Univariate binomial logistic regression performed on all PET/CT scans (n=3,295).

Characteristic	**B (SE)**	***P*-value**	**95% CI for odds ratio**		
			Odds ratio	**Lower**	**Upper**
Age	-0.047 (0.005)	<0.001	0.954	0.944	0.964
Sex (M compared to F)	-1.254 (0.185)	<0.001	0.285	0.199	0.410
BMI (kg/m^2)	-0.080 (0.017)	<0.001	0.923	0.893	0.954
Lean body mass (kg)	-0.073 (0.009)	<0.001	0.930	0.913	0.946
Basal metabolic rate	-0.001 (0.000)	<0.001	0.999	0.998	0.999
Fasting serum glucose (mmol/l)	-0.308 (0.078)	<0.001	0.735	0.631	0.856
Injected ^{18}F-FDG dose (MBq)	-0.004 (0.002)	0.062	0.996	0.992	1.000
Time of scan	0.000 (0.000)	0.019	1.000	1.000	1.000
Temperature on scan date (°C)					
Minimum	-0.064 (0.015)	<0.001	0.938	0.912	0.965
Mean	-0.064 (0.014)	<0.001	0.938	0.913	0.964
Maximum	-0.059 (0.012)	<0.001	0.942	0.920	0.965
Temperature on preceding day (°C)	-0.061 (0.014)	<0.001	0.941	0.915	0.968
Minimum	-0.067 (0.014)	<0.001	0.935	0.910	0.961
Mean	-0.055 (0.012)	<0.001	0.946	0.924	0.969
Maximum					
Preceding 3 days' temperature (°C)					
Minimum	-0.059 (0.014)	<0.001	0.941	0.917	0.970
Mean	-0.072 (0.014)	<0.001	0.930	0.905	0.957
Maximum	-0.058 (0.012)	<0.001	0.943	0.921	0.966
Preceding week's temperature (°C)					
Minimum	-0.066 (0.015)	<0.001	0.936	0.909	0.964
Mean	-0.069 (0.015)	<0.001	0.933	0.906	0.961
Maximum	-0.057 (0.013)	<0.001	0.945	0.922	0.969
Mean monthly temperature (°C)	-0.061 (0.016)	<0.001	0.941	0.912	0.970
Hours of sunlight on scan date	-0.057 (0.029)	0.05	0.944	0.892	1.000
Total monthly hours of sunlight	-0.004 (0.002)	0.005	0.996	0.992	0.999

3.4.2.2 Multivariate regression analysis of ^{18}F-FDG BAT prevalence

Multivariate binomial logistic regression, using the three approaches described in section 3.2.5, was performed on those variables which appeared *a priori* plausible from the univariate analysis.

Multivariate analysis using the forced entry method, after adjustment for other variables, revealed that lower age, female sex, lower BMI, time of day (earlier), and lower mean temperature in the preceding 3 days remained as significant predictors of increased ^{18}F-FDG BAT prevalence (Table 3-7). In effect the probability of detecting ^{18}F-FDG BAT on PET/CT increases as these variables decrease. The impact of time of day on ^{18}F-FDG BAT prevalence appears imperceptibly small (B coefficient = 0.000), although this is due to the units of measurement being small (seconds). If this had been expressed in hours the effect would be greater.

Higher minimum temperature in the preceding 3 days was also shown to be an independent predictor of ^{18}F-FDG BAT prevalence, *i.e.* the higher the minimum temperature in the 3 days prior to scanning, the greater the odds of detecting ^{18}F-FDG BAT on PET/CT. This regression model correctly predicted ^{18}F-FDG BAT status in 94.7% of cases. It is noteworthy that the prevalence of ^{18}F-FDG BAT was 5.3%; this model correctly predicted all negative scans, but not the positive scans.

Fasting serum glucose (lower), maximum (lower) temperature on the day of scanning, and minimum (lower) temperature in the preceding week approached statistical significance but in all cases the odds ratio 95% confidence intervals cross 1, and therefore the direction of effect cannot be determined.

Table 3-7: Binomial multivariate logistic regression (forced entry technique) performed on all scans (n=3,295) showing determinants of ^{18}F-FDG BAT.

Characteristic	B (SE)	*P*-value	95% CI for odds ratio		
			Odds ratio	Lower	Upper
Constant	4.891 (0.933)				
Age	-0.046 (0.005)	< 0.001	0.955	0.946	0.965
Sex (M compared to F)	-1.267 (0.1854	<0.001	0.282	0.196	0.404
BMI (kg/m^2)	-0.078 (0.016)	<0.001	0.925	0.896	0.956
Fasting serum glucose (mmol/l)	-0.158 (0.082)	0.054	0.854	0.727	1.002
Time of scan	0.000 (0.000)	0.034	1.000	1.000	1.000
Temperature on scan date (°C)					
Minimum	0.017 (0.077)	0.826	1.017	0.874	1.183
Mean	0.071 (0.064)	0.270	1.073	0.947	1.217
Maximum	-0.110 (0.060)	0.066	0.895	0.796	1.007
Temperature on preceding day (°C)					
Minimum	0.061 (0.050)	0.228	1.063	0.963	1.173
Mean	0.009 (0.159)	0.954	1.009	0.739	1.379
Maximum	0.095 (0.088)	0.283	1.099	0.925	1.306
Preceding 3 days' temperature (°C)					
Minimum	0.110 (0.056)	0.048	1.116	1.001	1.245
Mean	-0.367 (0.159)	0.021	0.693	0.507	0.946
Maximum	0.001 (0.082)	0.989	1.001	0.852	1.176
Preceding week's temperature (°C)					
Minimum	-0.103 (0.054)	0.055	0.902	0.812	1.002
Mean	0.118 (0.121)	0.328	1.125	0.888	1.427
Maximum	-0.019 (0.065)	0.787	0.767	0.981	1.115
Mean monthly temperature (°C)	0.049 (0.048)	0.487	1.032	0.945	1.126
Hours of sunlight on scan date	0.031 (0.045)	0.574	1.043	0.900	1.209
Total monthly hours of sunlight	0.000 (0.003)	0.926	1.000	0.995	1.005

R^2 goodness of fit = 0.072 (Cox and Snell), 0.212 (Nagelkerke)

Both methods of stepwise multivariate regression also revealed that age, sex, BMI and time of day remained independent predictors of ^{18}F-FDG BAT prevalence (Table 3-8). There was some discordance between the two techniques for meteorological variables however: forward stepwise regression revealed that the preceding day's mean temperature was a significant predictor, while backwards stepwise regression identified that mean temperature in the preceding 3 days was a significant predictor.

Table 3-8: Stepwise forwards and backwards binomial logistic regression for all scans (n=3,295) showing significant predictors of ^{18}F-FDG BAT for each regression model.

Variable	*Forward stepwise technique*			*Backward stepwise technique*		
	B (SE)	***P*-value**	**OR (95% CI)**	**B (SE)**	***P*-value**	**OR (95% CI)**
Constant	3.895 (0.677)	-	-	4.726 (0.808)	-	-
Age (years)	-0.048 (0.005)	<0.001	0.953 (0.945-0.962)	-0.045 (0.005)	<0.001	0.956 (0.947-0.965)
Sex (M)	-1.236 (0.182)	<0.001	0.291 (0.203-0.415)	-1.230 (0.182)	<0.001	0.292 (0.205-0.417)
BMI (kg/m^2)	-0.077 (0.016)	<0.001	0.925 (0.896-0.956)	-0.077 (0.016)	<0.001	0.926 (0.897-0.956)
Glucose (mmol/l)	-	-	-	-0.154 (0.080)	0.056	0.857 (0.732-1.004)
Time of scanning (hh:mm:ss)	0.000 (0.000)	0.054	1.000 (1.000-1.000)	0.000 (0.000)	0.028	1.000 (1.000-1.000)
Preceding days' mean temp (°C)	-0.081 (0.015)	<0.001	0.922 (0.895-0.950)	-	-	-
Preceding 3 days mean temp (°C)	-	-	-	-0.083 (0.015)	<0.001	0.920 (0.893-0.948)

Goodness-of-fit tests for forward regression: 0.067 (Cox and Snell), 0.196 (Nagelkerke R^2); Backwards regression: 0.068 (Cox and Snell R^2), 0.200 (Nagelkerke R^2)

3.4.3 Regression analysis of ^{18}F-FDG prevalence on first PET/CT scans

When analysis is restricted to the first scans only, 149/2,685 of patients (5.5%) showed evidence of ^{18}F-FDG BAT uptake.

The above findings were largely mirrored when the logistic regression was confined to patients' initial scans. With the exception of the injected dose of ^{18}F-FDG, all variables were significant predictors of ^{18}F-FDG BAT prevalence on univariate logistic regression analysis (Appendix A, supplementary table 1). Multivariate logistic regression analysis revealed lower age, female sex, lower BMI, and earlier time of day to be significant predictors of ^{18}F-FDG BAT prevalence (Appendix A, supplementary table 2). The impact of lower serum glucose and lower mean temperature in the preceding 3 days upon ^{18}F-FDG BAT prevalence approached statistical significance. This model correctly predicted ^{18}F-FDG BAT status in 94.4% of cases.

3.4.4 Multicollinearity testing

Multicollinearity is a problem in multiple regression in which variables are highly correlated with each other, making it difficult to separate out the effects of individual variables and potentially introducing bias into the regression model [210].

Multicollinearity is most likely to be an issue with the temperature data. This is apparent when the pattern of mean, minimum and maximum temperature fluctuation throughout the study period are compared (Figure 3-12). Furthermore temperature is closely mirrored by total monthly sunshine. Collinearity calculations confirm this to be the case (Table 3-9). The variance inflation factor (VIF) is a measure of how much each coefficient's variance is affected by multicollinearity - a value >1 suggests that multicollinearity may be biasing the regression model, while values >10 indicates a significant issue [210]. High VIF values were detected for all temperature data implying a strong linear relationship between some of these variables.

Figure 3-12: Seasonal variation in monthly temperature, and mean monthly sunshine.

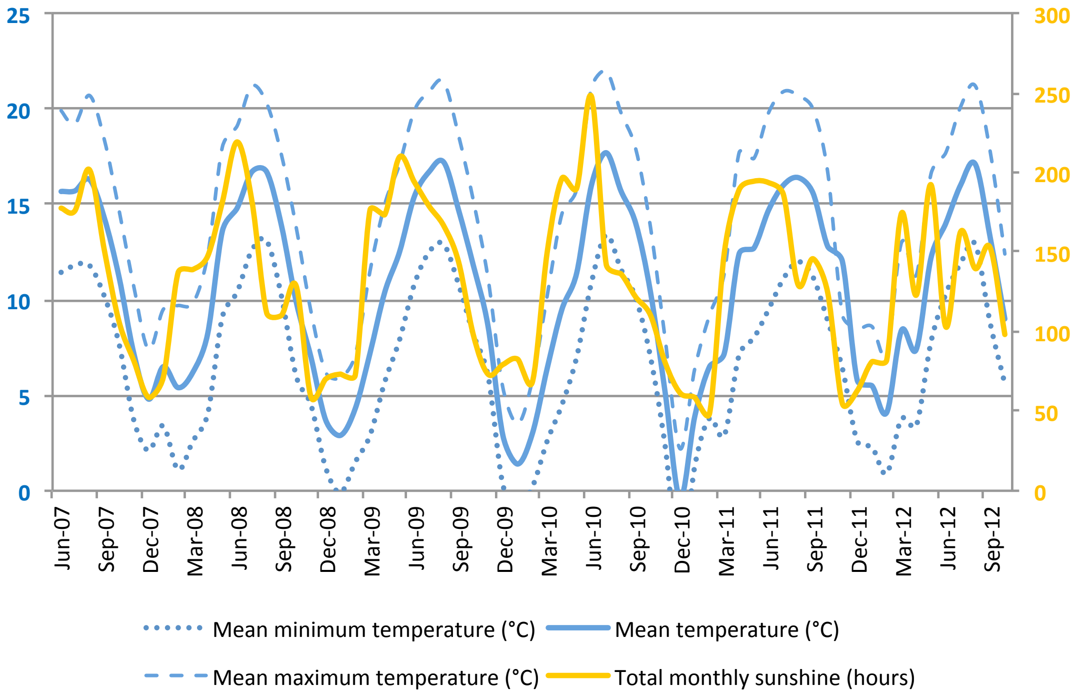

The variables most affected by multicollinearity were identified by calculating the Spearman's *rho* correlation coefficient for all combinations of variable (Supplementary table 3, Appendix A).

The most highly correlated variables (*i.e.* those with a correlation coefficient >0.9) were removed incrementally until all VIF values fell within acceptable limits (Table 3-9). Multivariate binomial logistic regression was repeated on the remaining variables which identified age, sex, BMI, and minimum temperature on the preceding day to be significant predictors of the presence of ^{18}F-FDG BAT occurrence (Table 3-10).

Table 3-9: Multicollinearity calculations for predictors of ^{18}F-FDG BAT prevalence.

Variable	VIF	VIF (following removal of covariates)
Age (years)	1.045	1.041
Sex	1.016	0.010
BMI (kg/m^2)	1.011	1.008
Fasting serum glucose (mmol/l)	1.059	1.055
Time of scan (hh:mm:ss)	1.038	1.022
Temperature on scan date (°C)		
Minimum	21.126	-
Mean	18.679	-
Maximum	20.708	-
Temperature on preceding day (°C)		
Minimum	10.026	1.222
Mean	107.486	-
Maximum	43.906	-
Preceding 3 days' temperature (°C)		
Minimum	12.807	-
Mean	103.850	-
Maximum	42.542	-
Preceding week's temperature (°C)		
Minimum	11.540	-
Mean	55.765	-
Maximum	24.699	-
Mean monthly temperature (°C)	8.222	-
Hours of sunlight on scan date (h)	2.037	1.456
Total monthly hours of sunlight (h)	2.558	1.708

Table 3-10: Multivariate binomial logistic regression of predictors of ^{18}F-FDG BAT prevalence following removal of covariates.

Characteristic	**B (SE)**	***P*-value**	**95% CI for odds ratio**		
			Odds ratio	**Lower**	**Upper**
Constant	3.897 (0.813)				
Age (years)	-0.045 (0.005)	<0.001	0.956	0.947	0.965
Sex	-1.214 (0.182)	<0.001	0.297	0.208	0.424
BMI (kg/m^2)	-0.075 (0.016)	<0.001	0.928	0.898	0.958
Fasting serum glucose (mmol/l)	-0.147 (0.080)	0.066	0.863	0.737	1.010
Time of day (hh:mm:ss)	0.000 (0.000)	<0.001	1.000	1.000	1.000
Min temp on preceding day (°C)	-0.059 (0.017)	0.001	0.943	0.912	0.975
Hours of sunlight on scan date (h)	-0.013 (0.036)	0.725	0.987	0.919	1.060
Total monthly hours of sunlight (h)	-0.002 (0.002)	0.304	0.998	0.994	1.002

Goodness-of-fit tests for forward regression: 0.066 (Cox and Snell), 0.194 (Nagelkerke R^2)

Time of day was a significant predictor of ^{18}F-FDG BAT in both the forced entry and backwards regression models (Table 3-10 and Table 3-11), and approached statistical significance (*p*=0.056) in the forwards regression model (Table 3-11).

Table 3-11: Stepwise forwards and backwards binomial logistic regression for all scans (n=3,295) following removal of covariates, showing significant predictors of ^{18}F-FDG BAT prevalence for each regression model.

Variable	***Forward stepwise technique***			***Backward stepwise technique***		
	B (SE)	***P*-value**	**OR (95% CI)**	**B (SE)**	***P*-value**	**OR (95% CI)**
Constant	2.847 (0.659)			3.606 (0.785)		
Age (years)	-0.047 (0.005)	<0.001	0.954 (0.945-0.963)	-0.045 (0.005)	<0.001	0.956 (0.947-0.965)
Sex (M)	-1.215 (0.181)	<0.001	0.297 (0.208-0.423)	-1.209 (0.181)	<0.001	0.299 (0.209-0.426)
BMI	-0.076 (0.016)	<0.001	0.927 (0.898-0.957)	-0.072 (0.867)	<0.001	0.928 (0.899-0.958)
Glucose	-	-	-	-0.143 (0.079)	0.072	0.867 (0.742-1.013)
Time of day	0.000 (0.000)	0.056	1.000 (1.000-1.000)	0.000 (0.000)	0.031	1.000 (1.000-1.000)
Preceding day's min temp	-0.067 (0.015)	<0.001	0.935 (0.908-0.963)	-0.069 (0.015)	<0.001	0.934 (0.906-0.962)

Goodness-of-fit tests for forward regression: 0.064 (Cox and Snell), 0.189 (Nagelkerke R^2); Backwards regression: 0.068 (Cox and Snell R^2), 0.200 (Nagelkerke R^2)

3.4.5 Comparison of differences between ^{18}F-FDG BAT prevalence on first and second PET/CT scans

McNemar's test with Yates' continuity correction assesses the significance of the difference between two correlated proportions, as in this case where 22/422 (5.2%) of patients with multiple scans showed ^{18}F-FDG BAT uptake on their first scan, while 26/422 (6.2%) showed it on the second (Table 3-12), which were not significantly different (p=0.596; χ^2=0.281, 1 degree of freedom, odds ratio 0.778, 95% CI 0.358 to 1.655).

Table 3-12: 2x2 contingency table showing concordance in ^{18}F-FDG BAT uptake between first and second PET/CT scans.

		Second scan		Total
		^{18}F-FDG BAT positive	^{18}F-FDG negative	
First scan	^{18}F-FDG BAT positive	8	14	22
	^{18}F-FDG BAT negative	18	382	400
	Total	26	396	422

Of the 22 patients who showed ^{18}F-FDG BAT uptake on their first scan, only 8 (36.4%) also showed it on their second scan. Conversely 18 patients who showed no evidence of ^{18}F-FDG BAT on their baseline PET/CT, had uptake on their second PET/CT. Therefore the presence or absence of ^{18}F-FDG BAT on baseline PET/CT is a poor predictor of uptake on second (or subsequent) scans, and therefore one cannot assume that a patient is genuinely BAT negative on the basis of an initial negative scan.

3.4.6 Sensitivity and specificity of PET/CT in detecting ^{18}F-FDG BAT

Of the 422 patients with multiple PET/CT scans, 45 showed ^{18}F-FDG BAT uptake on at least one scan, but only 22 showed it on their initial scan (Table 3-13). This equates to a sensitivity of 48.9%, specificity of 100%, positive predictive value of 100% and negative predictive value of 94.3%. Although on the face of it these values are reassuring, almost half of those patients with ^{18}F-FDG BAT would be missed if analysis was confined to the first scan.

Table 3-13: Contingency table showing proportion of patients with ^{18}F-FDG BAT activity correctly identified on their first PET/CT.

		Overall BAT status		Total
		^{18}F-FDG BAT positive	^{18}F-FDG BAT negative	
First scan	^{18}F-FDG BAT positive	22	0	22
	^{18}F-FDG BAT negative	23	377	400
	Total	45	373	422

3.4.7 Cumulative prevalence of ^{18}F-FDG BAT on serial PET/CT scans

The impact of repeated scanning on the likelihood of detecting ^{18}F-FDG BAT was assessed by calculating the cumulative prevalence of ^{18}F-FDG BAT on serial scans, in similar manner to that described by Lee *et al.* [187].

Four hundred and twenty two patients had more than one PET/CT scan. There was a trend towards higher ^{18}F-FDG BAT prevalence with greater number of scans, *viz.* 4.7% in those scanned once, 7.8% in those scanned twice, 15.1% when scanned three times, 20.8% four, 25.0% five, and 33.3% in those scanned six times (Table 3-14 and Figure 3-13). Exceptionally five patients were scanned more than 6 times, but these were considered outliers; the patient who underwent 10 scans was a child (14.5 years of age at the first scan), as was the only patient who showed ^{18}F-FDG BAT uptake after 6 scans (16.9 years at first scan), both of whom would be expected to have a higher prevalence. For those scanned two, three, four, five and six times, the likelihood of detecting ^{18}F-FDG BAT within an individual increased by 3.1%, 7.3%, 5.7%, 4.2% and 8.3% respectively. This equates to a mean probability of a patient being ^{18}F-FDG BAT positive increasing by 5.8% with each additional scan (at least as far as 6 scans, when the prevalence plateaus at approximately 30%). These conclusions should be treated with caution, however, due to the comparatively small numbers of patients who showed ^{18}F-FDG BAT activity on multiple scans.

Table 3-14: Cumulative prevalence of ^{18}F-FDG BAT on serial PET/CT scans.

Number of scans performed	Number of patients	Number of individuals with positive scans (%)	Incremental change in prevalence	Number of positive scans (%)
1	2,263	107/2,263 (4.7%)		107/2,263 (4.7%)
2	309	24/309 (7.8%)	3.1%	29/618 (4.7%)
3	73	11/73 (15.1%)	7.3%	13/219 (5.9%)
4	24	5/24 (20.8%)	5.7%	12/96 (12.5%)
5	8	2/8 (25.0%)	4.2%	5/40 12.5%)
6	3	1/3 (33.3%)	8.3%	3/18 (16.7%)
7	1	0/1 (0%)	-	0/7 (0%)
8	3	1/3 (33.3%)	-	1/24 (4.2%)
9	0	-	-	-
10	1	1/1 (100%)	-	5/10 (50.0%)

Figure 3-13: Cumulative prevalence of ^{18}F-FDG BAT with increasing numbers of scans.

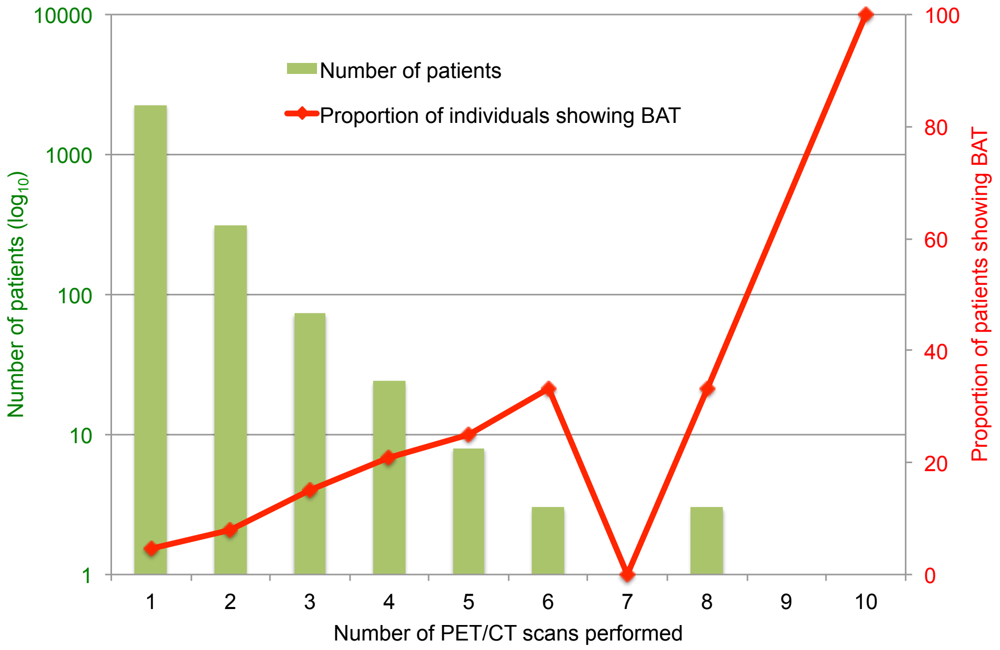

3.5 Summary

In this chapter we sought to identify meteorological and demographic factors which were predictors of higher ^{18}F-FDG BAT prevalence. The overall prevalence was 5.3%, with female gender, younger age, lower BMI, lower serum glucose, earlier time of day and lower temperature being predictive of higher ^{18}F-FDG BAT prevalence. We identified that the likelihood of a PET/CT showing ^{18}F-FDG BAT increased by approximately 5.8% for each additional scan, plateauing at a prevalence of approximately 30%.

Multivariate analysis identified younger age, female sex, lower BMI and earlier time of day as significant predictors or BAT occurrence. We also identified that lower temperatures were also predictive of ^{18}F-FDG BAT occurrence, although it was not clear whether it was the temperature on the preceding day or preceding 3 days which was most important as these were highly correlated.

Chapter 4: Predictors of ^{18}F-FDG BAT volume and activity on PET/CT

4.1 Aims

In the preceding chapter we identified multiple environmental and demographic factors which are associated with higher ^{18}F-FDG BAT prevalence. In this chapter we shall determine whether these variables correlate with ^{18}F-FDG BAT volume and metabolic activity.

4.2 Subjects and methods

4.2.1 Subject selection

All 3,295 eligible PET/CT scans of the 2,685 patients introduced in Chapter 3 between June 2007 and August 2012 were included.

4.2.2 Data collection

As described in section 3.2.2, the biological and meteorological metrics which appeared *a priori* plausible were recorded.

4.2.3 Image analysis

All eligible PET/CT scans (n=3,295) were reviewed to identify those with evidence of ^{18}F-FDG BAT uptake (n=175). Commercially available image fusion software (Mirada XD 3.4, Mirada Medical Ltd, Oxford, UK) was used to semi-automatically define isocontours around putative ^{18}F-FDG BAT depots on axial PET/CT scans (Figure 4-1), with a threshold set at an SUV of 2.5 g/ml using a similar technique to that described by

Huang *et al.* [203] and van Marken Lichtenbelt *et al.* [43]. We found that this threshold provided the best compromise between capturing the extent of ^{18}F-FDG uptake within BAT, whilst minimising artefactual ‘bleeding’ of signal into adjacent tissues. From this the volume (Figure 4-2) and SUVmax (*i.e.* the maximum SUV measurement within a region of interest) were calculated for each depot.

Figure 4-1: Semi-automatic selection of ^{18}F-FDG regions of interest by defining an isocontour set at SUV of 2.5 g/ml (a). Isocontours set at 2.0g/ml overestimate the extent of ^{18}F-FDG BAT uptake (b).

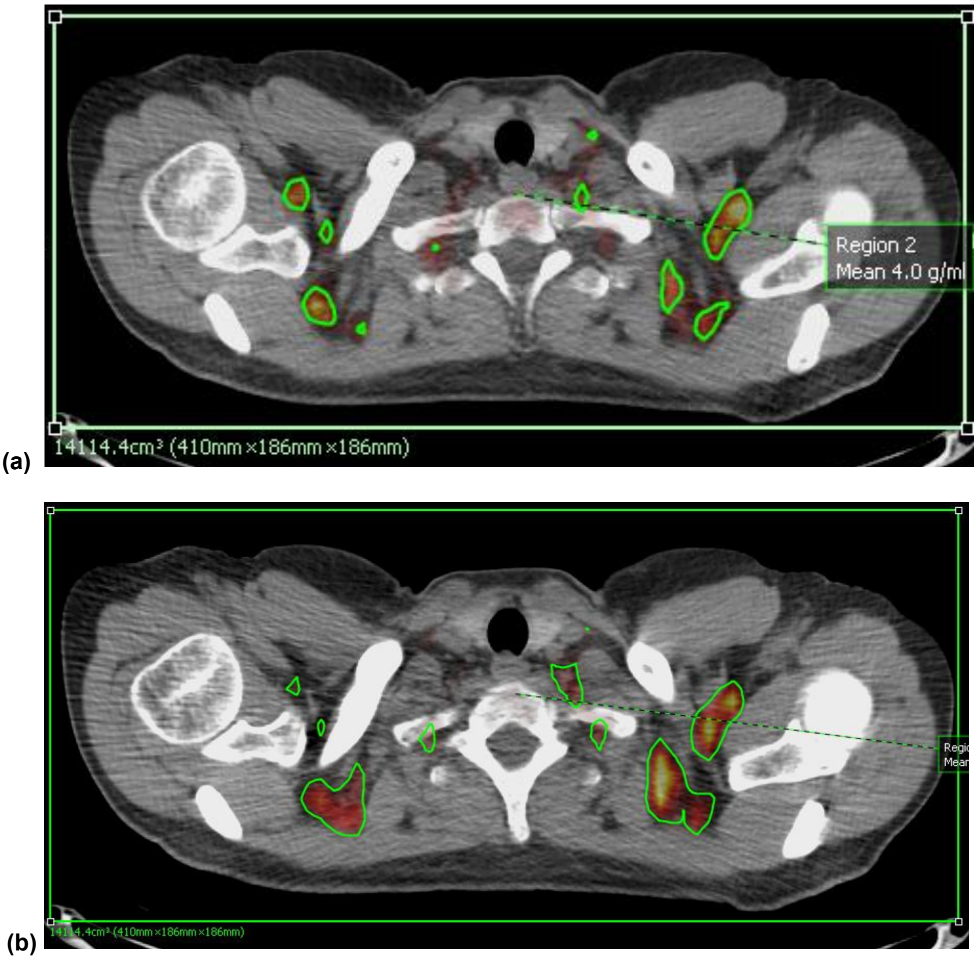

Figure 4-2: Coronal PET MIP image, showing isocontours around BAT from which volumes were derived.

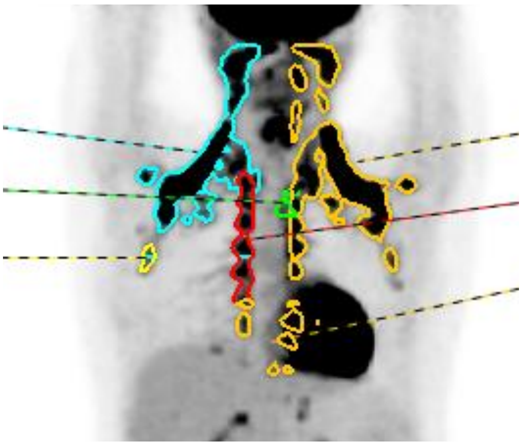

4.2.4 Statistical analysis

Normality testing using both the Kolmogorov-Smirnov (KS) and Shipiro-Wilk (SW) tests indicated that both ^{18}F-FDG BAT volume and SUVmax followed a non-normal distribution (KS statistic = 0.501, SW statistic = 0.120, $p<0.001$ for volume; KS = 0.529, SW = 0.213, $p<0.001$ for SUVmax). Both volume and SUVmax were heavily skewed due to there being 3,120/3,295 scans with no ^{18}F-FDG BAT uptake (Figure 4-3).

Figure 4-3: Frequency histogram showing distribution of ^{18}F-FDG BAT volumes.

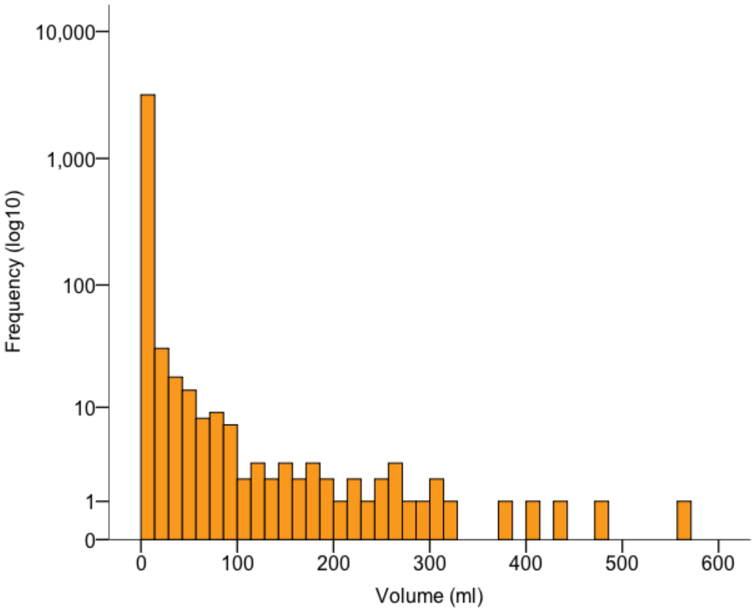

Following logarithmic transformation, $\log_{10}[^{18}$F-FDG BAT volume] followed a normal distribution using the Kolmogorov-Smirnov test (KS statistic = 0.099, *p* = 0.200) whereas the Shapiro-Wilk was borderline (SW statistic = 0.984, *p*=0.048) – likely due to some outliers with particularly high BAT volumes (Figure 4-4). Logarithmic transformation of SUVmax did not result in a normal distribution (KS statistic = 0.099, *p*<0.001; SW statistic = 0.9871, *p*=0.001). As logarithmic transformation excluded all ^{18}F-FDG BAT negative scans, transformation was not considered appropriate. Therefore linear regression was performed on the raw volume and SUVmax data. As conventional linear regression is not appropriate on these non-normally distributed data, non-parametric univariate and multivariate linear regression (Tobit analysis [211]) was performed on variables that seemed *a priori* plausible or which were found to be significant determinants of ^{18}F-FDG BAT prevalence.

Figure 4-4: Normal Q-Q plot showing almost normal distribution of $\log_{10}[^{18}$F-FDG BAT volume] except for those at the extremes.

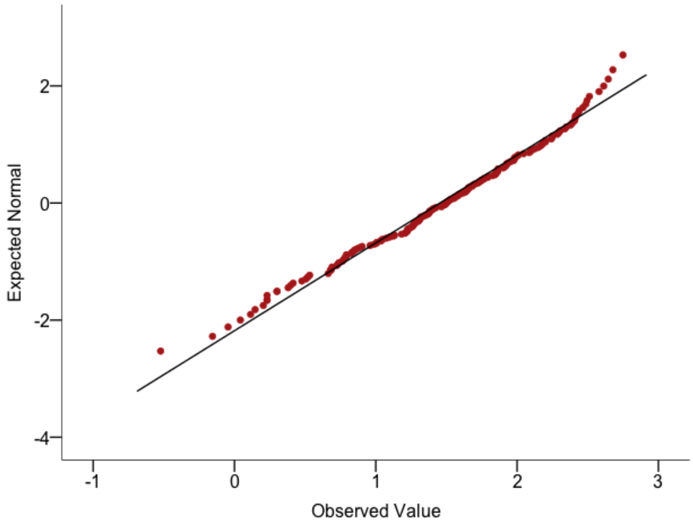

For PET/CT scans with evidence of ^{18}F-FDG BAT the association between both ^{18}F-FDG BAT volume and SUVmax, and variables was tested using Spearman correlation. Differences between ^{18}F-FDG BAT volume and SUVmax between groups (*i.e.* between sexes, BMI categories, fasting glucose status) were tested using the Wilcoxon-Mann Whitney or Kruskal-Wallis tests as appropriate. Missing values were replaced with mean or median values as appropriate.

Statistical analyses were performed using SPSS version 21.0 (SPSS IBM Corp., New York, USA) and GraphPad Prism version 5.0 for Windows (GraphPad Software, San Diego, USA). Tobit analyses were performed in R (R Foundation for Statistical Computing, Vienna, Austria).

4.3 Results

A strong positive correlation between ^{18}F-FDG BAT volume and SUVmax was observed (*r* = 0.870, *p*<0.0001; Figure 4-5) indicating that larger BAT volumes were associated with greater metabolic activity. The frequency distribution of ^{18}F-FDG BAT volume data was skewed, with the overwhelming majority of scans showing no evidence of BAT activity (Figure 4-3).

Figure 4-5: Scatterplot of ^{18}F-FDG BAT volume against SUVmax.

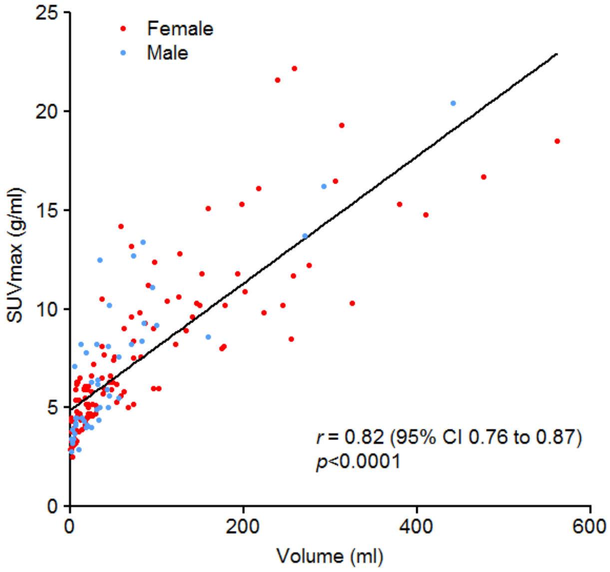

4.3.1 Factors associated with ^{18}F-FDG BAT volume

4.3.1.1 Sex

Females tended to have a higher mean ^{18}F-FDG BAT volume (6.79 ± 37.85ml) than males (volume = 1.39 ± 15.80ml), which was statistically significant (p <0.0001). However, when analysis is restricted to those PET scans showing ^{18}F-FDG BAT uptake (n=175) to account for the significant difference in BAT prevalence between sexes (see section 3.4.1.1), no significant difference in mean volume was observed between the sexes (p = 0.29; Figure 4-6).

Figure 4-6: Box and whisker plot showing no significant differences between mean ^{18}F-FDG BAT volume between sexes.

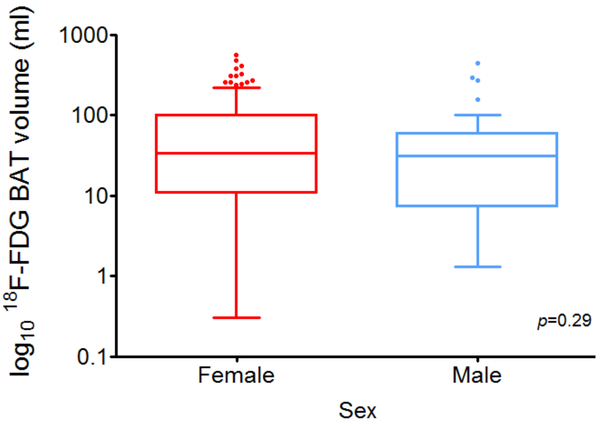

4.3.1.2 Age

When analysis was confined to ^{18}F-FDG BAT positive scans, there was a moderate inverse correlation between age and ^{18}F-FDG BAT volume (r = -0.308; Table 4-1) for both females (r = -0.308, p=0.0007) and males (r = -0.34, p = 0.0194; Figure 4-7). The difference between sexes approached statistical significance (p = 0.077).

Table 4-1: Spearman's correlations with ^{18}F-FDG BAT volume and SUVmax (= *p*<0.01, * = *p*<0.05).**

	All PET/CT scans (n = 3,295)		Positive PET/CT scans (n = 175)	
Variable	**Volume (ml)**	**SUVmax (g/ml)**	**Volume (ml)**	**SUVmax (g/ml)**
Sex	-0.136**	-0.136**	-0.080	-0.056
Age (years)	-0.160**	-0.159**	-0.308**	-0.239**
BMI (kg/m^2)	-0.106**	-0.106**	-0.016	0.028
Fasting serum glucose (mmol/l)	-0.071**	-0.071**	-0.002	-0.024
Injected ^{18}F-FDG dose (MBq)	-0.015	-0.015	-0.096	-0.095
Time of scan (hh:mm:ss)	-0.044*	-0.044*	-0.142	-0.092
Temperature on scan date (°C)				
- Minimum	-0.072**	-0.072**	0.134	0.107
- Mean	-0.075**	-0.076**	0.137	0.092
- Maximum	-0.079**	-0.079**	0.132	0.068
Temperature on preceding day (°C)				
- Minimum	-0.072**	-0.072**	0.248**	0.211**
- Mean	-0.080**	-0.080**	0.149**	0.114
- Maximum	-0.078**	-0.078**	0.145	0.112
Preceding 3 days' temperature (°C)				
- Minimum	-0.069**	-0.069**	0.179*	0.138
- Mean	-0.085**	-0.085**	0.186*	0.149*
- Maximum	-0.084**	-0.084**	0.171*	0.138
Preceding week's temperature (°C)				
- Minimum	-0.076**	-0.076**	0.126	0.121
- Mean	-0.081**	-0.081**	0.185*	0.144
- Maximum	-0.080**	-0.080**	0.158*	0.114
Mean monthly temperature (°C)	-0.066**	-0.066**	0.136	0.111
Hours of sunlight on scan date (h)	-0.030	-0.030	0.094	0.070
Total monthly hours of sunlight (h)	-0.046**	-0.047**	0.034	-0.021

Figure 4-7: Scatterplot showing inverse correlation between age and ^{18}F-FDG BAT volume for both genders.

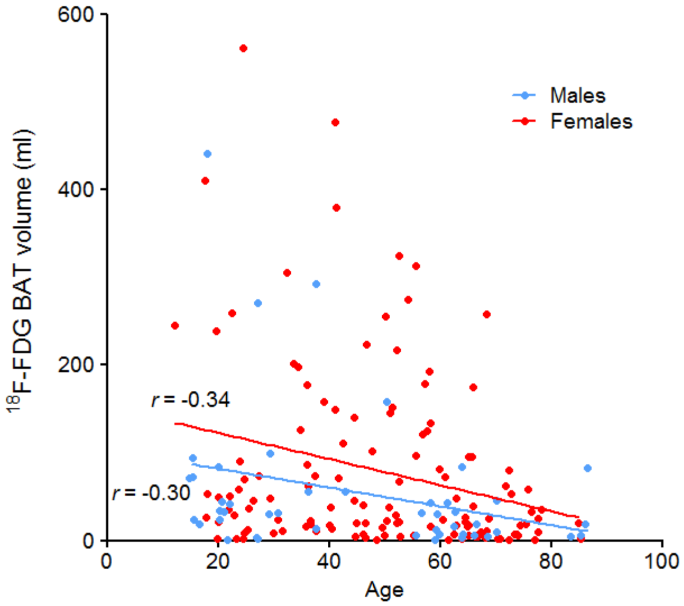

4.3.1.3 BMI

There was a weak inverse correlation between BMI and ^{18}F-FDG BAT volume (r = -0.106) which disappeared when analysis was confined to positive scans (r = -0.016; Table 4-1). Analysis of all 3,295 PET/CT scans according to BMI category showed that overweight and obese patients had a significantly lower mean ^{18}F-FDG BAT volume (2.95 ± 1.69ml and 1.75 ± 2.55ml respectively) than individuals with an ideal BMI (5.96 ± 34.36ml) which was statistically significant ($p<0.05$). Underweight patients also showed a lower volume (2.89 ± 14.58ml) but this was not statistically significant. However, when analysis is restricted to those ^{18}F-FDG BAT positive PET/CT scans (to account for the significant difference in ^{18}F-FDG BAT prevalence between BMI categories, highlighted in Figure 3-8), no statistically significant difference in volume was observed between BMI categories (p=0.41; Figure 4-8). Males tended to have a lower mean volume of ^{18}F-FDG BAT than females across all BMI categories (Figure 4-9), and became more pronounced for higher BMIs, although the differences between sexes were not statistically significant (Table 4-2). Nonetheless, the trend was towards diminishing BAT volumes with increasing BMI in males, with little corresponding change in BAT volume in females across BMI categories.

Figure 4-8: Box and whisker plot (with Tukey's hinges) showing no significant difference in ^{18}F-FDG BAT volume between BMI categories.

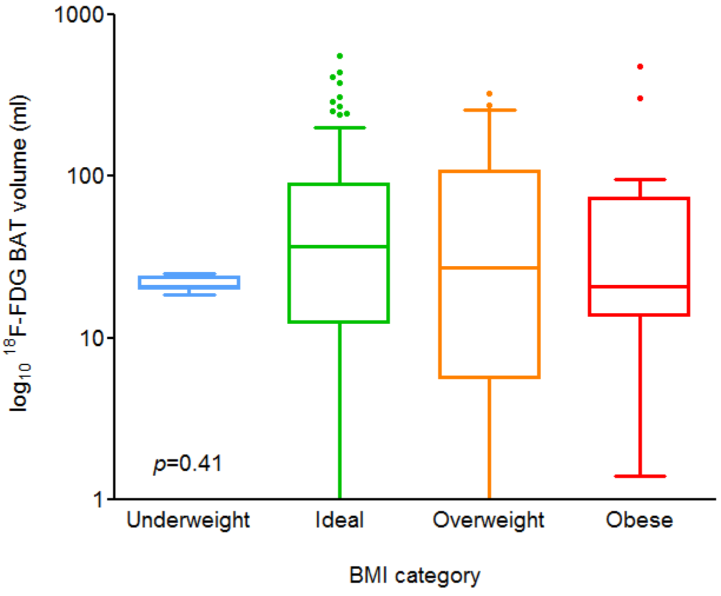

Figure 4-9: Scatterplot of ^{18}F-FDG BAT volume against BMI category (according to gender).

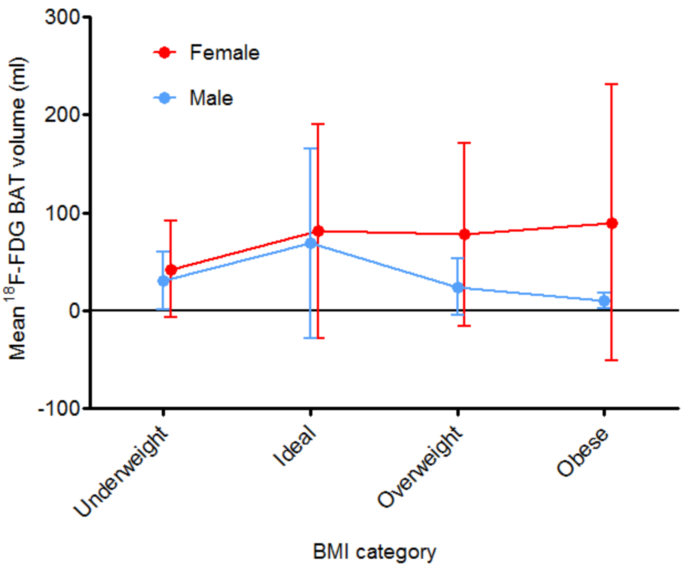

Table 4-2: Mean ^{18}F-FDG BAT volume for each BMI category according to sex.

BMI (kg/m^2)	^{18}F-FDG BAT volume (ml) in females (mean ± SD)	^{18}F-FDG BAT volume (ml) in males (mean ± SD)	Significance
Underweight (<18.5)	42.5 (49.7)	30.6 (29.1)	0.76
Ideal (18.5-24.99)	81.0 (109.4)	68.6 (96.5)	0.84
Overweight (25-29.99)	77.9 (93.3)	24.0 (28.7)	0.20
Obese (≥30)	89.8 (140.9)	10.4 (7.9)	0.08

4.3.1.4 Fasting serum glucose and injected ^{18}F-FDG dose

No clinically significant correlation between ^{18}F-FDG BAT volume and both fasting serum glucose and injected ^{18}F-FDG dose (Table 4-1) was found. Females were found to have a higher mean ^{18}F-FDG BAT volume for each glycaemic group although testing with 2-way ANOVA showed this not to be statistically significant (Figure 4-10).

Figure 4-10: Mean ^{18}F-FDG BAT volumes according to glycaemic groups.

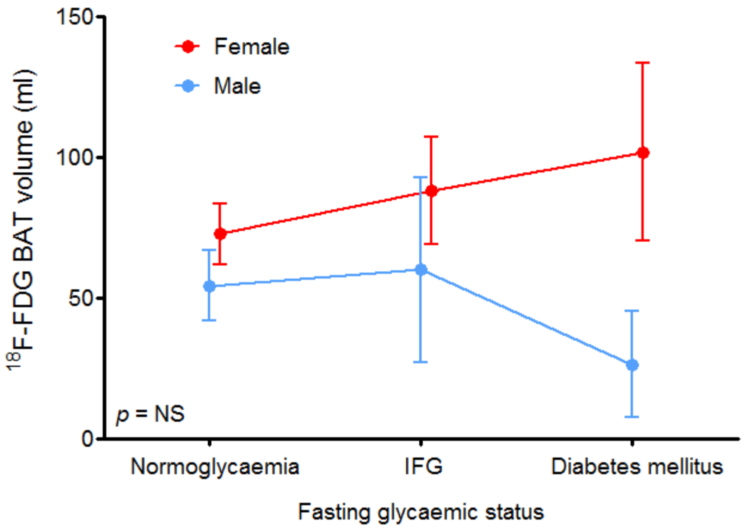

4.3.1.5 Environmental variables

A weak positive correlation was also identified between ^{18}F-FDG BAT volume (on positive PET/CT scans) for all temperature metrics as well as time of day (Table 4-1 and Table 4-3). The most pronounced correlation was with the preceding day's minimum temperature (r = 0.248). However, when analysed according to sex, no significant correlation between mean temperature and volume was seen (with the possible exception of males in whom there was a significant positive correlation between volume and mean temperature on the day of scanning; $r = 0.334$; Table 4-3). Women tended to have a more blunted response to temperature change than men (Figure 4-11), nonetheless, there was no significant difference between the sexes in terms of correlation between temperature and volume.

Figure 4-11: Scatterplot showing a weak positive correlation between mean temperature on the day of scanning and ^{18}F-FDG BAT volume.

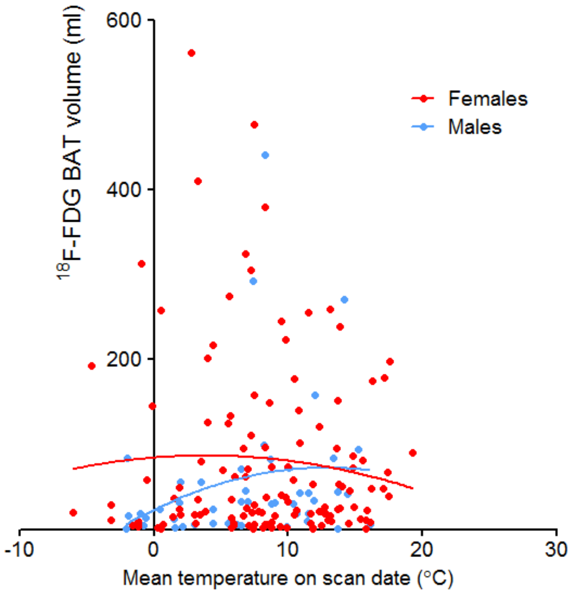

It is noteworthy that although there was an overall rather counter-intuitive positive correlation between volume and temperature (*i.e.* higher temperatures were associated with higher ^{18}F-FDG BAT volumes), the largest volumes occurred between approximately 0 and 10ºC (a pattern repeated for all temperature metrics) which is by no means warm. Above 10ºC there was a trend towards lower volumes (Figure 4-11) for all temperature metrics. Furthermore, there was also a consistent trend towards lower ^{18}F-FDG BAT volumes for very low temperatures (*i.e.* below 5ºC or so).

There was also a weak positive correlation between ^{18}F-FDG BAT volume and duration of sunlight on the day preceding scanning (r = 0.154, p = 0.043), but not on the day of scanning (r = 0.094), nor mean monthly sunlight duration (r = 0.018). Although prevalence of ^{18}F-FDG BAT showed a prominent seasonal variation (Figure 3-10), volume did not (p = 0.6696; Figure 4-12).

Table 4-3: Correlations between ^{18}F-FDG BAT volume and temperature by sex.

Time period (mean)	Overall Spearman's *r* correlation	Spearman's *r* for females (*p*-value)	Spearman's *r* for males (*p*-value)	*P* value of difference between sexes
Day of scanning	0.137 (*p*=0.072)	0.061 (0.492)	0.334 (0.023)	0.167
Preceding day	0.149 (*p*=0.050)	0.106 (0.230)	0.219 (0.143)	0.180
Preceding 3 days	0.186 (*p*=0.014)	0.165 (0.061)	0.242 (0.105)	0.196
Preceding week	0.185 (*p*=0.014)	0.153 (0.085)	0.266 (0.074)	0.192
Month	0.136 (*p*=0.074)	0.099 (0.264)	0.228 (0.127)	0.173

Figure 4-12: Mean ^{18}F-FDG BAT volume by month.

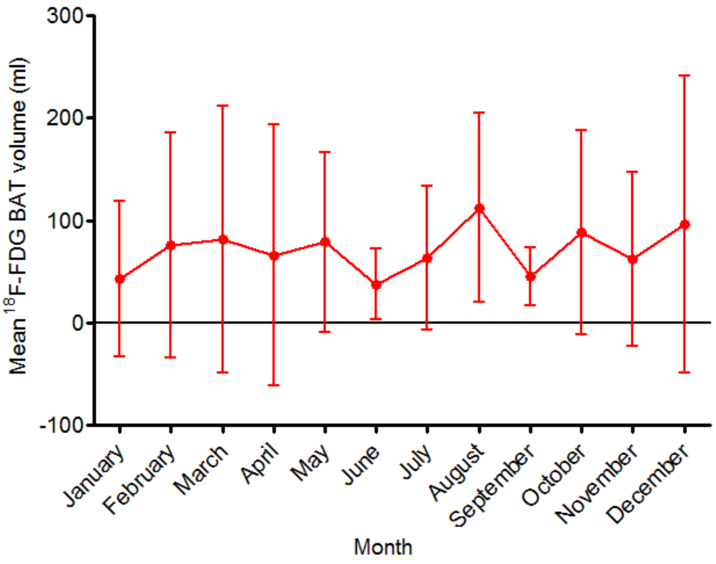

Subgroup analysis of the 15 subjects with multiple ^{18}F-FDG BAT positive scans showed that index scans (*i.e.* the PET/CT with the highest ^{18}F-FDG BAT volume) occurred throughout the year. The bubble plot at Figure 4-13, in which the size of each bubble is proportional to ^{18}F-FDG BAT volume, illustrates this pattern. Six out of fifteen subjects (40%) showed highest volumes in the winter (subjects A, C, F, J, L and M), followed by Autumn (B, E, K and O) and Spring (D, G, H and N) - 26.7% each. One subject (6.7%) showed their highest volume in the Summer (I).

Three subjects (B, D and L) underwent multiple PET/CT scans within the same calendar month (albeit in different years) which yielded different ^{18}F-FDG BAT volumes; subjects B and D both had negative scans in the same calendar month as their scans with the greatest ^{18}F-FDG BAT volume (94.3ml in September and 324.8ml in March respectively) and subject L had two scans with 111 ml and 20 ml in February.

Patient B underwent 10 scans (of which 5 were positive), which showed considerable monthly variation with approximately 70ml in the Spring, subsiding in the early Summer, then fluctuating throughout the Autumn and Winter. This highlights that volumes vary considerably within the same individual within a short period.

From this we were able to determine, for each season, the likelihood of a particular PET/CT scan being the index scan (Table 4-4). It is clear that, for those 15 subjects with multiple positive PET/CT scans, the likelihood of a particular scan being the index scan is six times higher in the Winter than the Summer.

Figure 4-13: Bubble plot showing monthly variation in ^{18}F-FDG BAT volume for 15 subjects with multiple positive scans. A: index scans (highest volume PET/CT scans for each subject); B: All scans (including subordinate and negative scans).

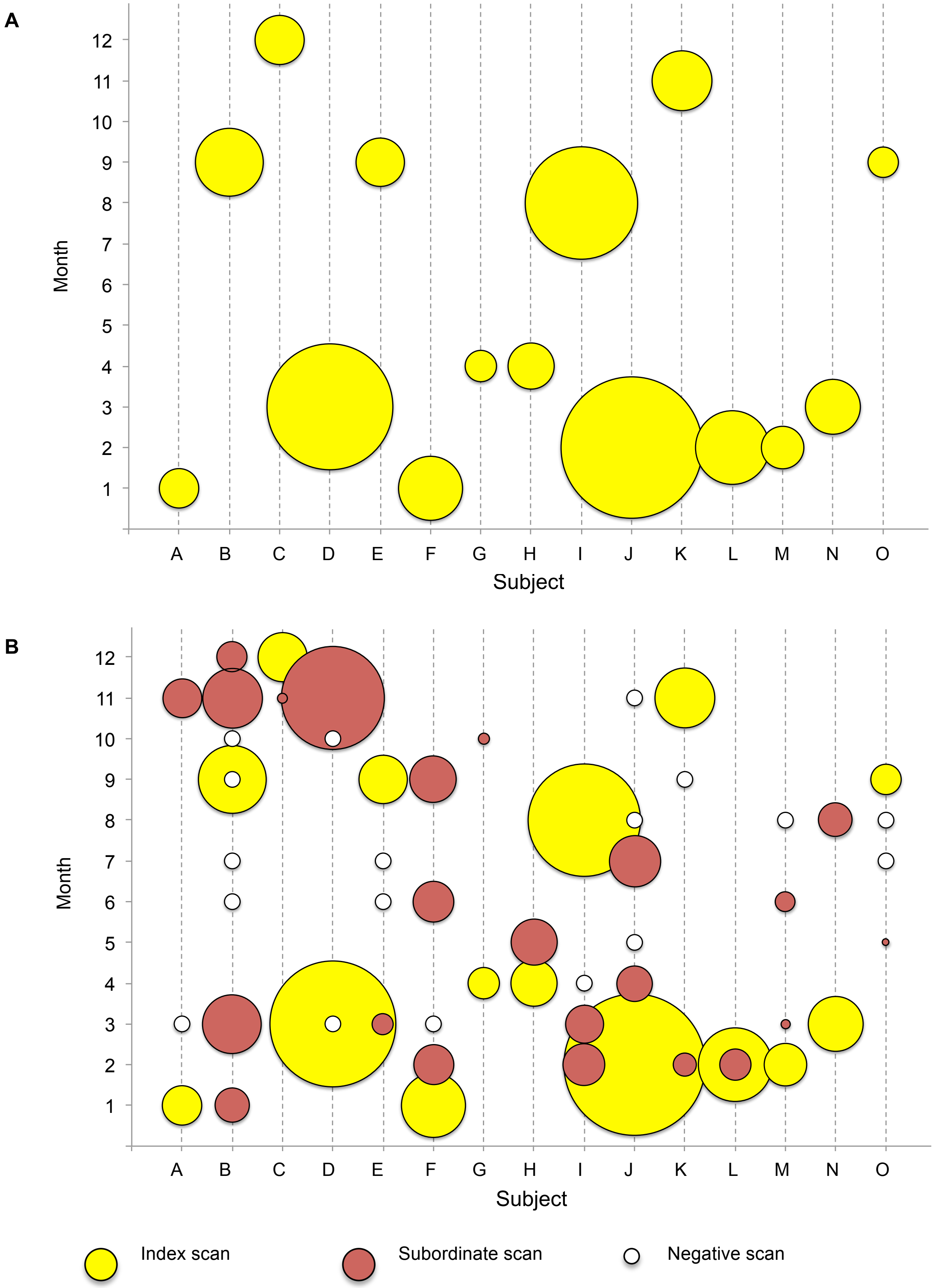

Table 4-4: Likelihood of an index scan being performed according to season.

Season	Number of index scans performed	Total number of scans performed	% of index scans
Winter	6	13	46.2%
Spring	4	16	25.0%
Summer	1	13	7.7%
Autumn	4	15	27.7%

4.3.2 Factors associated with ^{18}F-FDG BAT activity (SUVmax)

4.3.2.1 Sex

^{18}F-FDG BAT within females had a higher mean SUVmax (7.36 ± 4.12 g/ml) than in males (7.00 ± 3.82 g/ml) when analysis is restricted to the 175 ^{18}F-FDG BAT positive PET scans, although this was not statistically significant (*p* = 0.46; Figure 4-14).

Figure 4-14: Box and whisker plot showing no significant differences between mean ^{18}F-FDG BAT SUVmax between sexes (n=175).

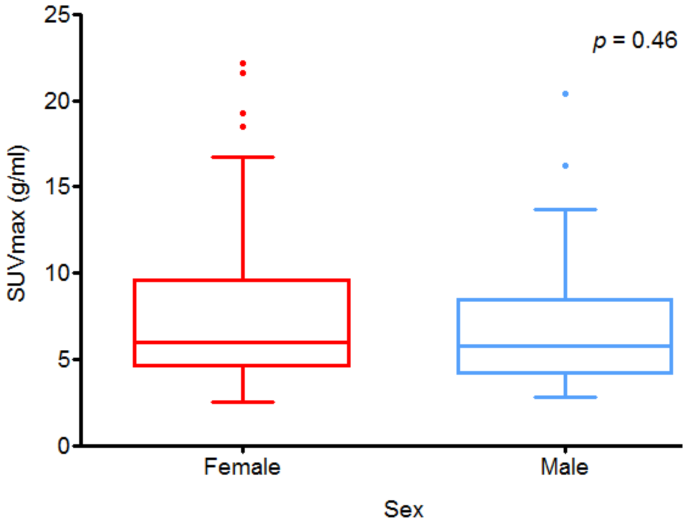

4.3.2.2 Age

Overall, there is a mild inverse correlation between age and SUVmax (*r* = -0.16, *p* < 0.001). This correlation is more pronounced when analysis is confined to positive scans only (r = -0.239, p = 0.0015). This inverse correlation between age and SUVmax is evident for both females (r = -0.211, 95% CI -0.375 to -0.033, p = 0.0171) and males (r = 0.288, 95% CI -0.540 to 0.011, p = 0.0519; Figure 4-15), and do not differ significantly (p=0.988).

Figure 4-15: Scatterplot showing inverse correlation between age and ^{18}F-FDG BAT SUVmax for both sexes (n=175).

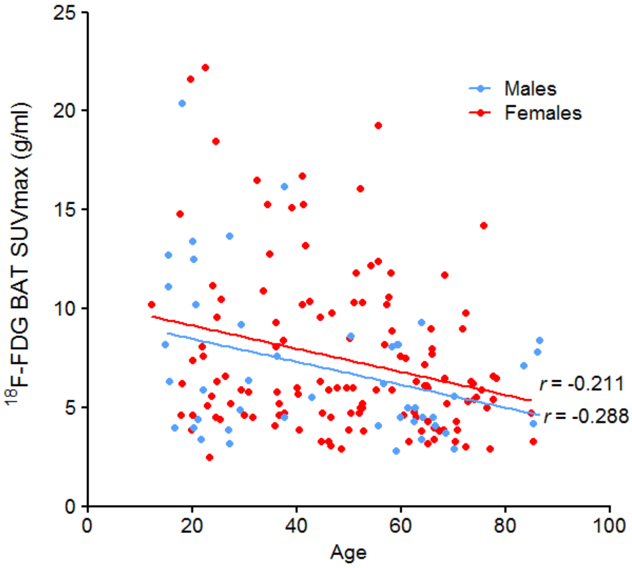

4.3.2.3 BMI

Although correlations between both BMI and fasting serum glucose, and SUVmax were observed when all scans were analysed (Table 4-1), no such correlation was present when analysis was confined to positive scans.

Similarly, although analysis of SUVmax across BMI categories for all scans showed a significantly lower SUVmax in overweight ($p < 0.05$) or obese patients ($p < 0.05$) compared with those with a normal BMI, no significant difference in mean SUVmax was identified between BMI categories when analysis was confined to the 175 positive scans ($p = 0.73$).

As with volume, there was a trend towards lower SUVmax in men for higher BMI categories (Figure 4-16), albeit not significant (*p* for interaction = 0.3075, using 2 way ANOVA).

Figure 4-16: Scatterplot of mean ^{18}F-FDG BAT SUVmax against BMI category (by gender).

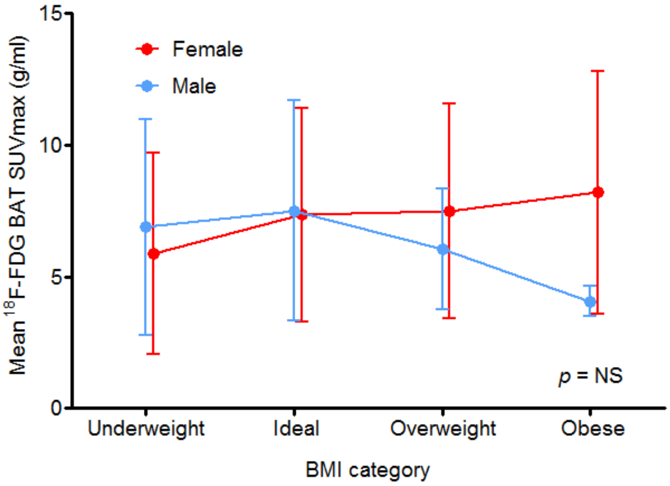

4.3.2.4 Fasting serum glucose and injected ^{18}F-FDG dose

As with volume, there was no significant correlation between SUVmax and both fasting serum glucose and injected ^{18}F-FDG dose (Table 4-1). No significant difference in mean SUVmax was observed between males and females in normoglycaemia or impaired fasting glucose. For those with a fasting serum glucose in the diabetes mellitus range, a significant difference did emerge (Figure 4-17).

Figure 4-17: Mean SUVmax against fasting glycaemic status (by gender).

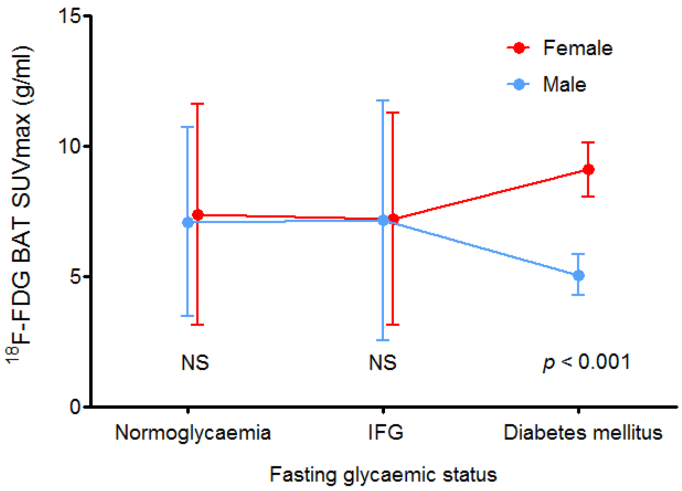

4.3.2.5 Environmental variables

The pattern of correlation between SUVmax and temperature on positive scans mirrored that of volume (section 4.3.1.5), with a somewhat counterintuitive weak positive correlation for ^{18}F-FDG BAT positive scans (Table 4-1), which was most significant for the preceding day's minimum temperature ($r = 0.211$).

As with volume, the correlation between SUVmax and temperature was stronger in males than in females (e.g. for mean temperature on the day of scanning, $r = 0.334$ for males, $r = 0.061$ for females; Figure 4-18), although they did not differ significantly.

Table 4-5: Correlations between ^{18}F-FDG BAT SUVmax and mean temperature by gender.

Time period (mean)	Overall Spearman's *r* correlation	Spearman's *r* for females (*p*-value)	Spearman's *r* for males (*p*-value)	*P* value of difference between sexes
Day of scanning	0.092 ($p = 0.228$)	0.061 (0.492)	0.334 (0.023)	0.167
Preceding day	0.114 ($p = 0.136$)	0.023 (0.798)	-0.117 (0.441)	0.740
Preceding 3 days	0.149 ($p = 0.050$)	0.135 (0.130)	0.192 (0.200)	0.660
Preceding week	0.144 ($p = 0.058$)	0.116 (0.192)	0.215 (0.151)	0.625
Month	0.111 ($p = 0.145$)	0.064 (0.472)	0.255 (0.087)	0.409

Figure 4-18: Scatterplot showing of mean temperature on the day of scanning against ^{18}F-FDG BAT activity (SUVmax) according to gender.

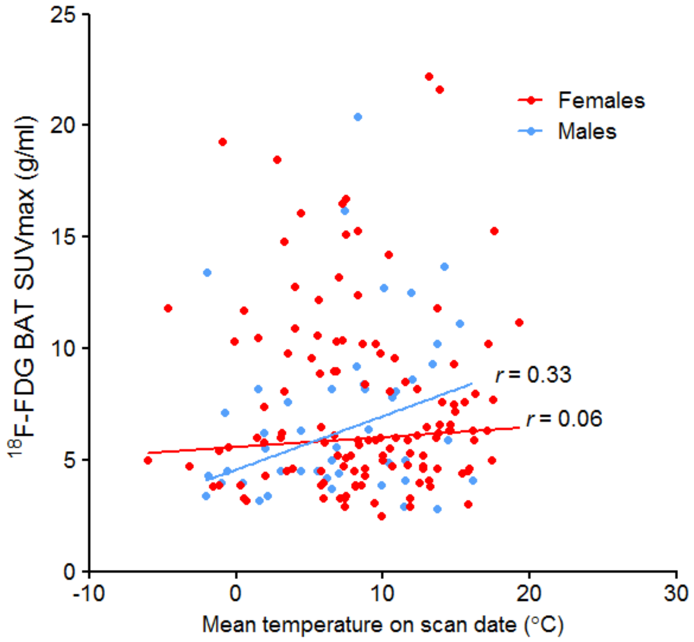

No significant correlation between mean SUVmax and time of day was observed for positive scans (*p* = 0.812; Figure 4-19).

Figure 4-19: Mean ^{18}F-FDG BAT SUVmax according to time of day.

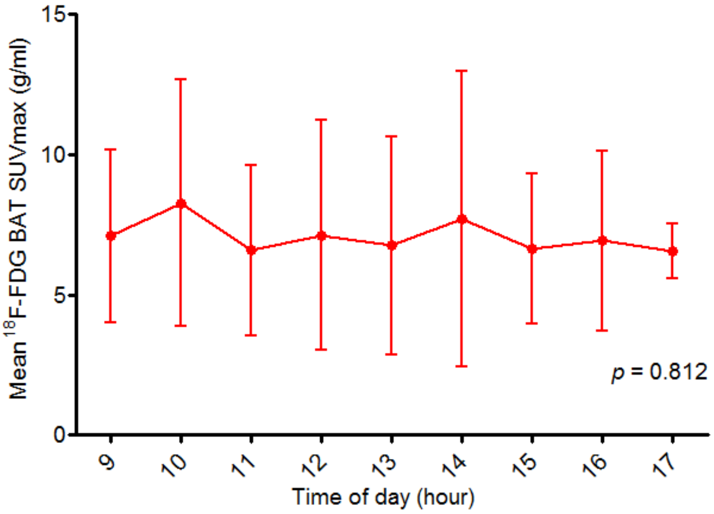

4.3.3 Linear regression analysis

As discussed above (section 4.2.4), ^{18}F-FDG BAT volume and SUVmax were not normally distributed. Despite logarithmic transformation, SUVmax failed normality testing, and the distribution of ^{18}F-FDG BAT volume data was borderline. Therefore the non-parametric Tobit regression model was used which is specifically designed for skewed data with a large percentage of values at the lower or upper limit [211].

4.3.3.1 Regression analysis of ^{18}F-FDG BAT mass

Stepwise multivariate Tobit analyses of the non-transformed mass data[a] from all scans (n=3,295) returned a model which showed age, sex, BMI, time of day, and maximum temperature on the day of scanning to be significant predictors of ^{18}F-FDG BAT mass (Table 4-6). Maximum temperature on the preceding day was also identified as a significant predictor of mass, although unlike the other variables, this has a positive coefficient of 28.7, indicating a positive relationship (*i.e.* that higher maximum temperatures are associated with a higher ^{18}F-FDG BAT mass).

---

[a] Mass was derived from volume by applying a multiplication factor of 0.92. Consequently there is a linear relationship between BAT mass and volume.

Table 4-6: Predictors of ^{18}F-FDG BAT mass on Tobit model univariate and multivariate regression analyses.

Variable (n = 3,295)	Univariate		Multivariate	
	Coefficient	*P*-value	Coefficient	*P*-value
Age	-4.64	<0.001	-4.13	<0.001
Sex (M compared to F)	-121	<0.001	-105	<0.001
BMI (kg/m^2)	-7.95	<0.001	-6.96	<0.001
Fasting serum glucose (mmol/l)	-24.3	<0.001	-	-
Time of scan	-0.19	<0.001	-0.215	<0.001
Temperature on scan date (°C)				
Minimum	-5.33	<0.001	-	-
Mean	-5.53	<0.001	-	-
Maximum	-5.23	<0.001	-34.8	0.005
Temperature on preceding day (°C)				
Maximum	-5.03	<0.001	28.7	0.020
Preceding week's temperature (°C)			-	
Mean	-6.10	<0.001		-
Mean monthly temperature (°C)	-4.96	0.001	-	-
Hours of sunlight on scan date	-6.10	-0.030	-	-
Total monthly hours of sunlight	-12.6	0.009	-	-

As identified in section 4.2.4, log$_{10}$[^{18}F-FDG BAT volume] passed normality testing using the Shapiro-Wilks test, therefore conventional parametric linear regression could reasonably be performed. Multivariate regression returned a model in which only age ($p < 0.001$) and minimum temperature on the preceding day ($p = 0.014$) were significant predictors of ^{18}F-FDG BAT volume (Table 4-7).

Table 4-7: Predictors of log$_{10}$[^{18}F-FDG BAT volume] on parametric univariate and multivariate linear regression.

	Univariate		**Multivariate**	
Variable (n=175)	B (SE)	*P*-value	B (SE)	*P*-value
Age	-0.010 (0.002)	<0.001	-0.011 (0.003)	<0.001
Sex (M compared to F)	-0.104 (0.115)	0.365	-0.127 (0.116)	0.272
BMI (kg/m^2)	-0.001 (0.011)	0.931	0.009 (0.012)	0.423
Fasting serum glucose (mmol/l)	0.027 (0.060)	0.657	0.109 (0.065)	0.093
Injected ^{18}F-FDG dose (MBq)	-0.002 (0.001)	0.081	-0.002 (0.001)	0.226
Time of scan	-1.2 x 10^{-5} (0.000)	0.073	-6.2 x 10^{-6} (0.000)	0.373
Temperature on scan date (°C)				
Minimum	0.016 (0.009)	0.089	-0.022 (0.047)	0.645
Mean	0.016 (0.009)	0.096	0.028 (0.037)	0.461
Maximum	0.014 (0.008)	0.101	-0.037 (0.037)	0.324
Temperature on preceding day (°C)				
Minimum	0.029 (0.009)	0.003	0.078 (0.032)	0.014
Mean	0.018 (0.009)	0.062	0.027 (0.102)	0.793
Maximum	0.015 (0.008)	0.066	-0.016 (0.056)	0.772
Preceding 3 days' temperature (°C)				
Minimum	0.019 (0.010)	0.052	-0.051 (0.036)	0.153
Mean	0.023 (0.010)	0.021	0.035 (0.104)	0.735
Maximum	0.017 (0.008)	0.045	-0.057 (0.055)	0.303
Preceding week's temperature (°C)				
Minimum	0.015 (0.010)	0.149	-0.039 (0.031)	0.214
Mean	0.023 (0.010)	0.026	0.096 (0.075)	0.206
Maximum	0.019 (0.009)	0.029	0.005 (0.043)	0.906
Mean monthly temperature (°C)	0.016 (0.011)	0.147	-0.014 (0.029)	0.627
Hours of sunlight on scan date	0.016 (0.020)	0.427	0.047 (0.049)	0.342
Total monthly hours of sunlight	0.000 (0.001)	0.689	0.001 (0.002)	0.516

4.3.3.2 Regression analysis of ^{18}F-FDG BAT activity (SUVmax)

Tobit regression analysis identified age, sex, BMI, time of day, maximum temperature on the day of scanning and on the preceding day to be significant predictors of ^{18}F-FDG BAT activity. Although conventional parametric linear regression could not be used on the non-normally distributed SUVmax data, given the high correlation between ^{18}F-FDG BAT and volume, it is likely that similar variables predict ^{18}F-FDG BAT activity as do volume.

Table 4-8: Predictors of ^{18}F-FDG BAT activity (SUVmax) on Tobit model univariate and multivariate regression analysis.

Variable (n = 3,295)	**Univariate**		**Multivariate**	
	Coefficient	*P*-value	Coefficient	*P*-value
Age	-0.378	<0.001	-0.334	<0.001
Sex (M compared to F)	-10.1	<0.001	-8.93	<0.001
BMI (kg/m^2)	-2.11	<0.001	-0.612	<0.001
Fasting serum glucose (mmol/l)	-0.679	<0.001	-0.803	0.121
Time of scan	-0.015	0.002	-0.017	<0.001
Temperature on scan date (°C)				
Minimum	-0.453	<0.001	-	-
Mean	-0.474	<0.001	-	-
Maximum	-0.451	<0.001	-2.88	0.006
Temperature on preceding day (°C)				
Maximum	-0.436	<0.001	2.34	0.025
Preceding week's temperature (°C)				
Mean	-0.528	<0.001	-	-
Mean monthly temperature (°C)	-0.426	<0.001	-	-
Hours of sunlight on scan date	-0.544	0.021	-	-
Total monthly hours of sunlight	-0.544	0.021	-	-

4.4 Summary

In this chapter we sought to identify which meteorological and demographic factors correlated with ^{18}F-FDG BAT volume and activity (SUVmax). When data from all 3,295 PET/CT scans is analysed (*i.e.* for both ^{18}F-FDG BAT positive and negative scans), those factors predicative of higher prevalence appear to correlate most highly with ^{18}F-FDG BAT volume and activity. Non-parametric multivariate linear regression (Tobit) analysis returned a model in which age, sex, BMI, time of day, maximum temperature on the day of scanning and on the preceding day to be significant predictors of both ^{18}F-FDG BAT volume and activity.

A different picture emerges if analysis is confined to scan data from ^{18}F-FDG BAT positive scans; multivariate regression analysis returned a model in which only age and minimum temperature on the preceding day are significant predictor of BAT volume.

Chapter 5: Occurrence of ^{18}F-FDG BAT uptake within anatomical compartments on serial PET/CT scans

5.1 Aims

In the preceding studies, we found that the prevalence, volume and activity of ^{18}F-FDG varies within a population and within individuals. In this study, we aim to determine whether ^{18}F-FDG BAT, regardless of its propensity to vary in volume and activity over time, occurs in consistent locations within individuals, or whether it occurs in a much more haphazard fashion.

5.2 Subjects and methods

All PET/CT scans which showed evidence of ^{18}F-FDG BAT activity in Chapter 3 were reviewed (175 scans in 152 patients) to determine whether ^{18}F-FDG BAT uptake occurred within each of four anatomical compartments: neck/supraclavicular fossae, mediastinum, paravertebral and peri-renal regions. ^{18}F-FDG BAT was considered present if it met the criteria outlined in section 3.2.4.

5.2.1 Image analysis

The presence or absence of uptake within these regions over time was plotted in a matrix to illustrate the pattern of activity over time for each patient. From the ^{18}F-FDG BAT volumes calculated in section 4.2.3 above, the scans with the largest volume of ^{18}F-FDG BAT were identified for each patient (the ‘index scan’), against which the patient’s other ^{18}F-FDG BAT positive PET/CT scans (the ‘subordinate scans’) were compared. Negative scans were excluded.

5.2.2 Statistical analysis

For each ^{18}F-FDG BAT positive PET/CT scan, the presence or absence of BAT within each of four anatomical compartments was recorded (*i.e.* cervical/supraclavicular fossae, paravertebral, mediastinal and peri-renal compartments), as was the pattern of distribution along the lines described by Ouellet *et al.* [133].

Further analysis was performed on the subgroup of patients with ^{18}F-FDG BAT uptake on sequential PET/CT Scans (n=15). The degree of concordance of ^{18}F-FDG BAT distribution across each patient's sequential positive scans was measured using pairwise percent agreement, Fleiss' kappa and Krippendorff's *alpha*[a] using the online calculator ReCal3 ("Reliability Calculator for 3 or more coders")[b] [212]. Although both tests are typically employed to measure the level of agreement among raters, this situation is similar in that we are faced with multiple 'raters' (*i.e.* multiple PET/CT scans over time) measuring multiple 'subjects' (*i.e.* the anatomical compartments). Unlike Cohen's kappa which is limited to two raters, Fleiss' kappa can be used to measure the agreement between any number of raters, and takes into account the level of agreement that would be expected by chance – which is of particular importance when the number of categories being measured is small, as in this study, where the likelihood of agreement by chance is high. Furthermore both tests may be used with nominal and ordinal data.

To determine whether there was a difference between mean ^{18}F-FDG BAT volume and the number of positive anatomical compartments, the Kruskal-Wallis test (a non-parametric variant of one-way ANOVA that compares the means of three or more unmatched groups) with Dunn's post tests was performed using GraphPad Prism 5.0 for Windows (GraphPad Software, San Diego, California, USA).

---

[a] Where $\alpha = 1$ indicates perfect agreement, $\alpha = 0$ indicates the absence of agreement, and $\alpha < 0$ indicates systematic disagreements greater than that expected by chance.

[b] http://dfreelon.org/utils/recalfront/recal3/

5.3 Results

5.3.1 Patterns of ^{18}F-FDG BAT uptake

Various patterns of ^{18}F-FDG BAT distribution were identified; ^{18}F-FDG BAT was most prevalent within the cervical/supraclavicular fossae ('SCF'), and was present in 162/175 (92.6%) of scans (Table 5-1), followed by the paravertebral compartment in 143/175 (81.7%). In no case was ^{18}F-FDG BAT confined exclusively to the peri-renal compartment.

In only 25/175 scans (14.3%) was ^{18}F-FDG BAT confined to a single compartment (patterns 1, 5, 13 and 14). The commonest pattern was of uptake within the cervical/SCF, paravertebral and mediastinal compartments (pattern 3), occurring in 37.7%.

Table 5-1: Distribution patterns of ^{18}F-FDG BAT on serial PET/CT scans.

Pattern (n=175)	Anatomical compartment				Number of scans
	Cervical / SCF	Paravertebral	Mediastinal	Peri-renal	
1	+	-	-	-	20 (11.4%)
2	+	+	-	-	34 (19.4%)
3	+	+	+	-	66 (37.7%)
4	+	+	+	+	29 (17.6%)
5	-	+	-	-	4 (2.3%)
6	+	-	+	-	10 (5.7%)
7	+	-	-	+	0 (0.0%)
8	+	+	-	+	2 (1.1%)
9	-	+	+	+	0 (0.0%)
10	-	+	-	+	3 (1.7%)
11	+	-	+	+	1 (0.6%)
12	-	+	+	-	5 (2.9%)
13	-	-	+	-	1 (0.6%)
14	-	-	-	+	0 (0.0%)
Number of scans	162 (92.6%)	143 (81.7%)	112 (64.0%)	35 (20.0%)	

5.3.2 ^{18}F-FDG BAT distribution patterns on serial ^{18}F-FDG BAT positive scans

The demographics of the subgroup consisting of 15 patients with ^{18}F-FDG BAT uptake on serial PET/CT scans are shown in Table 5-2; four were males (mean age 37.3 years) and 11 females (mean age 40.1 years). All underwent PET/CT scans as part of their routine workup for cancer. Table 5-3 shows the number of anatomical compartments containing ^{18}F-FDG BAT for both index scans (denoted by *) and subordinate scans. In only one aberrant case did the subordinate scan show ^{18}F-FDG BAT uptake within more anatomical compartments than the index scan (patient H). There was little difference in the ^{18}F-FDG BAT volumes between the two scans (43.6 ml and 43.5 ml) and this could be attributed to measurement error.

Table 5-2: Patient demographics of individuals with multiple positive PET/CT scans.

Subject	Age at first scan (years)	Sex	Diagnosis
A	57	Male	Squamous cell carcinoma of the lung
B	14	Male	Hodgkin’s lymphoma
C	20	Female	Hodgkin’s lymphoma
D	52	Female	Malignant melanoma
E	29	Female	Hodgkin’s lymphoma
F	20	Male	Hodgkin’s lymphoma
G	85	Female	Bronchogenic cancer
H	58	Male	Gastro-intestinal stromal tumour
I	22	Female	Hodgkin’s lymphoma
J	17	Female	Hodgkin’s lymphoma
K	37	Female	Breast cancer
L	43	Female	Oesophageal cancer
M	25	Female	Hodgkin’s lymphoma
N	36	Female	Cervical cancer
O	75	Female	Bowel cancer

Table 5-3: Anatomical compartments showing ^{18}F-FDG BAT on serial PET/CT scans.

Subject	Scan date (* = index scan)	^{18}F-FDG volume (ml)	Anatomical compartment			
			Cervical / SCF	Paravertebral	Mediastinal	Peri-renal
A	January 2009*	31.8*	1	1	1	0
	November 2011	30.8	1	1	1	0
B	March 2009	70.7	1	1	1	0
	September 2009*	94.3*	1	1	1	0
	November 2009	72.9	1	1	1	0
	January 2010	24.0	1	1	0	0
	December 2010	18.6	1	1	1	0
C	November 2009	2.0	1	1	0	0
	December 2009*	49.4*	1	1	0	0
D	November 2010	217.4	1	1	1	0
	March 2011*	324.8*	1	1	1	0
E	September 2010*	47.9*	1	1	0	0
	March 2011	9.1	1	1	0	0
F	January 2011*	84.0*	1	1	1	0
	June 2011	33.9	1	1	1	0
	September 2011	44.3	1	1	1	0
	February 2012	32.7	1	1	1	0
G	April 2012*	20.1*	0	1	0	1
	October 2012	2.5	0	1	0	1
H	April 2008*	43.6*	1	1	0	1
	May 2011	43.5	1	1	1	1
I	February 2011	35.8	1	1	1	0
	August 2011*	258.9*	1	1	1	1
	March 2012	29.5	1	1	1	0
J	February 2011*	409.7*	1	1	1	1
	April 2011	25.8	1	1	1	0
	July 2011	53.8	1	1	1	0
K	November 2011*	73.3*	1	1	1	0
	February 2012	10.9	1	1	1	0
L	February 2008*	111.1*	1	1	1	1
	February 2012	20.0	1	0	1	0
M	June 2009	8.0	1	0	0	0
	February 2010*	37.0*	1	0	0	0
	March 2009	1.7	1	0	0	0
N	August 2009	23.2	1	1	1	1
	March 2009*	61.7*	1	1	1	1
O	May 2011	0.9	0	1	1	0
	Sep 2009*	18.9*	1	1	1	0

Furthermore both scans were performed in the Spring, approximately three years apart. In the remaining 14 cases, the index scan showed uptake within at least as many anatomical compartments as the subordinate scans (Figure 5-1). In those cases where the index scan showed a much greater ^{18}F-FDG BAT volume than the subordinate scans (subjects I, J, L and possibly O), ^{18}F-FDG BAT was present in more compartments on the index scan than the subordinate scans.

Figure 5-1: Bar chart showing the number of anatomical depots on serial scans for 15 patients (orange = index scan, blue = subordinate scan).

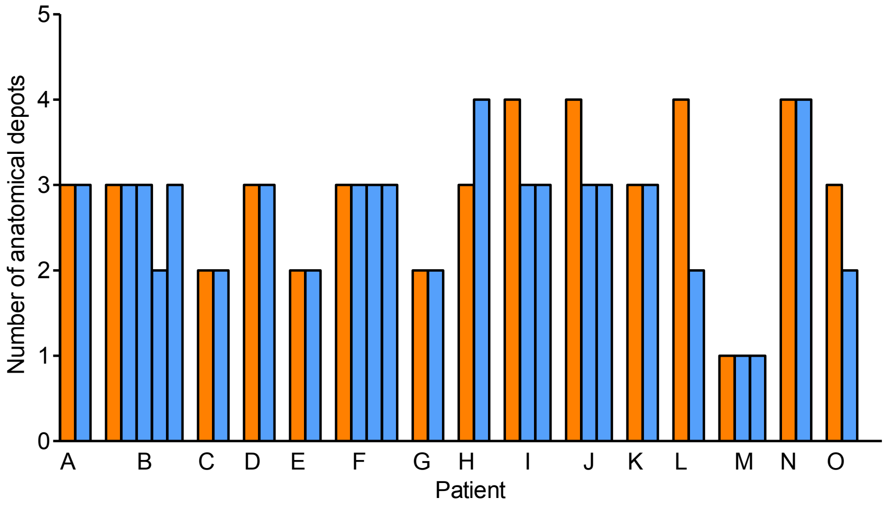

Table 5-4 shows the inter-rater reliability calculations for the 15 subjects with multiple ^{18}F-FDG BAT positive scans. Nine subjects (60%) showed ^{18}F-FDG BAT uptake within the same anatomical compartments on serial scans (100% pairwise agreement, Fleiss' $\kappa = 1$, Krippendorff's *alpha* = 1), greater than that expected by chance. Most prominent among these was patient F who showed 100% concordance in ^{18}F-FDG BAT distribution across four scans performed over a 13 month period. Also worthy of note is subject B who underwent five ^{18}F-FDG BAT positive scans, which showed a high level of concordance in terms of ^{18}F-FDG BAT distribution (mean pairwise agreement 90%, Fleiss' $\kappa = 0.762$, Krippendorff's $\alpha = 0.774$) - higher than that expected by chance. Four subjects (I, J, L and O) showed a lower inter-rater agreement; three disagreed on a single anatomical compartment only, resulting in a Fleiss' κ statistic of 0.4 - 0.467 indicating fair-to-moderate agreement according to the criteria of Landis and Koch [213] shown in Table 5-5. Patient L is noteworthy insofar as there is discordance between two anatomical depots on two PET/CT scans (performed 4 years apart, both in February) resulting in poor agreement (Fleiss' κ = -0.333).

The inter-observer reliability for subject H's scans are lower than would be expected by chance. This subject only had two positive scans, and there is doubt as to whether the index scan has been correctly identified as both have similar ^{18}F-FDG BAT volumes (*vide supra*, page 119).

Table 5-4: Inter-rater reliability calculations for serial ^{18}F-FDG BAT positive PET/CT scans.

Patient	Average pairwise agreement (%)	Fleiss' k	Fleiss (observed agreement)	Fleiss (expected agreement)	Krippendorff's α
A	100	1	1	0.625	1
B	90	0.762	0.9	0.58	0.774
C	100	1	1	0.5	1
D	100	1	1	0.625	1
E	100	1	1	0.5	1
F	100	1	1	0.625	1
G	100	1	1	0.5	1
H	75	-0.143	0.75	0.781	0
I	83.3	0.4	0.833	0.722	0.45
J	83.333	0.4	0.833	0.722	0.45
K	100	1	1	0.625	1
L	50	-0.333	0.5	0.625	-0.167
M	100	1	1	0.625	1
N	100	Undefined due to invariant values			1
O	75	0.467	0.75	0.531	0.533

Table 5-5: Landis and Koch's criteria for interpreting kappa statistics [213].

κ	**Interpretation**
< 0	Poor agreement
0.01 – 0.20	Slight agreement
0.21 – 0.40	Fair agreement
0.41 – 0.60	Moderate agreement
0.61 – 0.80	Substantial agreement
0.81 – 1.00	Almost perfect agreement

Unsurprisingly, there was a moderately strong positive correlation between the number of anatomical compartments showing ^{18}F-FDG BAT activity and the corresponding BAT volume in those patients with ^{18}F-FDG BAT positive scans (r = 0.72, 95% CI 0.63 – 0.78, p <0.0001), and the subgroup of 15 patients with multiple scans (r = 0.57, 95% CI 0.31 – 0.76, p <0.001). Although on the face of it this would seem obvious, the mean ^{18}F-FDG BAT volume increases in a super-linear fashion as the number of involved anatomical compartments increases, *i.e.* mean volume in 1 compartment = 9.3 ± 11.7ml; 2 compartments = 20.39 ± 19.36ml; 3 compartments = 77.67 ± 74.5ml and 4 compartments = 205.0 ±145.2ml (Figure 5-2).

Figure 5-2: Box and whisker plot showing super-linear relationship between the number of compartments showing ^{18}F-FDG BAT uptake and mean BAT volume.

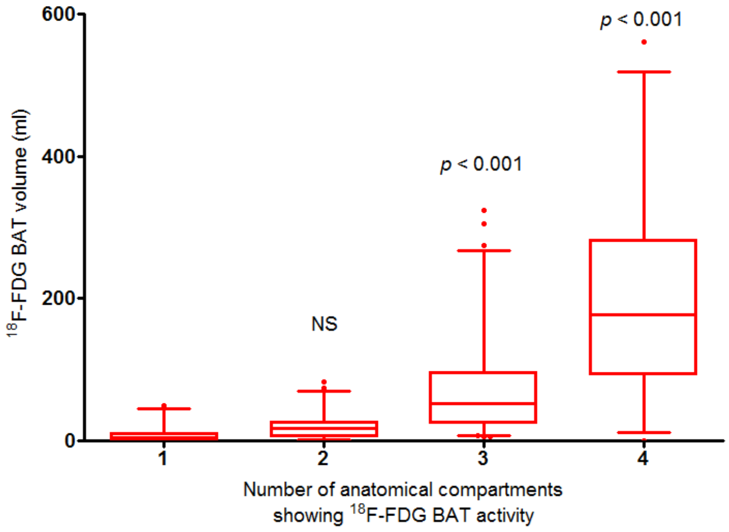

5.4 Summary

In this chapter we analysed the patterns of ^{18}F-FDG BAT on serial PET/CT scans in 15 patients with the aim of determining the consistency of BAT uptake across multiple scans.

After identifying each patient's 'index' scan (*i.e.* the PET/CT scan with the largest volume of ^{18}F-FDG BAT), the pattern of BAT uptake was compared against that in the patient's other scans. We identified considerable consistency across multiple scans with 9/15 showing ^{18}F-FDG BAT uptake in the same anatomical compartments across multiple scans. For 5/15 patients, there was uptake within more anatomical compartments on the index scan.

This suggests that the 'index' scan provides a fairly accurate representation of ^{18}F-FDG BAT uptake on scans with lesser BAT activity. As a consequence, the index PET/CT scan may provide a useful baseline against which other imaging modalities can be compared.

Chapter 6: Colocalisation analysis of ^{18}F-FDG BAT uptake on serial PET/CT scans

Colocalisation is a well-established technique in microscopy [214], particularly in the field of fluorescence and dual-colour confocal microscopy in which it is used to quantify the degree of agreement between two images or image stacks. The location of different fluorescently labelled molecules (fluorochromes) are compared to determine whether they occur in the same subcellular location (Figure 6-1, showing red and green channels corresponding to different fluorochromes). Colocalisation analysis has been used successfully in fluorescence microscopy to demonstrate that particular proteins are associated with organelles including plasma membrane [215], mitochondria [216] and nuclei [217].

There are essentially two approaches:

- Intensity correlation in which pixel (or voxel) intensities in one image or image track (or 'channel') are compared with the signal intensities of corresponding voxels in another channel;
- Object–based analysis [215] which evaluates the degree of spatial overlap of objects. Objects may be considered colocalised if either the centre of mass (centroid) of one object lies within the area of another (centre/particle coincidence; Figure 6-1 F); or the 'nearest neighbour approach' (Figure 6-1 G) in which two objects are considered colocalised if their centres of mass lie within a certain distance (e.g. the optical resolution of the microscope – typically 0.2μm in light microscopy).

Figure 6-1: Object-based colocalisation analysis using centre/particle coincidence (from Bolte *et al.* [218]).

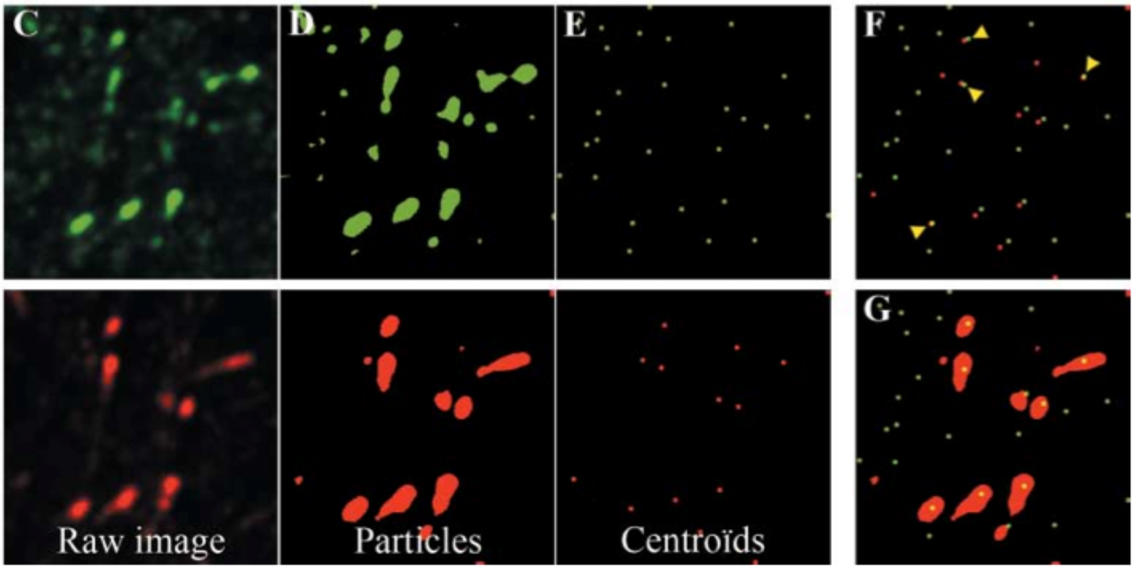

The colocalisation of two images can be evaluated visually, quantitatively and statistically. Visual evaluation of colocalised images is the simplest approach in which images are either compared side-by-side or one image is superimposed over another to demonstrate that the tissues of interest occur in the same location.

To date, co-occurrence of ^{18}F-FDG BAT on serial PET/CT scans or between different imaging modalities (*e.g.* PET and MR) has taken the form of rather simplistic qualitative analysis in which images are juxtaposed images showing BAT in different compartments. Although this does provide a good representation of where colocalisation occurs, it is not possible to present all images, and one is invited to make the assumption that these selected images are representative in the absence of quantitative evidence. Therefore, quantitative object-based colocalisation analysis offers an alternative approach for comparing ^{18}F-FDG BAT across different scans.

Both the intensity correlation and object-based analyses may be subjected to statistical tests to quantify the degree of colocalisation. Pearson's correlation coefficient (PCC) is the best known [219]. This describes the proportion of variability in one channel caused by variability in the second channel. This does not provide a true quantification of the degree of colocalisation, but rather an estimate of the strength of association between two images. The coefficient varies from -1 (inverse correlation or exclusion), 0 (the absence of correlation) to +1 (perfect correlation), which can be difficult to interpret [214].

Better suited to object-based analysis is Manders' colocalisation coefficient (MCC), particularly when the numbers of objects differ between the two channels. This technique generates two coefficients: 'M1' (the proportion of objects in channel A that overlaps with channel B) and 'M2' (proportion of objects in channel B that overlaps with channel A) to describe the degree of fractional overlap [220], and the coefficient ranges from 0 (no overlap) to 1 (100% overlap). This is better suited to describing how images compare with each other, and as in this case of Chapter 5, how images compare with an index image.

PCC and MCC may be used in three-dimensional analysis as part of wider object-based analysis. The major drawback of these techniques is the necessity to segment the object of interest from the background. This has already been addressed above by defining ROIs around areas of ^{18}F-FDG BAT detected semi-automatically on PET/CT.

Although prevalent within microscopy, the results can be ambiguous and do not take into account the level of overlap that could be expected by chance. Several approaches have been developed to address this by comparing the observed colocalisation coefficients against those of randomly generating images to generate some form of statistical significance. The observed coefficients between two channels may be considered significant if it is greater than 95% of randomised images. The principle is demonstrated in Figure 6-2 C, which shows a probability distribution curve from PCC measurements from multiple randomised images, while the red line indicates the PCC of the original images – which is significantly higher. D shows a means of summarising the results.

Figure 6-2: Probability distribution function from randomised images (from Bolte and Cordelières [218]).

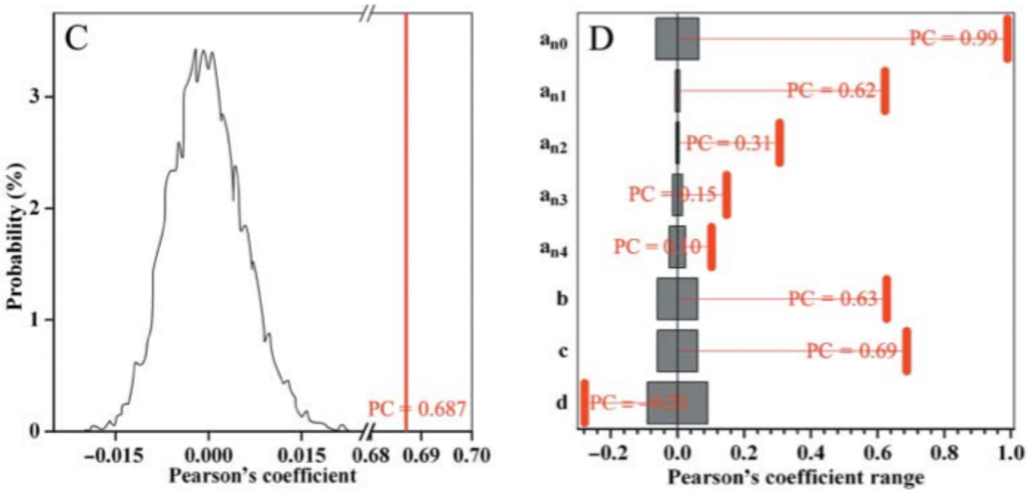

Various approaches for generating randomised images have been described. The approach described by Costes [221] scrambled one of the images or image stacks by splitting it up into blocks, which are then randomly shuffled. The block size is user-defined, but should be equal to or greater than the size of the objects within the image, but in light microscopy is typically equal to the point spread function of the image. However this technique destroys the spatial relationships of the image, such that voxels are no longer adjacent to their original neighbours, and instead lie next to voxels from other parts of the image [214]. This has the effect of producing a probability distribution curve that is narrower than the original images, which result in spuriously high significance values [221, 222]

An alternative approach is that of ‘frame translation’. Van Steensel [217] proposed comparing the observed colocalisation coefficient between two channels, with the coefficient obtained by incrementally shifting one of the channels in a single axis. Fay [223] described a similar method in which the random channels are generated by translating one image in all three axes.

This technique, borrowed from microscopy, presents a novel alternative means to quantitatively analyse the distribution of ^{18}F-FDG BAT on serial PET/CT scans.

6.1.1 Aims

Building on the findings from Chapter 5, which showed a high level of concordance of ^{18}F-FDG BAT distribution across serial PET/CT scans, we set out to evaluate individual ^{18}F-FDG BAT deposits to determine whether they occur in fixed or variable locations over time, and whether they are activated in a piecemeal or global manner. From this we aim to determine whether the 'index' PET/CT scan (the scan showing maximal ^{18}F-FDG BAT activity) is a reliable standard against which other imaging modalities may be compared.

6.1.2 Subjects and method

The 38 serial ^{18}F-FDG BAT positive scans for the 15 patients introduced in Chapter 5 were reviewed. As described above ROIs corresponding to ^{18}F-FDG BAT were selected semi-automatically by defining isocontours set at an SUV of 2.5 g/ml around areas of ^{18}F-FDG uptake within adipose tissue (as identified on CT). This was performed using the proprietary image fusion software Mirada XD 3.4 (Mirada Medical Ltd, Oxford, UK).

The 'index scan' (the PET/CT scan with the largest volume of ^{18}F-FDG BAT) was identified for each subject, which formed the baseline against which subordinate scans were compared.

As patient positioning was not uniform across serial scans (Figure 6-3), it was necessary to register images with respect to the index scan using a combination of automatic rigid and non-rigid registration as appropriate using XD 3.4. The quality of image registration was verified visually using the in-built visualisation tool within Mirada XD 3.4, which displayed a mosaic composed of the index image, interspersed with parts of the registered subordinate image (Figure 6-4), as well as an overlay (Figure 6-5).

The registered images were imported into ImageJ 1.48 [224, 225] for analysis. ROIs were traced around the isocontours defined above, and converted to a mask. Subsequent colocalisation analysis was performed upon these stacks of mask images, all of which were registered to the index scan.

Figure 6-3: Subordinate CT superimposed over the index CT prior to image registration.

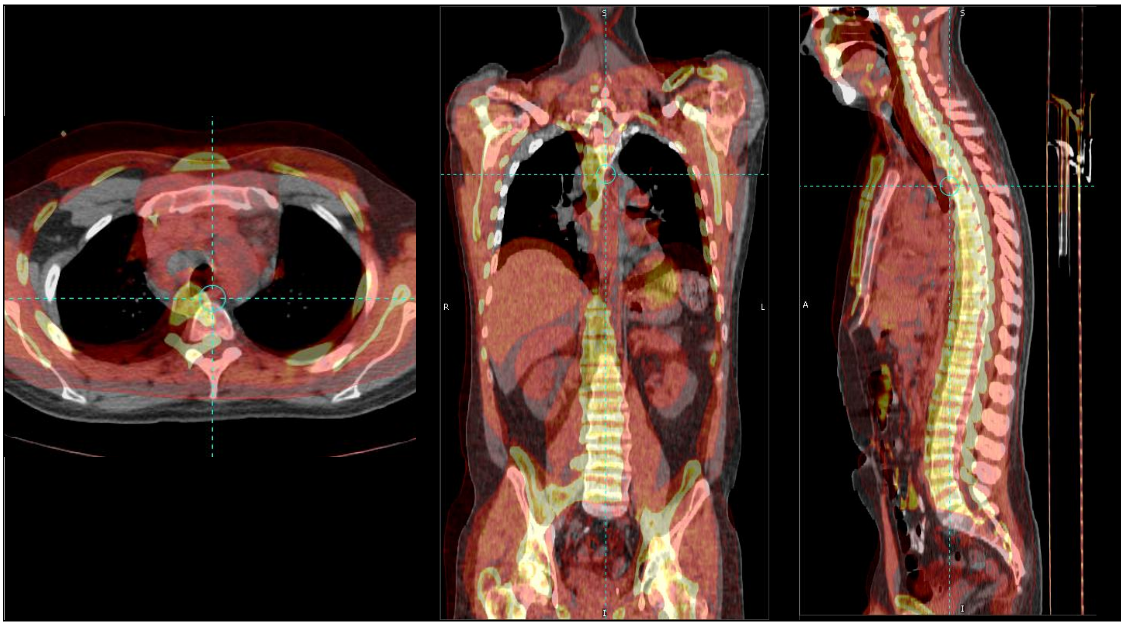

Figure 6-4: Graphical user interface of the visualisation tool within Mirada XD 3.4.

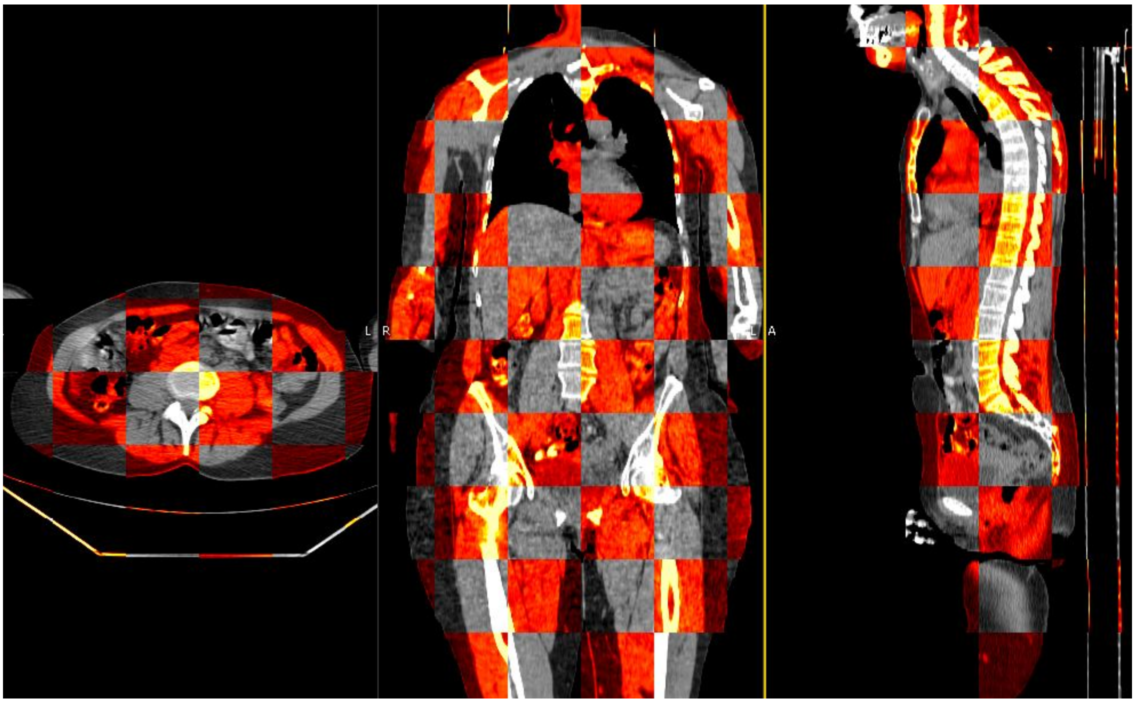

Figure 6-5: The same case shown in Figure 6-3 following automatic rigid registration.

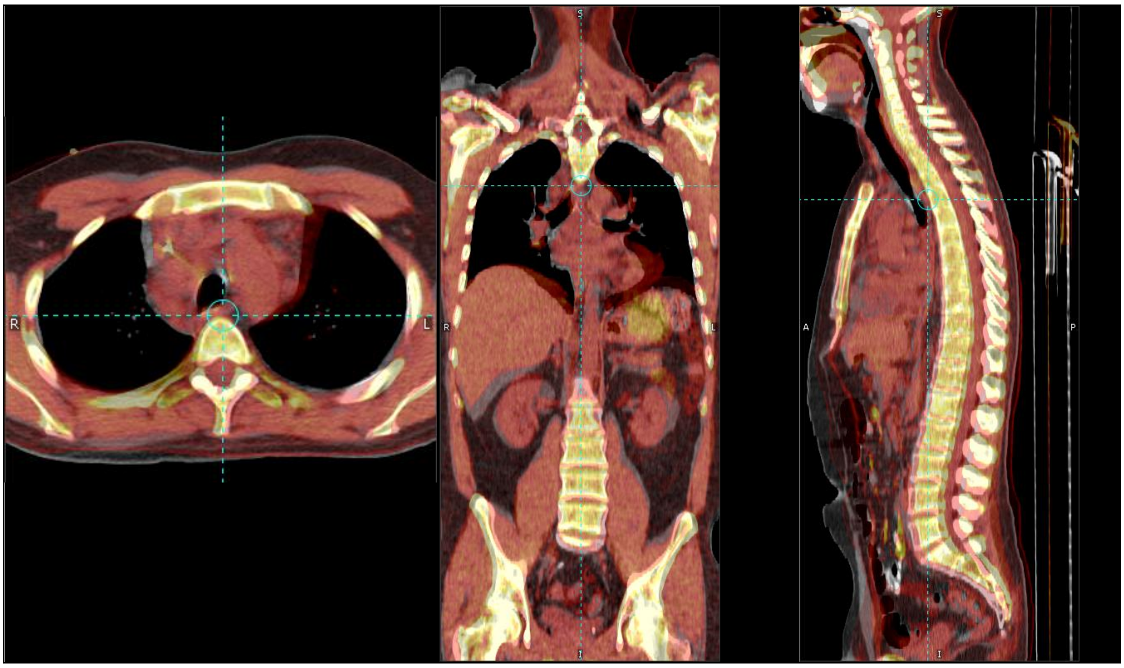

6.1.2.1 Image analysis

Masks were created from the ^{18}F-FDG BAT ROIs identified in Chapter 4 using ImageJ. Colocalisation analysis was performed upon these stacks of mask images using the ImageJ plugin JACoP (Just Another Colocalisation Plugin) 2.0 [218, 226] to determine whether individual ^{18}F-FDG BAT depots occurred in the same sites on serial scans, and specifically whether they occurred in the same areas as on the index PET/CT scan. JACoP is a compilation of general colocalisation tools, and works with 3D stacks. Manders' correlation coefficients were calculated to describe the fractional overlap of ^{18}F-FDG BAT on each subordinate scan with respect to the index scan (Figure 6-6). This produces 2 coefficients: 'M1' describes the proportion of ROIs from the index scan which overlap the subordinate scan, and 'M2' is the converse. Plundering set theory notation, 'M1' may be defined as 'index ∩ subordinate', and 'M2' as 'subordinate ∩ index.

Additionally, the number of ^{18}F-FDG BAT ROIs within each scan, and the proportion which colocalised were recorded.

Figure 6-6: Visual representation of colocalisation analysis on serial PET/CT scans.

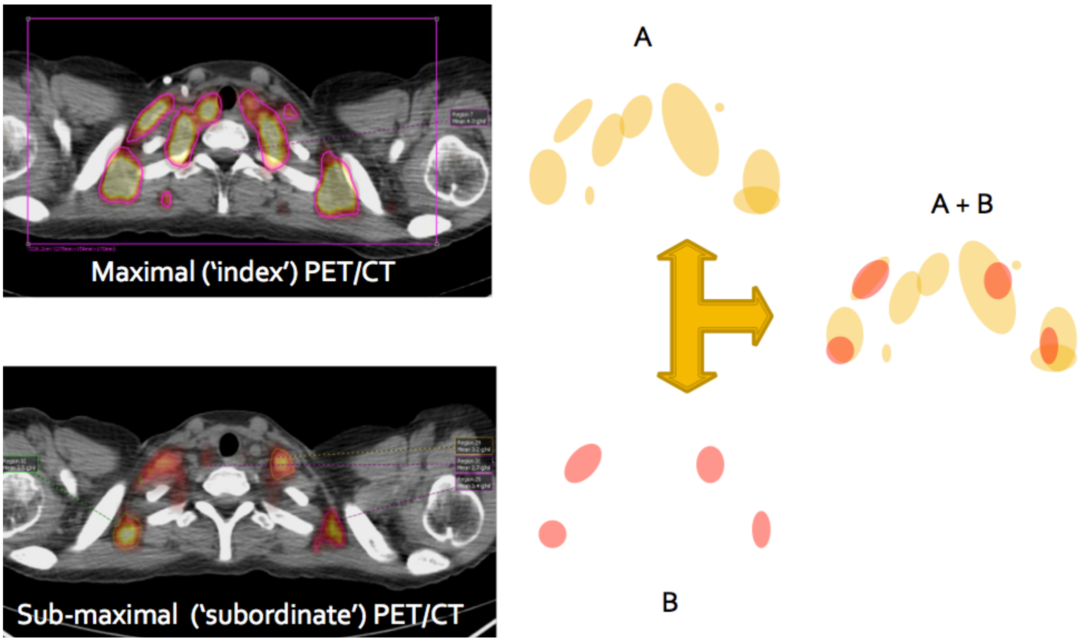

6.1.2.2 Statistical analysis

To determine whether the degree of colocalisation was greater than that expected by chance, the calculated colocalisation coefficients were compared with those derived from randomised images using the CDA (Confined Displacement Algorithm) plugin for ImageJ [222]. This implements a variation of the frame translation/image-shift method, but has the advantage of confining the randomisation to within a predefined envelope of potential interaction – in this case the body compartment, as we are only interested in colocalisation in parts of the body where BAT is likely to occur (Figure 6-7). The envelopes were constructed by automatic thresholding of CT images, to segment out background. Probability distribution curves were generated as a function of displacement, against which the baseline colocalisation coefficients were compared.

Figure 6-7: Production of an ‘envelope of interaction’ through segmentation of a CT image.

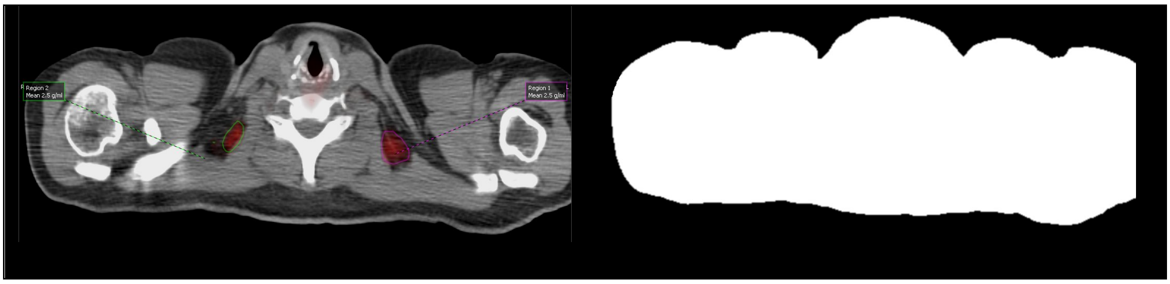

6.1.3 Results

6.1.3.1 Quantification of colocalised ^{18}F-FDG BAT ROIs

Figure 6-8 illustrates a typical colocalised image of the upper thorax for subject B, with the ^{18}F-FDG BAT ROIs from the index scan (red) and subordinate scans (green), and areas of colocalisation as yellow.

Figure 6-8: Axial PET/CT of the upper thorax showing colocalised ^{18}F-FDG BAT ROIs between index (yellow) and subordinate (green) scans.

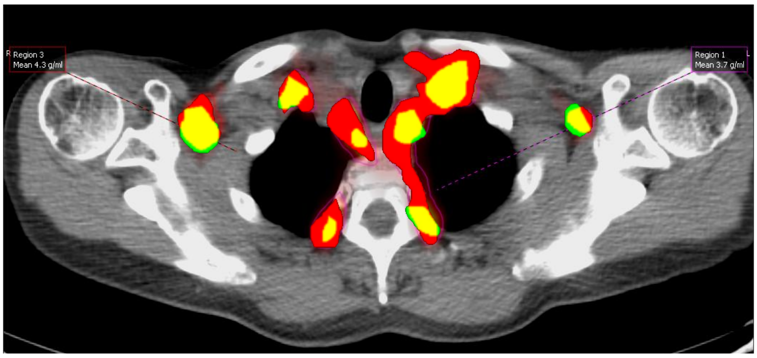

The number of ^{18}F-FDG BAT ROIs for each subject’s subordinate scans together with the number which colocalise with the index scans are presented in Figure 6-9. For each subject, the number of ROIs within each of their subordinate scans were compared with the index scan to determine which ROIs colocalised. The number of colocalised ROIs are shown as yellow; the ROIs on the subordinate scan which did not colocalise as green, and the index scan ROIs which did not colocalise as red. In most cases, the overwhelming majority of ROIs on subordinate scans colocalise with ROIs on the index scan. It is also noteworthy that those subjects with a high degree of ‘subordinate $\cap$

index' colocalisation, who had multiple subordinate scans (subjects B, F, I, J, M) tended to show a consistently high level of colocalisation across all their subordinate scans. This is exemplified by Figure 6-10, which shows slices through the supraclavicular fossa for two typical cases: subject I, a 22-year old female with Hodgkin's lymphoma with three scans performed 13 months apart; and subject J, a 17-year old female with Hodgkin's lymphoma with three positive scans over a five month period. This shows ^{18}F-FDG BAT uptake in the same area on 3 scans performed between February and July 2011. Both cases demonstrate ^{18}F-FDG BAT uptake within the subordinate scans occurs largely within the niduses of greatest radiotracer uptake on the index scan. Although larger ^{18}F-FDG BAT deposits tended to fragment into smaller niduses, we identified a strong correlation between the number of ^{18}F-FDG BAT ROIs and the total volume (r = 0.83; Figure 6-11) indicating that the number of objects is a good indicator of volume.

Figure 6-9: Stacked bar chart showing the proportion of colocalised ^{18}F-FDG BAT ROIs for each subordinate scan with respect to the index scan.

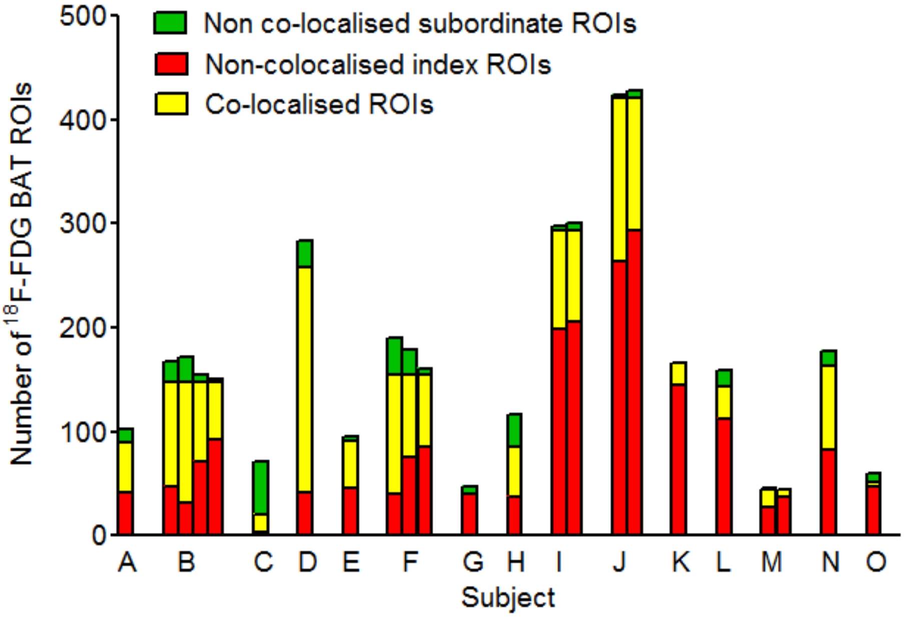

There was wide variation in the number of ROIs on subordinate scans between subjects ranging from 8 (subject G) to 242 (subject D), which had some bearing on the extent of colocalisation. Although there was only a weak correlation between the number of ROIs on the subordinate scan and the extent of ‘subordinate ∩ index’ colocalisation (*r* = 0.186; Figure 6-12), those with the lowest proportion of colocalised ROIs (subjects C, G, H and O) also had some of the lowest numbers of ^{18}F-FDG BAT ROIs on their subordinate scans (Figure 6-13).

Figure 6-10: Serial PET/CT scans showing colocalised ^{18}F-FDG BAT ROIs for 2 subjects (I & J).

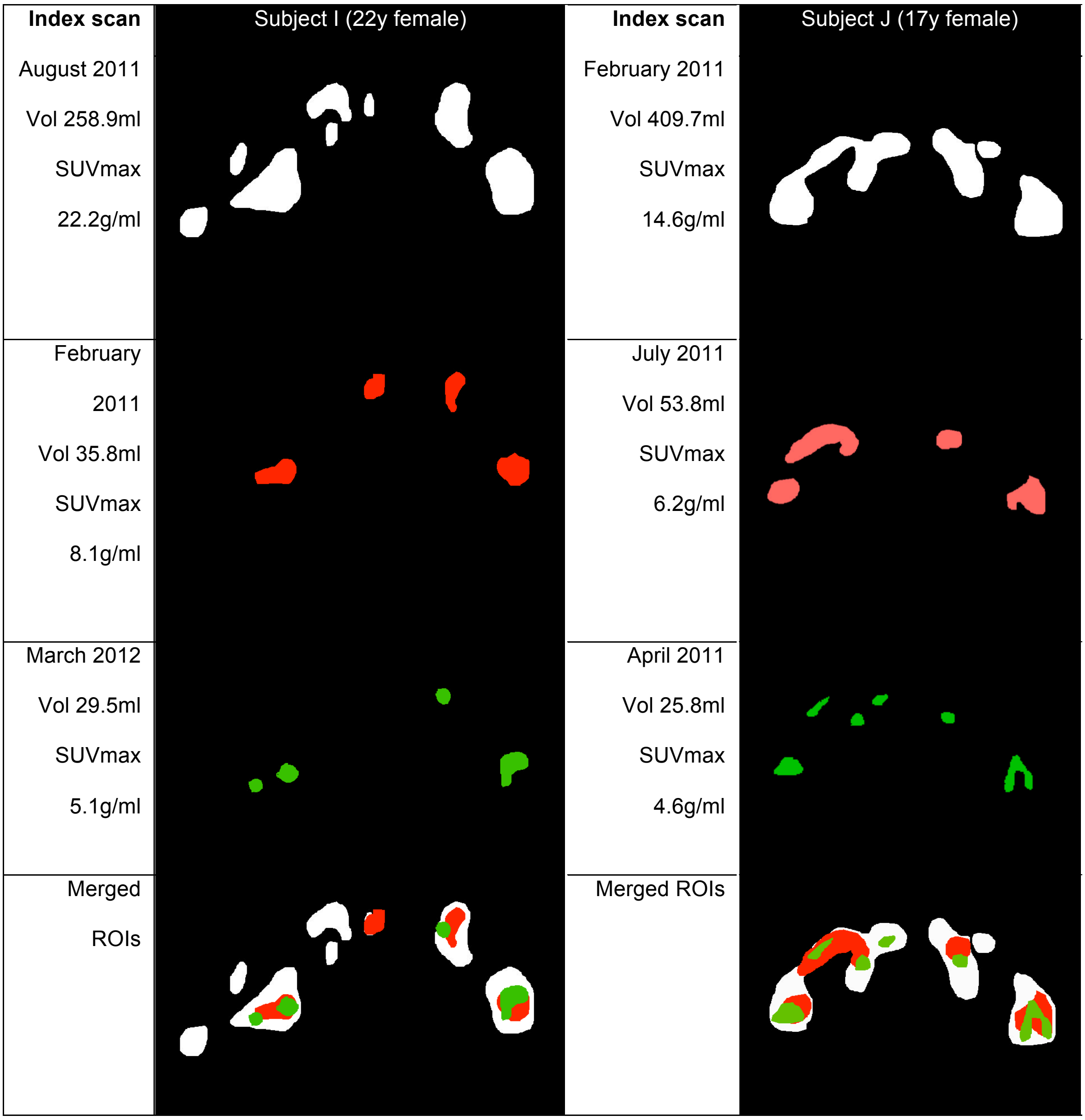

Figure 6-11: Scatterplot showing strong correlation between number of ^{18}F-FDG BAT ROIs and volume.

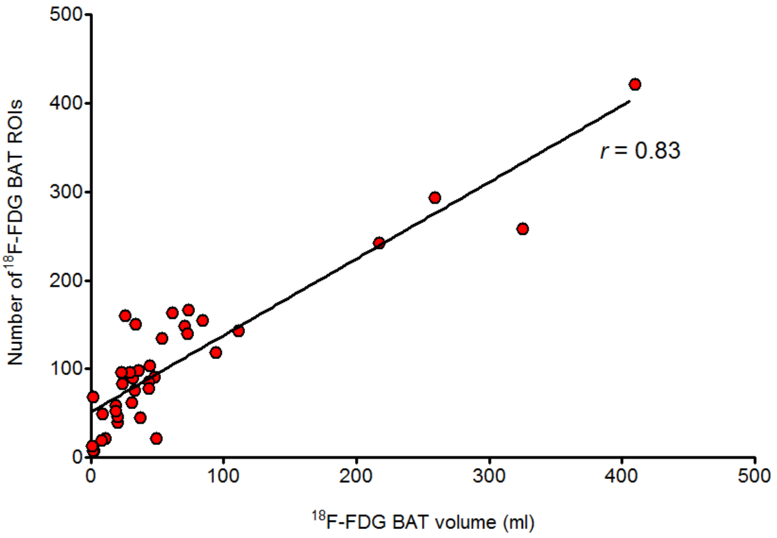

Figure 6-12: Correlation between number of ROIs on subordinate scan, and percentage colocalised ROIs.

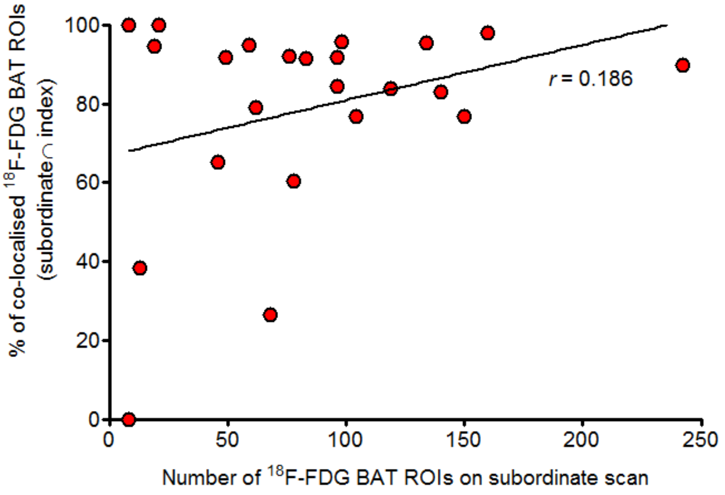

Figure 6-13: Proportion of ^{18}F-FDG BAT ROIs on subordinate scans colocalising with index scan (subordinate ∩ index).

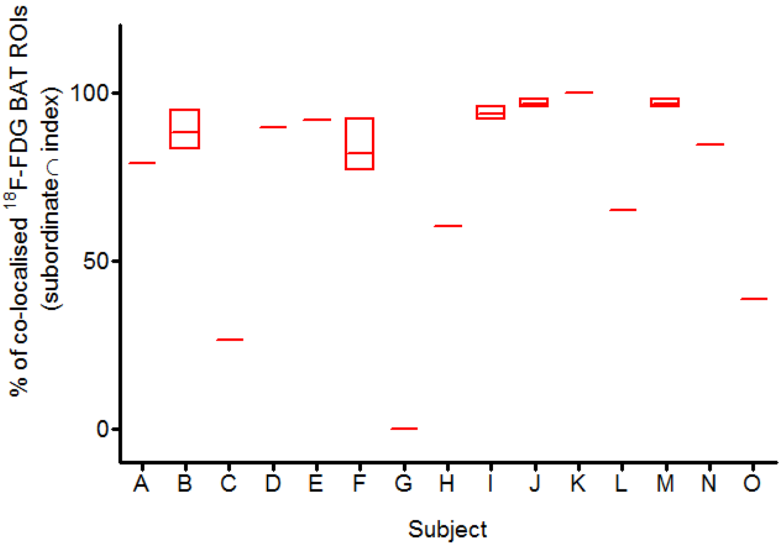

6.1.3.2 Manders' correlation and significance testing

Manders' overlap calculations with significance testing using the confined displacement algorithm produced the plots seen in Figure 6-14. The M1 coefficient (the proportion of ^{18}F-FDG BAT voxels on the index scan colocalising with the subordinate scan) is not pertinent to this study, as the index scans were selected on the basis of having the greatest volume of ^{18}F-FDG BAT. Figure 6-14 'A' shows the M2 correlations coefficients for the randomised images as a function of displacement. From this, a probability distribution curve is produced (Figure 6-14 'B') which allows comparison of the original M2 coefficient (pink line at 0.89), with the randomised values (mean 0.13, 95% confidence intervals of 0.02-0.41 denoted by black arrows).

Figure 6-14: Probability distribution curve of the randomised M2 coefficients.

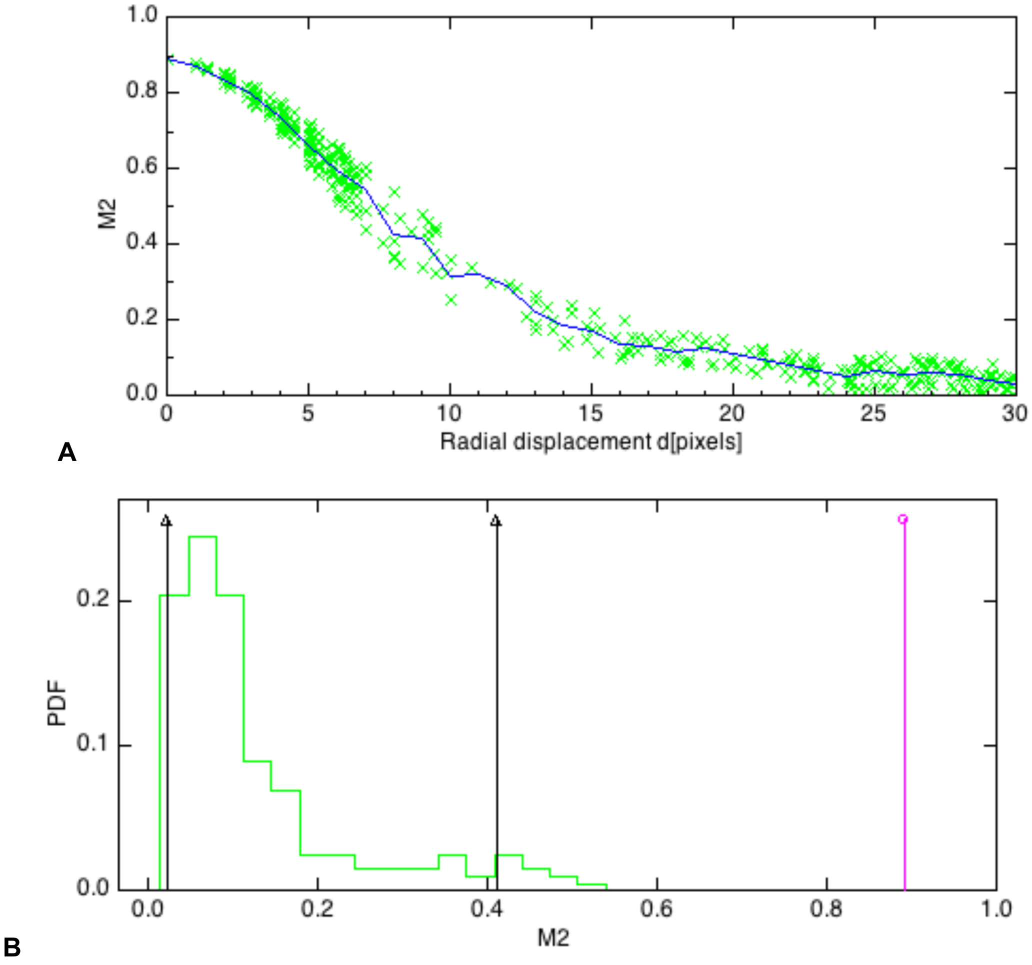

With one exception (subject G), in whom no colocalisation occurred, all scans yielded an M2 coefficient greater than that expected by chance (Figure 6-15).

Nineteen of the 23 subordinate scans (82.6%; belonging to subjects B to F, I to K, and M to O) yielded M2 coefficients greater than 0.7 (*i.e.* > 70% of the voxels within the ^{18}F-FDG BAT ROIs on the subordinate scan colocalised with those on the index scan). Two additional scans (subjects A and L) were just below this threshold (M2 coefficients of 0.69 and 0.67). Two scans (subjects G and H) yielded low M2 coefficients; subject H showed an M2 coefficient of 0.54. Subject G showed no colocalisation at all – this was an atypical case, as a section of paravertebral ^{18}F-FDG BAT uptake on the index PET/CT scan could not be distinguished from an area of metabolically active pleural disease and was therefore excluded.

Figure 6-15: Manders' M2 colocalisation coefficients for each subordinate scan (red), with randomised M2 coefficients (grey boxes denotes 95% CI).

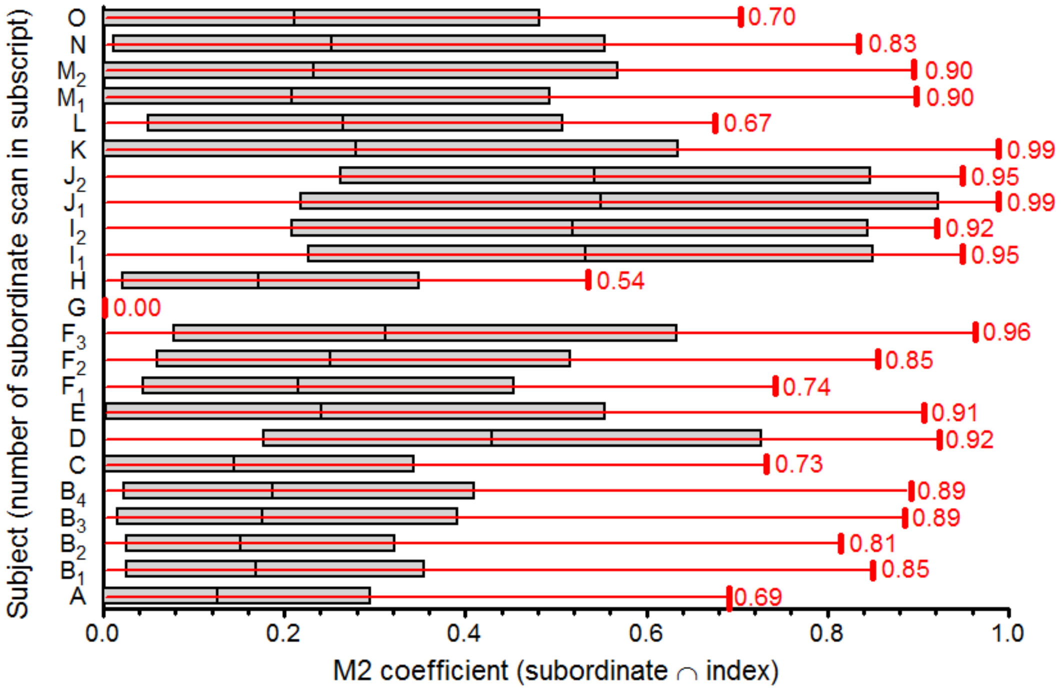

As with the colocalisation of ROIs, those subjects who achieved a high M2 coefficient on one subordinate scan, tended to score consistently highly on multiple subordinate scans.

If all voxels on the subordinate scans colocalised with the index scan, the M2 coefficient would be 1. Partial colocalisation (*i.e.* when ROIs partially intersect, but few voxels coincide) is a potential explanation, but the strong correlation between the proportion of colocalised ROIs (identified in Figure 6-9) and corresponding M2 coefficients ($r = 0.8821$, $p < 0.0001$; Figure 6-16) suggests that is not a major factor. If partial colocalisation were a major factor, a high number of colocalised ROIs would be accompanied by low M2 coefficient.

To explore this possibility further, a Bland-Altman plot (Figure 6-17) was produced to compare the proportion of colocalised ROIs and the proportion of colocalised voxels (*i.e.* Manders' coefficient). In all but two cases, there was no consistent bias, and that there was no consistent difference between the degree of colocalisation identified by the two techniques. The two outliers are subjects C and O, both of whom demonstrated colocalisation in a small proportion of ROIs on the subordinate scan (26.5% and 38.5% respectively), but a greater proportion of colocalised voxels (M2 coefficients 0.73 and 0.70 respectively).

Figure 6-16: Scatterplot showing a strong correlation between the proportion of colocalised ^{18}F-FDG BAT ROIs and M2 colocalisation coefficient.

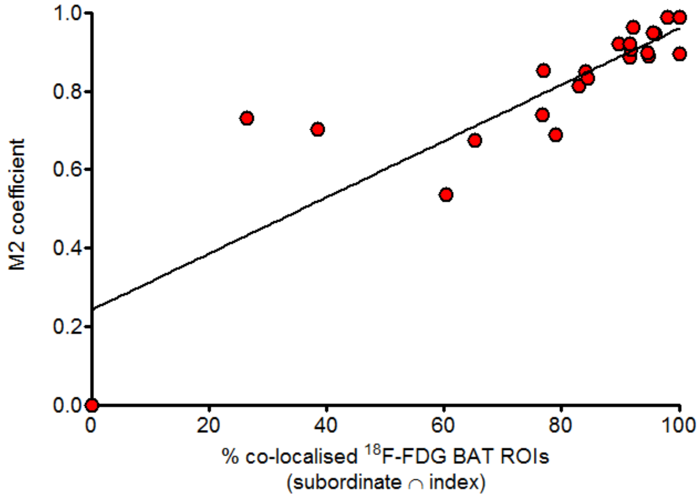

Figure 6-17: Bland-Altman plot comparing proportions of colocalised ^{18}F-FDG BAT ROIs and M2 coefficients.

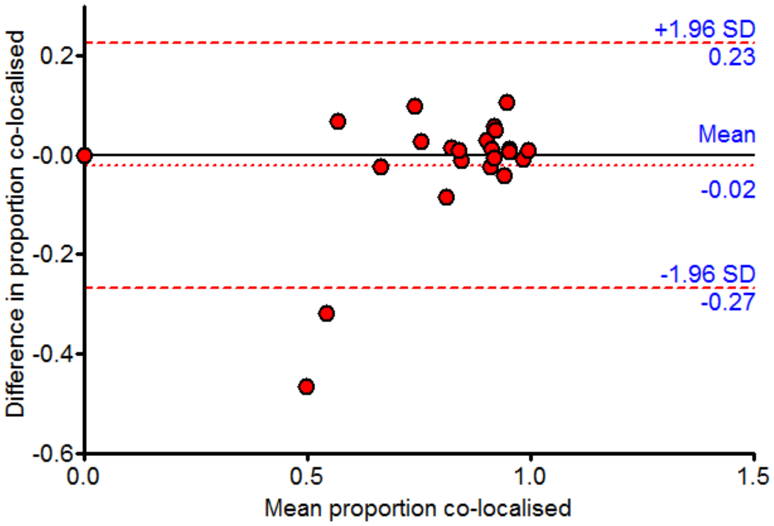

6.1.4 Summary

In this study we used a modified method of colocalisation analysis to quantify the degree to which individual ^{18}F-FDG BAT depots colocalise across serial PET/CT scans. We identified that the degree of colocalisation was dependent on the number of BAT deposits (*i.e.* the more deposits, the greater the degree of colocalisation). Nonetheless in 14/15 cases the degree of ^{18}F-FDG BAT colocalisation between serial PET/CT scans was high, and significantly higher than would be expected by chance.

Chapter 7: Identification and quantification of BAT on magnetic resonance imaging

7.1 Basic principles of MR imaging

7.1.1 MR physics

MR imaging is made possible by the fact that some subatomic particles have magnetic polarity. Only nuclei with an odd number of nucleons (protons or neutrons) demonstrate this property (*e.g.* ^{1}H, ^{11}Na, ^{13}C and ^{15}P), and MR imaging primarily relies on ^{1}H nuclei (single protons) due to their relative abundance (10^{9} ^{1}H nuclei per 1 mm^{3} of tissue) compared with other nuclei (*e.g.* 88 M for ^{1}H, 16 mM for ^{17}O).

Apart from spin, protons possess mass and charge, which generates magnetic properties similar to tiny dipole magnets. In nature they are randomly orientated due to the Earth's magnetic field being extremely weak (approximately 5 x 10^{-5} Tesla, abbreviated to 'T'). When subjected to a strong uniform static external magnetic field ('B_0'), such as that produced by the solenoid of an MR scanner, the protons align along ('parallel', a low energy state of approximately 0.2 μeV at 1 T) or against ('anti-parallel', a high energy state of approximately 0.4 μeV at 1 T) the magnetic field. If the number of parallel and anti-parallel protons were equal their magnetisations would cancel out resulting in no net magnetisation. In fact slightly more protons align parallel than anti-parallel; in the case of a 1 T magnetic field, approximately seven per million additional dipoles are parallel than anti-parallel, resulting in a tiny net magnetisation in the parallel direction (*i.e.* approximately 7 x 10^{19} protons per mm^{3} of water [227]). It is these 'excess' protons and the resulting net magnetisation that are detectable by MR imaging. The smaller the field, the smaller this difference, and the poorer the resulting signal, hence the rationale for high magnetic field strengths.

By convention, the net magnetisation may be resolved into two vectors: longitudinal m_z (*i.e.* along the B_0 or z axis) and transverse m_{xy}, which combine to produce a net sum vector m (Figure 7-1). In a static magnetic field $m_{xy} = 0$ as all the dipoles cancel each other out in the transverse direction. When the spin is perturbed by an external magnetic field, the protons precess around the direction of the magnetic field resulting in a magnetic moment (Figure 7-1) – akin to a spinning top.

Figure 7-1: The magnetic vectors associated with a precessing proton (a) resolved into transverse (m_{xy}) and longitudinal (m_z) components (b) (adapted from Pooley *et al.* [228]).

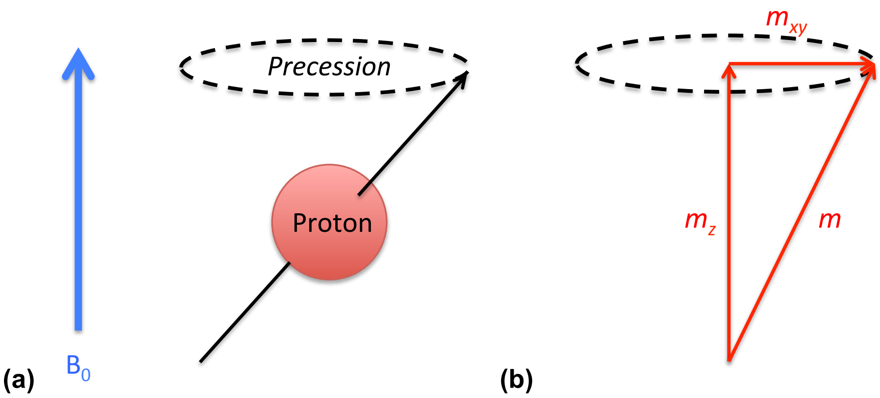

The speed at which nuclei precess or 'Larmor frequency' (ω_0) is a product of the magnetic field strength (B_0) and a constant (Equation 7-1). This constant is the 'gyromagnetic ratio' (γ) and is constant for particular nuclei *e.g.* H^1 = 42.6 MHz/T, ^{13}C = 10.7 MHz/T [229]

Equation 7-1: The Larmor equation.

$$\omega_0 = B_0 \times \gamma$$

Consequently at a field strength of 1.5 T, the Larmor frequencies for ^1H and ^{13}C nuclei are 63.9 MHz and 16.1 MHz respectively. The high gyromagnetic ratio of ^1H produces a stronger signal than other nuclei, which makes it an attractive target for MR imaging.

7.1.2 Generating an MR signal

This phenomenon is exploited in MR imaging. If the ^{1}H nuclei are stimulated with a short radiofrequency (RF) pulse perpendicular to B_0 at the appropriate Larmor frequency, protons precess together at the Larmor frequency (phase coherence), resulting in tipping of the net magnetisation vector away from M_z to M_{xy} (Figure 7-2). The duration and amplitude of the applied RF pulse determines the extent to which the net magnetisation is deflected away from B_0. When the transverse RF pulse is switched off the protons precess in the transverse plane for a short time, inducing an alternating current in RF receiver coils within the MR machine via Faraday induction, which are then amplified.

Figure 7-2: An RF pulse at the correct Larmor frequency displaces net magnetisation from being in a net longitudinal (z) direction (a) into the transverse (xy) plane (b) (adapted from Pooley *et al.* [228].)

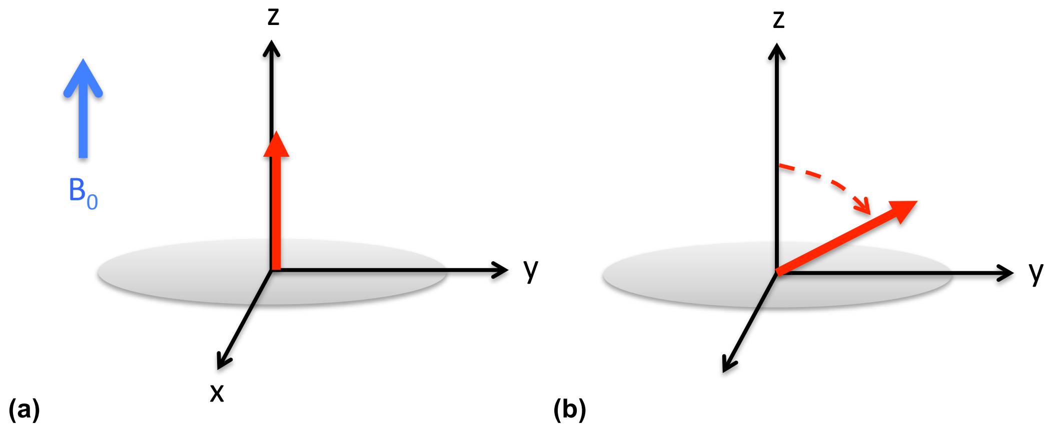

7.1.3 Free induction decay

Once the deflecting RF pulse is switched off, the dipoles rapidly return to their original state. This manifests on the vector diagram as M_z increasing as longitudinal magnetisation recovers, and M_{xy} decreasing as transverse magnetisation dissipates. The speed at which this occurs varies between different tissue types.

There are two mechanisms by which the net magnetisation decays which form the basis for MR imaging sequences: ‘spin-lattice’ and ‘spin-spin’ relaxation.

7.1.4 Spin-lattice relaxation (T_1 recovery)

The energised dipoles dissipate energy into the surrounding molecular lattice, resulting in them gradually realigning longitudinally parallel or anti-parallel to the B_0 axis, with a corresponding increase in net M_z magnetisation. This occurs in an exponential manner (Figure 7-3) expressed algebraically in Equation 7-2 (where t = time, $T1$ = T1 recovery time in ms).

The rate at which longitudinally recovery occurs is defined by the time constant T_1 which is the time it takes for M_z to recover to approximately 63% of its maximum value. T_1 varies with magnetic field strength, and between tissues types. Large slow-moving molecules (*e.g.* fat) absorb energy resulting in a short T_1 time. Small molecules (*e.g.* free water) are less effective at absorbing energy, resulting in a comparatively long T_1 time, and by extension the greater the proportion of free water within tissue, the longer its T_1.

Figure 7-3: T_1 recovery curve of longitudinal magnetisation M_z (adapted from Pooley *et al.* [228]).

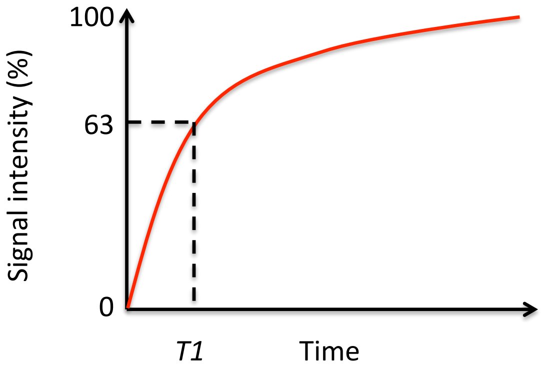

Equation 7-2: T1 longitudinal recovery curve equation.

$$M_z(t) = M_0\left(1 - exp\left(\frac{-t}{T1}\right)\right)$$

The difference in T1 recovery time between tissues is the source of contrast in T1-weighted images. In Figure 7-4 the T1 recovery curves of two tissues are schematically represented; tissue 1 with a short T1 recovery time, and tissue 2 with a longer T1 time. If images were acquired immediately after the deflecting RF pulse was switched off, there would be negligible signal. Conversely if images were acquired when all net M_z magnetisation had fully recovered (time point B on Figure 7-4) image contrast would be poor. Tissue contrast is greatest when the T1 curves are maximally separated (time point A on Figure 7-4) and are termed 'T1-weighted' images. These show tissues with long T1 times, which recover their longitudinal magnetisation slowly (*e.g.* water, cerebrospinal fluid, dental enamel and cortical bone) as dark, and tissue with short T1 times (fat and soft tissue) as bright.

Figure 7-4: T1 recovery curves for two tissues demonstrating maximum tissue contrast at time point A (adapted from Pooley *et al.* [228]).

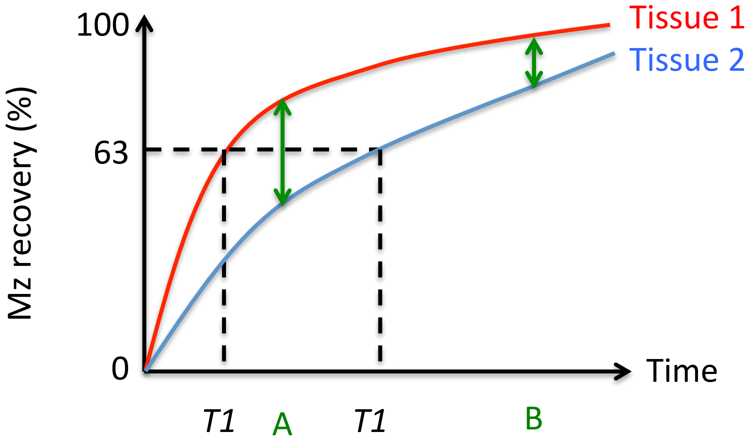

7.1.5 Spin-spin relaxation (T_2 decay)

Energy is also transferred between adjacent protons, causing some to precess at slightly different speeds, resulting in a loss of phase coherence (de-phasing), and a consequent reduction in net transverse M_{xy} magnetisation (Figure 7-5). De-phasing is largely due to inhomogeneities within the magnetic field, but also varies between tissue types. The rate at protons de-phase and net transverse magnetisation decays is defined by the time constant T_2, which is the time it takes for M_{xy} to decay to approximately 37% of its original value (Figure 7-5(b) and Equation 7-3).

Figure 7-5: De-phasing of net M_{xy} magnetisation (a) results in a loss of net transverse magnetisation as shown on the T2 decay curve (b) (adapted from Pooley *et al.* [228]).

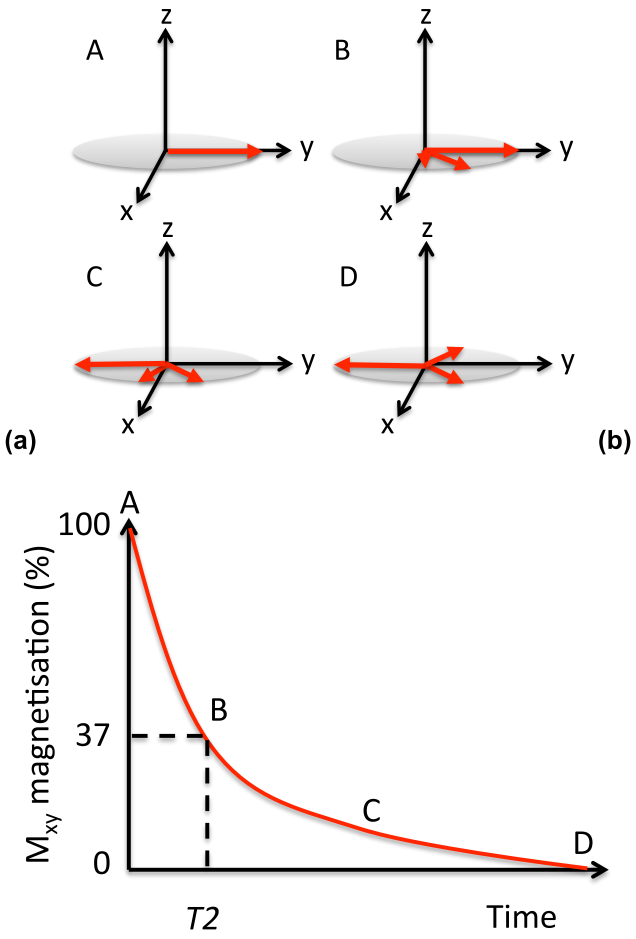

Equation 7-3: T2 transverse magnetisation decay curve equation.

$$M_{XY}(t) = M_{xy}(\mathbf{0}) \times exp\left(\frac{-t}{T2}\right)$$

Local magnetic field variation is greatest in large molecules in which atoms are fixed. This results in low T_2 times - indeed the T_2 time in dental enamel, cortical bone and metal is so short, that it can only be imaged using specialised ultra short echo sequences. Field variation is least in freely moving molecules including water, which average out local magnetic field variations resulting in a high T_2 time. Consequently the greater the water content within a tissue, the longer its T_2 time.

The difference in T2 between tissues is the source of contrast in T2-weighted images (Figure 7-6). If images were acquired immediately after the deflecting RF pulse was switched off, there would be poor contrast between tissues (time point A on Figure 7-6), conversely if images were acquired when all net M_{xy} magnetisation had fully decayed, signal intensity would be low (time point B). Therefore 'T2-weighted' images are acquired at a time point when the T2 decay curves are maximally separated and the tissue contrast is greatest. T2-weighted images show tissues with short T2 times which de-phase rapidly (*e.g.* fat and soft tissues) as relatively dark, while water and cerebrospinal fluid have very long T2 times and appear bright.

Figure 7-6: T2 decay curves for two tissues showing effects of tissue contrast (adapted from Pooley *et al.* [228]).

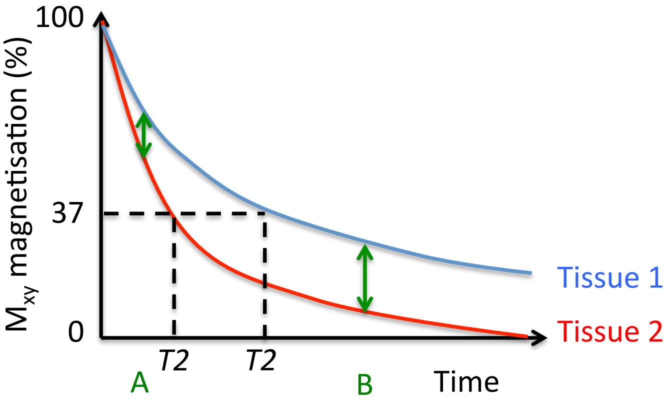

In reality, due to a combination of engineering imperfections in magnets and magnetic field distortion caused by the patient themselves, the spin-spin interactions are amplified, and free-induction T_2 decay occurs much quicker than would be expected. Instead, free induction decay of T_2 is called T_2*, and is in the order of a few milliseconds.

7.1.6 MR sequences

As discussed above, scans may be weighted to demonstrate the T1 or T2 characteristics of tissues. Weighting is determined by the adjusting the timing parameters TE and TR. TE (echo time) is the delay between the deflecting transverse RF pulse, and the point at which the resulting echo is measured. TR (repetition time) is the delay between respective transverse magnetisation pulses.

T1-weighted images require a short TE (approximately 20ms to minimise effects of T2 decay) and a relatively short TR (approximately 500 ms, to maximise T1 weighting). Conversely, T2-weighted images require a long T2 time (approximately 80 ms, to maximise T2 contrast), and a long TR (approximately 2,000 ms to minimise T1 effects). There are two main types of MR pulse sequences in clinical practice: spin-echo and gradient-echo sequences [230].

7.1.6.1 Spin-echo sequence

As T2* decay occurs so much more rapidly that T2, the spin-echo pulse sequence was developed to counter the unwanted T2* effects whilst preserving the T2 effects of tissues. This technique re-phases the protons by applying a 180° RF pulse to the de-phasing protons. This pulse has the effect of inverting the net magnetisation over to the opposite axis, such that more slowly precessing protons are ‘ahead’ and the faster precessing protons are ‘behind’. The protons re-phase when the faster precessing protons ‘catch up’ which induces a signal within the RF receiver coil.

A faster variant of this if the turbo spin-echo (or fast spin echo) pulse sequence, which applies multiple 180° refocusing pulses in rapid succession within each TR interval. By collecting a number of echoes in each TR interval, scanning time can be reduced.

7.1.6.2 Gradient recalled echo (GRE)

Scan time may also be reduced by reducing the tip angle. Thus far, we have described the transverse RF pulse as tipping the net magnetization at 90° to the B_0 axis. An RF pulse of shorter duration would tip fewer protons transversely, resulting in a smaller ‘tip angle’ (*e.g.* 20° or 30°) and a correspondingly smaller transverse magnetisation. Unlike spin-echo sequences, GRE sequences do not employ a 180° refocusing pulse which allows for shorter TE times. As a result image acquisition is much faster, but is susceptible to magnetic field inhomogeneities. Consequently GRE images tend to be T2* weighted [230].

7.1.6.3 Fat-water separation techniques

The fact that spin-spin relaxation differs between tissue types may be exploited to differentiate between them.

The hydroxyl bonds in water exert a smaller magnetic field upon the proton than the carbon-hydrogen bond in lipid molecules. As a result protons in lipids precess at a different speed than in water [227]. Dixon is credited with using this ‘chemical shift’ to differentiate between fat and water [231]. By selecting a TE when the lipid and water protons are in-phase (TE = 4.2 msec at 1.5 T), their signal will be summated to produce a water plus fat image [230]. Imaging at a TE when the water and lipid protons are exactly out-of-phase (TE = 2.1 msec at 1.5 T) will result in a cancelling out of signal to produce a water minus fat image.

Adding the in- and out-of-phase images produces a water-only image, and subtracting them produces a fat-only image (Figure 7-7). From these images the fat fraction may be calculated using Equation 7-4, (where F = fat-only, W = water-only) and a fat fraction image generated.

Figure 7-7: Dixon imaging with derived fat fraction image of a pork chop[a].

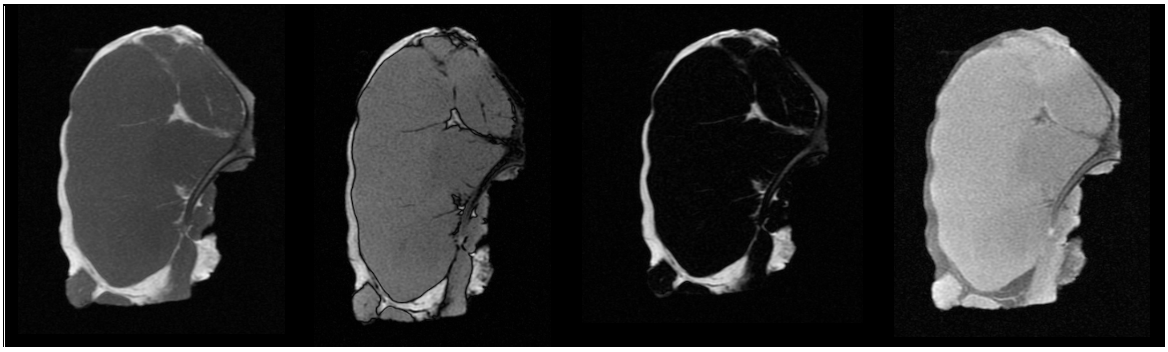
In-phase (IP) Out-of-phase (OP) Fat-only (F) Water-only (W)

Equation 7-4: Calculation of fat fraction from Dixon images.

$$Fat\ fraction = \frac{F}{F + W}$$

Figure 7-8: Fat fraction image derived from Dixon images.

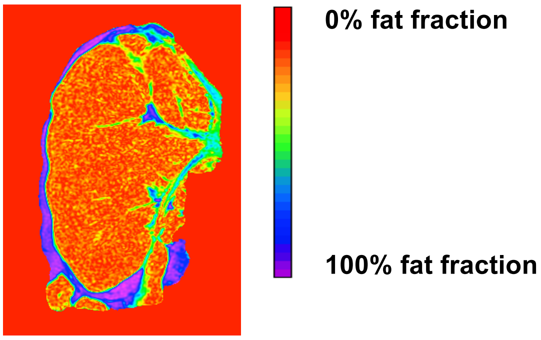

The classical two-point Dixon method identifies a single peak fat peak based on the CH_2 group and may not identify other species of fat *e.g.* $-CH_2-$, $-HC{=}CH-$ and $–CH_3$ [232]. Newer multi-peak techniques have been developed to address this including IDEAL-Quant and IDEAL-IQ (General Electric Medical Systems, Milwaukee, USA).

---

[a] Acquired by the author using a 3-point IDEAL FSE pulse sequence with the following parameters: TR/TE = 133, 11.5, flip angle 90°, number of signal average 6, field of view = 200 x 200 mm, voxel size = 0.39 x 0.39 mm, slice thickness/spacing (mm) = 5/6

The IDEAL ‘iterative decomposition of water and fat with echo asymmetry and least-squares estimation’ technique was developed by Reeder *et al.* [233] to address problems with artefacts with previous techniques, as well as in response to the introduction of modern multichannel RF receiver coils. The IDEAL technique produces uniform fat suppression and reduces artifacts from magnetic field inhomogeneities and chemical shift between fat and water. In addition IDEAL is approximately 30% faster than common Dixon methods, and produces a higher signal-to-noise ratio [234], and is therefore more accurate in fat quantification. In addition the IDEAL sequence automatically generates the four images shown in Figure 7-7.

Adipose tissue comprises multiple different fat molecules, each with different chemical spectra [235]. Consequently the chemical spectrum of adipose tissue is complex and difficult to model [236]. Rapid T2* relaxation caused by iron overload in the liver has been shown to influence fat fraction estimation using Dixon methods [237].

7.2 BAT identification on MR

Prior to the advent of PET, the only means of detecting BAT were *post mortem*, biopsy, or indirectly by measuring energy expenditure in response to BAT stimulation [2].

PET allows detection of BAT *in vivo*, but is hampered by various factors including the opportunistic nature of BAT detection, the requirement that the BAT be metabolically active in order that the ^{18}F-FDG radiotracer is taken up, and its susceptibility to external factors - most notably temperature.

Although some small prospective studies have subjected healthy volunteers to PET/CT for the purposes of BAT identification [43, 238, 239], the high ionising radiation burden [240] and the costly radiotracer limit the role of PET/CT role in BAT identification in larger populations [241]. The Ionising Radiation (Medical Exposure) Regulations 2000 [242] require all medical ionising radiation exposures be justified, and it would be difficult to justify the widespread use of PET solely for the purposes of BAT identification. Therefore there is a need for a reliable, non-invasive and safe method for BAT detection *in vivo*. Such a method would be a necessary prerequisite before the efficacy of novel pharmacological therapies which modulate weight through the manipulation of BAT could be tested. Unlike PET, MR does not require the administration of radioactive isotopes and also boasts superior spatial resolution, potentially allowing small BAT depots to be identified. Unlike PET, MR also has the potential to demonstrate BAT regardless of its level of metabolic activity [243].

7.2.1.1 Murine studies

Increasingly efforts to identify BAT using MR have capitalised on the biochemical and morphological differences between BAT and WAT. MR spectroscopic studies have shown that both BAT and WAT exhibit a strong spectral peak corresponding to lipid (specifically fat containing the methylene group), but BAT also showed a prominent water peak, indicating high water content [241, 244, 245] of approximately 48.5%, compared with 7.1% in WAT [244]. MR spectroscopy has also revealed differences between the fat spectra of BAT and WAT, implying slightly different lipid profiles including lower levels of unsaturated triglycerides in BAT [244]. MR spectroscopy is able to separate lipid peaks and water with comparable sensitivity to tissue biopsy. A drawback of *in vivo* spectroscopy is the limited spatial resolution, therefore MR imaging-based methods should provide superior resolution. T1-weighted MR is able to separate fat and water *in* vivo, due to fat having a short T1 relaxation time (300 ms) compared with approximately 1,000 ms for water-containing tissues [246].

Further work has been directed into BAT identification on the basis of morphological differences between BAT and WAT, specifically that brown adipocytes contain numerous small intracellular lipid vacuoles, whereas WAT typically contain a large unilocular lipid droplet and limited cytoplasm [36, 67, 247]. Consequently BAT has a higher water content than WAT [246]. Although size differences of adipocytes are below the typical spatial resolution of MR there is a positive correlation between adipocyte size and fat fraction [248]. Fat quantification techniques exploiting fat-water separation using methods based on the Dixon chemical-shift technique, and the time-dependent phase difference between fat and water, have been shown to produce precise quantification of fat-fraction [249], with comparable accuracy to MR spectroscopy [250]. Consequently Dixon-based techniques have been used with some success in the quantification of body fat content [251], hepatic steatosis [249, 252] and fat content within muscle [232, 250]. The multi-peak spectral model used by IDEAL is undoubtedly more accurate than the single-peak model used in traditional Dixon imaging [253], and although the lipid profile of BAT and WAT differ subtly on MR spectroscopy, this does not impact significantly upon the overall fat fraction [254].

MR chemical-shift based water-fat separation techniques have successfully exploited differences in the fat and water fraction between BAT and WAT to identify *in vivo* BAT within rodents [245, 255, 256]. IDEAL was first used to characterise BAT was in 2010 [241] on excised tissue samples and *post mortem* carcasses. This confirmed that BAT has a significantly lower fat fraction (58% ± 8%) than WAT (92% ± 2%). That BAT has a broader and lower fat fraction range (37-70%) than WAT (90-93%) has been confirmed on subsequent studies [241, 253, 257, 258].

A single study comparing *in vivo* MR and ^{18}F-FDG PET against histological evaluation in rats [243], found that BAT volumes obtained from in- and out-of-phase MR (if preceded by a spectral presaturation inversion recovery – SPIR pulse) showed a significantly stronger correlation with histological findings (r = 0.89 p = 0.017) than PET/CT (r = 0.15 p = 0.78). ^{18}F-FDG PET/CT consistently underestimated the true volume of BAT, while conventional in- and out-of-phase imaging tended to overestimate BAT volume [243].

BAT also demonstrates greater vascularity and sympathetic innervation than WAT [67]. Dense vascularity and the abundance of iron-laden mitochondria gives BAT its distinctive reddish-brown colour [73]. Rich vascularity and the presence of iron is known to shorten T2* relaxation time [259, 260], In addition, as perfusion and oxygen consumption increase within metabolically active BAT, accumulation of deoxyhaemoglobin can also shorten T2* – indeed this is the basis for functional imaging. Consequently studies have sought to exploit the differences in iron content and blood flow between BAT and WAT, and its effect on T2 and T2* time. Significantly lower T2* values have been demonstrated in BAT than WAT [241, 253]. There is less consensus regarding whether T2 values differ between BAT and WAT [244, 261], although significant differences have only be described at high magnetic field strengths [261].

Variation in T2* values between studies (Table 7-1) have been attributed to differences in blood composition between live and dead animals [241]. The reciprocals of T2 and $T2^*$, known as R2 and $R2^*$, are directly proportional to iron concentration and have been validated in studies of hepatic and cardiac iron overload [262].

Table 7-1: Fat fraction and T2* differences between BAT and WAT.

Study	BAT fat fraction (%)	WAT fat fraction (%)	BAT T2* (ms)	WAT T2* (ms)	Comments
Rodents					
Hu *et al.*, 2010 **[241]**	51 ± 8	92 ± 2	9 - 20	11 - 50	Juvenile
	62 ± 7	93 ± 2			Adults
	39-42%				*In vivo* juvenile
	52-64%				*In vivo* adult
Hamilton *et al.*, 2011 **[244]**	51.5%[a]	92.9%[a]	-	-	MR spectroscopy of mice (n=7)
Chen *et al.*, 2012 **[261]**	-	-	57.8 ± 3.9 [b]	83.1 ± 2.2 [b]	*In vivo* rat study (n=9)
Hu *et al.*, 2012 **[253]**	61.8 ± 5.5	95.2 ± 0.9	13.3 ± 5.5	22.3 ± 2.6	Lean
	90.2 ± 1.2	98.8 ± 0.8	18.0 ± 0.7	23.7 ± 1.7	Obese
Rasmussen *et al.*, 2013 **[258]**	43.7 ± 7.8	73.3 ± 10.4			*Ex vivo*
	43.0 ± 14.1%	67.9 ± 15.6%			*In situ*
Smith *et al.*, 2013 **[256]**	30-90%	>90%	-	-	Mice (n=8)
Humans					
Rasmussen, *et al.* **[258]**	c.30%	67.7 ± 4.6%	-	-	Neonates (n=22)
Hu *et al.*, 2012 **[263]**	41.9 ± 6.3%	>90%	-	-	Single post mortem case report
Hu *et al.*, 2013 **[264]**	29.7	89.8	14.7	21.6	Post mortem infant Infants (n=3) adolescents
	39.2-72.5	92.5-96.0	18.4-20.6	43.9-44.7	
	52.0-80.6	87.4-91.3	12.5-19.4	28.8-35.0	
	86.9-93.9	82.8-95.4	19.4-33.4	33.1-40.1	

---

[a] Hamilton reports the water fraction in BAT at 48.5%, and within WAT as 7.1%, from which the fat fractions are calculated

[b] T2 time rather than T2*

					(n=3) Adults (n=2)
Hu *et al.,* 2013 **[265]**	36.0 ± 8.2 68.7 ± 12.1		18.7 ±2.6 17.2 ± 3.8		Infants (n=9) Teenagers (n-18)
Hu *et al.,* 2013 **[266]**	38.2 ± 11.5 72.5 ± 12.1	77.9 ± 9.1 86.2 ± 6.5	18.8 ± 4.8 18.0± 3.6	21.0 ± 5.9 27.2 ± 6.8	Infants (n=12) Children (n=39)
Van Rooijen *et al.*, 2013 **[267]**	65.2 ± 7.0	81.5 ± 5.4	-	-	Adults (n=11)
Lundstrom *et al.*, 2014 **[268]**	82.8 ± 5.0	86.2 ± 4.6	-	-	Adults (n=9)
Hu *et al.*, 2014 **[269]**	29.8 ± 8.0		-	-	Neonates (controls, n=5)

Collectively, these studies have shown that murine BAT has different MR characteristics than WAT. Murine studies have tended to involve *ex vivo* scanning of excised tissue, post mortem scanning of rat carcasses or *in vivo* scanning of anaesthetised rodents. *In vivo* BAT imaging in rodents has also focussed on the interscapular fat pad as it is the largest and most easily identifiable BAT depot, and is classically a triangular or trapezoidal-shaped bi-lobed structure between the scapulae [245]. Knowledge of the distribution of BAT in adult humans is less predictable [244], and unlike rodents, adult humans do not possess a discrete BAT organ along the lines of the interscapular fat pad.

7.2.1.2 Human studies

There are comparatively few quantitative studies evaluating MR appearances of BAT in humans, and these have tended to focus on infants in whom BAT is more prevalent and extensive. Non-shivering thermogenesis has been studied in infants using thermography

[270], which although providing information on BAT activity, does not provide quantitative information on BAT volume [258].

MR appearances of BAT have been described in the context of disease, specifically hibernomas and phaeochromocytomas. BAT associated with phaeochromocytoma has been described as being of slightly higher signal intensity than muscle on T1-weighted imaging, and heterogeneously hyperintense with respect to muscle on T2-weighted imaging. High signal is maintained on chemical fat-suppressed T2-weighted imaging, with some loss of signal on fat-suppressed T1-weighted imaging [271]. The earliest non-oncological descriptions of BAT in infants on MR were case reports. Large BAT deposits were identified in a pre-term neonate using MR (and subsequently confirmed following biopsy), in whom it was described as a confluent soft tissue mass extending from the neck to the chest of intermediate signal intensity, homogenously iso-intense to muscle on T1-weighted imaging, and homogeneously hyperintense to fat on T2-weighted imaging [272].

Subsequently, Dixon-based multi-echo water-fat MR was used to identify BAT in a 3-month-old infant *post mortem* [263]. BAT exhibited a lower fat fraction (41.9 ± 6.3%) than WAT (>90%), while concomitant CT showed correspondingly higher attenuation values within BAT (20.8 ± 3.8 Hounsfield units) than WAT (approximately -60 HU to -100 Hounsfield units), reflecting the differences in fat content. BAT was confirmed subsequently following biopsy. Differences in fat fraction have also used to identify interscapular BAT in 8 infants *post mortem* and confirmed on the basis of gene expression profiling [273].

Rasmussen *et al.* [258] identified *in vivo* BAT deposits in a cohort of 22 neonates, based on fat fraction maps with high levels of inter- and intra-observer reliability Although there was no validation against either PET/CT or histopathological analysis.

In a series of studies by Hu *et al.* [265, 266, 269], cohorts of neonates, infants, children and teenagers underwent GRE MR scanning to characterise BAT *in vivo*. BAT depots were manually identified around fat in the supraclavicular fossae based on *a priori* knowledge of likely BAT distribution. Nonetheless the fat fraction within BAT depots was lower than in subcutaneous WAT, although the difference diminished with age. These studies were limited by the fact that BAT was identified *a priori* without any histopathological confirmation or PET correlation.

A small number of studies have also shown a lower fat fraction within BAT in adults, with validation against PET. Hu *et al.* [274], in a small study of adult oncology patients (n=2) who underwent PET/CT, compared the fat fraction and T2* relaxation times within the interscapular fat [sic] in two subjects, one ^{18}F-FDG BAT positive and the other negative. Notwithstanding that the uptake was erroneously described as being within the interscapular region, whereas the uptake actually occurred within the supraclavicular fossae, a lower fat fraction and T2* value was observed within the supraclavicular fat of the ^{18}F-FDG BAT positive subject than the negative subject (in whom values were indistinguishable from WAT).

The same method of crude *a priori* identification was also used to characterise BAT *in vivo* in a heterogeneous cohort of nine subjects [264]. BAT was confirmed by PET/CT in 5 cases, and for the *post mortem* case by biopsy. This showed a progressively higher fat fraction with age; approximately 29.7 to 72.5% in children, 52.0 to 80.6% in adolescents and 86.9 to 93.9% in adults, which were, with the exception of one case, significantly lower than WAT. A similar trend towards higher T2* relaxation times with increasing age were also reported. The fat fraction within BAT was much higher than had hitherto been reporting in children and neonates, and were much closer to WAT. Lundström *et al.* [268], in a small study of 9 subjects using the same method of crude *a* *priori* BAT identification, reported a high fat fraction (82.8 ± 5.0%) within BAT, which was nonetheless significantly lower than within WAT (86.2 ± 4.6%).

These studies have all sought to characterise pre-defined areas of presumed BAT. Attempts at prospective identification solely on the basis of imaging findings without *a priori* knowledge are few and far between. In 2012, Gifford *et al.* [275] identified probable BAT solely on the basis of calculated fat fraction in two human adults, but did not provide histological confirmation nor correlation with PET/CT. Reddy *et al.* [188][a] were able to visually identify BAT on anatomical fat-only spin-echo MR images in a single adult with a large volume of BAT. They reported moderate inter-observer variability, and provided PET/CT, histological and immunohistochemical confirmation. When applied to a wider sample visual identification tended to underestimate BAT on MR compared with PET/CT [276].

Chen *et al.* [277] also used spin-echo MR imaging to identify BAT in 5 human adults on the basis of water-saturation efficiency and water-fat contrast. Both techniques yielded similar BAT volumes to PET/CT.

As the difference in fat fraction between BAT and WAT is thought to reduce with age [264, 266, 268], prospective BAT identification on the basis of fat fraction becomes increasingly difficult.

Few have successfully identified BAT prospectively in adult humans without relying on *a priori* knowledge of likely BAT location [188, 258, 267, 273, 275], and have tended to focus on the interscapular fat pad and supraclavicular BAT depots.

---

[a] The team of which the author is a member

Chapter 8: Retrospective identification and characterisation of BAT on MR in rats and humans

In the preceding chapters, we showed that although the amount of ^{18}F-FDG BAT demonstrated varies widely between (and within) individuals, uptake tends to occur in fixed locations on serial PET/CT scans. In this chapter we shall identify and characterise BAT on MR in adult humans, based on *a priori* knowledge of the ^{18}F-FDG BAT uptake on PET/CT.

Unlike ^{18}F-FDG PET/CT which detects metabolically active BAT, MR may be able to identify anatomical rather than functional BAT, and that MR could be used to identify BAT irrespective of its level of metabolic activity. Therefore we hypothesise that the MR characteristics of BAT do not change significantly over time.

8.1 Aims

In this chapter we shall identify and characterise BAT on MR based on *a priori* knowledge.

The first half of the chapter describes a *post mortem* murine study, in which we aim to characterise the fat fraction and T2* relaxation time of interscapular BAT and subcutaneous WAT within excised tissue specimens and *in situ* on a clinical 3T MR scanner.

For the second half of the chapter we shall use the same MR sequences in adult humans in whom we have *a priori* knowledge of BAT location from concomitant PET/CT scans, to characterise BAT.

In both cases we aim to determine whether there is a difference in the fat fraction and T2* relaxation times between BAT and WAT in rats and humans, and therefore whether it would be possible to exploit these characteristics to identify BAT prospectively on MR.

We shall also explore whether these MR characteristics vary over time, and therefore whether the MR appearances are affected by the functional status of BAT.

8.2 Validation of an MR foodstuff phantom to test fat fraction

In this study we seek to validate the IDEAL MR sequences using a phantom composed of foodstuffs of varying fat content.

8.2.1 Subjects and methods

8.2.1.1 Phantom development

Universal containers containing foodstuffs of known fat content (olive oil 100% and 20%, butter, semi-skimmed milk and 0.9% saline) were produced to validate the 3-point IDEAL sequence and fat calculation.

Fat content was calculated based on advertised fat content, and fat fraction calculated using density approximations for each foodstuff obtained from The Physics Hypertextbook (http://physics.info/density).

8.2.1.2 Scanning protocol

Universal containers were scanned on a GE Optima MR360 1.5T MR scanner (General Electric Medical Systems, Milwaukee, USA) using a HD wrist coil.

A three-point IDEAL 2D FSE was obtained in an axial plane through the universal containers using the following parameters: TR/TE (ms) = 105/13.75, field-of-view (mm) = 180 x 180, voxel size (mm) = 0.35 x 0.35 x 5, number of slices/slice gap (mm) = 3/5, number of signal averages = 9, bandwidth = 244.141.

8.2.1.3 Statistical and image analysis

Fat fraction maps were generated using ImageJ [224, 225, 278] from the fat and water IDEAL images using the formula in Equation 7-4. Regions of interest were defined within each universal container, and the mean fat fraction compared with that derived from the advertised fat content.

8.2.2 Results

Mean fat fraction values from ROIs placed on the fat fraction maps (Figure 8-1) of the foodstuff phantoms were comparable to the advertised fat content (Table 8-1), although there was some signal heterogeneity within the liquids presumably as a result of eddy currents or flow phenomena. At very high fat fractions (*e.g.* pure olive oil) the calculated fat fraction was approximately 12% lower than the actual fat fraction. At lower fat fractions, the IDEAL sequence tended to overestimate the fat fraction compared to actual fat content.

Figure 8-1: Calculated fat fraction images of various foodstuffs with known fat content.

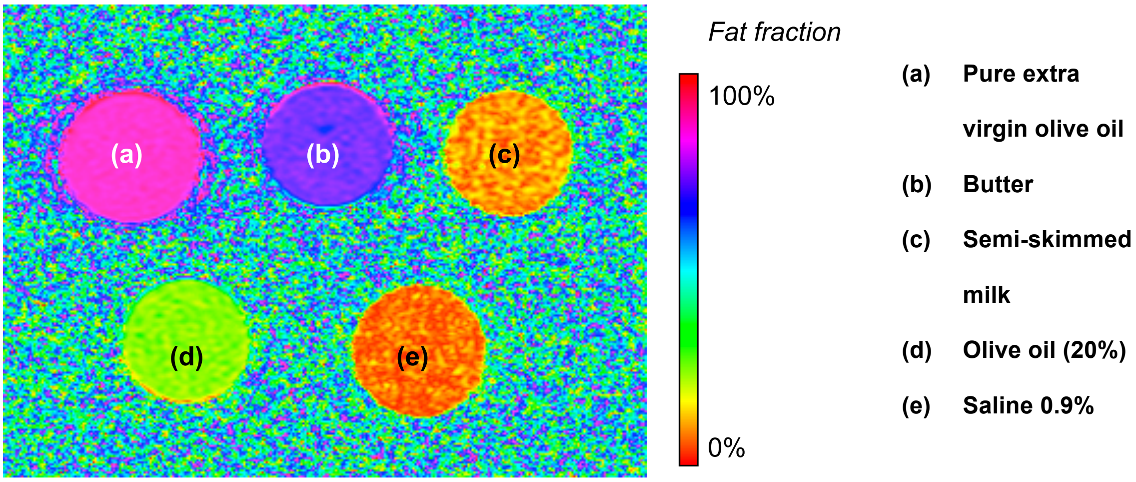

Table 8-1: Advertised and calculated fat fractions of foodstuff phantoms.

	Advertised fat content (%)	Calculated fat fraction (%)
(a) Extra virgin olive oil	99.5[a]	86.9 ± 0.7
(b) Butter	64.8	73.5 ± 1.7
(c) Semi-skimmed milk	1.7	9.2 ± 3.3
(d) Olive oil	20	25.0 ± 1.9
(e) Saline 0.9%	0	5.9 ± 2.9

8.3 *Ex vivo* and *in situ* BAT characterisation in rats using MR

8.3.1 Subjects and methods

8.3.1.1 Subject selection and preparation

Four male Wistar rats (mean mass 300g, age 6-8 weeks) reared on an *ad libitum* diet were used. Two were kept warm (30°C) and two kept in the cold (4°C) for 8 hours prior to sacrifice[b]. The interscapular BAT, omental WAT and subcutaneous WAT were dissected from one of each group and photographed to demonstrate the macroscopic difference between BAT and WAT.

The tissue specimens and rat carcasses were promptly transported to the MR scanner; those from the rats kept warm were transported at ambient temperature, and those from the cold rats were kept on ice.

---

[a] Based on a reported fat content of 91.3g/100ml and a density of 0.918g/ml for olive oil; 1.8g/100ml and a density of 1.033g/ml for skimmed cows' milk, 1.004 g/ml for 0.9% NaCl, 59g/100ml and density of 0.911g/ml for butter, performed at 20°C and 1 atm (The Physics Hypertextbook http://physics.info/density)

[b] All pre- and peri-mortem animal work was carried out by the Department of Life Sciences, University of Warwick

8.3.1.2 Scanning protocol

The excised tissue samples and rat carcasses were scanned on a GE Optima MR360 1.5T MR scanner (General Electric Medical Systems, Milwaukee, USA) using a HD wrist coil.

A three-point IDEAL 2D FSE sequence was used to obtain images through the upper thorax of the rat carcasses to include the interscapular fat using the parameters shown in Table 8-2. In addition a 2D GRE T2* mapping sequence was performed upon the dissected tissue specimens and rat carcasses using the parameters with the same coverage as the IDEAL sequence, using the parameters summarised in Table 8-2.

Table 8-2: MR scanning parameters for the *ex vivo* and *in situ* rat studies.

	Dissected tissues		**Rat carcasses**	
Parameter	IDEAL	T2*	IDEAL	T2*
TR (ms)	400	64.8	303	64.2
TE1[a] / ΔTE[b] (ms) / no.	14.2	2.3 / 4.9 / 6	13.1	2.5 / 5.0 / 6
Flip angle	-	20°	-	20°
No. of signal averages	9	1	6	1
Bandwidth	195.312	244.141	325.547	244.141
Slice thickness (mm)	2.7	2.7	2.7	2.7
Field-of-view (mm)	120 x 120	120 x 120	120 x 120	120 x 120
Voxel size (mm)	0.23 x 0.23 x 2.70	0.23 x 0.23 x 2.70	0.47 x 0.47 x 2.70	0.47 x 0.47 x 2.7
Slices	7	7	12	12
Slice gap (mm)	3	3	3	3

---

[a] First TE

[b] Echo spacing

8.3.1.3 Image calculation and analysis

The interscapular fat pad was identified on the anatomical fat-only IDEAL images, as this is the most easily identifiable BAT deposit within rodents. Regions of interest were drawn around the margins of the interscapular fat pad and excised BAT, together with corresponding ROIs within the subcutaneous adipose tissue, and transposed onto the fat fraction and T2* images.

Fat fraction maps were generated from the fat and water IDEAL images according to the equation in Equation 7-4 using ImageJ. T2* relaxation maps were calculated using the open source MRIAnalysisPak [279] plugin[a] for ImageJ. T2* relaxation curves were constructed using exponential decay, which uses a simplex algorithm to fit the values from each image in a stack to the formula in Equation 8-1.

Equation 8-1: Formula describing the mono-exponential decay for T2* relaxation.

$$S_n = S_0 exp\left(\frac{-TE_n}{T2}\right)$$

8.3.1.4 Statistical analysis

Calculated fat fraction and T2* values for BAT and WAT were compared using Kruskal-Wallis test with Dunn’s correction for pairwise comparisons.

8.3.1.5 Ethics

Ethical approval was obtained from the National Research Ethics Committee at Birmingham East, North and Solihull Research Ethics Committee (NHS REC reference 11/H1206/3).

---

[a] Developed by the Center for Comparative Neuroimaging (CCNI) at the University of Massachusetts Medical School and The Small Animal MRI Laboratory at Harvard Medical School/Brigham & Women’s Hospital. Available from imagej.nih.gov/ij/plugins/download/misc/MRIAnalysisPak

8.3.2 Results

8.3.2.1 *Ex vivo* scanning of excised tissue specimens

Figure 8-2 demonstrates the macroscopic differences between BAT and WAT, specifically the characteristic deep red/brown colour of BAT reflecting its high mitochondrial content and greater vascularity.

The calculated fat fraction images demonstrate differences in fat fraction between the excised tissue specimens to which a false colour scale has been applied (Figure 8-3). At both 4°C and 30°C, BAT has a green/yellow colour (corresponding to a fat fraction of approximately 60%), while WAT is coloured orange (corresponding to a fat fraction of approximately 80%). The areas of blue correspond to skeletal muscle fragments.

Figure 8-2: Dissected BAT and WAT specimens from male Wistar rates kept in the cold (4°C) and warm (30°C).

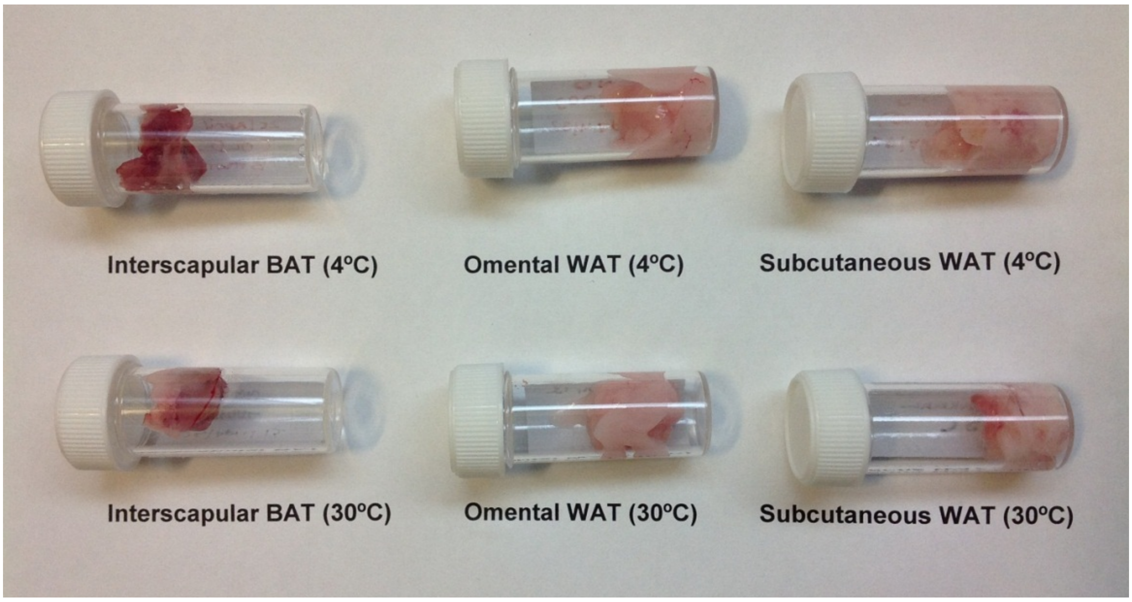

Figure 8-3: Calculated fat fraction maps showing (from left to right) interscapular BAT, omental WAT and subcutaneous WAT specimens, from rats kept at (a) 4°C, and (b) 30°C.

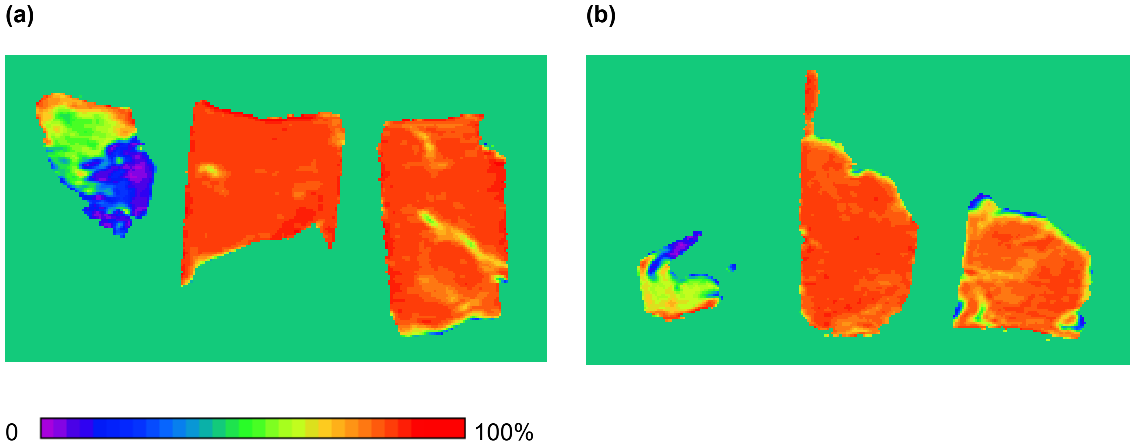

At both 4°C and 30°C, interscapular BAT showed a lower fat fraction than both omental and subcutaneous WAT (Figure 8-4 and Table 8-3) which was statistically significant ($p<0.001$).

All pairwise comparisons were found to be significantly different except for the two interscapular BAT groups; although the fat fraction within interscapular BAT excised from the rat kept at 4°C (58.9 ± 10.1%) was lower than that kept at 30°C (62.4 ± 8.6%), this was not statistically significant. At both temperatures, omental WAT showed a slightly higher fat fraction (82.5 ± 2.0% at 4°C, 81.4 ± 3.1% at 30°C) than subcutaneous WAT (80.7 ± 4.2% at 4°C, 78.0 ± 4.9% at 30°C) which was statistically significant ($p<0.001$).

Figure 8-4: Box and whisker plot (showing 1-99 percentiles) showing fat fractions within dissected interscapular BAT, omental WAT and subcutaneous WAT.

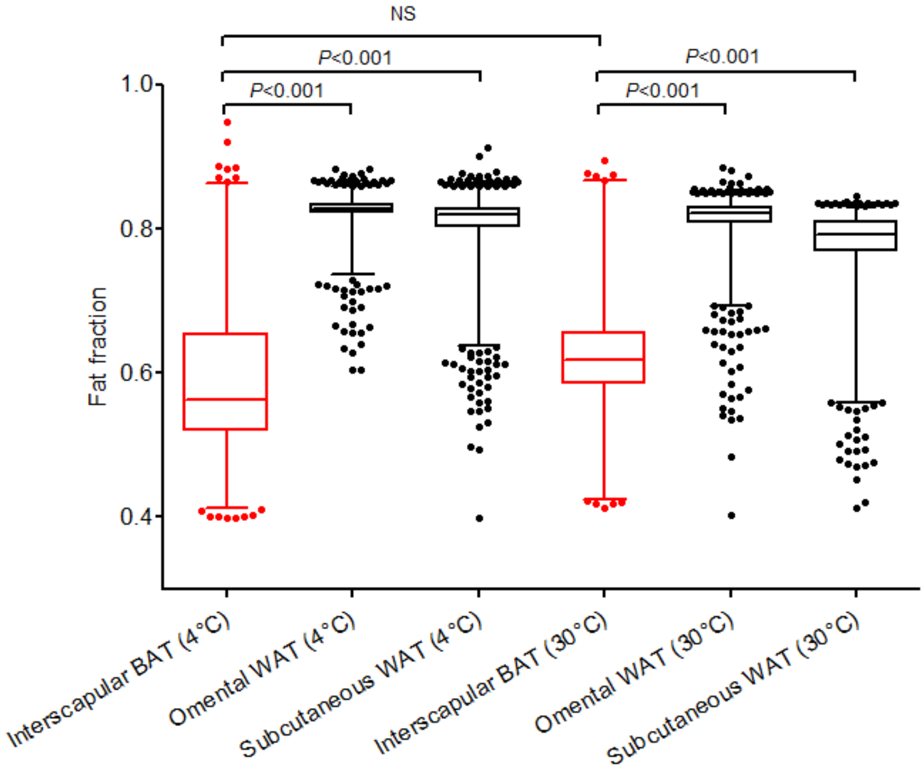

Table 8-3: Fat fraction and T2* values within excised BAT and WAT samples.

	Mean fat fraction ±SD (%) at 4°C	Mean fat fraction ±SD (%) at 30°C	Mean T2* value ±SD (ms) at 4°C	Mean T2* value ±SD (ms) at 30°C
Interscapular BAT	58.9 ± 10.1	62.4 ± 8.6	13.7 ± 4.9	20.5 ±10.2
Omental WAT	82.5 ± 2.0	81.4 ± 3.1	34.6 ± 15.7	39.4 ± 18.9
Subcutaneous WAT	80.7 ± 4.2	78.0 ± 4.9	37.6 ± 16.8	32.9 ± 16.5

The T2* relaxation times within interscapular BAT specimens were lower than for both omental and subcutaneous WAT (Figure 8-5). This was statistically significant at both 4°C and 30°C (Table 8-3 and Figure 8-6). The mean T2* value within the BAT specimen from the rat kept at 4°C (13.7 ± 4.9 ms) was significantly lower than at 30°C (20.5 ± 10.2 ms, $p<0.001$).

Figure 8-5: T2* map of (from left to right) interscapular BAT, omental WAT and subcutaneous WAT specimens, from rats kept at (a) 4°C, and (b) 30°C.

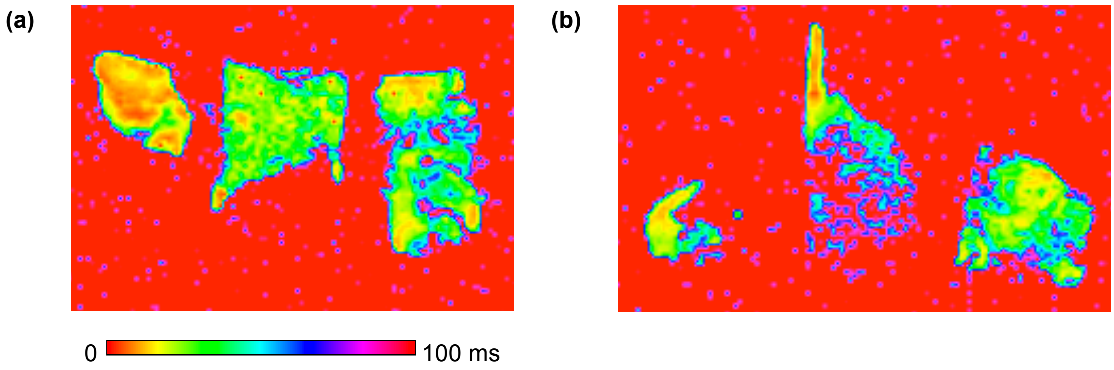

Figure 8-6: Box and whisker plot (showing 1-99 percentiles) showing T2* values within dissected interscapular BAT, omental WAT and subcutaneous WAT.

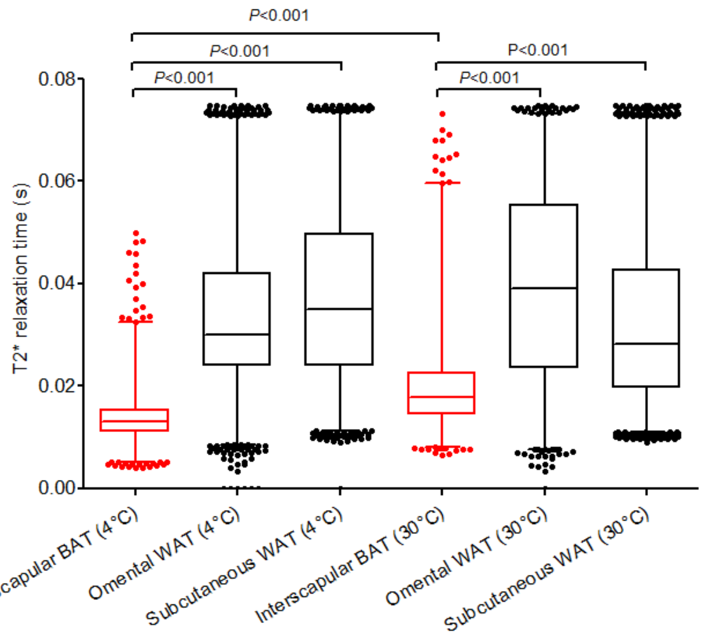

A scatterplot of calculated fat fraction against T2* relaxation time (Figure 8-7) for ROIs drawn around interscapular BAT (red), omental (yellow) and subcutaneous (green) WAT demonstrate that BAT and WAT form discrete data clusters.

Figure 8-7: Scatterplot of fat fraction and T2* value for the *ex vivo* specimens at 4°C.

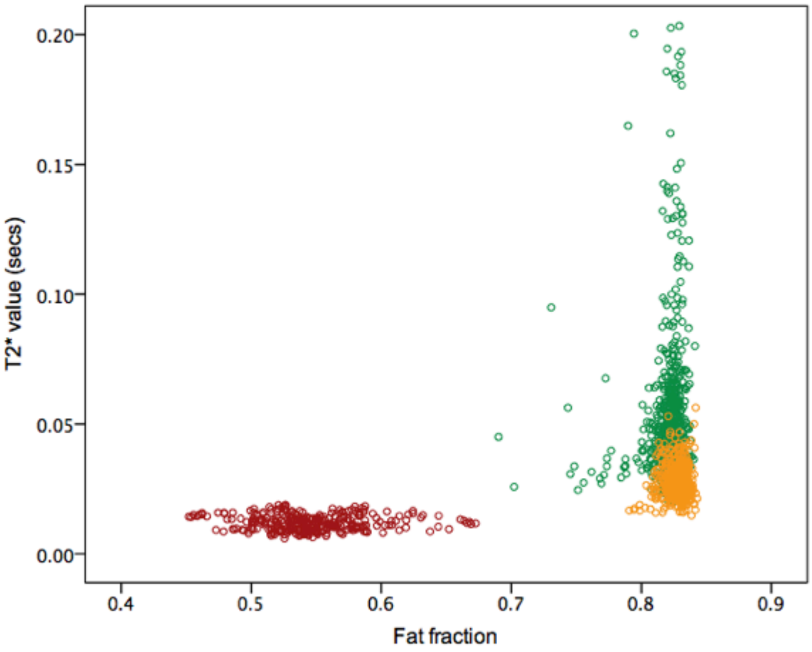

8.3.2.2 *In situ* scanning of rat carcasses

Axial IDEAL fat-only images through the upper thoracic region demonstrate the classical triangular bi-lobed interscapular fat pad in the dorsal subcutaneous fat (Figure 8-8). As with the *ex vivo* samples, the calculated fat fraction within interscapular BAT was significantly lower than subcutaneous WAT *in situ* (p<0.001) for rats kept at both 4°C and 30°C (Table 8-4 and Figure 8-9), although the fat fraction within interscapular BAT at 30°C was significantly higher (62.2 ± 6.5%) than at 4°C (44.7 ± 5.4, p<0.001). Although the T2* times within interscapular BAT (28.2 ± 101.7 ms at 4ºC, and 19.1 ± 3.1 ms at 30ºC) were significantly shorter than in subcutaneous WAT (57.1 ± 113.2 ms at 4ºC, and 26.0 ± 12.8 ms at 30ºC; Figure 8-10) the small size of the ROIs within the rat kept at 4ºC resulted in very wide standard deviations.

Figure 8-8: Axial fat-only IDEAL MR sequence through the upper thorax at the level of the interscapular fat pad (yellow arrow) at (a) 4°C and (b) 30°C, showing low fat fraction within the interscapular BAT (c) and (d).

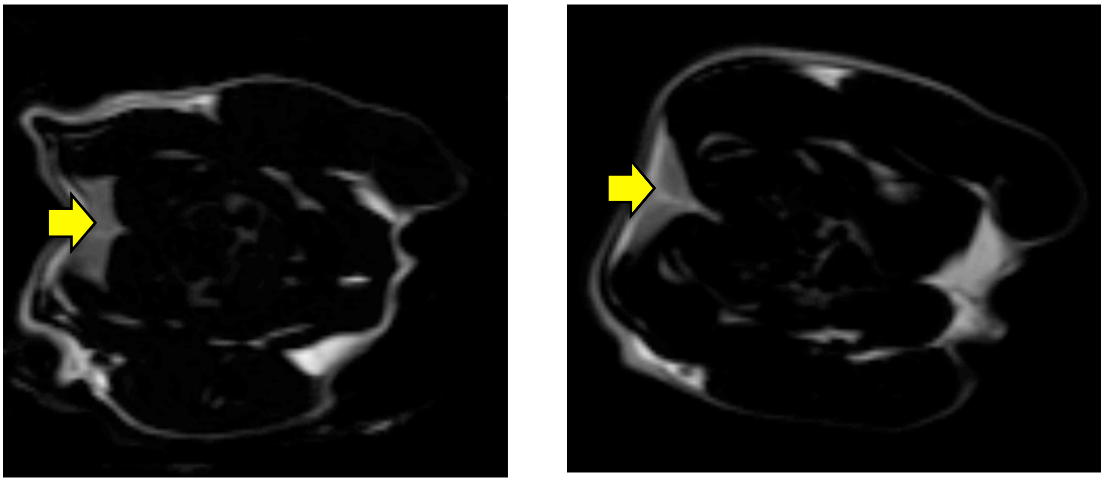

(a) Fat only image (4°C)

(b) Fat only image (30°C)

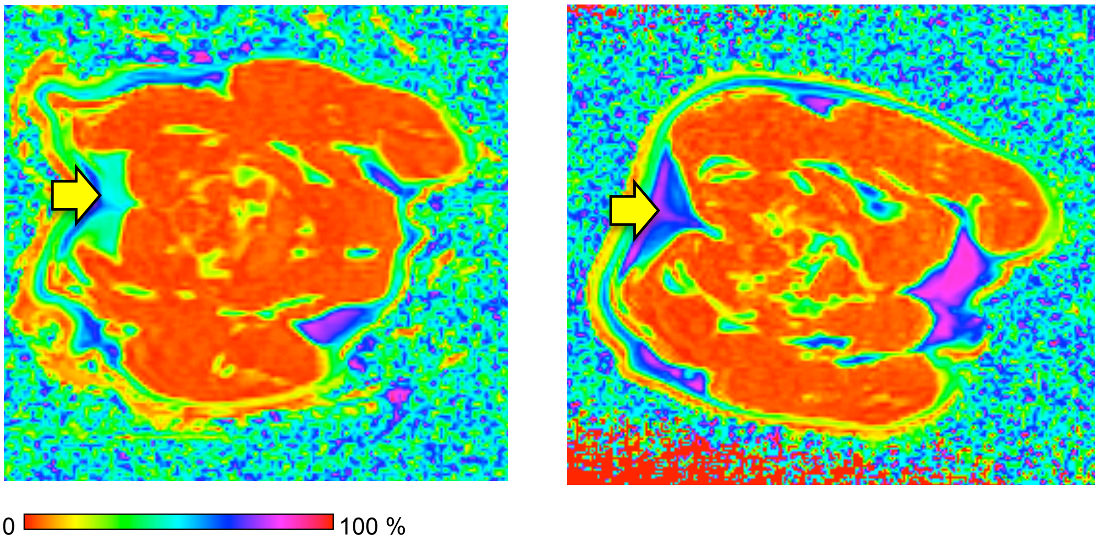

(c) Fat fraction map (4°C)

(d) Fat fraction map (30°C)

Table 8-4: Fat fraction and T2* values within *in situ* BAT and WAT

	Mean fat fraction ±SD (%) at 4°C	**Mean fat fraction ±SD (%) at 30°C**	**Mean T2* value ±SD (ms) at 4°C**	**Mean T2* value ±SD (ms) at 30°C**
Interscapular BAT	44.7 ± 5.4	62.2 ± 6.5	28.2 ± 101.7	19.1 ± 3.1
Subcutaneous WAT	72.9 ± 7.3	83.0 ± 3.5	57.1 ± 113.2	26.0 ± 12.8

Figure 8-9: Box and whisker plot (with Tukey's hinges) showing fat fraction of *in situ* BAT and WAT within rat carcasses at 4°C and 30°C.

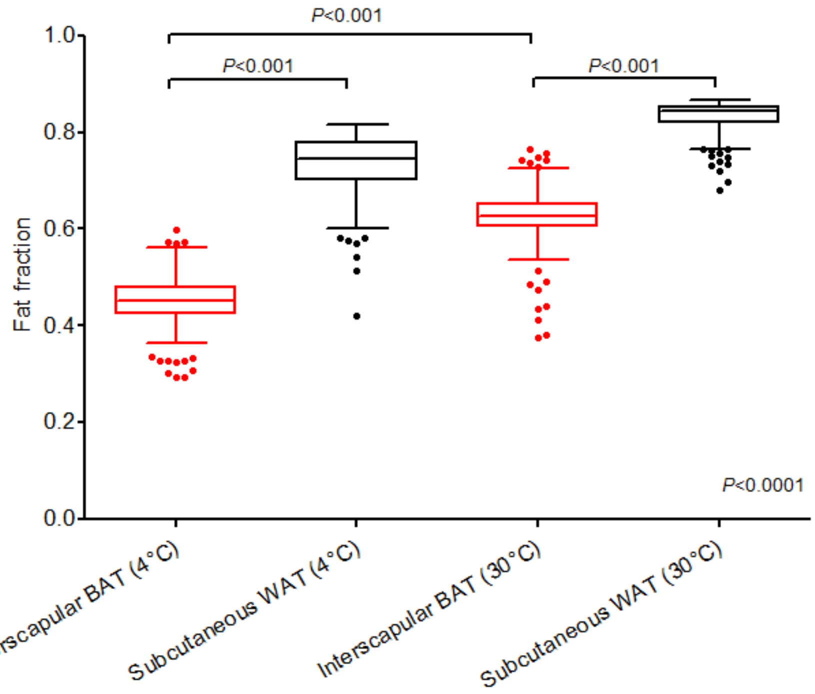

Figure 8-10: T2* map through the upper thorax showing shorter T2* relaxation time within the interscapular fat pad (yellow arrow) at (a) 4°C and (b) 30°C.

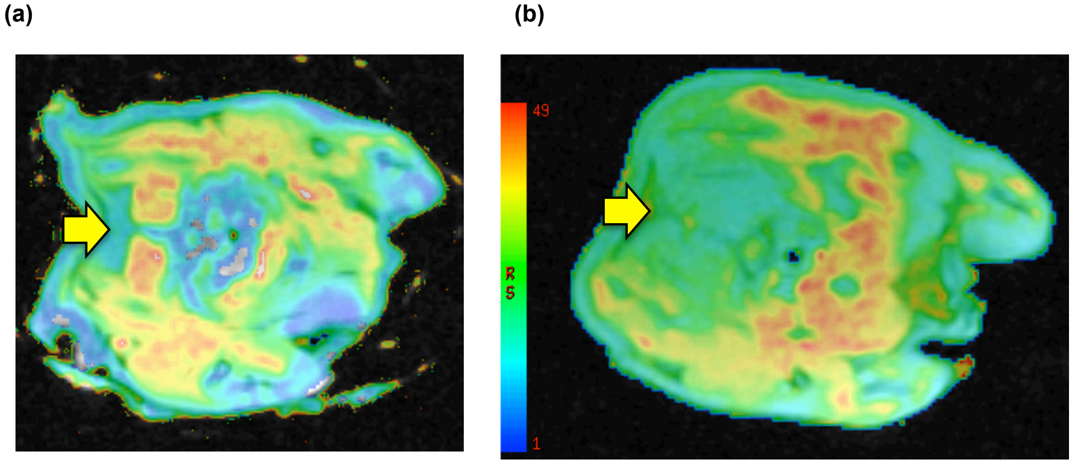
(a) **(b)**

8.4 *In vivo* BAT characterisation in adult humans using MR

8.4.1 Subjects and methods

8.4.1.1 Subject selection

Twenty-four adult patients were recruited (14 females, 10 males; mean age 43.9 ± 18.9 years, range 18-78). Recruitment occurred in two waves; the first was an opportunistic sample (n=13) of whom only two exhibited prominent quantities of ^{18}F-FDG BAT ('BAT06' and 'BAT13'). In addition two patients did not undergo concomitant PET/CT scans ('BAT03' and 'BAT04'), and therefore their BAT status was not known. Consequently a second more defined group of subjects were recruited from the population studied in chapters 3-4 (BAT13-18) on the basis of having high ^{18}F-FDG BAT uptake on PET/CT.

In addition six BAT negative controls were identified and recruited on the basis of consistently absent ^{18}F-FDG BAT uptake on serial PET/CT scans (BAT19-24). These patients were also selected to be age- and sex-matched to patients BAT13-18.

8.4.1.2 Scanning protocol

Scanning was performed on a GE Signa HDxt 3T MR scanner (General Electric, Milwaukee, USA) with a quad-channel cardiac receiver coil placed anteriorly across the upper thorax and cervical region.

A 3-point IDEAL FSE pulse sequence was performed with the following parameters: TR/TE = 440/10.7 to 11.2 ms, flip angle = 90°, number of signal averages (NEX) = 3, field of view = 300 x 300 to 380 x 380mm, voxel size (mm) 0.59 x 0.59 to 0.7 x 0.7. Various slice thicknesses were obtained to explore to impact of volume averaging, *i.e.* 5 mm with 5.3 cm spacing (BAT01-13, 20) and 2.3mm with 2.8mm spacing (BAT03, 13-24). Between 30 and 33 contiguous axial slices were acquired in an interleaved manner from the upper cervical to mid-thoracic region during free breathing. In addition T2* mapping sequences were obtained with the same coverage as the IDEAL sequences for 12 patients (BAT13-24) with the following parameters: TR/TE1/ ΔTE (ms) = 300/3.2/5.4, flip angle = 20°, number of signal averages = 0.75.

To assess MR changes within BAT over time, serial scans were obtained for some patients (BAT01, 06-08, 10, 11 and 13).

8.4.1.3 Image analysis

Following data reconstruction, fat fraction maps were produced offline from the separated fat and water images as described above using ImageJ. T2* maps were also produced offline using the MRIAnalysisPak plugin for ImageJ .

Fat fraction images maps were then thresholded with a lower limit set at 50% to exclude non-fat tissues.

Two methods of BAT identification were used: manual segmentation of fat in the supraclavicular fossae, and transposition of ^{18}F-FDG BAT ROIs from PET scans onto the MR. WAT regions of interest were defined by freehand segmentation within the dorsal subcutaneous adipose tissue.

8.4.1.3.1 Method 1 - manual segmentation of supraclavicular fat

In chapter 5 we showed that ^{18}F-FDG BAT, when present, occurs in the supraclavicular fossae in 92.6% cases. ROIs were defined within the supraclavicular fossae using the 'eroded range limited' technique validated by Lundström *et al.* [268, 280], based on the assumption that BAT, if present, will most likely occur in these anatomical areas. Crude 'BAT' ROIs were defined manually within the supraclavicular fossae on contiguous slices, after which a lower range limit on fat fraction of 50% was set to exclude non-fatty tissues, followed by morphological edge erosion to reduce edge effects from adjacent tissue interfaces (Figure 8-11).

Figure 8-11: Crude supraclavicular ROIs superimposed over thresholded fat fraction images.

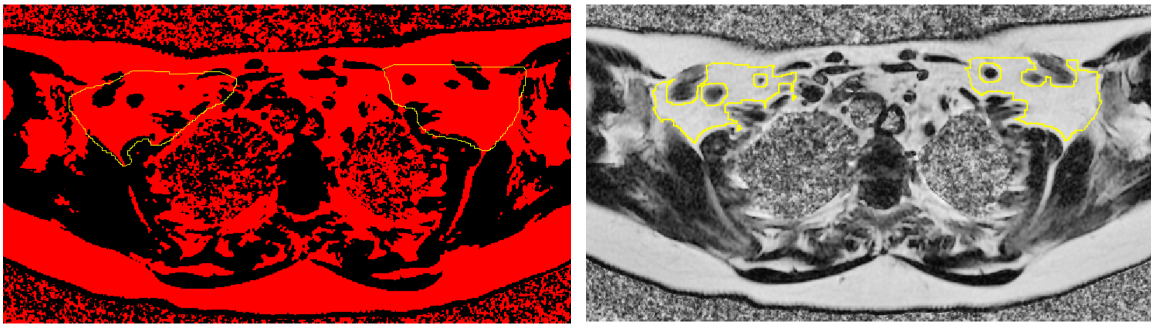

(a) Superimposition of crude ROI over the 50% thresholded fat fraction image

(b) Following application of a morphological edge erode algorithm to exclude tissue interfaces

8.4.1.3.2 Method 2 - transposition of ^{18}F-FDG BAT ROIs from PET/CT to MR

PET/CT scans containing ^{18}F-FDG BAT ROIs were registered to the MR scans using Mirada XD 3.4 image fusion software (Mirada Medical Ltd, Oxford, UK) employing a combination of automatic rigid and non-rigid registration, with manual placement of fiducial markers as necessary. Where multiple positive PET/CT scans had been performed for a patient, the index scan with the greatest ^{18}F-FDG BAT volume was used. The quality of image registration was verified visually using the in-built ‘chequerboard’ visualisation tool (Figure 8-12 A). The extent of deformable registration applied was also assessed using a displacement grid (Figure 8-12 B), in which the length and direction of the arrows represent the magnitude and direction of deformation. The magnitude of deformation was compared across different anatomical areas (*viz.* neck, upper and mid mediastinum, supraclavicular fossae and axillae) to determine the impact of arm position (*i.e.* whether the PET/CT was acquired with the arms elevated or alongside the torso) on the degree of deformation required to register images. Areas where image registration proved unsuccessful (typically the axillae), or where large degrees of deformation were required, were not included in further BAT analysis.

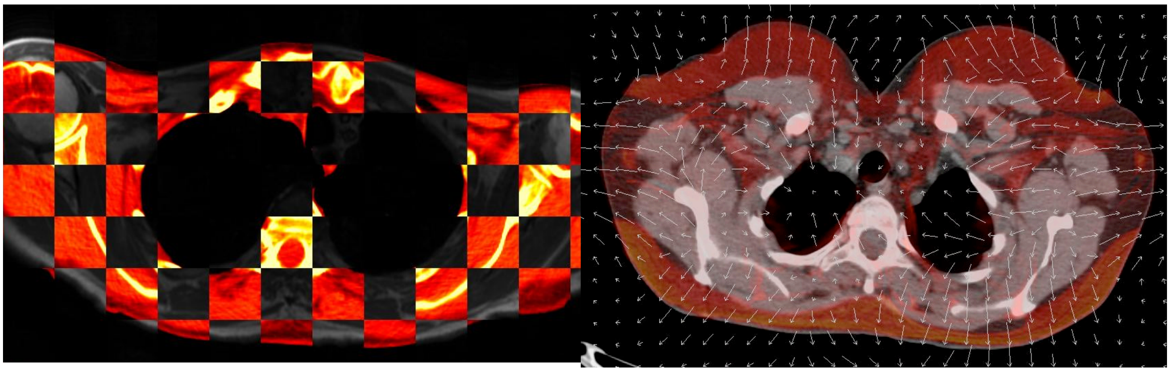

Figure 8-12: Verification of PET/CT and MR co-registration.

(a) 'Chequerboard' validation of co-registered PET/CT and MR images

(b) Displacement grid showing the degree of deformation required to register the images

^{18}F-FDG BAT ROIs defined in chapter 4 were then transposed onto the MR scans (Figure 8-13 a). WAT ROIs were manually defined within the dorsal subcutaneous adipose tissue, and non-adipose tissue was excluded from analysis by thresholding the fat fraction images, with a lower limit set at 50% (Figure 8-13 b).

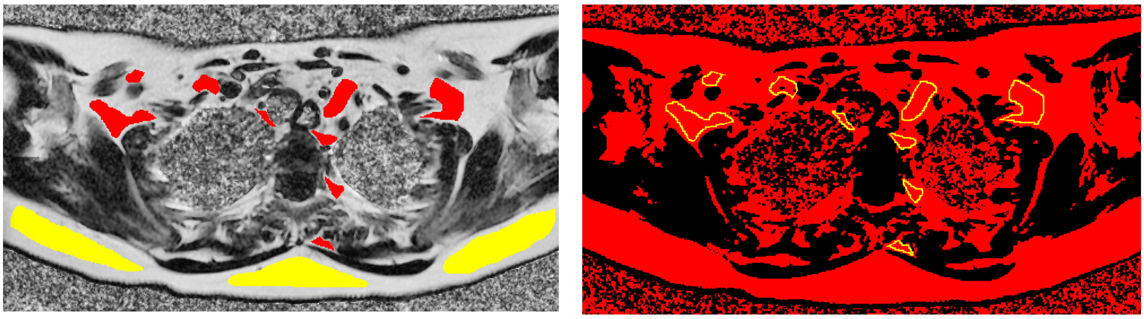

Figure 8-13: Position of ^{18}F-FDG BAT and subcutaneous WAT ROIs.

(a) Transposed ^{18}F-FDG BAT ROIs (red) transposed upon the fat fraction map (red), and manually defined WAT ROIs (yellow)

(b) ^{18}F-FDG BAT ROIs overlaid upon the thresholded fat fraction image to exclude non-adipose tissue (black)

8.4.1.4 Statistical analysis

The impact of arm position (*i.e.* whether PET/CT scans were performed with the arms up or down) on the degree of deformation required for PET/CT and MR image co-registration was analysed using Kruskal Wallis analysis with Bonferroni post tests.

Calculated fat fraction and T2* values for BAT and WAT were compared using the unpaired t-test, and fat fraction across serial scans were compared using ANOVA. Analysis was performed using GraphPad Prism version 5.00 for Windows (GraphPad Software, San Diego, California, USA). Significance was defined as $p < 0.05$.

8.4.1.5 Ethics

Written informed consent was obtained from human participants and appropriate ethical approval was obtained from the National Research Ethics Committee at Birmingham East, North and Solihull Research Ethics Committee (NHS REC reference 11/H1206/3). NHS Trust approval was obtained from the Research and Development office of University Hospitals Coventry and Warwickshire NHS Trust.

8.4.2 Results

8.4.2.1 Impact of arm position upon quality of image registration

Kruskal Wallis analysis with Bonferroni post tests showed that arm position had the greatest impact upon the extent of image deformation in the axillae, but had no significant impact in the neck, mediastinum, supraclavicular fossa (SCF), or paravertebral regions (Figure 8-14). Therefore subsequent analysis of BAT was not performed in the axillae when the index PET/CT scans were acquired with the arms elevated.

Figure 8-14: Pairwise comparison of magnitude of image deformation required to register PET/CT and MR according to arm position.

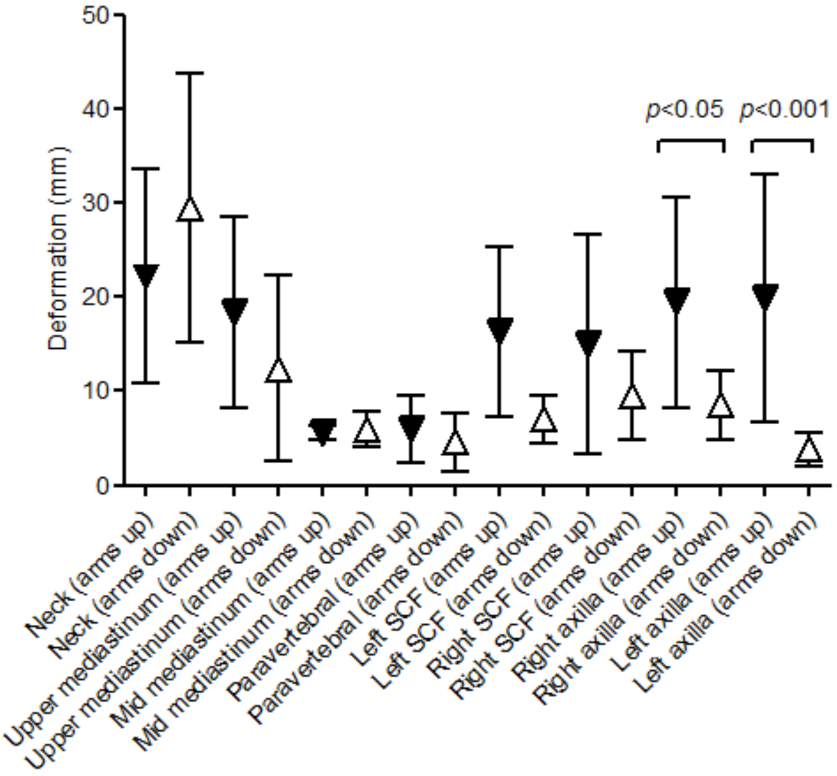

8.4.2.2 Sample demographics

Patients recruited during the first wave of opportunistic recruitment tended to be older (mean age 50.3 ± 20.7 years, range 21-78). In addition there was considerable variation in the ^{18}F-FDG volume on the concomitant PET/CT scan (Table 8-5); with only two showing more than 100 ml of ^{18}F-FDG BAT ('BAT06' and 'BAT13'). BAT13 was an outlier in terms of the volume of BAT and was the subject of a case report published separately [188].

Three patients underwent multiple ^{18}F-FDG BAT positive PET/CT scans and have already been studied in chapters 5 and 6 (and the corresponding patient identifiers denoted within parenthesis in Table 8-5): 'BAT06' (patient D) underwent 4 scans of which 2 were positive; 'BAT09' (patient H) underwent 2 PET/CT scans, both of which were positive; and BAT10 (patient E) underwent 4 scans of which two were positive.

In these cases the index PET/CT scan was used as a standard against which the MR scan was compared. The remainder (except for 'BAT03' and 'BAT04') had only a single ^{18}F-FDG BAT positive scan.

Table 8-5: Opportunistic sample of patients (n=13) recruited to the first phase of the study.

Subject	Age (years)	Sex	^{18}F-FDG BAT volume (ml) [percentile]	Diagnosis
BAT01	65	Male	7.4 [22nd]	Lymphoma
BAT02	67	Male	19.1 [37th]	Lung cancer
BAT03	37	Female	-	Thyrotoxicosis
BAT04	78	Male	-	Multinodular goitre
BAT05	65	Female	17.5 [34th]	Bowel cancer
BAT06 (D)	53	Female	324.8 [97th]	Metastatic melanoma
BAT07	26	Male	3.0 [9th]	Testicular seminoma
BAT08	21	Male	24.2 [45th]	Hodgkin's lymphoma
BAT09 (H)	61	Male	43.6 [59th]	Gastro-intestinal stromal tumour
BAT10 (E)	30	Female	47.9 [62nd]	Hodgkin's lymphoma
BAT11	73	Female	52.9 [64th]	Gastro-intestinal stromal tumour
BAT12	27	Female	45.6 [61st]	Hodgkin's lymphoma
BAT13	24	Female	561.5 [100th]	Hyperparathyroidism-jaw tumour syndrome

The second sample of six patients recruited (Table 8-6) on the basis of having high levels of ^{18}F-FDG BAT uptake on PET/CT were on average younger (mean age 36.7 ± 16.1 years, range 18-56), including one who was re-recruited from the first wave (BAT13). In addition, six age (± 5 years) and sex-matched controls were identified and recruited on the basis of showing consistently absent ^{18}F-FDG BAT uptake across serial PET/CT scans.

Table 8-6: Recruited patients with high ^{18}F-FDG BAT uptake (n=6), and age- and sex-matched controls (n=6).

Subject	Age (years)	Sex	^{18}F-FDG BAT volume (ml) [percentile]	Diagnosis
^{18}F-FDG BAT positive subjects				
BAT13	24	Female	561.5 [100th]	Hyperparathyroidism-jaw tumour syndrome
BAT14	56	Female	312.6 [97th]	Mucinous rectal cancer
BAT15	27	Male	270.6 [94th]	Hodgkin's lymphoma
BAT16	18	Male	441.4 [99th]	Teratoma
BAT17	54	Female	275.2 [95th]	Bowel cancer
BAT18	41	Female	149.4 [85th]	Solitary pulmonary nodule
^{18}F-FDG BAT negative controls				
BAT19	24	Female	0	Lymphoma
BAT20	54	Female	0	Submandibular gland carcinoma
BAT21	29	Male	0	Seminoma
BAT22	23	Male	0	Hodgkin's lymphoma
BAT23	59	Female	0	Non-Hodgkin's lymphoma
BAT24	41	Female	0	Vaginal carcinoma

8.4.2.3 Difference in fat fraction between BAT and WAT

Mean fat fraction was significantly lower within ^{18}F-FDG BAT ROIs transposed from positive PET/CT scans (74.0 ± 6.5%) than subcutaneous WAT ROIs (78.8 ± 6.0%, p = 0.0016). Figure 8-15 shows the aggregate mean fat fractions for all patients within the study. It is noteworthy that although the mean fat fraction in ^{18}F-FDG BAT ROIs is lower than subcutaneous WAT, there is considerable overlap. Therefore a single cut-off point to differentiate between BAT and WAT is unlikely to be generalisable to all patients.

Overall, the fat fraction within crude SCF ROIs (78.7 ± 4.6%) did not differ significantly from subcutaneous WAT (p = 0.4562), even if analysis is confined to those patients with evidence of ^{18}F-FDG BAT uptake on PET/CT (p = 0.3072). The fat fraction within crude supraclavicular fossa ROIs did not differ significantly between ^{18}F-FDG BAT positive (78.5 ± 4.6%) and negative individuals (79.5 ± 5.1%, p = 0.6; Figure 8-16).

Figure 8-15: Scatter dot plot showing mean WAT and BAT fat fractions.

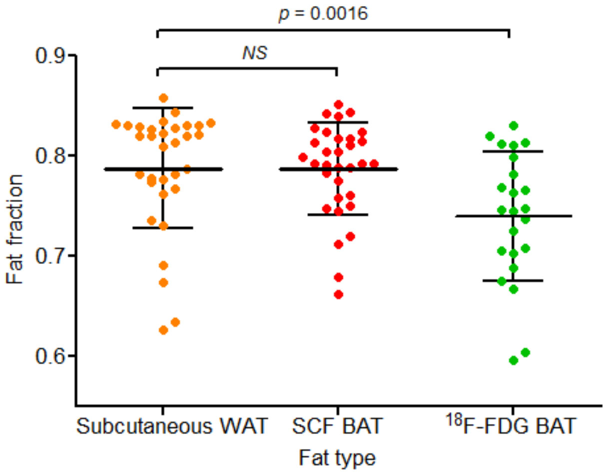

Figure 8-16: Fat fraction within crude supraclavicular fossa ROIs in ^{18}F-FDG BAT positive and negative individuals.

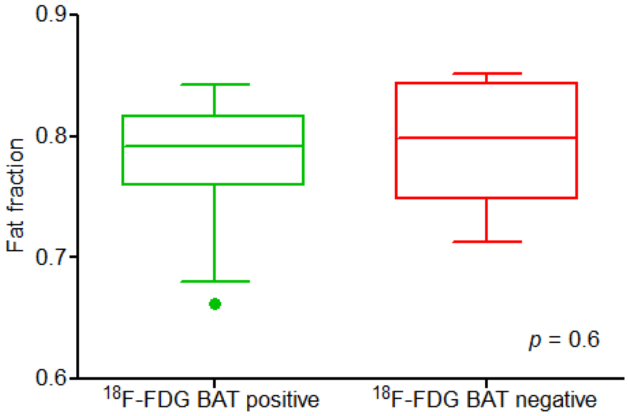

At an individual level the fat fraction within the supraclavicular fossa was comparable to subcutaneous WAT in most cases (Table 8-7). Only five patients (BAT02-05, 13) showed a significantly lower fat fraction within the supraclavicular fossa than in subcutaneous WAT. For BAT03 and BAT04, the true BAT status could not be determined as they did not undergo concomitant PET/CT scans. The remaining subjects showed either no significant difference in fat fraction between the supraclavicular fossa and subcutaneous WAT, or a lower fat fraction within WAT. Three patients (BAT07, 20 and 21) showed a fat fraction within subcutaneous WAT below 70%; of these BAT07 had a low volume of ^{18}F-FDG BAT on PET/CT (7.0 ml), and BAT20-21 were ^{18}F-FDG BAT negative. This erroneously low fat fraction is likely due to the subcutaneous fat layer being thin, increasing the effects of volume averaging artefact.

There is a weak positive correlation between BMI and fat fraction (Figure 8-17) within both subcutaneous WAT (r^2 = 0.22) and ^{18}F-FDG BAT (r^2 = 0.23), albeit not statistically significant. This points towards higher fat fractions with increasing adiposity, and lower fat fractions within leaner subjects, possibly indicating a greater propensity to volume averaging artefact.

Figure 8-17: Variation in WAT and ^{18}F-FDG BAT fat fraction with BMI.

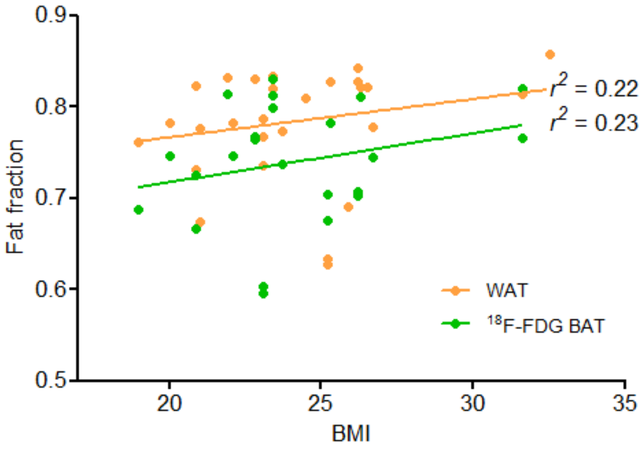

Table 8-7: BAT and WAT fat fraction (on first MR scan) according to patient.

Subject	**Mean WAT fat fraction (± SD) %**	**Crude SCF ROIs**		**Transposed ^{18}F-FDG BAT ROIs**	
		Mean fat fraction (± SD)	***P* value**	**Mean fat fraction (± SD)**	***P* value**
BAT01	83.0 ± 3.2	80.5 ± 5.8	0.0789	76.4 ± 5.5	0.0173
BAT02	82.3 ± 2.8	79.1 ± 4.9	0.0237*	72.5 ± 6.4	<0.0001
BAT03	83.5 ± 1.6	78.9 ± 5.0	<0.0001*	-	-
BAT04	81.1 ± 2.7	77.3 ± 6.1	0.0013*	-	-
BAT05	84.3 ± 1.3	79.3 ± 5.5	0.0034*	70.3 ± 7.4	<0.0001
BAT06	77.8 ± 2.4	79.2 ± 5.6	0.073	74.5 ± 6.3	0.0002
BAT07	62.7 ± 4.6	68.0 ± 4.9	0.0004	70.5 ± 6.5	0.0548
BAT08	73.6 ± 4.6	74.4 ± 5.4	0.2526	59.6 ± 6.1	0.0003
BAT09	78.2 ± 3.2	78.9 ± 5.1	0.3528	74.6 ± 7.5	0.0643
BAT10	82.7 ± 2.2	84.2 ± 4.7	0.0243	78.2 ± 6.0	0.0001
BAT11	82.0 ± 2.2	81.8 ± 5.6	0.427	76.6 ± 6.5	0.0005
BAT12	78.2 ± 3.4	77.5 ± 5.4	0.296	74.7 ± 5.5	0.002
BAT13	83.1 ± 1.3	81.0 ± 5.0	0.0293	81.2 ± 4.2	<0.0001
BAT14	83.2 ± 2.4	84.0 ± 4.4	0.0879	81.4 ± 6.5	0.0011
BAT15	76.2 ± 7.3	76.0 ± 4.8	0.4262	68.8 ± 7.3	<0.0001
BAT16	73.1 ± 5.9	72.0 ± 5.3	0.1538	66.7 ± 6.8	<0.0001
BAT17	82.1 ± 3.3	82.4 ± 5.5	0.3609	81.1 ± 6.3	0.0698
BAT18	77.3 ± 3.7	79.2 ± 5.1	0.0139	73.7 ± 7.6	<0.0001
BAT19	78.7 ± 3.6	79.9 ± 5.4	0.3088	-	-
BAT20	67.4 ± 5.1	71.3 ± 5.1	0.0087	-	-
BAT21	69.1 ± 6.9	74.8 ± 6.1	0.0008	-	-
BAT22	82.1 ± 2.8	85.2 ± 4.9	<0.0001	-	-
BAT23	85.8 ± 2.2	84.4 ± 5.7	0.0844	-	-
BAT24	81.0 ± 3.0	82.4 ± 5.3	0.0365	-	-

8.4.2.3.1 Impact of MR slice thickness upon fat fraction

The BMI-dependent variation in fat fraction within both WAT and ^{18}F-FDG BAT is much more pronounced on MR images acquired with a slice thickness of 2.5mm (r^2 = 0.45 for ^{18}F-FDG BAT and 0.316 for WAT) than at 5mm (r^2 = 0.06 for ^{18}F-FDG BAT and 0.002 for WAT; Figure 8-18). This implies that narrower slice thickness may have greater sensitivity in detecting differences in fat fraction with increasing BMI.

Figure 8-18: Variation in WAT and ^{18}F-FDG BAT fat fraction according to MR slice thickness

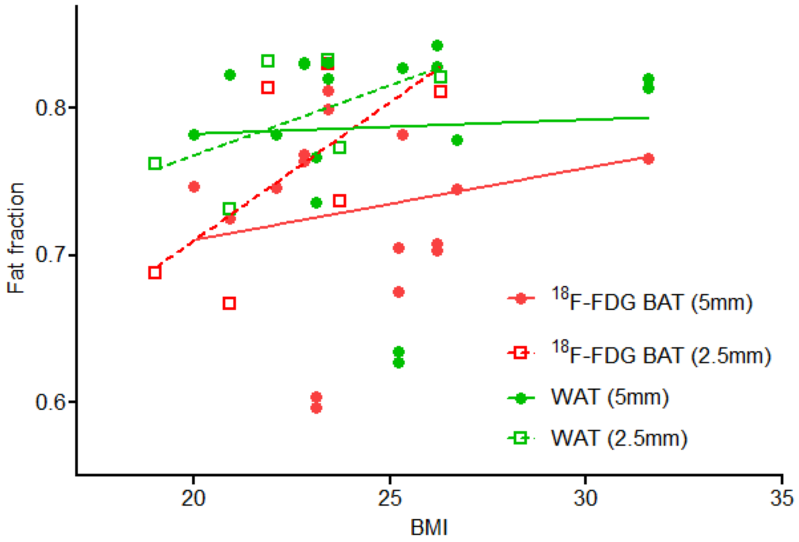

8.4.2.4 Difference in T2* relaxation time between BAT and WAT

The mean T2* values within the crude supraclavicular fossae (SCF) ROIs defined in section 8.4.1.3.1 were highly variable. T2* relaxation times tended to be slightly higher within the SCF of BAT negative individuals (BAT19-24) than those with evidence of ^{18}F-FDG BAT on PET/CT (Table 8-8) although the differences were not statistically significant (Figure 8-19).

In most cases the T2* values within the SCF was higher than within the subcutaneous WAT, whereas one would expect the converse: a lower mean T2* value within the SCF of BAT positive individuals. This pattern was only evident in three patients (BAT13-15), in whom the difference was statistically significant in one (BAT13).

In the case of transposed ^{18}F-FDG BAT ROIs, no significant difference between the T2* values of BAT and WAT were identified except for a spuriously high BAT T2* value in BAT16 (Table 8-8).

Table 8-8: T2* relaxation times within BAT and WAT.

Subject	Mean WAT T2* value (± SD) in ms	Crude SCF ROIs		Transposed ^{18}F-FDG BAT ROIs	
		Mean T2* value (± SD) in ms	*P* value	Mean T2* value (± SD) in ms	*P* value
BAT13	15.9 ± 11.1	3.3 ± 7.9	<0.0001	14.1 ± 9.6	0.3252
BAT14	29.7 ± 17.7	26.4 ± 18.1	0.2467	32.0 ± 18.9	0.4544
BAT15	9.0 ± 7.1	5.4 ± 13.9	0.0704	10.9 ± 7.2	0.0997
BAT16	29.5 ± 8.3	38.2 ± 21.9	0.0403	40.5 ± 24.5	0.0007
BAT17	33.0 ± 14.7	80.5 ± 69.2	0.0004	54.7 ± 48.8	0.2273
BAT18	30.5 ± 14.9	87.2 ± 63.6	<0.0001	52.0 ± 41.6	0.0011
BAT19	31.4 ± 11.3	97.2 ± 69.6	<0.0001	-	-
BAT20	28.1 ± 9.0	50.8 ± 0.0	0.0024	-	-
BAT21[a]	-	-	-	-	-
BAT22	30.4 ± 10.7	68.3 ± 51.3	0.0001	-	-
BAT23	49.2 ± 20.9	84.5 ± 73.0	0.4067	-	-
BAT24	24.4 ± 15.1	45.6 ± 45.8	0.0287	-	-

Overall there was no significant difference in mean T2* relaxation time between either the SCF ROIs or transposed ^{18}F-FDG BAT ROIs, and subcutaneous WAT (Figure 8-20). This, in conjunction with the large variation in these T2* relaxation data make this an unreliable discriminator of BAT in this study.

---

[a] No T2* data were available for BAT21

Figure 8-19: T2* relaxation times within crude supraclavicular fossa ROIs in ^{18}F-FDG BAT positive and negative individuals.

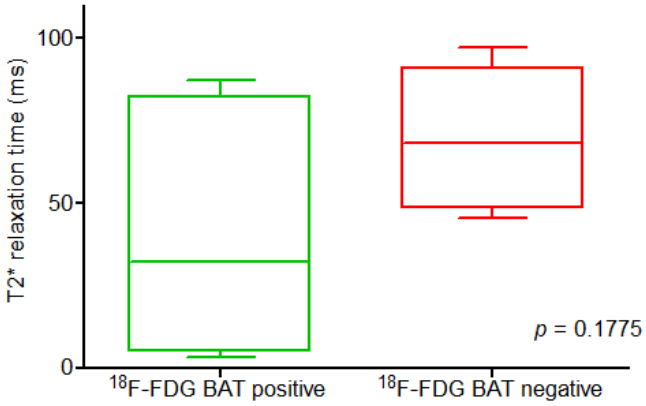

Figure 8-20: Scatter dot plot showing mean WAT and BAT T2* relaxation time for each MR scan.

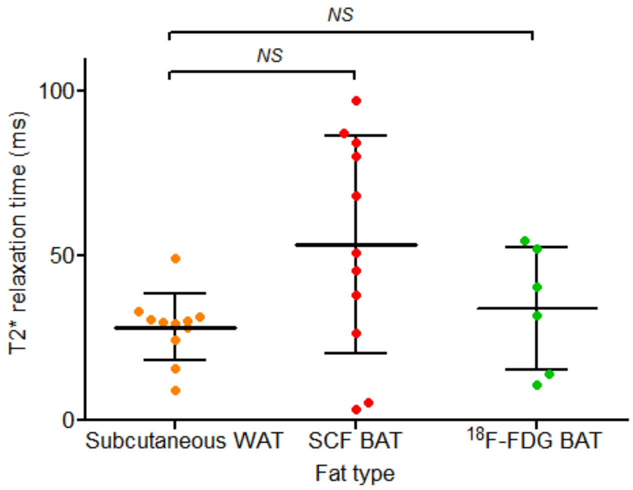

8.4.2.5 Variation in fat fraction on serial MR scans

Eight patients underwent serial MR scans, of whom six showed evidence of ^{18}F-FDG BAT activity on PET/CT (Table 8-9). In most cases fat fraction within the supraclavicular fossa ROIs showed little variation over time (Figure 8-21). It is noteworthy that the patients who did show significant variation in fat fraction over time were BAT20, in whom ^{18}F-FDG BAT uptake was consistently absent across three PET/CT scans, and BAT03 who did not undergo PET/CT. BAT06, a 53-year old female who showed 324.8ml of ^{18}F-FDG BAT on PET/CT showed a change in fat fraction of 3% which was not statistically significant.

Table 8-9: Serial fat fraction measurements in the supraclavicular fossae.

Subject	Scan 1 SCF fat fraction (%)	Scan 2 SCF fat fraction (%)	Scan 3 SCF fat fraction (%)	*P* value
BAT01	80.5 ± 5.8	80.4 ± 5.7	-	0.9566
BAT03	78.9 ± 5.0	81.7 ± 4.9	-	0.0147
BAT06	79.2 ± 5.6	75.8 ± 5.0	-	0.1760
BAT07	68.0 ± 4.9	66.2 ± 5.2	-	0.1162
BAT08	74.4 ± 5.4	75.0 ± 5.3	-	0.6679
BAT11	81.8 ± 5.6	81.5 ± 5.8	-	0.8298
BAT13	81.0 ± 5.0	81.3 ± 5.1	82.9 ± 5.4	0.2211[a]
BAT20	71.3 ± 5.1	78.4 ± 5.8	-	<0.0001

Figure 8-21: Variation in fat fraction within supraclavicular fossa ROIs on serial MR scans.

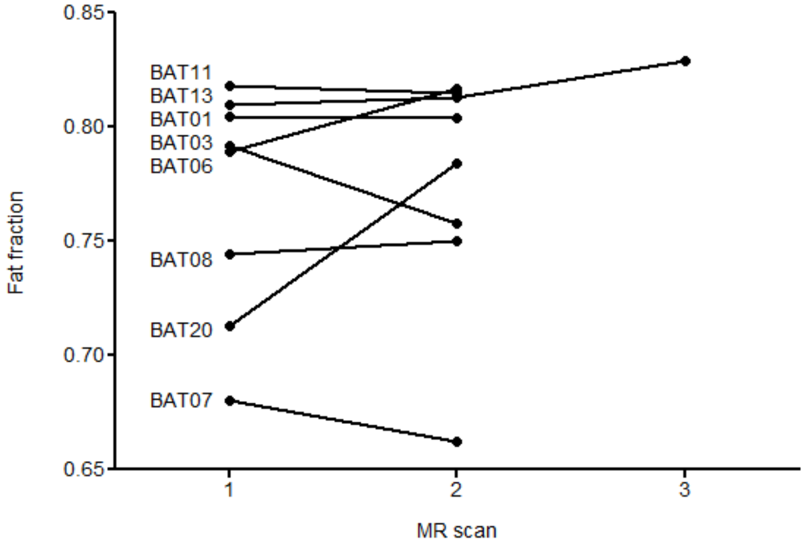

Several patients also showed unexpected variation in subcutaneous WAT fat fraction over time (Table 8-10 and Figure 8-22). The most significant variation in WAT fat

---

[a] Performed using one-way analysis of variance (ANOVA)

fraction was seen in BAT03, 06, 08, 13 and 20. It is noteworthy that two of these (BAT03 and 20) also showed variability in fat fraction within the supraclavicular fossa, implying that fluctuations within the supraclavicular fossae may be erroneous.

Table 8-10: WAT fat fraction measurements on serial MR scans.

Subject	Scan 1 WAT fat fraction (%)	Scan 2 WAT fat fraction (%)	Scan 3 WAT fat fraction (%)	*P* value
BAT01	83.0 ± 3.2	83.1 ± 2.8	-	0.8729
BAT03	83.5 ± 1.6	82.9 ± 1.7	-	0.0428
BAT06	77.8 ± 2.4	82.8 ± 2.0	-	<0.0001
BAT07	62.7 ± 4.6	63.4 ± 5.4	-	0.700
BAT08	73.6 ± 4.6	76.7 ± 4.0	-	0.0047
BAT11	82.0 ± 2.2	81.4 ± 2.1	-	0.1982
BAT13	83.1 ± 1.3	82.0 ± 1.5	83.3 ± 2.9	<0.0001[a]
BAT20	67.4 ± 5.1	77.6 ± 4.5	-	<0.0001

Figure 8-22: Variation in fat fraction within subcutaneous WAT on serial MR scans.

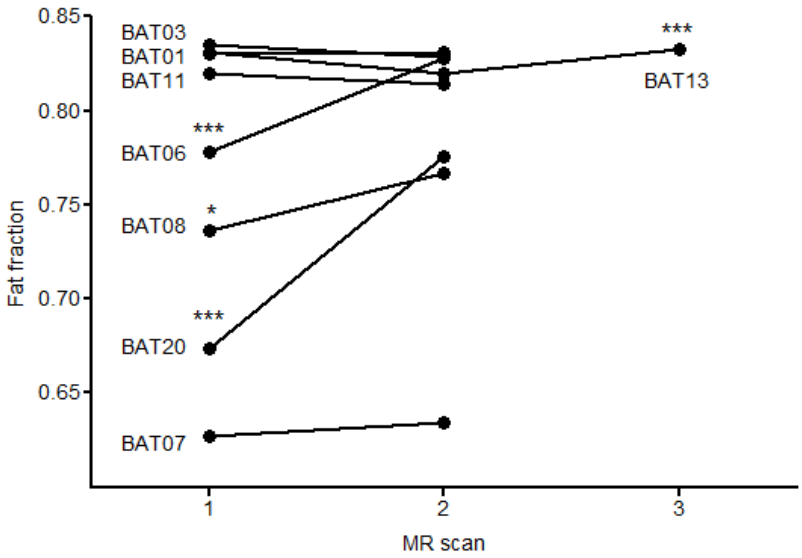

---

[a] Performed using one-way analysis of variance (ANOVA)

There was significant variation in calculated fat fraction within transposed ^{18}F-FDG BAT regions of interest for BAT06, BAT11 and BAT13 (Table 8-11 and Figure 8-23) although the magnitude of the differences was small (-4.3% in BAT06, 5.4% in BAT11 and -1.3% in BAT13). This variation does not appear to follow a seasonal variation (Figure 8-24).

Table 8-11: Serial fat fraction for ^{18}F-FDG BAT regions of interest.

Subject	Scan 1	Scan 2	Scan 3	*P* value
	BAT fat fraction (%)	BAT fat fraction (%)	BAT fat fraction (%)	
BAT01	76.4 ± 5.5	76.8 ± 6.7	-	0.91
BAT06	74.5 ± 6.3	70.8 ± 6.4	-	0.001
BAT07	70.5 ± 6.5	67.5 ± 6.4	-	0.51
BAT08	59.6 ± 6.1	60.4 ± 7.2	-	0.85
BAT11	76.6 ± 6.5	82.0 ± 6.5	-	0.0016
BAT13	81.2 ± 4.2	79.9 ± 5.1	83.0 ± 4.6	<0.001

Figure 8-23: Variation in fat fraction within ^{18}F-FDG BAT on serial MR scans.

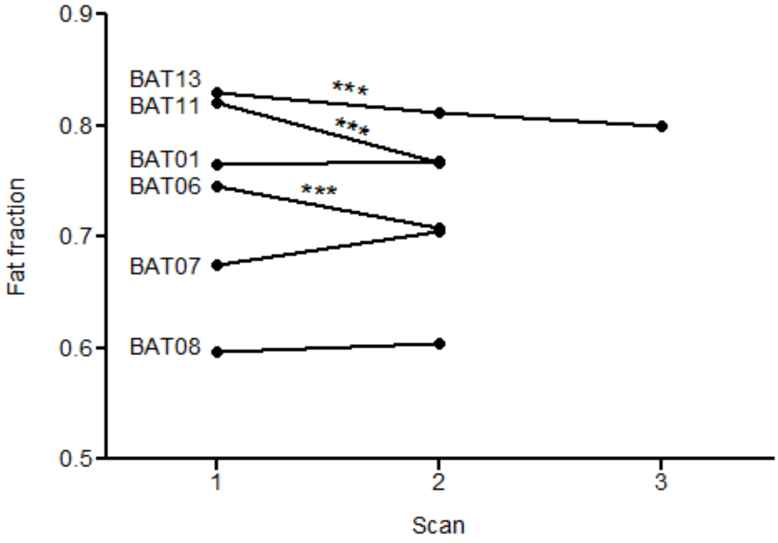

Figure 8-24: Seasonal variation in fat fraction within transposed ^{18}F-FDG BAT ROIs. Red lines correspond to BAT06, 11 and 13 in whom the fat fraction varied significantly.

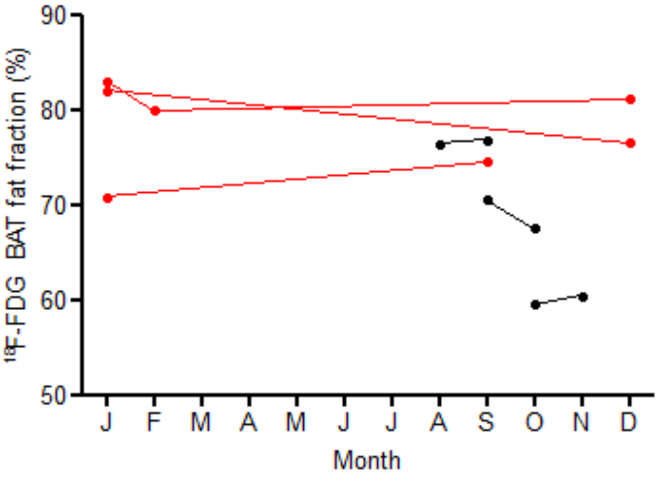

8.5 Summary

In this chapter we compared fat fraction and T2* relaxation times within BAT and WAT in rats and humans.

In a *post* mortem murine study we found that interscapular BAT fat fraction and T2* time were significantly lower in both excised tissue specimens and when scanned *in vivo*. We identified variation in BAT fat fraction with temperature, suggesting that fat fraction is dynamic in response to the functional state of BAT.

In adult humans, we found that the mean fat fraction within BAT (identified *a priori* using transposed ^{18}F-FDG BAT ROIs from PET/CT) was significantly lower than within subcutaneous WAT. The mean fat fraction within the ROIs defined in the supraclavicular fossae (the area most likely to contain BAT based on previous work in chapter 5) and subcutaneous WAT did not differ significantly which calls into question the effectiveness of this method of segmentation. There was considerable variation in BAT fat fraction between patients therefore a single cut off value to differentiate BAT and WAT is unlikely to be generalisable to all patients.

No consistent difference in T2* relaxation time was observed between subcutaneous WAT and BAT (using either method of *a priori* identification). We also identified that BAT is oftentimes more prominent on the fat only IDEAL sequence than on the fat fraction maps.

We also identified significant variation in fat fraction within both supraclavicular fossae and subcutaneous WAT on serial scans. Causes for variation in BAT and WAT will be discussed further in chapter 10, but include seasonal variation in fat composition and variation in BMI (though no variation in BMI was seen to account for the WAT variation in this study). Variation may also be due to technical factors including measurement error, image mis-registration or volume averaging artefact due to difference in position within the scanner.

Chapter 9: Prospective identification of BAT in rats and adult humans on MR imaging

9.1 Introduction

In the previous chapter we identified a difference in fat fraction between BAT and WAT in both rats *post mortem* and adult humans *in vivo*.

In the previous chapter we intimated that there might be a difference in MR signal between BAT and WAT on the fat-only IDEAL MR sequences. Chen *et al*. similarly found that signal intensity of BAT was lower than WAT using FSE sequences [261].

In this chapter we shall explore whether it is possible to identify BAT prospectively on MR solely on the basis of its MR characteristics, without recourse to *a priori* knowledge.

9.2 Aims

In this chapter we will evaluate the contrast between BAT and WAT on the fat-only IDEAL FSE MR sequence. We then aim to determine the possibility of identifying BAT prospectively solely on the basis of perceived differences in signal intensity.

In this chapter we will aim to identify BAT on the basis of differences in fat fraction. The identified BAT will then be compared retrospectively against the ^{18}F-FDG BAT uptake on the index PET/CT scans.

Study I: Visual identification of BAT on fat-only IDEAL MR images

9.2.1 Subjects and methods

9.2.1.1 Subject selection

The scans of the 16 adult patients (9 females, 7 males; mean age 44.2 ± 19.3 years, range 18 – 73 years) recruited in the previous chapter on the basis of having ^{18}F-FDG BAT uptake on PET/CT (162.3 ± 177.7 ml, range 3.0 – 561.5 ml) were evaluated. Seven patients (BAT06, BAT13-18) showed high volumes of ^{18}F-FDG BAT uptake on PET/CT (*i.e.* above the 85th percentile), whereas five (BAT01, 02, 05, 07, 08) were below the 50th percentile.

9.2.1.2 Scanning protocol

As detailed in the previous chapter, scanning was performed on a GE Signa HDxt 3T MR scanner (General Electric, Milwaukee, USA) using the scanning parameters summarised in the previous chapter.

9.2.1.3 Image analysis

Raw DICOM (Digital Imaging and Communications in Medicine) images of the fat-only IDEAL MR sequences were analysed offline using ImageJ.

To quantify differences in perceived signal intensity between BAT and WAT on these, the contrast to noise ratio (CNR) between ^{18}F-FDG BAT regions of interest (previously identified in chapter 4) and subcutaneous WAT (defined in chapter 8) was calculated on a slice-by-slice basis for each patient using Equation 9-1. CNR describes the relationship of signal intensity between two regions on an MR image, scaled to image noise (normally taken to be background air).

To compensate for variations in MR signal within each slice arising from RF non-uniformity or inhomogeneities in the receiver coil, a field bias map was also subtracted semi-automatically using the *A posteriori shading correction 514 v3* plugin [281] for ImageJ.

Equation 9-1: Contrast to noise formula.

$$CNR = \frac{Signal_{WAT} - Signal_{BAT}}{Background\ noise}$$

The images of selected patients were reviewed by two reviewers; rater 1 a speciality registrar in clinical radiology with approximately 5 years' experience, and rater 2 a specialty registrar in endocrinology – both with approximately 2 years' experience in BAT imaging. Rater 1 reviewed all MR scans (BAT01, 02, 05-18), while rater 2 only reviewed the MR scans for patients with high ^{18}F-FDG BAT volumes on PET/CT (BAT06, 13-18).

The raw DICOM images were reviewed on a dedicated PACS (picture archiving and communications system) workstation in optimal lighting conditions without reference to the PET/CT scans. The only permitted image manipulations were magnification, contrast enhancement and edge enhancement.

Each observer drew ROIs around areas of presumed BAT on the fat-only IDEAL images, identified on the basis of perceived lower signal intensity than adjacent WAT (henceforth referred to as 'BAT_{prosp}').

As the MR coverage was less than that of the PET/CT scans, the ^{18}F-FDG BAT volumes were recalculated based on the MR scan coverage. Volumetric images were produced from these truncated ^{18}F-FDG BAT ROIs, and both observers' prospectively identified BAT ROIs using ImageJ 3D viewer (Figure 9-1), from which volumes were calculated using the 3D Objects Counter v2.0 [282] plugin for ImageJ.

Figure 9-1: Surface-rendered image showing truncated ^{18}F-FDG BAT within the supraclavicular fossae (BAT06).

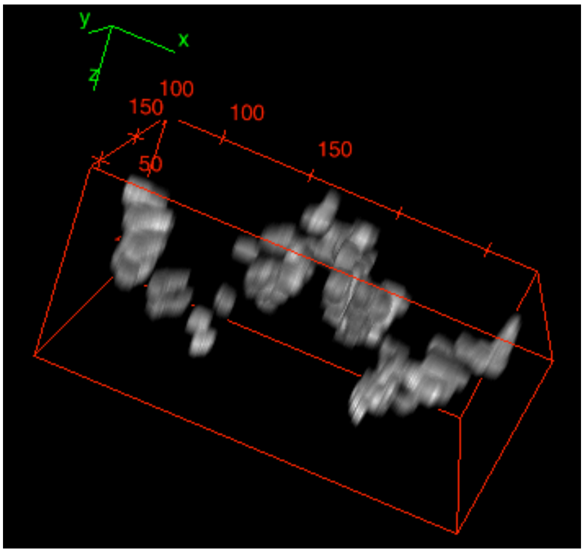

9.2.1.4 Statistical analysis

Contrast-to-noise ratio between ^{18}F-FDG BAT and WAT ROIs was analysed graphically using a box and whisker plot. The relationship between BMI and ^{18}F-FDG BAT volume, and CNR was evaluated using Spearman's correlation.

BAT$_{prosp}$ volumes were compared with those derived from truncated ^{18}F-FDG BAT ROIs using Bland-Altman plots to assess overall agreement, to determine whether the level of agreement varied according to the volume of ^{18}F-FDG BAT. The level of agreement between each rater's BAT$_{prosp}$ ROIs and ^{18}F-FDG BAT ROIs, and interobserver agreement was evaluated using intraclass correlation coefficient (ICC)[a] using an online statistical calculator[b]. ICC is a descriptive statistic used on quantitative parametric (or at least interval) data organised into groups (in this case patients). It describes how strongly values in the same group resemble each other, and can be used to assess the reproducibility of quantitative measurements made by different raters measuring the same quantity. ICC is considered superior to simple correlation as it may

---

[a] ICC of 0 - 0.2 indicates poor agreement, 0.3 - 0.4 indicates fair agreement, 0.5 – 0.6 indicates moderate agreement, 0.7 – 0.8 indicates strong agreement, and >0.8 indicates almost perfect agreement

[b] Statistics Toolbox. Department of Obstetrics and Gynaecology, the Chinese University of Hong Kong. http://department.obg.cuhk.edu.hk/researchsupport/IntraClass_correlation.asp

be adjusted for the effects of the scale of measurements to take into account differences in measurements between groups, and may be used for more than two raters [213].

The proportion of BAT$_{prosp}$ and ^{18}F-FDG BAT ROIs which colocalise were determined visually and analysed using percent pairwise agreement, and the degree of variability calculated using Cohen's or Fleiss' *kappa* as appropriate using the online calculator ReCal3 [283].

Colocalisation analysis was performed upon image stacks to determine the extent to which BAT$_{prosp}$ and ^{18}F-FDG BAT ROIs intersect using the JACoP ('Just Another Colocalisation Plugin') and CDA ('Confined Displacement Algorithm') plugins for ImageJ [218, 284], as described in chapter 6. Manders' correlation coefficients were calculated to describe the fractional overlap of BAT$_{prosp}$ and ^{18}F-FDG BAT ROIs. This yields two coefficients: 'M1' describing 'BAT$_{\mathrm{prosp}}$ ∩ ^{18}F-FDG BAT', and 'M2' describing '^{18}F-FDG BAT ∩ BAT$_{\mathrm{prosp}}$'). Pearson's correlation coefficients were also calculated for each pair of scans to quantify the overall level of agreement. To determine whether the degree of colocalisation was greater than that expected by chance, images were compared with a series of randomised images generated using a variation of the frame translation/image-shift method (as described in chapter 6).

9.2.2 Results

9.2.2.1 Differences in BAT and WAT signal intensity on fat only IDEAL sequences

We identified a variation in signal intensity between MR slices along the B_0 axis (Figure 9-2), which renders direct comparison of signal intensities on fat-only IDEAL MR images meaningless therefore. The contrast between BAT (derived from transposed ^{18}F-FDG BAT ROIs) and subcutaneous WAT, however, was unaffected by slice position (Figure 9-3).

Figure 9-2: Variation in signal intensity within BAT and WAT along the B_0 axis in a single patient (BAT13).

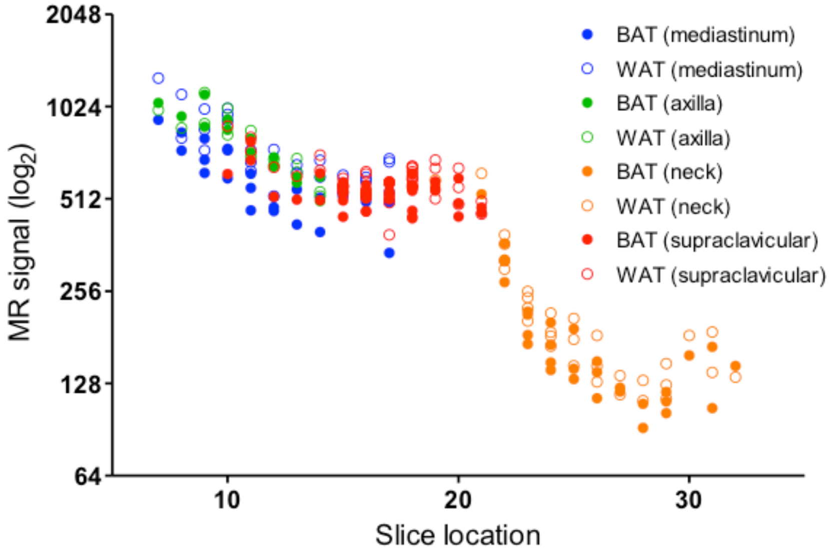

Figure 9-3: BAT:WAT signal ratio for ^{18}F-FDG BAT ROIs and matched WAT ROIs in a single patient (BAT13).

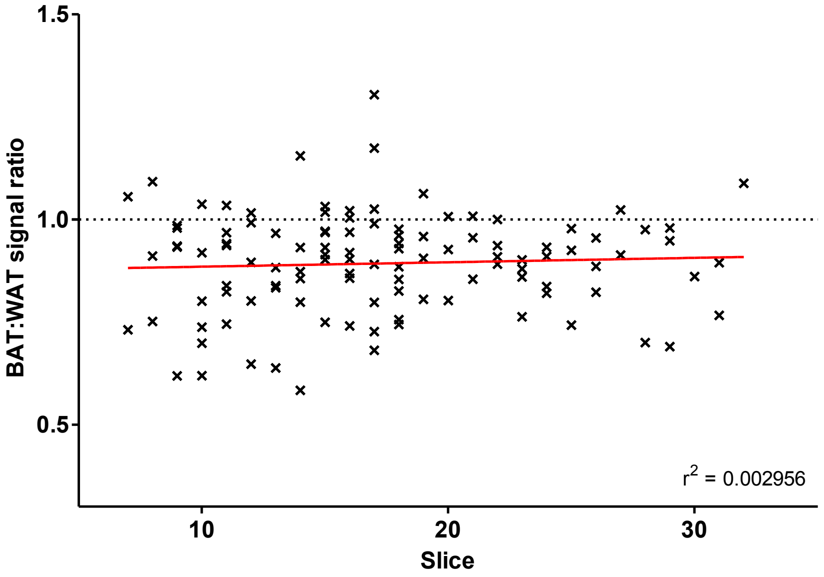

In most cases the MR signal within subcutaneous WAT was higher than within ^{18}F-FDG BAT ROIs on fat-only IDEAL sequences, with a consequent positive contrast to noise ratio (CNR). The exception was BAT07, with a mean CNR of -3.28 (Figure 9-4). This may be an aberrant result as BAT07 also had the lowest ^{18}F-FDG BAT volume (3.0 ml).

The higher the CNR, the greater the contrast between the two tissues of interest. Figure 9-4 demonstrates that higher CNRs occurred in those patients in whom scans were acquired with thicker slices of 5mm (BAT01, 02, 05-12) than at 2.5mm (BAT13-18). There is an apparent inverse correlation between CNR and ^{18}F-FDG BAT volume (r^2 = -0.397), although this was not statistically significant (p = 0.1278). This does, however, suggest that thinner slices may be associated with reduced contrast between presumed BAT and WAT on MR, likely due to increased background noise.

Figure 9-4: Box and whisker plot showing variation in contrast to noise ratio between patients.

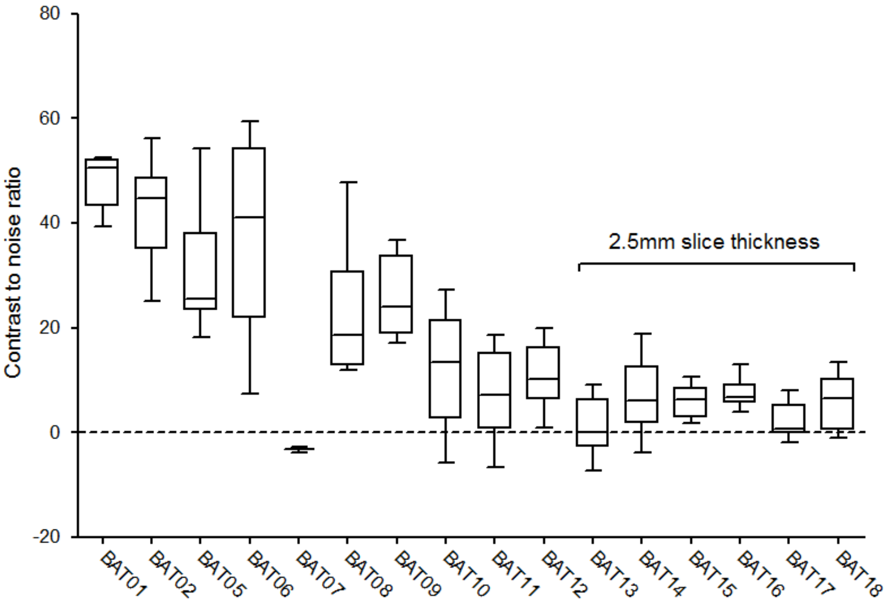

9.2.2.2 Prospective visual identification of BAT on the basis of perceived differences in signal intensity with respect to subcutaneous WAT

Due to the MR scans having a smaller coverage than the PET/CT from which the ^{18}F-FDG BAT ROIs were transposed, BAT volumes were recalculated to encompass the areas imaged by MR ('truncated ^{18}F-FDG BAT'). In addition, as co-registration of PET/CT with MR was not always successful in the axillae, axillary BAT was excluded from analysis. Consequently the truncated ^{18}F-FDG BAT volumes within the areas imaged by MR were considerably lower than the total ^{18}F-FDG BAT volume identified on PET/CT (Table 9-1).

Both reviewers tended to underestimate BAT volume compared to that derived from truncated ^{18}F-FDG BAT ROIs – particularly at higher ^{18}F-FDG BAT volumes. The mean absolute difference between BAT_{prosp} volume (for both raters) and truncated ^{18}F-FDG BAT volume was 46.5 ± 44.2 ml (Figure 9-5), although the level of bias was higher for rater 2 than for rater 1. Rater 1 overestimated BAT_{prosp} volumes in those patients with very low ^{18}F-FDG BAT volumes (BAT01, 07, 08), although it should be noted that rater 1 reviewed all MR scans, whereas rater 2 only reviewed those scans with high volumes of ^{18}F-FDG BAT (BAT06, 13-18).

Overall there was considerable inter-rater variability (ICC = 0.1154, indicating poor agreement). The BAT_{prosp} volumes generated by rater 1 showed a stronger correlation with truncated ^{18}F-FDG BAT volume (ICC = 0.3809, indicating fair agreement) than for rater 2 (ICC = 0.0181, indicating poor, indeed almost no, agreement). Although the ICC for BAT_{prosp} volumes was higher for rater 1 than rater 2, it does not necessarily follow that the BAT_{prosp} ROIs were colocalised with ^{18}F-FDG BAT on PET/CT.

Table 9-1: BAT$_{prosp}$ ROIs and volumes identified by raters.

Patient	^{18}F-FDG BAT volume (ml)	Truncated ^{18}F-FDG BAT volume (ml)	Truncated ^{18}F-FDG BAT ROIs (n)	Rater 1 BAT$_{prosp}$ ROIs (n)	Rater 1 BAT$_{prosp}$ volume (ml)	Rater 2 BAT$_{prosp}$ ROIs (n)	Rater 2 BAT$_{prosp}$ volume (ml)
BAT01	7.4	3.6	6	5	22.2	-	-
BAT02	19.1	9.2	14	10	4.5	-	-
BAT05	17.5	10.6	16	2	2.0	-	-
BAT06	324.8	102.1	73	12	22.1	39	3.3
BAT07	3.0	2.6	5	20	12.1	-	-
BAT08	24.2	5.3	7	15	17.2	-	-
BAT09	43.6	23.3	13	11	2.7	-	-
BAT10	47.9	12.8	31	12	11.5	-	-
BAT11	52.9	13.2	22	6	4.9	-	-
BAT12	45.6	20.9	34	7	1.8	-	-
BAT13	561.5	154.4	98	54	64.4	18	7.8
BAT14	312.6	107.6	152	41	16.3	12	1.9
BAT15	270.6	45.9	101	33	16.6	9	1.2
BAT16	441.4	69.4	181	14	6.4	8	1.3
BAT17	275.2	72.3	155	31	12.3	9	1.3
BAT18	149.4	67.2	125	48	24.6	10	1.7

Figure 9-5: Bland-Altman plot of BAT$_{prosp}$ and truncated ^{18}F-FDG BAT volumes for rater 1 (red) and rater 2 (blue).

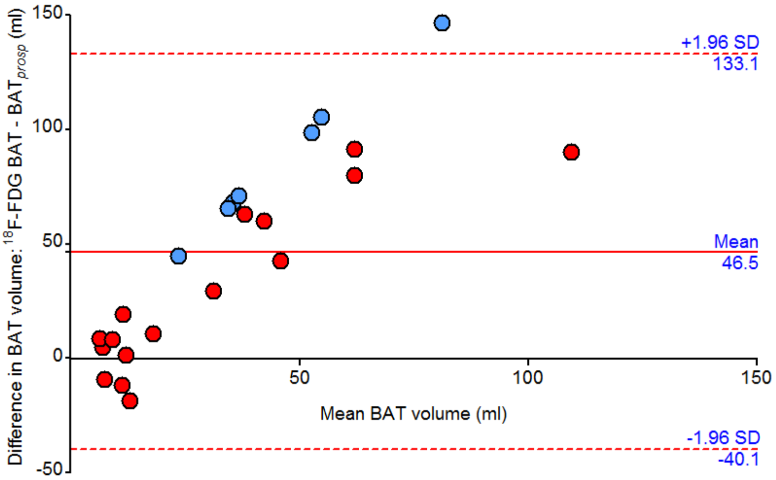

9.2.2.3 Colocalisation analysis of BAT$_{prosp}$ and ^{18}F-FDG BAT ROIs

Although the intra-class correlation between BAT$_{prosp}$ volumes truncated ^{18}F-FDG BAT volumes was higher for rater 1 than rater 2, this provides no detail about whether the individual ROIs themselves are coincident.

Visual inspection of a typical image upon which BAT$_{prosp}$ ROIs for rater 1 (coloured orange) and rater 2 (coloured red) and ^{18}F-FDG BAT ROIs (coloured yellow) have been superimposed (Figure 9-6) shows colocalisation in the mediastinum.

Figure 9-6: Colocalised BAT$_{prosp}$ and ^{18}F-FDG BAT ROIs in a single patient (BAT06).

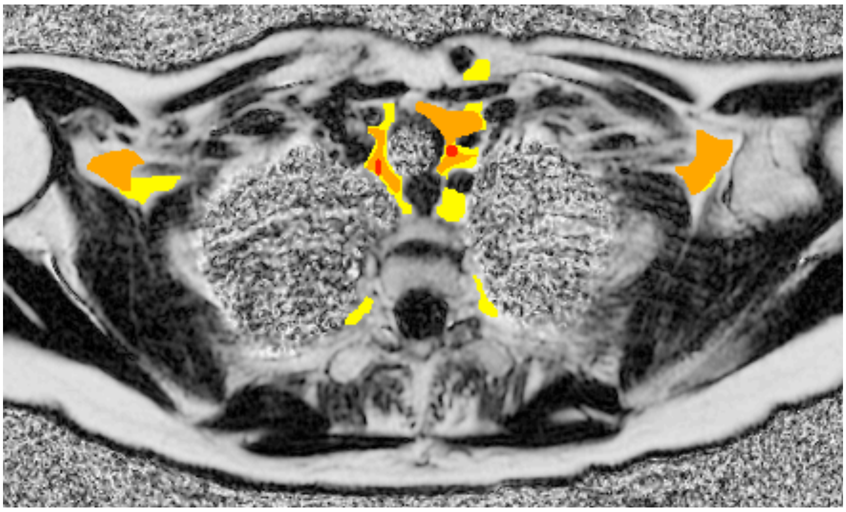

From this the proportion of colocalised ROIs is calculated (Figure 9-7). A higher proportion of BAT$_{prosp}$ ROIs coincided with ^{18}F-FDG BAT (51.6 – 100.0%) in patients with high BAT volumes on PET/CT (BAT06, 13-18), than for those with lower BAT volumes (Table 9-2).

A greater proportion of the BAT$_{prosp}$ ROIs identified by rater 1 colocalised with ^{18}F-FDG BAT ROIs than for rater 2 (Table 9-2 and Figure 9-7).

Figure 9-7: Stacked bar chart showing the proportion of colocalised BAT$_{prosp}$ and truncated ^{18}F-FDG BAT ROIs for each rater[a].

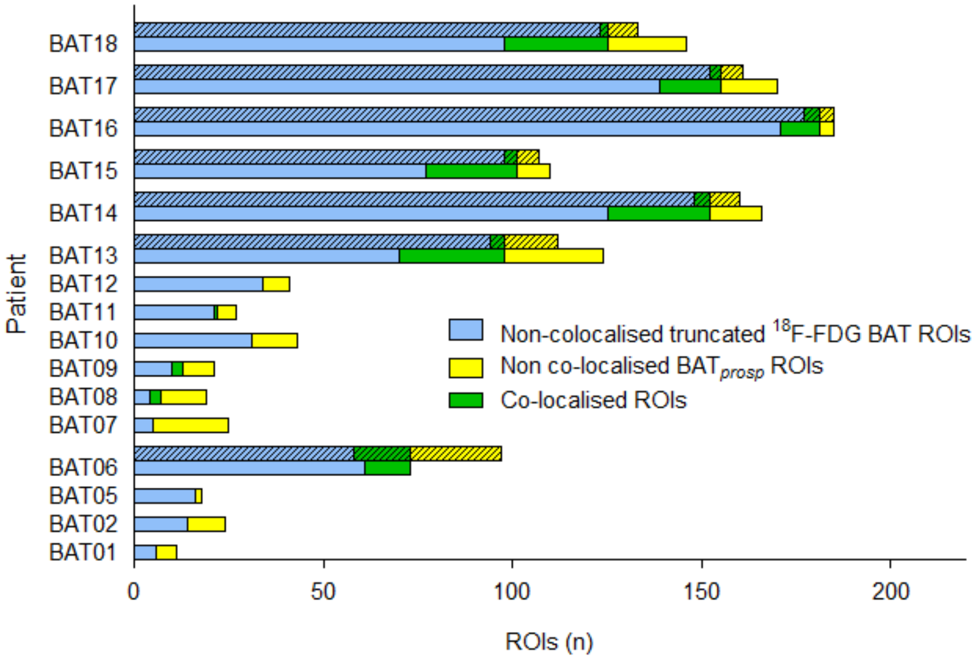

In seven cases identified by rater 1 (BAT06, 13-18), all of whom showed high BAT volumes on PET/CT, more than half of the BAT$_{prosp}$ ROIs coincided with ^{18}F-FDG BAT. Most prominent is BAT06 in whom all of the 12 BAT$_{prosp}$ ROIs identified by rater 1 coincided with ^{18}F-FDG BAT, compared with 15/39 BAT$_{prosp}$ ROIs identified by rater 2.

There was no colocalisation in six cases (BAT01, 02, 05, 07, 10 and 12), all of whom had comparatively small ^{18}F-FDG BAT volumes. All cases evaluated by rater 2 showed

---

[a] Hatched bars denote rater 2, and non-hatched bars denote rater 1

at least some coincidence between BAT$_{prosp}$ and ^{18}F-FDG BAT, although as stated previously rater 2 only evaluated the scans of patients with prominent ^{18}F-FDG BAT uptake (in whom the likelihood of colocalisation was highest).

Although a high proportion of BAT$_{prosp}$ ROIs colocalised with ^{18}F-FDG BAT for both raters, the average pairwise agreement tended to be low (Table 9-2), likely due to the small number of BAT*prosp* ROIs compared to the number of ^{18}F-FDG BAT ROIs. Consequently Cohen's κ values indicate no overall agreement between truncated ^{18}F-FDG BAT and BAT$_{prosp}$ for either rater.

Table 9-2: Coincidence statistics for BAT$_{prosp}$ and ^{18}F-FDG BAT ROIs for each rater.

Patient	Rater 1			Rater 2		
	Coincident BAT$_{prosp}$ ROIs (%)	Pairwise agreement (%)	Cohen's κ	Coincident BAT$_{prosp}$ ROIs (%)	Pairwise agreement (%)	Cohen's κ
BAT01	0.0	0.00	-0.984	-	-	-
BAT02	0.0	0.00	-0.946	-	-	-
BAT05	0.0	0.00	-0.246	-	-	-
BAT06	100.0	16.44	0.000	38.5	15.46	-0.536
BAT07	0.0	0.00	-0.471	-	-	-
BAT08	20.0	33.33	-0.127	-	-	-
BAT09	27.3	14.29	-0.734	-	-	-
BAT10	0.0	0.00	-0.673	-	-	-
BAT11	16.7	0.04	-0.427	-	-	-
BAT12	0.0	0.00	-0.395	-	-	-
BAT13	51.9	20.90	-0.550	22.2	3.57	-0.278
BAT14	65.9	16.27	-0.179	33.3	2.50	-0.105
BAT15	72.7	21.82	-0.172	33.3	2.80	-0.118
BAT16	71.4	5.41	-0.044	50.0	2.16	-0.044
BAT17	51.6	9.41	-0.189	33.3	1.86	-0.077
BAT18	56.3	19.85	-0.170	20.0	1.50	-0.127

9.2.2.4 Quantification of colocalised BAT$_{prosp}$ and ^{18}F-FDG BAT ROIs

Colocalisation coefficients were calculated for each rater's BAT$_{prosp}$ ROIs with respect to the ^{18}F-FDG BAT ROIs. As there were no coincident BAT$_{prosp}$ and ^{18}F-FDG BAT ROIs in six patients (BAT01, 02, 05, 07, 10, 12), no further colocalisation analysis was performed on these cases. Pearson's correlation coefficient, a marker of association between a pair of scans, fell within that expected by chance in two cases: BAT11 (for rater 1) and BAT18 (for rater 2). In all other cases the degree of correlation was greater than that expected by chance. There was, however, considerable variation in the Pearson's correlation coefficients between raters, with consistently higher values for rater 1 than rater 2. The values were nonetheless low with only three cases having a Pearson's correlation coefficient above 0.2 (BAT06, 13, 15).

Correlation was not significant for BAT11. The correlation was strongest for BAT06, 13 and 15 – all with large volumes of BAT on PET/CT. The degree of fractional overlap between BAT$_{prosp}$ and ^{18}F-FDG BAT (*i.e.* Manders' M1 coefficient) was higher for rater 1 in all cases (Figure 9-8).

Manders' M1 correlation coefficient was higher in patients with high ^{18}F-FDG BAT volumes (BAT06, 13-18), than for those with smaller volumes (BAT08-11). This is not altogether surprising, as the larger the ROIs, the greater the likelihood of colocalisation by chance. This is borne out by Figure 9-9, which shows a strong positive correlation between truncated ^{18}F-FDG BAT volume and the M1 coefficient for rater 1 ($r^2 = 0.84$). A weak inverse correlation between truncated ^{18}F-FDG BAT volume and M1 colocalisation correlation coefficient was identified for rater 2 although this was not statistically significant ($r^2 = -0.32$, $p = 0.50$).

In light of the comparatively high M1 and low M2 colocalisation coefficients, the low Pearson's coefficients are likely due to the disparity between the high number of ^{18}F-FDG BAT ROIs, and the low number of BAT$_{prosp}$ ROIs.

Figure 9-8: Pearson's colocalisation coefficients (red bar) with randomised values (grey bars with 95% CI) of BAT$_{prosp}$ ROIs against ^{18}F-FDG BAT ROIs for each rater.

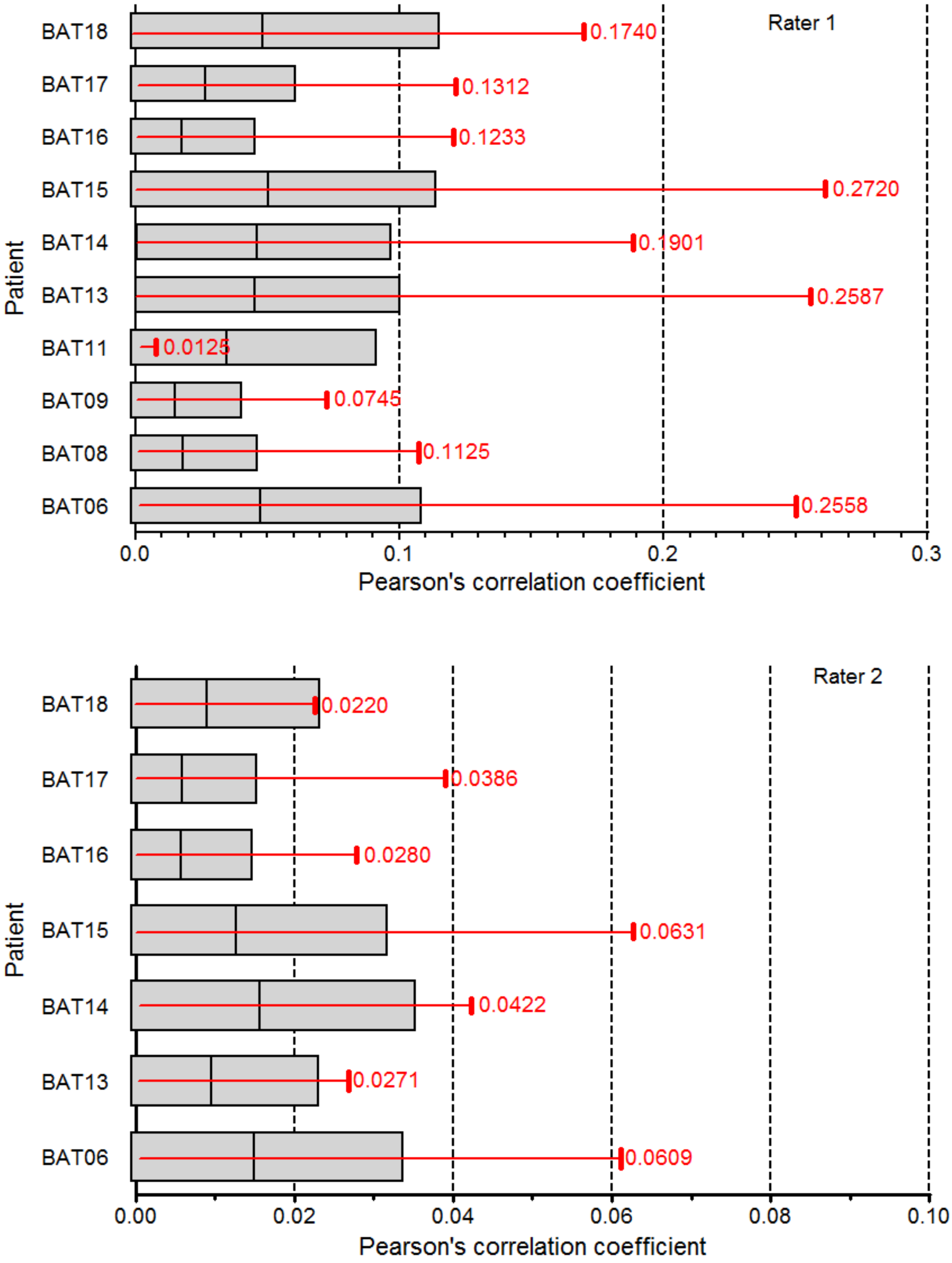

Table 9-3: Manders' colocalisation coefficients for each rater against ^{18}F-FDG BAT.

	Rater 1		Rater 2	
Patient	**M1**[a]	**M2**[b]	**M1**	**M2**
BAT06	0.552	0.119	0.245	0.015
BAT08	0.060	0.202	-	-
BAT09	0.101	0.055	-	-
BAT11	0.020	0.007	-	-
BAT13	0.399	0.170	0.124	0.006
BAT14	0.493	0.074	0.331	0.005
BAT15	0.455	0.163	0.389	0.01
BAT16	0.410	0.037	0.211	0.003
BAT17	0.321	0.054	0.287	0.005
BAT18	0.290	0.106	0.141	0.003

Figure 9-9: Scatterplot of ^{18}F-FDG BAT volume against M1 colocalisation coefficients for rater 1 (red) and rater 2 (blue).

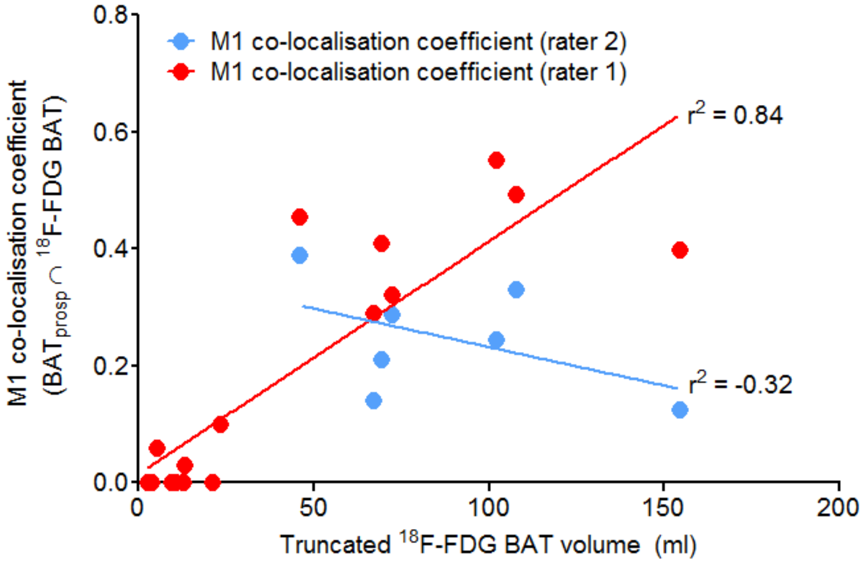

---

[a] Fraction of BAT$_{prosp}$ ROIs colocalising with truncated ^{18}F-FDG BAT ROIs (BAT$_{prosp}$ ∩ ^{18}F-FDG BAT)

[b] ^{18}F-FDG BAT ∩ BAT$_{prosp}$

9.2.2.5 Inter-rater variability

On the preceding pages we described considerable variation between raters 1 and 2 in terms of the number of BAT_{prosp} ROIs, and the proportion which correctly colocalise with ^{18}F-FDG BAT.

The proportion of colocalised BAT_{prosp} ROIs across both raters, described by the pairwise agreement (Table 9-4), was highest for BAT13 at 24.1%, but considerably lower for the rest. Consequently the Cohen's κ measure of inter-rater agreement was low (indeed negative) in all cases, indicating no overall agreement.

Although the proportion of colocalised ROIs between raters was low, the degree to which rater 2's BAT_{prosp} ROIs overlapped those of rater 1 (*i.e.* 'M2 correlation coefficient') was quite high in some patients, *e.g.* 58.6% of BAT_{prosp} voxels identified by rater 2 for BAT13 colocalised with those defined by rater 1, and over 40% of BAT_{prosp} voxels for BAT15 and 17 colocalised with those of rater 1.

This is in contrast to the low M1 values, in which no more than 7% of rater 1's BAT_{prosp} voxels colocalised with those of rater 2. This likely reflects differences in the number of ROIs as, with the exception of BAT06, rater 1 tended to identify more ROIs. Also, as is evident on Figure 9-6, the BAT_{prosp} ROIs identified by rater 1 tended to be larger (101.3 ± 62.8 voxels) than for rater 2 (29.9 ± 15.4 voxels).

Table 9-4: Inter-rater variability statistics for raters 1 and 2.

Patient	Colocalised ROIs (n)	Pairwise agreement (%)	Cohen's κ	Pearson's colocalisation coefficient	M1[a]	M2[b]
BAT06	4	8.5	-0.383	0.0493	0.026	0.092
BAT13	14	24.1	-0.143	0.2034	0.070	0.586
BAT14	2	3.9	-0.454	0.0484	0.016	0.147
BAT15	5	13.5	-0.233	0.1095	0.029	0.403
BAT16	0	-	-	-	-	-
BAT17	4	0.1	-0.306	0.1532	0.050	0.464
BAT18	2	3.7	-0.245	0.0724	0.019	0.276

9.3 Identification of BAT using MR and ^{18}F-FDG PET/CT in an human adult with histological and immunohistochemical confirmation [188]

Thus far, we have relied on PET/CT as the standard against which MR has been compared.

This is an opportune point to address the issue of whether ^{18}F-FDG BAT uptake genuinely represents BAT, by summarising a case report for BAT13, an exemplar with the greatest volume of ^{18}F-FDG BAT (561.5 ml) in our study, or for that matter, in the wider BAT literature.

'BAT13', a 25-year old Caucasian female was diagnosed with hyperparathyroidism-jaw tumour (HPT-JT) syndrome on the basis of biochemical and radiological findings.

PET/CT (performed using the parameters summarised chapter 3) showed a 0.5 mm right inferior parathyroid adenoma, and a giant cell granuloma in the right mandible, as well as extensive areas of avid ^{18}F-FDG uptake within the suprasternal, supraclavicular and mediastinal fat.

---

[a] Fraction of rater 1's BAT*prosp* ROIs intersecting with those of rater 2 ('rater 1 ∩ rater 2')

[b] Rater 2 BAT*prosp* ∩ rater 1 BAT*prosp*

An IDEAL MR sequence was also performed (using the parameters summarised in chapter 8) which showed a distinct area of low signal intensity within the suprasternal notch, corresponding to the avid ^{18}F-FDG uptake on PET/CT.

The mandibular lesion was enucleated, which histopathological analysis showed to be a giant cell granuloma. Genetic analysis confirmed the diagnosis of HPT-JT, which showed her to have a heterozygous mutation for a T to C nucleotide substitution in exon 2 of *CDC73* (c.191T>C), also called the *HRPT2* gene, which encodes for parafibromin [285].

During surgery, a sample of adipose tissue corresponding to an area of avid ^{18}F-FDG uptake on PET/CT consistent with BAT, was also excised from the suprasternal region (shown by the white arrows in Figure 9-10). Staining[a] with haematoxylin and eosin (H&E) demonstrated small multilocular adipocytes with multiple small lipid vacuoles characteristic of brown adipocytes (Figure 9-11a, denoted by the white arrow), in contrast to the large unilocular white adipocytes. Immunohistochemical staining with Vectastain Elite ABC Kit (Vector Laboratories, PK-6101) and rabbit anti-UCP1 (1:500, Sigma U6382) confirmed BAT due to the presence of abundant mitochondria containing UCP1 (Figure 9-11b).

In publishing this case our group was the first to show BAT in a live adult human on both PET/CT and MR with immunohistochemical confirmation, [188]. In addition, this case formed part of an MD thesis [124].

---

[a] Histopathological and immunohistochemical analysis performed by Dr Yen C. Yeo, Consultant Histopathologist at University Hospitals Coventry and Warwickshire NHS Trust

Figure 9-10: Fused (a) ^{18}F-FDG PET/CT and (b) fat-only IDEAL MR images of the upper thorax.

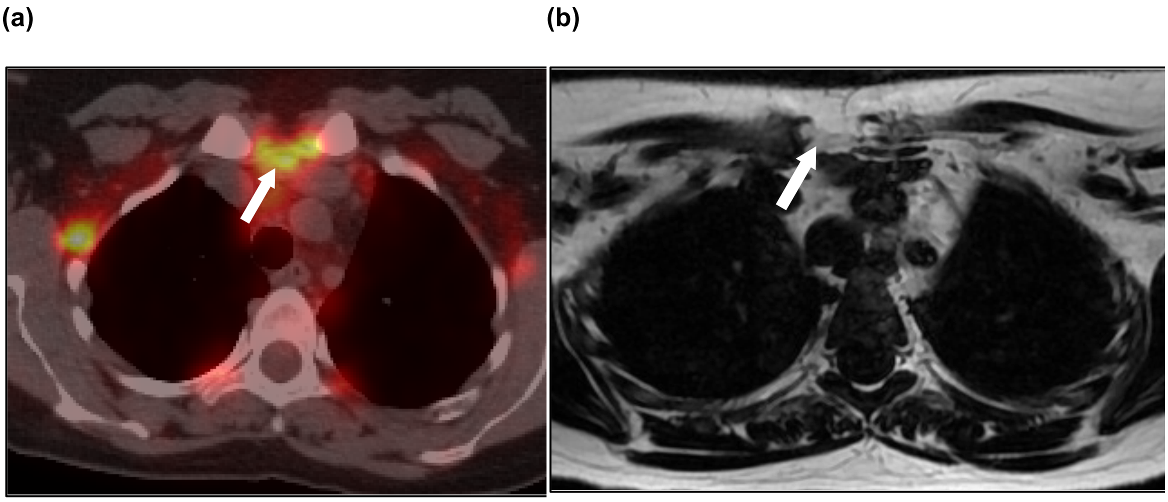

Figure 9-11: Histopathological specimens from the suprasternal adipose tissue stained with (a) H&E and (b) UCP1 confirming BAT.

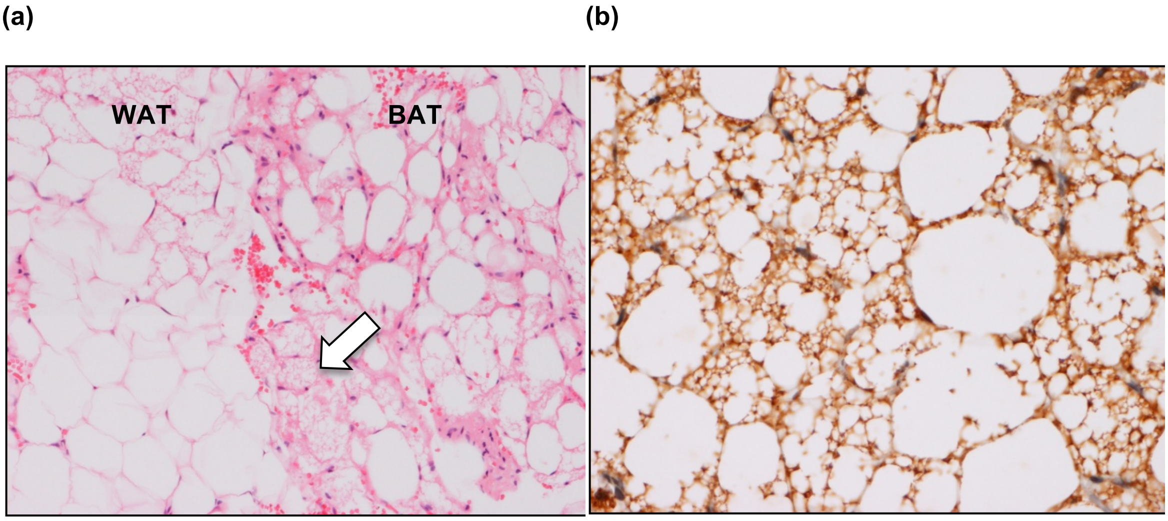

9.4 Study II: prospective identification of BAT using fat fraction images

In the previous chapter we demonstrated differences in fat fraction between BAT and WAT both *ex vivo* and *in situ* for rats. We showed the difference to be much less in adult humans. In this study we aim to identify an optimum threshold for separating BAT from WAT using fat fraction images in the hope that regions of BAT can be prospectively identified.

9.4.1 Subjects and methods

9.4.1.1 Subject selection

Four male Wistar rats (mean mass 300g, age 6-8 weeks) reared on an *ad libitum* diet were sacrificed and underwent MR scanning as described in chapter 8.

In addition, 16 adult humans with evidence of ^{18}F-FDG BAT on PET/CT also underwent IDEAL MR as previously described in chapter 8.

9.4.1.2 Image analysis

MR images were post-processed offline using ImageJ to produce fat fraction maps. Fat fraction values of constituent voxels within ^{18}F-FDG BAT and subcutaneous WAT ROIs defined previously were measured using the 'individual pixel calculation in ROI' macro for ImageJ. For the human subjects, a fat mask was produced with a lower threshold set heuristically at 50% fat fraction to exclude areas which were not predominantly fat.

9.4.1.3 Statistical analysis

Receiver operator characteristic analyses (ROC) were performed to determine the optimal thresholds for classifying BAT [286]. The ROC curve plots true positivity rate (sensitivity) against false positive rate (100-specificitiy) for different cut-off points. The area under the curve (AUC), a measure of how well a parameter distinguishes between two groups, and the optimal threshold for discriminating between BAT and WAT was chosen using Youden's J statistic (Equation 9-2) [287], which may be used in ROC analysis to identify the point on the ROC curve, furthest above the line of unity (*i.e.* the line of no-discrimination) [288].

Equation 9-2: Youden's J statistic for calculating the optimal cut-off point for ROC analysis.

$$J = Sensitivity + Specificity - 1$$

Regions of presumed BAT were prospectively identified (BAT$_{prosp}$) by segmenting the fat fraction images according to these thresholds, and an edge erode algorithm applied to remove tissue interfaces.

In the adult human sample the accuracy of the BAT$_{prosp}$ ROIs was tested using colocalisation analysis against ^{18}F-FDG BAT ROIs derived from co-registered PET/CT. Volumes derived from the BAT$_{prosp}$ ROIs were also compared to truncated ^{18}F-FDG BAT using Bland-Altman plots and intraclass correlation coefficients.

9.4.2 Results

9.4.2.1 ROC analysis of dissected interscapular BAT in rats

Receiver operator characteristic (ROC) analysis of the voxels within the *ex vivo* WAT and interscapular BAT specimens showed excellent tissue separation (Figure 9-12), with an AUC of 0.928.

Figure 9-12: ROC curve for excised murine interscapular BAT samples.

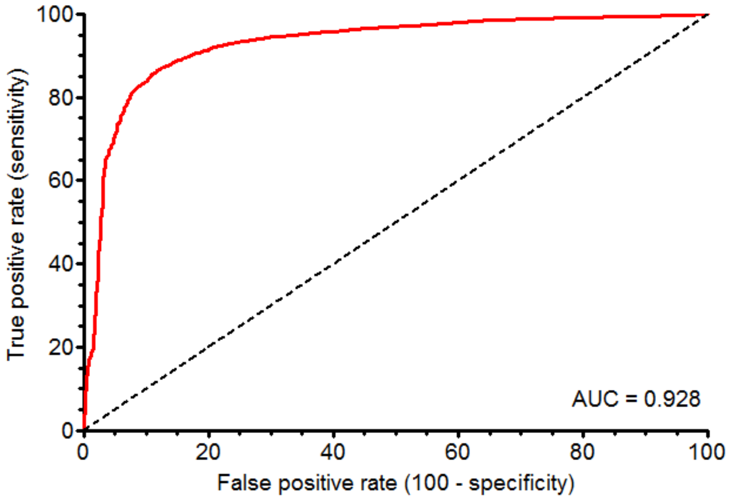

Adopting an upper threshold of 75% fat fraction and lower threshold of 40% correctly classified BAT 99.6% of the time with a specificity of 84.7%. Applying these thresholds to the fat fraction image of excised tissue BAT and WAT specimens (Figure 9-13) successfully segmented BAT, shown by the user-defined red ROIs. Following edge erosion, the BAT_{prosp} ROIs become much more defined (Figure 9-14). The optimal cut-off, as defined by Youden's J statistic was a fat fraction of 73.6%, with a sensitivity of 86.7% and specificity of 88.1%.

Figure 9-13: Fat fraction images of (from left to right) *ex vivo* interscapular BAT, omental WAT and omental WAT (thresholded at 40-75%) from rats kept at (a) 4ºC and (b) 30ºC.

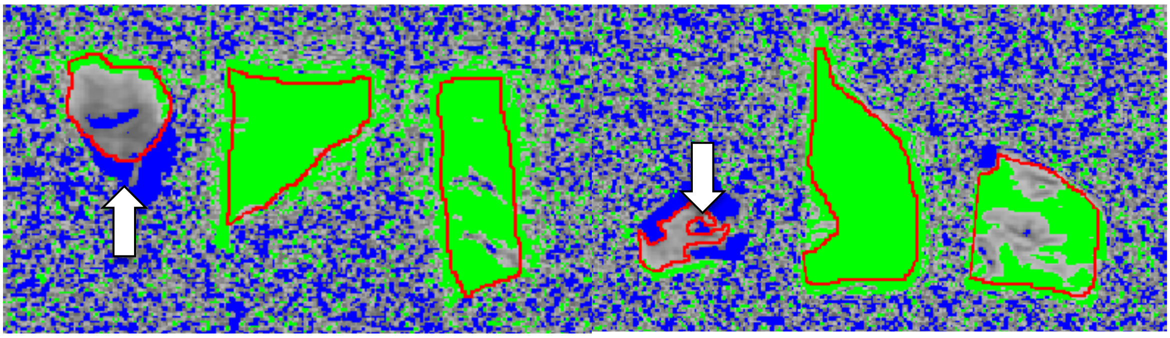

Figure 9-14: Fat fraction images following edge erosion of the samples in Figure 9-13

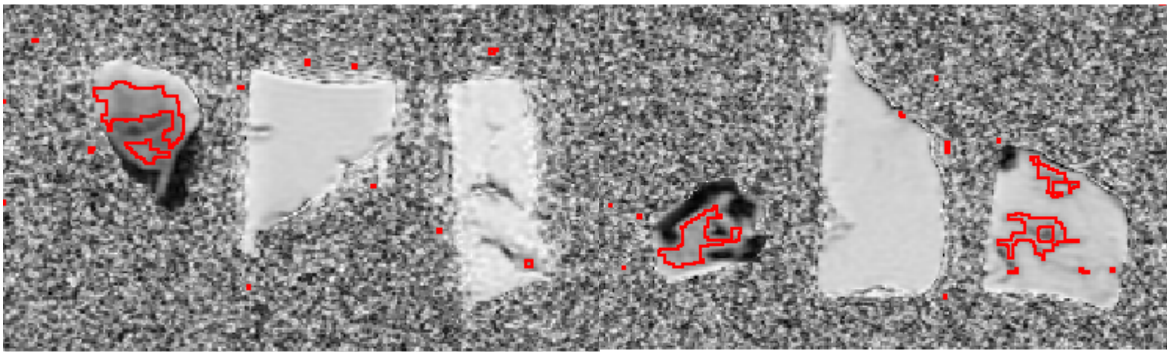

9.4.2.2 ROC analysis of *in situ* interscapular BAT in rats

For the identification of *in situ* BAT high AUCs of 0.997 (95% CI 0.994 – 1.000, p <0.0001) for the rat housed at 30ºC, and 0.998 (95% CI 0.996 – 1.001) for the rat housed *ante mortem* at 4ºC were identified, indicating excellent separation between interscapular BAT and subcutaneous WAT (Figure 9-15). An upper threshold set at 70% fat fraction and a lower threshold of 50% fat fraction correctly classified BAT with a sensitivity of 100% and specificity of 98.73%. Applying these thresholds to the fat fraction images of the rat housed at 30ºC produced excellent segmentation of the interscapular fat pad (white arrow in Figure 9-16), while excluding subcutaneous WAT (yellow arrow). The mask produced following thresholding (Figure 9-16b) includes interfaces between adipose tissue and muscle, which are effectively removed following application of the edge erode algorithm (Figure 9-16c). Youden's index identified the optimal cut-off point to discriminate BAT and WAT in the rat housed at 30ºC to be 75.8% fat fraction (sensitivity 99.3%, specificity 94.9%), and 57.8% (sensitivity 99.4%, specificity 96.7%) for the rat housed at 4ºC.

Figure 9-15: ROC curve for *in situ* interscapular BAT for the rat housed at 30ºC.

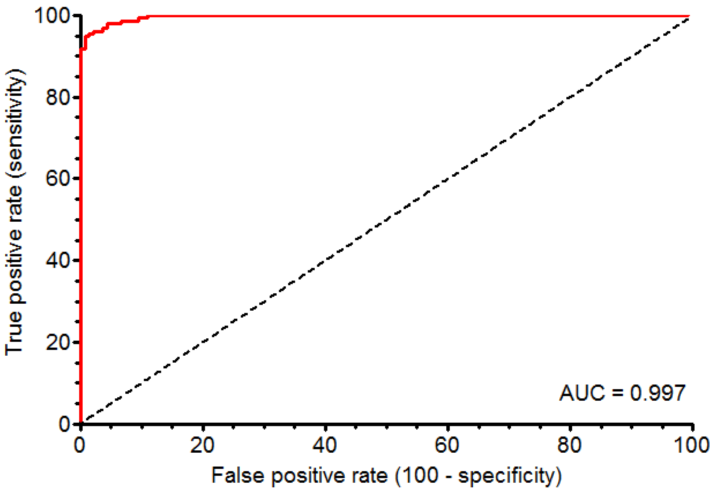

Figure 9-16: (a) Axial fat fraction images through the upper thorax of the rat housed at 30°C (thresholded at 50-70% fat fraction); (b) mask and (c) following edge erosion.

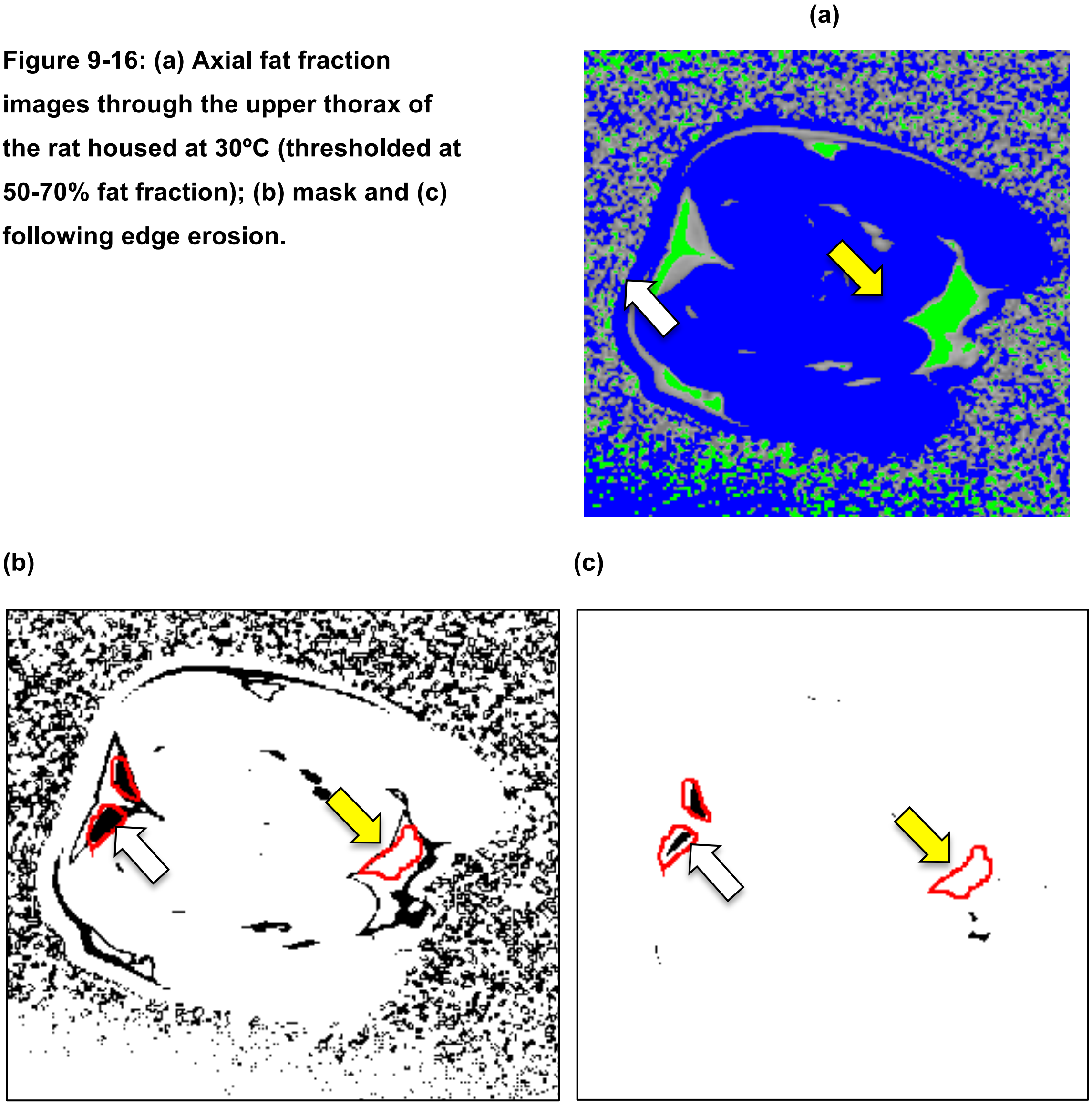

9.4.2.3 ROC analysis of *in situ* BAT in adult humans

ROC analysis showed marked variation in AUC across human adults (Table 9-5 and Figure 9-17).

Fat fraction was most effective in distinguishing between BAT and WAT for ‘BAT06’ in whom the high AUC of 0.924 indicates high discriminatory power, and the optimal cut-off value of 80% fat fraction detected BAT with a sensitivity of 84.1% and specificity of 88.8%. Similar levels of sensitivity and specificity were also obtained for ‘BAT02’ and ‘BAT05’ in whom the optimal cut-off values to differentiate between BAT and WAT were comparable at 80.1% and 81.0% respectively. A high AUC

(0.838) was also seen for ’BAT08’, with high sensitivity and specificity, although the optimal cut-off value was markedly lower at 68.1%.

Table 9-5: Receiver operator statistics for BAT and WAT discrimination within ^{18}F-FDG BAT positive human adults (n=16).

Patient	AUC for voxels (95% CI)	*J statistic*	Optimal cut-off (% fat fraction)	*Sensitivity* | *Specificity*
BAT01	0.678 (0.651 – 0.705)	0.372	81.0	0.547 | 0.825
BAT02	0.842 (0.832 – 0.853)	0.594	80.1	0.783 | 0.812
BAT05	0.899 (0.888 – 0.909)	0.830	81.0	0.844 | 0.986
BAT06	0.924 (0.921 – 0.926)	0.729	80.0	0.841 | 0.888
BAT07	0.248 (0.226 – 0.271)	0.208	71.8	0.300 | 0.908
BAT08	0.838 (0.813 – 0.863)	0.567	68.1	0.752 | 0.811
BAT09	0.599 (0.586 – 0.611)	0.223	74.8	0.387 | 0.836
BAT10	0.560 (0.545 – 0.575)	0.280	78.3	0.349 | 0.927
BAT11	0.662 (0.649 – 0.676)	0.432	77.9	0.489 | 0.944
BAT12	0.578 (0.568 - 0.588)	0.238	73.2	0.332 | 0.906
BAT13	0.500 (0.496 - 0.504)	0.218	78.3	0.264 | 0.955
BAT14	0.533 (0.530 – 0.537)	0.2084	79.2	0.286 | 0.923
BAT15	0.762 (0.757 – 0.765)	0.391	74.9	0.775 | 0.616
BAT16	0.710 (0.706 – 0.714)	0.278	68.8	0.559 | 0.708
BAT17	0.557 (0.553 – 0.561)	0.201	85.3	0.348 | 0.853
BAT18	0.577 (0.572 – 0.581)	0.208	71.2	0.300 | 0.908

Fat fraction was only moderately effective in discriminating BAT and WAT in four patients (BAT01, 11, 15, 16), of whom two had large BAT deposits. In eight patients, however, ROC analysis showed fat fraction to be a poor means of discriminating between BAT and WAT (BAT07, 09, 10, 12-14, 17, 18). The AUC was lowest for ‘BAT07’ (0.248) in whom the subcutaneous adipose tissue layer was very thin, rendering the WAT ROIs susceptible to the effects of volume averaging.

Somewhat surprisingly, ROC analysis showed fat fraction to be less effective in discriminating between BAT and WAT in many patients with large ^{18}F-FDG BAT deposits on PET/CT (BAT13, 14, 17, 18), and that of the four cases with high AUC values (BAT02, 05, 06 and 08) three had small BAT volumes.

The patients with the highest AUCs had an optimal cut-off of 80.0 – 81.0% fat fraction, but there was considerable variation across the sample. Even allowing for the low AUC, the sensitivity is unacceptably low in many cases, with nine patients having a sensitivity below 50% (BAT07, 09-14, 17, 18) of whom four had a sensitivity below 30%. Therefore, although it is possible to identify a cut-off for some cases, it is not possible to identify a single universal cut-off point to differentiate BAT and WAT in all adult humans.

Figure 9-17: Typical ROC curves for BAT and WAT discrimination in human adults, showing examples of good (a), moderate (b) and poor (c) BAT discrimination.

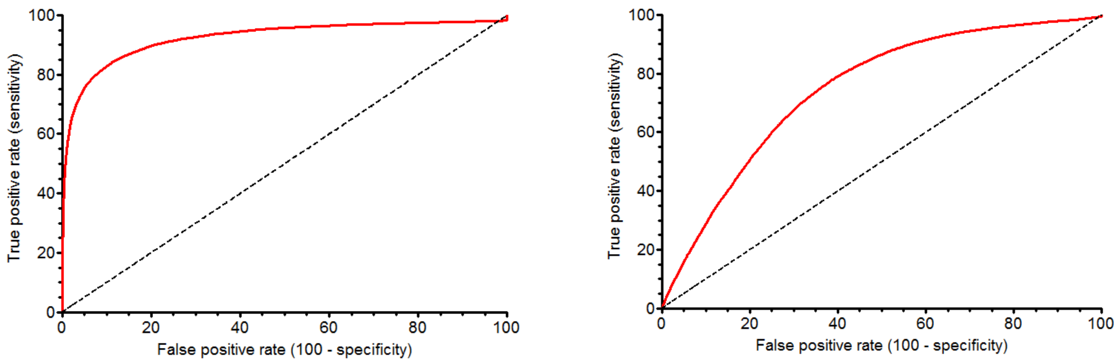

(a) BAT06 (AUC = 0.924)

(b) BAT15 (AUC = 0.762)

(c) BAT17 (AUC = 0.557)

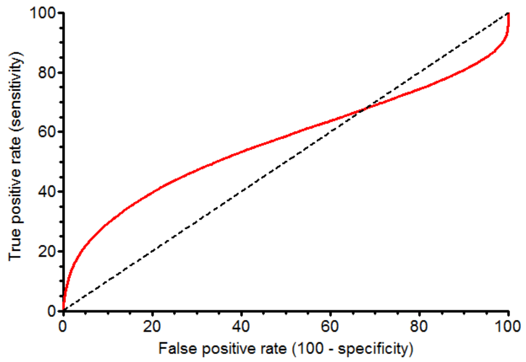

9.4.2.4 Prospective identification of BAT based on heuristic fat fraction thresholding

Fat fraction images were thresholded with a lower limit set at 50% to exclude non-fat tissues. The upper limits were defined for each patient separately according to the J statistic arising from ROC analysis (Table 9-5) to exclude WAT.

Figure 9-18 shows a typical image for BAT06 in which thresholded BAT$_{prosp}$ (green) and ^{18}F-FDG BAT (red) voxels are merged, with areas of colocalisation shown as yellow. Unlike the technique of visual identification which produced discrete ROIs, this heuristic technique produced less defined ROIs which made ROI-based analysis impractical, therefore voxel-based analysis was performed.

Figure 9-18: Merged colocalised ^{18}F-FDG BAT and edge-eroded BAT$_{prosp}$ ROIs (BAT06).

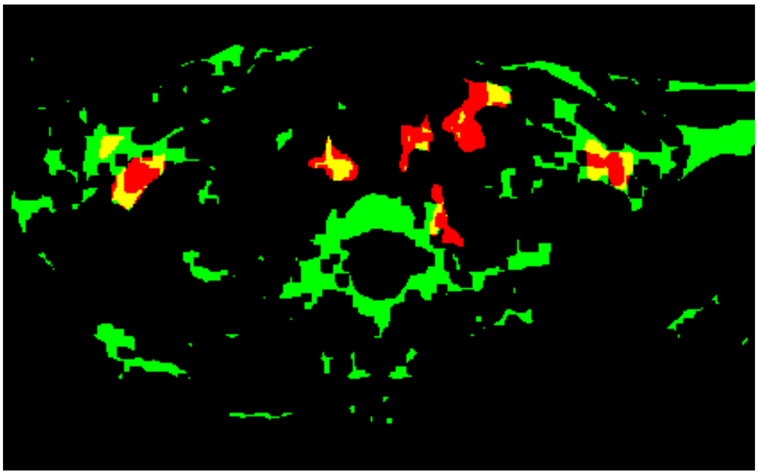

Colocalisation analysis showed many of the ^{18}F-FDG BAT ROIs intersected with BAT$_{prosp}$ ROIs, most notably BAT02, 05, 07 and 15 (Table 9-6). A higher degree of colocalisation occurred in three patients (BAT02, 05, 06), although the Pearson's correlation coefficients and Manders' overlap coefficients were typically low indicating low levels of colocalisation. In most cases the degree to which the BAT$_{prosp}$ ROIs colocalised with the ^{18}F-FDG BAT ROIs derived from PET/CT were no greater than expected by chance (BAT01, 02, 08-13, 17, 18).

Furthermore this technique tended to underestimate BAT volume in patients with large ^{18}F-FDG BAT volumes on PET/CT (Figure 9-19).

Table 9-6: Colocalisation statistics for BAT$_{prosp}$ and ^{18}F-FDG BAT ROIs (following edge erosion).

Patient	BAT$_{prosp}$ volume (ml)	Intersecting ROIs	Pearson's colocalisation coefficient; R (d=0)	R (d = rand)[a]	95% CI	Sig	M1[b]	M2[c]
BAT01	323.21	2/6	0.005	0.003	-0.001 | 0.012	No	0.093	0.000
BAT02	306.81	11/14	0.021	0.012	0.000 | 0.029	No	0.190	0.002
BAT05	570.97	12/16	0.024	0.005	-0.002 | 0.013	Yes	0.290	0.002
BAT06	609.33	3/7	0.119	0.036	0.018 | 0.054	Yes	0.311	0.047
BAT07	61.58	4/5	0.004	0.010	-0.001 | 0.005	Yes	0.038	0.000
BAT08	26.44	0/7	0	0	0	No	0	0
BAT09	108.18	6/13	0.010	0.012	-0.001| 0.037	No	0.037	0.004
BAT10	175.53	7/31	0.006	0.034	-0.000 | 0.011	No	0.045	0.001
BAT11	289.95	11/22	0.013	0.006	-0.001 | 0.017	No	0.214	0.001
BAT12	56.335	8/34	0.016	0.007	0.000 | 0.017	No	0.042	0.007
BAT13	235.00	23/98	0.005	0.01	0.002 | 0.227	No	0.023	0.005
BAT14	66.71	31/152	0.004	0.022	0.006 | 0.050	Yes	0.013	0.010
BAT15	28.82	59/101	0.055	0.013	0.002 | 0.026	Yes	0.067	0.051
BAT16	18.28	65/181	0.053	0.004	-0.002 | 0.015	Yes	0.042	0.075
BAT17	401.23	65/155	0.014	0.014	0.007 | 0.022	No	0.095	0.008
BAT18	9.72	11/125	0.005	0.002	-0.001 | 0.010	No	0.004	0.013

---

[a] Mean Pearson's correlation coefficient for the randomised images.

[b] M1 = proportion of ^{18}F-FDG BAT ROIs overlapping BAT$_{prosp}$ ROIs.

[c] M2 = proportion of BAT$_{prosp}$ ROIs overlapping ^{18}F-FDG BAT ROIs.

Figure 9-19: Bland-Altman plot of BAT$_{prosp}$ and ^{18}F-FDG BAT ROIs.

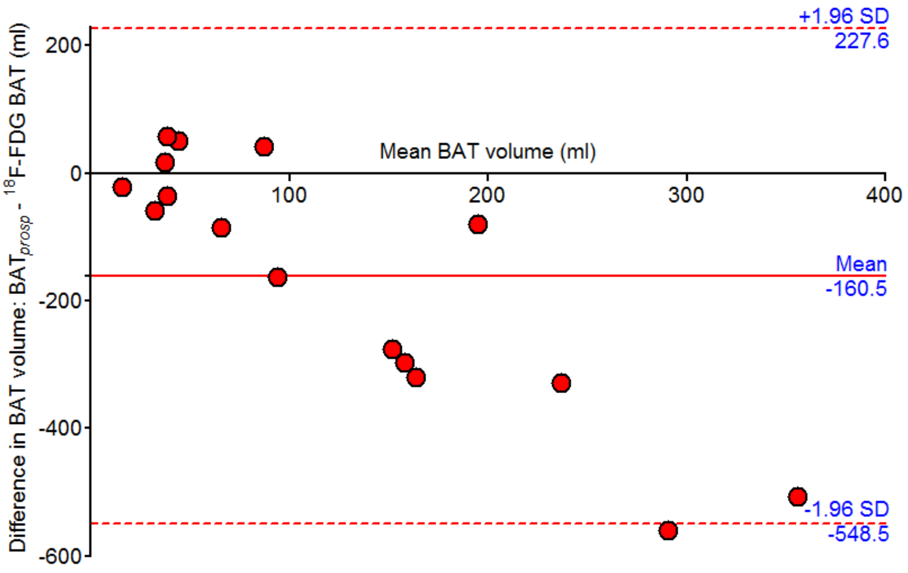

9.5 Summary

In this chapter we evaluated two methods for identifying BAT prospectively on MR: visual inspection based on perceived differences in signal intensity on fat-only IDEAL, and semi-automatic discrimination based on differences in fat fraction.

Visual inspection was moderately successful in identifying BAT in some cases, particularly in the hands of a radiologist. This technique did tend to underestimate volume in patients with larger volumes of ^{18}F-FDG BAT on PET/CT however.

Although we discovered significant differences in fat fraction between BAT and WAT in adult humans *in vivo* (chapter 8), it was not possible to define a single cut-off point to differentiate these tissues. Therefore we used receiver operator curve analysis to heuristically identify optimum thresholds for each patient. This technique was moderately effective in a small number of patients but produced inconsistent results, with fairly poor levels of colocalisation against ^{18}F-FDG BAT uptake.

Both techniques underestimated BAT volume – particularly in those patients with higher ^{18}F-FDG BAT volumes. BAT is dynamic, therefore it is possible that it involuted in the interval between the PET/CT sand MR scans. Conversely, in cases where these techniques appear to have overestimated BAT volume, it is possible that this represented hitherto unidentified BAT (particularly given that BAT on the PET/CT scans was not maximally stimulated). This is considered unlikely as many BAT_{prosp} foci lay within the dorsal subcutaneous adipose or tissue layer which is not known to contain BAT.

Chapter 10: Discussion

10.1 Summary of the thesis

Following the serendipitous discovery of ^{18}F-FDG BAT on PET/CT scans in adult humans, coupled with insights into its effects on body weight and metabolism, interest in BAT research in humans has piqued [2, 289]. Prior to this, BAT was considered to be largely absent in adult humans, or at the very most of little if any physiological importance [290]. The current view is that BAT persists into adulthood in the majority of humans [187], in whom it continues to play a significant metabolic role, and its absence or dysfunction has been linked to obesity [23, 42, 291]. Indeed, the potential importance of BAT is such, that its reclassification as a new human organ has been advocated [24, 189, 292].

In chapter 1 we summarised the physiological role of BAT, and highlighted its importance in human metabolism research as a potential means of managing obesity. Any novel pharmacological interventions which seek to regulate human obesity through the manipulation of BAT, would require the development of a reliable biomarker. The ultimate aim of this thesis is to evaluate the reliability of ^{18}F-FDG PET/CT and MR imaging as imaging biomarkers for *in situ* BAT in human adults.

In chapter 2 we described how ^{18}F-FDG PET/CT has been used to demonstrate metabolically active BAT in humans. To date, most studies evaluating the prevalence of BAT in humans have involved retrospective analyses of PET/CT scans performed within clinical settings, typically for the diagnosis, staging and monitoring of oncological disease. Despite PET/CT scanning protocols being developed to suppress physiological ^{18}F-FDG uptake within BAT to reduce the risk of false positive diagnoses, PET/CT remains the standard against which other imaging modalities are compared in the field of BAT research. Due to the lack of standardisation in these retrospective studies, there is considerable variation in ^{18}F-FDG BAT prevalence throughout the literature, and there is currently no consensus regarding BAT prevalence within human adults [189].

In chapters 3 and 4 we performed a large retrospective study of ^{18}F-FDG BAT prevalence on 3,295 consecutive PET/CT scans in 2,685 individuals at a single institution. We found that, for a single scan, the point prevalence of ^{18}F-FDG BAT is in the order of 5%. This is undoubtedly an underestimate of the true prevalence, as we found that the likelihood of an individual demonstrating ^{18}F-FDG BAT increases the more PET/CT scans an individual undergoes – plateauing at approximately 30%. We evaluated the impact of different demographic and meteorological factors upon the prevalence, volume and level of activity of ^{18}F-FDG BAT and found that ^{18}F-FDG BAT is highly variable both between and within individuals.

In chapters 5 and 6 we explored the distribution patterns of ^{18}F-FDG BAT in a subgroup of 15 patients who, having undergone multiple PET/CT examinations, showed evidence of ^{18}F-FDG BAT on multiple scans. We found that that ^{18}F-FDG BAT uptake not only occurs within the same anatomical compartments across serial scans within an individual, but often occurred within fixed depots. From this we proposed that, each individuals 'index scan' (*i.e.* the scan with the greatest volume of ^{18}F-FDG BAT) was a reliable representation of the pattern of ^{18}F-FDG BAT uptake on their other positive scans, and could therefore be used as a standard against which other imaging modalities could be compared.

In chapter 7 we described how MR imaging has hitherto been used to discriminate BAT and WAT based on histological differences, most notably fat fraction and T2* relaxation time. Although shown to be an effective means of tissue discrimination in in murine studies and in human children, results in human adults have been less consistent. Therefore for chapter 8, we performed IDEAL MR scans in 16 adult humans with ^{18}F-

FDG BAT uptake on PET/CT. BAT (identified *a priori* by co-registering with PET/CT) had a lower signal intensity on IDEAL MR than subcutaneous WAT, and that fat fraction within BAT was significantly lower.

In chapter 9 we sought to exploit these differences to identify BAT prospectively. Identifying BAT on the basis of visually perceived differences in signal intensity on raw DICOM images was reasonably effective in patients with large ^{18}F-FDG BAT volumes, but tended to underestimate BAT volume. Although there was considerable inter-rater variability, this technique proved fairly effective in a single patient with copious quantities of ^{18}F-FDG BAT, whom we singled out in a case report [188].

10.2 Determinants of BAT prevalence on ^{18}F-FDG PET/CT

This study, a moderately large retrospective study of BAT prevalence on 3,295 consecutive PET/CT scans at a single centre, showed evidence of BAT in 5.7% of individuals (and 5.3% of scans) which is broadly similar to the figures reported in other retrospective PET-based studies [38, 127-136, 182, 186, 187, 190, 193-199, 204]. Inclusion of multiple scans for the same patient has the potential to introduce bias as each scan is not independent, and as a result some authors have restricted their analyses to patients' initial scans to avoid clustering [293]. We found that such an approach had little appreciable impact on prevalence, which in our study reduced only slightly to 5.5%.

In any event, these estimates of point prevalence are undoubtedly underestimates. Dedicated prospective studies suggest that the true prevalence may be much higher than retrospective studies suggest – somewhere between 33% [42] and almost 100% on some PET/CT studies [43, 44], and 84% on post-mortem studies [37], although the latter studies tended to be much smaller.

We showed that the absence of ^{18}F-FDG BAT uptake on a single scan is a poor predictor of overall BAT status (overall sensitivity 48.9%). Furthermore the likelihood of an individual having ^{18}F-FDG BAT increased the more scans they had, therefore the overall sensitivity of 48.9% is likely an upper estimate. By calculating the cumulative ^{18}F-FDG BAT prevalence on serial scans, we showed that prevalence on the first is 4.7%, increasing by 5.8% for each additional scan before plateauing at approximately 30% for those with 6 or more scans. Lee *et al.* [187], in an analysis of serial PET/CT scans on 145 patients, showed that the mean probability of identifying BAT increased by 13% with each additional scan, increasing from 8.5% for a single scan, to 65% with more than four scans. Similarly Rousseau *et al.* [191] identified that the prevalence increased the more scans a patient underwent. These figures are comparable to some of the dedicated prospective PET studies.

10.2.1 Demographic factors

In line with most other studies [38, 127, 128, 135, 185-187, 194, 199], we identified a much higher prevalence of ^{18}F-FDG BAT in females than males (8.7% versus 2.5%), a trend that was apparent across almost all age groups. This has been interpreted as representing a genuine sexual dimorphism in adult humans [38, 199, 294]. Some studies, however, have revealed a similar ^{18}F-FDG BAT prevalence in males and females [42]. Therefore it has been suggested that the reported differences in prevalence between sexes may be erroneous, particularly in light of recent prospective studies which have reported a very high ^{18}F-FDG BAT prevalence in males [43]. Nedergaard *et al.* [189] concluded that there is probably no real difference in true BAT prevalence between the sexes – at least not for younger individuals, and probably reflects different activation thresholds between sexes. Apropos of this, we identified significant differences in ^{18}F-FDG BAT prevalence between sexes for older adults (over 40 years), but not in those who were younger (below 40 years).

We did not evaluate whether there were differences in ^{18}F-FDG BAT prevalence between ethnic groups, although similar prevalences have been reported in south Asian [295], Korean [190] and black South African [198] populations, as in Caucasian populations.

It is recognised that for a given temperature, a higher proportion of females than males feel cold [296] which may be related to differences in adiposity, and may be the cause or effect of differences in ^{18}F-FDG BAT prevalence between sexes.

We identified a higher prevalence of ^{18}F-FDG in those with normal BMI than for those who were overweight or obese in line with other studies [43, 191, 297]. In light of this, and the differences in obesity levels between the sexes, it is tempting to ascribe differences in ^{18}F-FDG BAT prevalence to BMI, although we found no significant difference in mean BMI between males and females. BMI does not, however, accurately reflect adiposity in different ethnic groups, sexes and for those at the extremes of BMI due, in part, to differences in body proportion and its inability to differentiate between fat and fat-free mass [298]. More accurate quantification of lean body mass (LBM) may alternatively be obtained by using the formulae devised by Morgan *et al.* [299] which takes into account sex, weight and height (Equation 10-1). Alternatively whole body composition analysis using the ‘BodPod’ air-displacement plethysmography method may be used.

Equation 10-1: Equations for calculating lean body mass.

$$\boldsymbol{LBM\ (men) = [1.10 \times weight\ in\ kg] - \left[128 \times \left(\frac{weight\ in\ kg}{height\ in\ cm}\right)^{2}\right]}$$

$$\boldsymbol{LBM\ (women) = [1.07 \times weight\ in\ kg] - \left[148 \times \left(\frac{weight\ in\ kg}{height\ in\ m}\right)^{2}\right]}$$

We also identified an inverse correlation between age and ^{18}F-FDG BAT prevalence, with BAT being most prevalent in those who were younger, in line with comparable large retrospective studies [204]. For both age and BMI, males tended to show a consistently lower prevalence than females, a similar observation to that described by Persichetti *et al.* [204] who identified that the association between ^{18}F-FDG BAT and BMI was more evident in women. Some studies found that age and BMI co-vary, and that lower prevalence figures with increasing age have may be attributed to increasing BMI with age [36, 113], although we identified no such correlation. An alternative hypothesis for the age-related decrease in BAT postulates that the stimulatory effects of sex hormones are lost with increasing age, resulting in BAT involution [189].

The demographics of the study sample merit further comment; a high proportion of the sample were older adults (mean age 61 years) with the greatest number of PET/CT scans being performed in the 60-70 year group). Given the large disparity between ^{18}F-FDG BAT prevalence with age (approximately 30% in those under 30 years, falling to approximately 5% in those above 60 years), the sample is skewed towards older age groups which yield an erroneously low overall prevalence figure. Therefore it may be illuminating to present an age-standardised prevalence.

10.2.2 Glycaemic status

Glycaemic status also correlated with ^{18}F-FDG BAT prevalence, being much more prevalent in those who were normoglycaemic (6.5%), than those with impaired fasting glycaemia (4.4%) or diabetes mellitus (1.9%). As for age and BMI, females showed a consistently higher prevalence than males. In hyperglycaemic states, the amount of glucose available for transport into metabolically active tissues is increased, and would compete with ^{18}F-FDG, resulting in less FDG being taken up than in normogylocaemic states.

The appropriateness of using ^{18}F-FDG PET/CT to gauge the prevalence of BAT has been questioned. As described in chapter 2, ^{18}F-FDG PET/CT relies on uptake of the radiolabelled glucose analogue ^{18}F-FDG, which is somewhat at odds with the belief that preferred substrate for BAT is triglyceride stored within the tissue [300]. Decreased lipid content within activated BAT has been described [67, 266], as has loss of free fatty acids within interscapular BAT in mice following noradrenergic stimulation [301]. Lipolysis of these lipid stores is thought to account for the higher CT attenuation values within active BAT compared to inactive BAT [302, 303]. As the lipid stores become expended, lipid is actively taken up from the circulation, regulated by β–adrenergic activated transcription of the lipoprotein lipase gene [304, 305]. The current view is that although fatty acids are required to activate UCP1 initially [306], the brown fat mitochondria are then able to metabolise carbohydrates in addition to fatty acids. This view is supported by the high levels of enzymes which oxidise carbohydrate including pyruvate within brown adipocyte mitochondria [307]. Further evidence comes from studies of cold acclimatised rodents, in which energy expenditure is up to three times higher than the basal level, of which 75% occurs within BAT. The respiratory quotient (a form of indirect calorimetry estimated from exhaled CO_2) allows the metabolised substrate to be derived; lipid metabolism would yield a respiratory quotient of 0.70, whereas these rodent studies actually yield a respiratory quotient of 0.80-0.85, implying a mixture of carbohydrate and fatty acid substrates [98]. Indeed it has been suggested that one of the functions of BAT is that of glucose disposal [189].

10.2.3 Circadian fluctuation

Univariate analysis also identified a correlation between photoperiod and BAT prevalence. Using binary logistic regression analysis, we sought to identify the variables which correlate most strongly with ^{18}F-FDG BAT prevalence. All methods of multivariate binary logistic regression returned models which identified age (younger), sex (female), BMI (lower) and time of day (earlier) as independent predictors of higher ^{18}F-FDG BAT prevalence. The same determinants were also identified when regression analysis was restricted to patients' first scans, implying that the perceived problem of data clustering highlighted above is not significant.

Several studies have shown short photoperiods to be associated with BAT activation in the Djungarian (Siberian) hamster (*Phodopus sungorus*) through activation of lipoprotein lipase [308], as well as increasing both mass and GDP-binding within brown adipocyte mitochondria [309]. Similar findings have been reported in other small mammals [310-313] and humans [127].

Short photoperiod has also been shown to suppress prolactin secretion from the pituitary in male golden (Syrian) hamsters (*Mesocricetus auratus*) [314]. Prolactin has been shown to induce UCP1 in sheep [315], although the consensus view is that prolactin has a suppressor effect upon BAT activity within hamsters [316, 317] and humans [318]. Indeed Tan *et al.* [319] suggest that excessive nocturnal light exposure in modern societies may be a contributory factor to human obesity. Multivariate analysis, however, did not show photoperiod to be a significant predictor of ^{18}F-FDG BAT status.

Prevalence varied throughout the day, with a significant drop in prevalence from its highest level at 09:00 (7.0%), dropping to 0% at 17:00. Although this may reflect diurnal temperature fluctuations, we did not have access to hour-by-hour temperature data to test this hypothesis. A circadian rhythm of ^{18}F-FDG uptake within interscapular BAT in mice has been described [320], although the authors describe peak uptake occurring after 9 hours of daylight, whereas we showed a peak in prevalence in the morning which then diminished throughout the day.

Alternatively, variation in BAT prevalence may accompany circadian rhythms in physiological processes. Many hormones, for example, have been shown to modulate BAT activity including prolactin, melatonin and corticosteroids, all of which show circadian variation. Low corticosteroid levels (*e.g.* following adrenalectomy in rats) have been shown to increase purine nucleotide binding in BAT, which normalises following corticosteroid infusion [321]. Melatonin production closely mirrors BAT activity [2], and melatonin binding sites have been identified in the cell membrane of mature brown adipocytes in Siberian hamsters, which have been implicated in mediating photoperiodic effects [322]. It has been therefore been suggested that melatonin may induce both hypertrophy and activation of BAT [319]. This would seem plausible, as melatonin biosynthesis within the pineal gland follows both a circadian and seasonal variation, and declines with age [323, 324], presenting a possible mechanism for decreased ^{18}F-FDG BAT with age. In rats no change in interscapular BAT mass or activity was observed following pinealectomy [325]. Nonetheless melatonin supplements have been suggested as a novel therapeutic means of stimulating BAT activity in humans [319].

Cyclical changes may also be the result of variations in adenosine 3':5' cyclic monophosphate (cAMP), which have been shown to fluctuate during the wake-sleep cycle in the anteroventral-medial hypothalamus, and on a seasonal basis within interscapular BAT [326]. This may account for our findings of a strong seasonal trend in ^{18}F-FDG BAT prevalence, being highest in the winter months, and lowest in the summer. There was a moderately strong inverse correlation between mean monthly temperature and ^{18}F-FDG BAT prevalence, with the highest prevalence in February (10.8%) and the lowest in July (1.6%), albeit not statistically significant. Saito *et al.* [42], in a dedicated study in which patients were scanned in the summer and again in the winter, following acute cold exposure to maximise ^{18}F-FDG BAT activity, found that uptake was much more prevalent in the winter.

Not only does BAT show quantitative seasonal variation, qualitative variation in terms of composition within BAT has been described in the big brown bat (*Eptesicus fuscus*) [327], which has been attributed to different rates of fatty acid oxidation throughout hibernation. Seasonal variation in the morphology of BAT adipocytes has also been reported in the non-hibernating common shrew (*Sorex araneus*), specifically an increase in capillary vascularity and mitochondrial cristae density [328], implying greater activity. It is feasible, therefore, that human BAT may undergo similar morphological seasonal variation.

10.2.4 Effect of temperature upon ^{18}F-FDG BAT

The stimulatory effect of cold upon BAT recruitment in rodents is well known [2, 329]. Most comparable retrospective studies have found a similar pattern [38, 128, 129, 194], but not all [191]. On average, ^{18}F-FDG BAT positive scans were acquired at lower temperatures than negative scans, but the effect of outdoor temperature is less clear-cut than other determinants. Although there is a clear inverse correlation between all temperature metrics and ^{18}F-FDG BAT prevalence on univariate analysis (with the highest prevalence within winter months), multivariate analysis yielded inconsistent results. One technique indicated lower mean temperature in the preceding 3 days to be a significant predictor, whereas the stepwise techniques identify the preceding day's mean temperature and preceding 3 days' mean temperature to be significant predictors. This inconsistency may be due to an underlying problem with multicollinearity between the temperature variables. Nonetheless, there is a pattern of increased prevalence with lower temperatures, and it would seem plausible that a lag period would be necessary between exposure to a cold stimulus, and activation of BAT. Increased ^{18}F-FDG BAT has been widely reported as an acute response to cold weather [194], most likely through cold-induced sympathetic stimulation via adrenergic receptors, which in turn drives glucose uptake.

The effect of temperature regulation is evident in prospective studies including by Saito *et al.* [42] who identified that following exposure to cold (19ºC) for 2 hours, 17/32 young adults (23-35 years) and 2/24 older adults (38-65 years) showed substantial ^{18}F-FDG BAT uptake, which was also confirmed histopathologically. On repeat scanning at 27ºC, no ^{18}F-FDG BAT uptake was evident. Similarly Zukotynski *et al.* [200] compared the prevalence of ^{18}F-FDG BAT in children and young adults before and after a change in scanning protocol; when scanned in cool conditions (21ºC), ^{18}F-FDG BAT prevalence was 27% and remained fairly constant throughout the year. When scanned in warm conditions (24ºC), the prevalence dropped to 9% and showed greater seasonal variation.

That cold exposure activates ^{18}F-FDG BAT is borne out by the fact that dedicated prospective studies, in which ambient temperature was reduced to around 16°C in combination with light clothing, showed a BAT prevalence in excess of 33% [36, 42-44, 113], much higher than in retrospective studies. Some prospective studies have sought to augment cold exposure by immersing feet in cold water to induce sympathetic activation of BAT. This technique has been criticised as being un-physiological, insofar as BAT is selectively innervated by dedicated sympathetic neurones which are activated by cold-sensitive centres in the brain, and is not normally innervated by general sympathetic outflow [2, 189].

Nonetheless, this highlights how responsive BAT is to small changes in temperature. The highly dynamic nature of BAT is well recognised. Short term exposure to cold (4°C) for 4 hours is sufficient to increase glucose uptake within BAT 2.3 fold [84], while exposure to thermoneutral conditions for 2.5 hours results in significantly decreased GDP binding within BAT [330]. BAT activity respond to temperature fluctuations within 30 minutes [43], and some authors suggesting it responds within as little as 10 minutes [331]. Therefore, although multivariate analyses imply it is the temperature in the preceding days which is an important determinant, implying some sort of sustained exposure to activate ^{18}F-FDG BAT, it captures the temperature to which individuals have been exposure better than temperature on the scan date. The majority of scans were performed before midday (2,019/3,269, 61.8%), therefore the mean temperature on the scan date may not be an accurate representation of the ambient temperature on the morning of the scan. As discussed above, analysis of changes in ^{18}F-FDG BAT prevalence against hour-by-hour temperature data may yield further information, rather than use of a daily mean.

This also highlights the opportunistic and probabilistic nature of BAT detection on retrospective ^{18}F-FDG PET/CT studies. Although cumulatively we surmised, based on analysis of serial scans, that ^{18}F-FDG BAT prevalence was approximately 30%, this is almost certainly an underestimate. Some individuals consistently failed to show any evidence of ^{18}F-FDG BAT despite undergoing multiple PET/CT scans, which may indicate that they may be genuinely BAT negative. The low prevalence on retrospective PET/CT-based studies is, at least in part, due to the fact that scanning protocols are optimised to suppress physiological ^{18}F-FDG uptake which could potentially result in false positive tumour diagnoses. Dedicated prospective studies, on the other hand, optimise scanning protocols to seek to maximally stimulate ^{18}F-FDG BAT. At our institution, ambient temperature within the PET suite is maintained at approximately 24ºC - sufficient to abolish most BAT activity. This has significant implications for our study. Not only is brief exposure to low ambient temperatures able to activate BAT, but exposure to warm temperatures (for as little at 15 minutes at 24°C) is sufficient to deactivate it in most subjects [192, 200, 202, 332-334]. Therefore BAT, even if present, may be quickly rendered metabolically inactive following a short period of warming.

There is compelling evidence in the literature that ^{18}F-FDG uptake within fat truly represents brown (or at least beige) fat [189]. We provided histopathological confirmation of this in a single exemplar based on characteristic histological and morpholological features of BAT (*i.e.* small multilocular adipocytes) and immunohistochemical staining with UCP1 antibody. The expression of UCP1 has hitherto been considered specific to BAT [36]. More recently the specificity of UCP1 has been challenged following the identification of UCP1 in both interscapular BAT and beige fat deposits in rodents [273]. Quantitative real-time PCR studies indicate that expression of the molecular marker *Zic1* is a better discriminator, being largely absent in beige fat [64].

10.2.5 Determinants of ^{18}F-FDG BAT volume and activity

Most studies have categorised ^{18}F-FDG BAT in a binary fashion into either ‘present’ or ‘absent’. Far fewer studies have sought to quantify the volume and activity of ^{18}F-FDG BAT [133], which can vary considerably both between, and within individuals. Human neonates are estimated to have between 40g and 200g of BAT, and human adults between 100g and 200g [125, 335, 336]. Therefore in chapter 4 we sought to identify which factors were predictive of ^{18}F-FDG BAT volume and metabolic activity (using SUVmax as a surrogate marker). ^{18}F-FDG BAT volume and SUVmax showed a very strong positive correlation, indicating that larger volumes of ^{18}F-FDG BAT were associated with greater metabolic activity, therefore it is likely that similar factors affect both. Alternatively, larger volumes may represent confluent sheets which take up ^{18}F-FDG homogenously, whereas smaller volumes may manifest as dispersed islands within larger areas of WAT, which would take up ^{18}F-FDG in a much more heterogeneous manner. Histological studies have shown that BAT often exists as islets scattered throughout larger sheets of WAT and skeletal muscle tissues [36, 337].

A similar pattern of determinants was observed with ^{18}F-FDG BAT volume and SUVmax as with prevalence, possibly due to the data being skewed by the large number of ^{18}F-FDG BAT negative scans. On average, ^{18}F-FDG BAT volume and SUVmax were higher in those who were female, younger and leaner which accords with the findings of similar large retrospective studies [38, 105, 127, 128, 134]. Time of day correlated weakly with volume and SUVmax, as did all temperature metrics.

A different pattern emerges if analysis is restricted to those scans with evidence of ^{18}F-FDG BAT uptake. Age becomes the strongest correlate, with higher volumes and SUVmax in younger individuals, which supports the classical assumption that BAT involutes with age. Sex, BMI and glycaemic status were no longer found to correlate with either volume or SUVmax. Although sex is not a significant correlate, we did identify a sex dimorphism, with males showing a lower ^{18}F-FDG BAT volume and SUVmax for age, BMI and glycaemic status. Furthermore, females' response to change in BMI and glycaemic status tended to be slightly more blunted than in males. Nonetheless these differences were not significant.

The strength of the correlation between time of day or ambient temperature, (particularly minimum temperature on the day preceding the scan) and both ^{18}F-FDG BAT and SUVmax also increased when analysis is confined to positive scans. We identified a somewhat counterintuitive positive correlation between ambient temperature (*i.e.* volume and activity *increase* with increasing ambient temperature) and both volume and SUVmax. Closer inspection of the data suggests that both ^{18}F-FDG BAT volume and SUVmax peak at between 0°C and 10°C, and drops off either side of this. 10°C is by no means warm, and is certainly sufficiently cold to activate BAT. It is also possible that cold exposure is only effective to a point; Freeman *et al.* [97] found that in warm acclimatised rats, a maximal response to cold stimulus was reached by 19°C. The effect of sub-zero outdoor temperatures in BAT activation may be offset by the turning up of central heating and wearing of warmer clothes.

We identified a difference between sexes in terms of in BAT activity and volume with temperature; at lower temperatures women tended to have higher ^{18}F-FDG BAT volume than males which may point to differences in temperature sensitivity between the sexes as discussed above. Higher levels of UCP1 have been reported in the interscapular fat pad of female rats compared with males, which implies a lower temperature threshold for cold-induced thermogenesis in females [338]. This trend was not apparent for SUVmax, for which females' response appeared blunted. It has been suggested that, on average, women feel cold at a higher temperature than men [296]. Nonetheless, these differences were not statistically significant.

Time of day correlated with ^{18}F-FDG BAT volume but less so with SUVmax, reflecting the highly dynamic nature of ^{18}F-FDG BAT. Unlike BAT prevalence, volume and SUVmax showed no consistent seasonal variation, with some individuals showing higher BAT volumes in the Spring and Summer months. Unlike BAT prevalence, which showed an acute response (*i.e.* varying with time of day), volume and SUVmax correlated most strongly with the minimum temperature in the preceding day, but also with temperature in the preceding 3 days, week and month to a lesser extent. The presence of BAT, and likely its level of metabolic activity, is likely an acute response to short periods of cold weather (in the order of 1-7 days) rather than to prolonged periods of average cold weather [194], although is it feasible that sustained exposure to cold is necessary to induce BAT hyperplasia or beige fat transdifferentiation.

It may be that prolonged cold exposure induces BAT hyperplasia or beige fat transdifferentiation, in which case a higher prevalence would follow sustained cold exposure. While acute cold exposure is sufficient to activate BAT [43, 44], a fact exploited in prospective studies of BAT prevalence in humans, this would only be sufficient to activate extant BAT (or beige fat) deposits. To effect a significant change in ^{18}F-FDG BAT volume (and activity, which strongly co-varies), may require either BAT hyperplasia or transdifferentiation of WAT into beige fat, which may require a sustained stimulation. Chronic cold exposure is believed to increase BAT volume [39, 129, 194], with no significant correlation identified between ambient temperature on the day of scanning and either ^{18}F-FDG BAT volume or SUVmax. Our results broadly mirror this, although the effect of chronic exposure on BAT volume and SUVmax is less clear-cut.

For both ^{18}F-FDG BAT mass and SUV, multivariate stepwise Tobit regression analysis returns a model which includes age, sex, BMI, time of day as independent predictors of ^{18}F-FDG BAT mass. Although we initially chose to measure ^{18}F-FDG BAT mass, this bears a linear relationship with volume, and is therefore effectively interchangeable with volume. Outdoor temperature was also identified as a significant independent predictor of both volume and SUVmax; maximum temperature on scan date and time of scanning for volume, and maximum temperature on the day of scanning and preceding day for SUVmax. Again, there is a perplexing positive correlation between preceding day's maximum temperature and both ^{18}F-FDG BAT volume and SUVmax. A possible explanation for this would be that ^{18}F-FDG BAT, rather than being stimulated by cold *per se*, is activated by change in temperature, *i.*e. the abrupt transition from a high maximum temperature on the preceding day, followed by a low temperature on the day of scanning. However, we identified no significant differences between ^{18}F-FDG BAT positive and negative scans in this regard.

We employed Tobit analysis to enable inclusion of the numerous negative scans [133]. If, as our study of ^{18}F-FDG BAT prevalence suggests, BAT is not ubiquitous, and rather than BAT activity being on a continuum, is genuinely and consistently absent in some individuals, it would be erroneous to include these individuals in such an analysis. It would be nonsensical to attempt to identify determinants of ^{18}F-FDG BAT volume or activity in individuals who, despite concerted attempts at stimulation, may never possess BAT. To address this, conventional multivariate regression on normalised ($\log_{10}$) ^{18}F-FDG BAT volume data was performed which returned a model that only included age and minimum temperature on the day preceding the scan as significant independent predictors of ^{18}F-FDG BAT volume. Although it was not possible to normalise SUVmax data, it is likely that similar determinants are predictive of both ^{18}F-FDG BAT volume and activity given the strong correlation between them ($r = 0.844$). Pace *et al.* [134] reported similar findings, including that age and outdoor temperature were independent predictors of SUVmax. Alternatively, the Tobit analysis could have been performed on the subgroup of individuals who showed ^{18}F-FDG BAT uptake on at least one scan, whom we know to be capable of expressing BAT.

Although outdoor temperature seems to be predictive of ^{18}F-FDG BAT volume and activity, it was not been possible to conclusively separate the effects of various temperature metrics to identify which is most significant due to significant collinearity - this would be better tested with a prospective study.

Our finding that increasing age is predictive of lower ^{18}F-FDG BAT volume may have implications for future therapies which aim to modulate BAT activity. If BAT volume does diminish with age, any therapy which stimulates BAT may be less effective in older adults.

10.3 Colocalisation of ^{18}F-FDG BAT on serial PET/CT scans

10.3.1 ^{18}F-FDG BAT distribution is fairly constant within individuals

In chapters 5 and 6 the distribution pattern of ^{18}F-FDG BAT uptake in sequential PET/CT scans in 15 patients was analysed. In all cases ^{18}F-FDG BAT uptake occurred within the thorax (mediastinum, supraclavicular or paravertebral compartments), and within the cervical/supraclavicular regions in 92.6% of scans similar to that described by Ouellet *et al.* [133]. Therefore, when validating an imaging modality for the purposes of BAT identification, restricting the coverage to the thorax, or even the supraclavicular fossae/neck should permit sufficient anatomical coverage.

We identified a super-linear relationship between the number of compartments and volume (*i.e.* a quadrupling of the number of compartments containing ^{18}F-FDG BAT, results in a greater than four-fold increase in BAT volume). The anatomical compartments were of unequal size. If, therefore, ^{18}F-FDG BAT appeared within the smaller anatomical compartments before the larger compartments, a super-linear relationship may result. This does not appear to be the case; the largest compartment was the cervical/supraclavicular region which accounted for the majority of instances (20/25) in which only a single compartment contained ^{18}F-FDG BAT. This could indicate some form of augmented or exponential response, such that ^{18}F-FDG BAT uptake accelerates as temperature decreases.

Inter-rater reliability calculations indicate that, although ^{18}F-FDG BAT volumes fluctuate widely within individuals, the pattern of distribution within anatomical compartments remains fairly consistent, with 9/15 patients showing uptake within the same anatomical depots on serial scans.

Following on from the work in chapter 4, in which we calculated ^{18}F-FDG BAT volumes, we were able to identify the ‘index scan’ for each patient (*i.e.* that with the greatest ^{18}F-FDG BAT volume). We found that the pattern of ^{18}F-FDG BAT uptake on the index scan was generally representative of uptake on scans with lower ^{18}F-FDG BAT activity (in 14/15 patients). Although, being a retrospective study, we were unable to determine whether the ^{18}F-FDG BAT uptake on the index scan represented maximally stimulated BAT - in all likelihood it was not, and still underestimates the true volume of BAT.

10.3.2 High degree of ^{18}F-FDG BAT colocalisation on serial PET/CT scans

In this study we sought to determine whether ^{18}F-FDG BAT depots occur within reproducible locations across serial PET/CT scans (*i.e.* whether it colocalises).

We explored two object-based colocalisation approaches: one testing whether ROIs intersect, and the other using voxels. Although both techniques showed a high degree of colocalisation (often exceeding 80%), neither were perfect. If all ^{18}F-FDG BAT uptake on the subordinate scans coincided with uptake on the index scans, there would be 100% colocalisation. This may be due to errors in image registration resulting in partial colocalisation. The PET is acquired over a period of 30 minutes or so, while the CT is acquired over seconds, therefore ^{18}F-FDG uptake within adipose tissue may erroneously appear in adjacent structures due to movement. We used a technique in which we adopted a high SUV threshold of 2.5 g/ml to semi-automatically segment ^{18}F-FDG BAT, and used the CT to restrict the resulting ROIs to adipose tissue. Therefore ^{18}F-FDG BAT uptake lying outside this envelope will have been excluded. Both the index and subordinate scans would be expected to be affected equally, but this may reduce the available voxels for colocalisation. Post acquisition image registration is imperfect, therefore genuine colocalisation between subordinate and index scans, particularly in scans with low ^{18}F-FDG BAT volumes, may go undetected.

Furthermore, despite collimation on the PET scanner, areas of avid ^{18}F-FDG uptake often show a rim of intermediate radiotracer uptake around a metabolically avid central nidus, which in our experience, became more pronounced around higher activity depots. We sought to minimise this by setting a high SUV threshold of 2.5g/ml to maximise specificity at the expense of reduced sensitivity, and exclude intermediate level ^{18}F-FDG uptake within the rim of ^{18}F-FDG BAT deposits (*i.e.* SUV 1.0 – 2.5 g/ml). We also found that this resulted in better anatomical delineation of ^{18}F-FDG BAT deposits. This threshold was higher than that used in comparable studies [133], and would therefore be expected to underestimate BAT. This would tend to impact on the less metabolically active subordinate scans, but should not have a major impact on the proportion of ^{18}F-FDG BAT on the subordinate scans which colocalises with BAT on the index scan.

The index scan is a fairly abstract construct. It was only possible to identify the index scan retrospectively based on the presumption that it demonstrates the greatest volume of ^{18}F-FDG of all the patient's scans, but there is no way of knowing the extent to which BAT was activated, and certainly not whether it was maximally stimulated. Given the scanning protocol adopted at our institution, the index scans are unlikely to represent maximally stimulated BAT. It is possible (and in the case of subject H, highly likely) that what we took to be index scans do, in fact, show sub-maximally stimulated BAT, and are in effect subordinate scans themselves. It would only be possible to test this hypothesis prospectively. Nonetheless, these data indicate that the uptake on the subordinate and index scan tends to occur in fixed sites on serial scans, and is likely to occur in the same site on a maximally stimulated scan, and that uptake within the index scan would likely correspond to that on a PET/CT scan acquired in a state of maximal BAT activation.

For the most part, both techniques performed well, and there was no consistent bias between them. Simple comparison of ROIs to determine whether they intersect is only semi-quantitative and would not reflect the true extent to which colocalisation occurs. Manders' technique for colocalisation of individual voxels is truly quantitative, but is susceptible to the size of the objects being colocalised (and may therefore be affected by our adoption of a high SUV cut-off); a single large colocalised object and innumerable tiny colocalised objects would produce a very low figure for the first technique, and a very high technique for the second. Manders' approach does have an additional advantage: for a busy image with multiple objects in both image stacks, some objects will overlap by chance which may be confused with genuine colocalisation. Manders' approach allows the measured colocalisation coefficient to be compared against multiple randomly generated images to determine whether it is significantly greater than that expected if there was only random overlap. We demonstrated that in most cases the degree of colocalisation between ^{18}F-FDG BAT uptake on serial scans was greater than that expected by chance.

By analysing sequential scans in 15 subjects using quantitative colocalisation, we have demonstrated that ^{18}F-FDG BAT uptake occurs in consistent locations on serial scans, and that BAT uptake on subordinate scans tends to also be evident on the index scan. Therefore, when a patient has undergone multiple PET/CT scans, the distribution of ^{18}F-FDG BAT on the index scan can be taken as being representative.

We have also shown that as activity reduces, the ^{18}F-FDG BAT deposits fragment into multiple small deposits, and localise to the foci of greatest ^{18}F-FDG BAT on the index scan, while other depots switch off (or demonstrate low activity below our segmentation threshold). Although this would imply that simple quantification of BAT on the basis of simple numerical comparison of ROIs may be misleading, the number of ROIs are a good indicator of total ^{18}F-FDG BAT volume.

Consistent areas of ^{18}F-FDG BAT uptake may imply fixed depots of classical BAT, which are up and down-regulated in much the same manner as a dimmer light switch, rather than beige fat, which one might expect to follow a much less consistent anatomical distribution manner.

10.4 Limitations of PET/CT in the identification of ^{18}F-FDG BAT

PET/CT is subject to several limitations, which limit its role in the field of BAT research. Most studies evaluating BAT prevalence have been retrospective observational studies of PET/CT scans performed as part of routine oncological treatment. Although some small studies have used PET/CT in healthy volunteers solely for the purposes of BAT identification, the high ionising radiation burden and costly radiotracer limits its role in larger populations, and would be difficult to justify ethically.

The commonest indication for the ^{18}F-FDG PET/CT scans was the assessment of cancer and its metastases, therefore the samples may not be truly representative of the wider population. Although some studies have reported a lower ^{18}F-FDG BAT prevalence in patients with active cancer [191, 203, 339], the consensus is that there is no correlation between the presence of ^{18}F-FDG BAT and of metastatic disease [133, 189].

PET/CT suffers from the significant disadvantage that it is only imaging metabolically active BAT. BAT is a highly dynamic facultative tissue and is only activated when non-shivering thermogenesis is required [2]. Even within the same individual BAT volume and SUVmax varies considerably between serial scans, even under controlled conditions [340]. As glucose uptake is directly proportional to metabolic activity [341, 342], inactive BAT will not accumulate ^{18}F-FDG and will not, therefore, be visible on PET/CT scans. The observation that some scans are apparently BAT negative, does not mean it is absent. Nor for that matter does it even indicate that it is not metabolically active. The activity may merely be at a low level below the threshold we set. Alternatively the volume of active BAT may lie below the spatial resolution of PET.

This is problematic as the scanning protocol is designed to suppress physiological ^{18}F-FDG uptake within BAT. The opportunistic nature of BAT detection means that *ad hoc* identification of BAT on PET will inevitably underestimate its true prevalence. This is borne out by the fact that prospective studies have shown a consistently higher prevalence than retrospective studies. The extent to which PET/CT underestimates BAT is apparent in studies of genetic expression profiles, which show BAT to be highly prevalent [56], even in subjects without evidence of ^{18}F-FDG BAT uptake [56, 105]. We sought to address this by evaluating patterns of uptake on serial scans, and found that uptake occurs in a fairly constant pattern within individuals.

The reliability of serial SUV measurements and their reproducibility may also be questioned. Longitudinal studies indicate that serial SUV measurements vary by 10-13% within the same patient, which may be reduced to 3-4% with good quality assurance programmes [343] and are therefore reproducible [344]. SUVmean has been shown to have higher reproducibility on serial PET scans than SUVmax [345], as the former derives its activity from a larger number of voxels, rather than a single voxel as in SUVmax.

The duration between ^{18}F-FDG administration and image acquisition may also affect SUV values. Our current protocol, scanning at 60 minutes post injection allows SUVmax to peak in 33.3% of cases, with the remainder peaking between 145 and 360 minutes post injection. Therefore scanning at 60 minutes may generate low SUVmax values [346]. SUVmax has also been shown to vary with age; Wehrli *et al.* [347] reported higher SUVmax values in the skin, adipose tissue and skeletal muscle with increasing age, which may accompany age-related differences in BMI.

Following the introduction of PET/CT in the 1990s, unexpected ^{18}F-FDG uptake was described in a symmetrical distribution in the neck and thorax, but the realisation that this could represent BAT did not come until 2002 [131]. Nedergaard *et al.* [101] considered that, based on the glucose uptake patterns, and the response of this tissue to physiological and pharmacological stimuli, the evidence that this tissue represented BAT was overwhelming. The only means of determining true BAT status is to subject biopsy specimens to immunohistochemical analysis. Areas of ^{18}F-FDG activity within fat have been confirmed histopathologically as being BAT based on the characteristic histological appearances and the presence of the UCP1 protein as determined by testing with anti-UCP1 antibodies [36]. There are, however, few studies in which histological confirmation of BAT has been provided as BAT depots are not readily accessible surgically, and have typically been sampled opportunistically during thyroid surgery. Sampling of BAT in human adults is also hampered by the fact that BAT forms small islets within larger sheets of WAT [36]. Therefore although we only had the opportunity able to provide histological confirmation in a single case (BAT13), there is ample evidence in the literature to allow us to extrapolate this to other ^{18}F-FDG BAT positive patients. PET/CT tends to underestimate BAT volumes, and traditional Dixon MR tends to overestimate BAT when compared to histopathological analysis, therefore the gold standard is autopsy [243].

There is nonetheless an element of doubt regarding the true nature of the tissue which we presume represents BAT on CT. There is compelling physiological and histological evidence that ^{18}F-FDG uptake within fat does represent BAT, which is further supported by immunohistochemical staining of excised samples with UCP1. We had the opportunity to obtain a sample of fat corresponding to an area of avid ^{18}F-FDG BAT uptake in an exemplar patient. This showed the histological characteristics of BAT, and stained positive for UCP1.

More recently the specificity for UCP1 has been called into questions as it has been shown to be present in both classical BAT as well as transdifferentiated beige fat [56]. As discussed previously, we showed a high degree of ^{18}F-FDG BAT colocalisation on serial PET/CT scans, which may imply classical BAT rather than beige fat

More recently, beige adipocytes have been identified as a distinct type of thermogenic fat in mice and humans [57, 63]. These beige adipocytes exhibit an intermediate phenotype between that of BAT and WAT in both rodents [62, 348] and, more recently, in humans [92, 273]. Indeed it has been suggested that cold-induced BAT is predominantly derived from transdifferentiation of white adipocytes [62, 92]. The specificity of UCP1 for classical BAT has also been undermined by the discovery that beige adipocytes also express UCP1 [60], but do not arise from the adipomyocyte lineage from which classical brown adipocytes are derived [48, 50, 51]. Similarly the presence of the transcription factor PRDM16, previously considered specific to classical BAT [50] has also been identified in beige adipocytes [189].

Wu *et al.* [57] found that the gene expression profile with adult humans BAT was closer to that of mouse beige adipocytes than to classical murine adipocytes, and concluded than BAT in human adults is in fact beige fat. UCP1 positive fat within the supraclavicular fossa in humans has also been identified as being beige fat on the basis of novel immune-histochemical markers and gene expression, specifically *Zic1* [273]. Jespersen *et al.* [56] found that the gene expression profile of classical BAT (*i.e.* up-regulation of *miR-206*, *miR-133b*, *LHX8* and *Zic1*, and down-regulation of *HoxC8* and *HoxC9*) co-exists with markers of beige adipocytes (*TBX1* and *TMEM26*) within supraclavicular fat in humans, which points to classical BAT and beige fat co-existing. This could account for our findings of high (but not perfect) colocalisation between subordinate and index PET/CT scans; those areas which consistently colocalise may represent classical BAT which may be wound up or down in response on external stimuli, while those that do not colocalise may represent transdifferentiated beige fat. If the totality of BAT evident on PET scans was transdifferentiated beige fat, the pattern of ^{18}F-FDG BAT could be expected to be much more variable.

The inherent limitations of PET in identifying BAT are well recognised and have been discussed above. These compromise the reliability of PET as a standard against which other imaging modalities can be compared. Foremost among these is the fact that maximum activity of PET is not always present on the scan. We sought to address this by using the 'index' PET/CT scan as the standard, as well as showing that ^{18}F-FDG BAT uptakes occurs in a consistent pattern within an individual on serial scans. Nonetheless these scans were performed for purposes other than the identification of BAT, and therefore undoubtedly underestimate its true extent.

10.5 MR studies

The fact that PET/CT only shows metabolically active BAT limits its ability to act as a gold standard in both a research and clinical setting. Inactive BAT is not demonstrated on PET/CT, and as a result would underestimate both its prevalence and volume. MR has been advocated as an alternative means of identifying anatomical BAT independent of its activity. We showed BAT activity to be highly variable in response to small changes in ambient temperature. In addition MR does not carry the significant ionising radiation burden of PET/CT which precludes its widespread use in healthy individuals, nor does it require the administration of expensive radiopharmaceuticals.

Building on our work on PET/CT, we were able to transpose ^{18}F-FDG BAT ROIs onto co-registered MR scans. From this we were able to characterise the signal characteristics of BAT and WAT on MR, specifically the calculated fat fraction and T2* relaxation time.

Ex vivo murine MR spectroscopy have shown differences in composition of BAT and WAT [244]. The most prominent of which is the prominent water peak within BAT which in WAT water forms a comparatively small part. In addition differences in the spectral patterns of BAT and WAT, including a lower proportion of unsaturated triglycerides in BAT compared with WAT, showed that BAT has a prominent water peak. Furthermore the fat peaks were more broadly spread out due to their iron content and induced magnetic field inhomogeneities.

MR exploits the fact that hydrogen nuclei within BAT and WAT have different resonant frequencies, and therefore has the potential to identify BAT independent of its degree of activation. Previous studies have successfully identified *in situ* BAT in rodents in both active [349] and inactive [241, 245, 255] states. In rodents BAT has been shown to have a lower fat fraction (37-70%) than WAT (90-93%), as well as being more heterogeneous [241].

10.5.1 Phantom validation of fat fractions derived from IDEAL MR

Fat fractions were calculated from IDEAL MR sequences which have hitherto been validated as producing reliable estimations of fat fraction. Nonetheless a phantom study in which we scanned five phantoms containing foodstuffs of different fat fraction showed some discrepancy between the reported fat content and the calculated fat fraction. This could be due to errors in the technique, post acquisition analysis or eddy currents within the fluid phantoms. Estimations of the fat content were calculated using approximations of density which may not be universally applicable, which could introduce further error.

10.5.2 Studies of fat fraction and T2* relaxation time in rats

We had an opportunity to conduct a *post mortem* study on four rats; two kept cold (4°C) and two kept warm (30°C) in the 8 hours prior to sacrifice. One rat from each group was dissected to excise WAT and interscapular BAT, while the remainder were scanned *in situ*. Many BAT studies have used rats and mice due to the ease with which BAT may be identified *a priori* as a macroscopically distinct conglomeration within the interscapular fat pad.

Mean fat fraction within the excised tissue specimens was significantly lower in BAT (58.9-62.4%) than WAT (78.0-82.5%), although BAT fractions were consistent irrespective of the temperature at which the rats were housed *ante mortem*. This was not the case when scanned *in situ*. Although BAT fat fraction was lower than WAT in both rats, BAT fat fraction within the rats housed at 4°C was significantly lower (44.7%) than that those housed at 30°C (62.2%). A similar pattern has been described by Smith et al. [256] who showed that fraction fluctuated in relation to temperature, reducing from 79.4% at 30°C, 61.8% at 23°C and 50.9°C at 16°C. This fluctuation in mean fat fraction follows recent change in BAT activity. It is probable that, prior to sacrifice, interscapular BAT within the rat kept at 4°C was active (as indicated by the lower fat fraction, implying lipolysis), while that within the rat kept at 30°C was likely inactive.

We identified a significantly lower T2* relaxation time within BAT than WAT in excised tissues. The T2* relaxation time of BAT excised from the rat kept at 4°C was significantly shorter than from the rat housed at 30°C. This also points to different degrees of metabolic activity between the two rats, with higher BAT perfusion/activity within the rat kept in the cold. This was not mirrored when scanned *in situ*, where the mean T2* time within BAT at 4°C (28.2 ± 101.7 ms) was higher than at 30°C (19.1 ± 3.1 ms). The large standard deviation (particularly at 4°C) makes it difficult to draw conclusions from these results, and did not prove helpful in discriminating between tissues types in rats when scanned *in situ*. It is noteworthy that there is a moderate positive correlation between fat fraction and T2* time (*r* = 0.6). This could indicate that as BAT becomes more active in lipid metabolism, fat fraction reduces, and has shown to be accompanied by an increase in local blood flow and increased iron content within mitochondria which in turn shortens T2* [241]. BAT is more highly vascularised than WAT in order that heat can be dissipated throughout the body. Although it has been suggested that MR techniques which measure tissue perfusion may have a role in separating BAT and WAT, we were unable to show this.

10.5.2.1 Limitations of animal studies

Most animal studies in BAT research have tended to involve *ex vivo* scanning of excised tissue samples, post mortem scanning of carcasses, or *in vivo* scanning of anaesthetised rodents. Scanning *post mortem* is potentially problematic due to differences in temperature, and the absence of respiratory motion, cardiac motion and vascular flow.

Lower fat fractions have been reported when scanning *in vivo* compared with *post mortem* which has been attributed to the absence of tissue perfusion [255], which may account for our observed differences between the *ex vivo* and *in situ* samples. It may be that this arises from differences in tissue preparation. Dissecting tissue could, by increasing available surface area for example, alter passive diffusion of oxygen compared with the *in vivo* samples.

For the rat housed at 30°C, mean BAT fat fraction was similar when scanned *ex vivo* or *in situ*. In the rat housed at 4°C however, the BAT fat fraction *increases from* 44.7% when scanned *in situ*, to 58.9% in the excised tissue specimens. This could be due to some underlying change in metabolic state, including that the effects of BAT activation (*i.e.* localised lipolysis) are reversed following tissue manipulation. Preparation of specimens in microscopy has been shown to induce cell stress as evidenced by absence of glycogen in BAT [350].

In vivo animal studies are further limited by the necessity of administering general anaesthesia to immobilise the animal. Although it has been suggested that the tissue characteristics of BAT are more reflective of chronic thermal exposure and should persist [256], inhalational volatile anaesthetic agents can acutely affect sympathetic activity and BAT activity [2, 351], resulting in a reduction in blood flow and oxygen consumption within tissues.

10.5.2.2 Dynamic nature of BAT

We also identified a small but significant difference in fat fraction between omental and subcutaneous WAT at both temperatures. This suggests that WAT is not homogenous and that its composition varies according to site. The fat fraction with human WAT varies according to location, with deep subcutaneous WAT containing a higher proportion of saturated fatty acids than superficial subcutaneous WAT, and visceral fat containing an even higher proportion [352]. These variations may reflect the underlying metabolic activity of the tissue. Therefore using subcutaneous WAT as a standard may not accurately reflect the full range of fat fraction within WAT. This should be borne in mind in any study which uses WAT fat fraction as a baseline against which BAT is compared.

In line with other murine studies, we identified BAT on the basis of *a priori* knowledge of its likely anatomical location (*i.e.* within the interscapular fat pad). Any attempt at identifying BAT prospectively on the basis of fat fraction would require it to have a significantly different fat fraction than WAT. As discussed above WAT is not metabolically inert and varies in both composition and morphology according to anatomical site, season and diet [353]. This may affect fat fraction would hamper any technique which seeks to differentiate BAT and WAT on the basis of fat fraction.

As discussed, BAT is also biochemically and histologically dynamic. Seasonal variation in fat composition within BAT has been described in the big brown bat (*Eptesicus fuscus*) [327], which has been attributed to different rates of fatty acid oxidation throughout hibernation. Seasonal variation in the morphology of BAT adipocytes has also been reported in the non-hibernating common shrew (*Sorex araneus*) [328]. As both hibernating and non-hibernating small mammals show seasonal variation in BAT composition, it is probable that human BAT may follow a similar pattern. The dynamic nature of BAT has also been shown in CT studies which have shown a higher CT attenuation in areas of active BAT than inactive BAT [302, 335] likely reflecting localised lipolysis. A corresponding decrease in lipid content in activated BAT has also been shown histopathologically in rats [302].

The morphological appearances of brown adipocytes vary according to functional state [37, 60, 62]. When stimulated by cold exposure or diet, lipid vacuoles within brown adipocytes are small and numerous. When the brown adipocytes are quiescent (*i.e.* warm ambient temperature or in fasting animals) the vacuoles increase in size before eventually coalescing into a single large vacuole [354]. This supports the hypothesis that BAT, if quiescent, accrues intracellular lipid thereby acquiring a WAT-like phenotype.

Multiple studies have confirmed that BAT composition changes according to its level of activity. An inverse correlation between fat-fraction and UCP1 activity indicates that fat fraction varies in response to the degree of metabolic activity [256]. Remodelling of BAT has also been described in interscapular BAT in mice incrementally exposed to low temperatures [301]. Similarly actively cooling human neonates with hypoxic ischaemic encephalopathy to 33°C for 48 hours has been shown to a significantly lower fat fraction compared with controls [269]. Remodelling of BAT involves a reduction in lipid content [67, 266, 268], higher vascularity and mitochondrial content [67, 266], increased perfusion [125] and blood oxygenation [266, 355]. BAT stimulation (following norepinephrine injection or prolonged cold exposure) results in a reduction in the proportion of unsaturated and polyunsaturated fatty acids.

BAT composition also varies with age, with higher levels of saturated fatty acids in juvenile rats than adults [350]. Variation in fat fraction with age has also been reported on MR in rodents [241, 253]. Differences in fat fraction between BAT and WAT in adult humans are less marked than in infants [268]. With increasing age, BAT is known to become phenotypically and spectroscopically similar to WAT [350] - particularly when quiescent [354].

Obesity is associated with BAT acquiring a more WAT-like phenotype, with higher fat fraction and decreased T2* relaxation times on MR [253]. At one extreme, genetic knock-out studies in obese *obs/obs* mice in whom UCP1 has been disabled, BAT fat fraction was much higher than in lean mice [248], and is almost as high as in WAT.

These data suggest that the MR characteristics of BAT vary in response to acute cold exposure, and that cold stress depletes intracellular lipid stores within BAT, and are therefore reflective of tissue activity. Methods of BAT identification which rely on fat fraction may be less effective in detecting metabolically inactive BAT due to their increased fat fraction.

The activation state of BAT has further implications with respect to MR. It is recognised that the chemical shift of the spectral peaks of BAT and WAT are temperature dependent which could affect the ability of Dixon-based techniques for fat quantification. It has been suggested that a temperature increase in active BAT could affect the chemical shift position of fat and water molecules [356] which could impact upon their corresponding fat fraction. It has been suggested that MR, and in particular

MR spectroscopy, should be able to discriminate between BAT and WAT irrespective of the tissue's metabolic activity [244] as BAT and WAT spectra should be affected equally. The small temperature increase generated by non-shivering thermogenesis is unlikely to make a significant difference *in vivo* – probably amounting to less than a 2% change in the resulting BAT fraction [241], although lower fat fractions have been reported when scanning *in vivo* compared with *post mortem*.

It was believed that MR had the potential to detect BAT regardless of its state of metabolic activation [243]. It appears that fat fraction within BAT varies according to its level of metabolic activity. Therefore MR would demonstrate functional rather than structural BAT. Ultimately it is not the volume that will determine the degree of uncoupling and therefore non-shivering thermogenesis, but the activity.

10.5.3 Studies of fat fraction and T2* relaxation time in adult humans

BAT studies in adult humans are hampered by the fact that, unlike in rodents, BAT does not form discrete easily identifiable depots which can be identified on the basis of *a priori* knowledge alone. We used two approaches to circumvent this, and thereby identify and characterise *in vivo* BAT in adult humans; the first was a probabilistic approach, and the second involved transposition of ^{18}F-FDG BAT ROIs from PET/CT onto co-registered MR scans.

For our probabilistic approach, we built on our findings from chapter 5 which showed that ^{18}F-FDG BAT, when present, occurred within the supraclavicular fossae and neck in 93% of scans. By defining ROIs around these compartments, and applying thresholding (to exclude non-fat) and morphological edge erosion (to exclude tissue interfaces) we were able to define ROIs within minimum operator bias. The probabilistic technique has been used with some success previously by Lundström *et al.* [268, 352], who used it to detect a 2% decrease in BAT fat fraction following 3 hours of cold exposure using a gradient echo sequence at 1.5T. We identified no significant difference in fat fraction between the supraclavicular fossae and subcutaneous WAT using this technique. It is possible that in our hands this technique is insufficiently sensitive to identify the very small changes reported previously. Although we also used a 3 Tesla scanner, we adopted a spin echo sequence, rather than a gradient echo sequence, which would affect tissue contrast. Although this technique provides a semi-quantitative measure of fat fraction within the defined space, it does not quantify BAT volume *per se*, which limits its wider appeal in testing the response of BAT to pharmacological stimulation.

Our second method in which ^{18}F-FDG BAT ROIs were transposed from PET/CT onto MR did show a significant difference in fat fraction between BAT and WAT, albeit with considerable variation in fat fraction between individuals. WAT fat fraction, which served as the standard, remained constant across serial scans for many patients (most notably BAT13 in whom WAT fat fractions were 83.1%, 82.0% and 83.3% respectively). A stable fat fraction within WAT provides a benchmark against which BAT may be compared. In some patients however (most prominently in BAT20, 06) WAT fat fraction varied considerably across serial scans. This may be due to genuine seasonal variation in WAT composition. In both BAT20 and BAT06, the dorsal subcutaneous fat layer was thin which would be particularly susceptible to the effects of volume averaging artefact and motion artefact, compared with thicker fat layers in other patients. This inter-subject variability coupled with the plasticity (in terms of activity and morphology) of both BAT and WAT makes it unlikely that a single universal cut-off point to differentiate between BAT and WAT on the basis of fat fraction alone would be appropriate in all cases.

T2* relaxation time has been suggested as a potential means of identifying BAT [274] due to its greater vascularity and mitochondrial content, although we identified no significant difference between BAT and WAT.

10.5.3.1 Limitations of our approach to image registration and segmentation

Each of the techniques we used to identify BAT have advantages and disadvantages. The probabilistic technique in which the supraclavicular fat is manually segmented does not require a concomitant PET/CT scan, and is independent of the activation state of BAT. This technique does, however, require manual segmentation (albeit of a well defined anatomical compartment) which may introduce an element of operator bias. The ROIs defined within the supraclavicular fossae and neck were large, and will predominantly comprise WAT. Therefore small changes in fat fraction within BAT may be diluted, which would reduce the sensitivity of this technique. This is borne out by our results which showed no significant difference in mean fraction within these supraclavicular ROIs between ^{18}F-FDG BAT positive and negative subjects.

The technique of transposition is heavily dependent on there being metabolically active BAT on PET/CT, which we have shown to be highly variable in both prevalence, volume and activity. Transposing ROIs from PET/CT to MR minimises operator bias but is heavily reliant on accurate image registration, therefore there is the potential for non-fat tissues to be mis-registered resulting in spuriously low mean fat fraction within ROIs. Conversely the mean fat fraction within transposed ROIs may be increased by the presence of interspersed WAT, as well as being spuriously increased by the presence of mis-registered areas of adjacent WAT. The comparatively long image acquisition times of PET/CT and MR will inevitably result in some mis-registration due to respiratory and cardiac motion, therefore it is likely that both confounders co-exist, which will reduce reliability of fat fraction measurements within transposed ^{18}F-FDG BAT ROIs on MR.

10.5.3.2 Prospective identification

Building on these findings from chapter 8, we sought to identify *in vivo* BAT on MR on the basis of its imaging characteristics. We then tested the accuracy of theses techniques quantitatively against our standard of PET/CT by using a novel implementation of object-based colocalisation techniques developed in light microscopy.

Visual inspection was moderately successful in identifying BAT in some cases, particularly in the hands of a radiologist. This technique did tend to underestimate volume in patients with larger volumes of ^{18}F-FDG BAT on PET/CT however.

Although we discovered significant differences in fat fraction between BAT and WAT in adult humans *in vivo* (chapter 8), it was not possible to define a single cut-off point to differentiate these tissues. Therefore we used receiver operator curve analysis to heuristically identify optimum thresholds for each patient. This technique was moderately effective in a small number of patients but produced inconsistent results, with fairly poor levels of colocalisation against ^{18}F-FDG BAT uptake. Although we were not able to reliably identify BAT on MR in all cases, this technique may be useful in identifying a research group, amongst those without co-morbidities in whom PET/CT scans may not be a viable option.

Both techniques underestimated BAT volume – particularly in those patients with higher ^{18}F-FDG BAT volumes. BAT is dynamic, therefore it is possible that it involuted in the interval between the PET/CT sand MR scans. Conversely, in cases where these techniques appear to have overestimated BAT volume, it is possible that this represented hitherto unidentified BAT (particularly given that BAT on the PET/CT scans was not maximally stimulated). This is considered unlikely as many BAT_{prosp} foci lay within the dorsal subcutaneous adipose or tissue layer which is not known to contain BAT.

We have published a case report of an exemplar patient in whom we were fortunate to be able to identify BAT *in vivo* on MR with a high degree of colocalisation with PET/CT. We were also fortunate to be able to obtain immunohistochemical confirmation of BAT – one of the first groups to do so. We recognise that this was a fairly unique case with very large quantities of BAT, and that this method did not allow us to consistently demonstrate BAT on MR in a larger sample.

Although our human sample was small (n=24), the population from which we were able to recruit was limited to the 152 patients with evidence of ^{18}F-FDG BAT on PET/CT. Most PET/CT scans were performed in older patients for oncological disease, many of whom had died in the interim.

Our initial phase of recruitment was opportunistic and yielded a sample with a mean age of 50.3 years, many of whom showed low BAT volumes on PET/CT (and 2 did not undergo concomitant PET/CT). Therefore for our second wave of targeted recruitment we approached younger patients (mean age 36.7 years) in whom we would expect BAT prevalence and volume to be higher.

Of the 24 human subjects, 21 either had cancer or were being investigated for suspected oncological disease. As discussed above, the consensus is that cancer status is not a significant determinant of BAT. Therefore our findings should be generalisable to the wider population. As this was a retrospective study we were not able to control for certain potential confounders including medication status. This is a potential confounder as many commonplace pharmacological agents have been shown to modulate BAT activity including spironolactone [353], baclofen [106], propranolol [183], ephedrine and nicotine [357].

In most cases there was a considerable temporal gap between the PET/CT and MR scans being performed, often within different seasons and at different ambient temperatures. BAT could vary considerably in the intervening period, potentially even involuting altogether.

We could convincingly demonstrate a difference in fat fraction between BAT and WAT identified *a priori*. What is more difficult is to identify BAT prospectively without prior knowledge. We found that the difference in fat fraction between BAT and WAT was typically small in humans, and certainly not large enough to robustly differentiate between these tissues using these techniques. Methods to enhance signal contrast between these tissues may enhance the accuracy of this technique.

10.5.3.3 Choice of MR sequence

The multi-peak fat spectral model used by IDEAL is able to discriminate between fat and water pulses, and provides accurate fat fraction from 0 to 100%. Fat contains multiple spectral peaks [241, 350], therefore IDEAL is intrinsically better than the traditional Dixon method as it models multiple peaks of the fat spectrum, while the traditional Dixon chemical shift method only models a single fat peak corresponding to the methylene group. The accuracy of fraction may be confounded by T1 and T2* effects [236, 358]. T1 effects may be reduced by using low flip angles (*i.e.* by adopting a GRE sequence rather than spin echo sequence). BAT and WAT have different spectral signatures in terms of their chemical composition, lipid profile, and the proportion of saturated and unsaturated fats [244, 350]. Hamilton *et al.* [244] found that murine BAT and WAT had different MR spectral signatures, with a prominent water peak indicating high water content in BAT. In addition the spectral peaks within BAT were slightly broadened possibly due to higher iron content or magnetic field inhomogeneities within the sample. Therefore the accuracy of IDEAL in separating BAT from WAT could be improved by adopting a spectral profile unique to BAT [241]. The accuracy of Dixon-based methods assume a pre-defined spectral model of triglycerides in order that water and fat signal may be separated within a voxel. It is recognised that susceptibility artefact and temperature changes can shift the fat spectrum with respect to the water peak [359], although this effect only becomes significant as the fat-fraction approaches 50%, and for large temperature offsets [360]. The temperature difference between BAT and WAT is likely to be small (in the order of a few degrees) [238], and is unlikely to impact upon the accuracy of Dixon-based imaging.

Traditional Dixon methods are adequate for separating fat and water signals, and are sufficient for qualitative use [361], but using three or more echoes improves accuracy in water-fat separation. Our choice of scanning technique was pragmatic as we only had access to the 3-point IDEAL sequence. Although this performs well against spectroscopy it may not identify all fat spectral peaks, therefore most studies have adopted 6-echo Dixon methods due to their superior accuracy [362] and enhanced separation of BAT and WAT.

Many studies have also employed gradient echo (GRE) MR sequences to demonstrate differences in fat fraction between BAT and WAT [241]. T1-weighted sequences provide the best anatomical definition of the structures [245], and although spin-echo (SE) sequences may yield lower contrast between the tissues, FSE sequences have been used to identify BAT with some success [261]. Spin-echo IDEAL sequences are less effective at separating fat and water peaks than GRE [255], particularly for those fat peaks which lie close to the water peak such as the olefinic acid groups [363] which may erroneously be identified as water, potentially underestimating the true fat fraction [364]. GRE sequences are sensitive to susceptibility effects which perturb the local magnetic field, including that generated by haemoglobin [262] which is abundant on brown adipocyte mitochondria. Susceptibility effects are less of a problem for SE sequences due to the 180° refocussing pulse which counteracts the susceptibility gradients. Indeed the best way to minimise susceptibility effects is to use a spin-echo sequence [365] (hence the decreased sensitivity in BAT identification on spin echo IDEAL). In addition the short acquisition time of GRE sequences means that T2* measurements may be performed in a single breath-hold [262], thereby minimising the effects of respiratory motion.

10.5.3.4 Technical scanning factors

Image contrast in our study was potentially limited by a variety of other factors. Our first wave of volunteers underwent MR scanning at a slice thickness of 5mm. The choice of slice thickness in MR scanning is a compromise; larger slice thicknesses are susceptible to volume averaging artefact, whereby multiple tissue types occur within a voxel, which generates an averaged MR signal. This may be particularly problematic when attempting to identify BAT which tends to occur in small foci within larger expanses of WAT [36, 37]. We found that reducing slice thickness to 2.5mm in six patients contributed to a reduced contrast-to-noise ratio which may negate any improvement in volume averaging artefact. Fat fraction using IDEAL MR has been used successfully to identify BAT interspersed within the interscapular fat in rats [241]. In adults, however, necessity dictated that we adopted a larger field of view, with a corresponding reduction in spatial resolution. Although large confluent BAT deposits would still be evident, small islets may not. Even with a resolution of 0.6mm, Hu *et al.* [241] recognised the potential impact of partial volume effects - particularly at tissue interfaces. To guard against potential false-positive identification of BAT at tissue interfaces, it has been suggested that it may be necessary to rely on *a priori* knowledge of common sites of BAT deposition [2, 37].

Images were acquired during free breathing which occasionally resulted in blurred images. This may be addressed by acquiring images whilst the patients hold their breath which is better suited to the faster GRE sequences. Respiratory gating (in which images are acquired at a fixed point in the respiratory cycle) may minimise motion artefact from breathing, although this would render the scanning time prohibitively long. A third alternative would be to reorder the phase-encoding steps according to the phase of the respiratory cycle [366]. MR data are collected during each stage of the respiratory cycle thereby limiting variation to a single cycle of respiration, rather than several cycles, without increasing scanning time. This technique of respiratory-ordered phase encoding (ROPE) works well in patients with regular respiratory cycles, but less well in those with irregular breathing pattern.

Although we sought to use PET/CT to identify areas of likely BAT on MR, the scans were not performed concurrently; they were often performed in different seasons, and in some cases years (mean interval 47.8 ± 50.5 weeks, range 1.4 – 258.1 weeks). As BAT is dynamic it is not possible to exclude hyperplasia or involution in the intervening period between the two scans.

Quantitative MR using proton density fat fraction derived from chemical-shift water-fat MR has been validated as a means of quantifying fat mass in pigs [367], with high levels of reproducibility [368]. Although we demonstrated significant differences in the fat fraction of BAT and WAT in both rats and humans, our attempts to identify BAT on the basis of fat fraction did not yield consistently reliable results. Although our technique, which utilised the 3-point IDEAL FSE sequence at 3T did not work consistently in our hands, we present a novel implementation of quantitative colocalisation analysis which may assist in validating future work.

Chapter 11: Future directions

In this thesis we explored the role of two imaging modalities in the detection and quantification of *in vivo* BAT in humans. We demonstrated the highly variable nature of ^{18}F-FDG PET/CT, and the comparatively poor sensitivity and specificity of MR imaging in detecting BAT. Future BAT research requires an accurate means of quantifying BAT, and there is a need for imaging techniques with superior accuracy to those explored in this thesis.

11.1 The future of PET/CT in BAT detection and quantification

Most studies evaluating BAT prevalence on PET/CT are retrospective, which hinders direct comparison between studies. The adoption of standardised protocols (*i.e.* standardised temperature, diet, clothing) for calculating BAT prevalence, mass and activity in PET studies would facilitate comparison of PET/CT studies.

A potential limitation of ^{18}F-FDG PET/CT is that glucose is not the preferred substrate of BAT, therefore the development of PET radiotracers specific to fatty acid uptake within BAT may be more appropriate [5]. Novel radioactive tracers have been developed which are preferentially taken up by BAT. One such novel radiotracer is 4-^{18}F-fluorobenzyltriphenyl phosphonium (^{18}F-FBnTP) which accumulates in mitochondria as a function of uncoupling, and is washed out during thermogenesis [369]. This radiotracer has the potential to detect inactive BAT as well as quantifying thermogenic activity.

As discussed at length above ^{18}F-FDG PET/CT reflects metabolic activity of BAT. The sensitivity of these techniques may be enhanced by stimulating BAT beforehand. Thus far dedicated prospective studies of BAT prevalence have sought to stimulate the dense sympathetic innervation in order to activate BAT. The commonest means of stimulating sympathetic BAT is cold, including intermittently dipping feet in cold water [44, 125], although it has been suggested that this method is not physiological as BAT is selectively activated through dedicated sympathetic nerve fibres activated by cold-sensitive centres in the brain rather than through general sympathetic outflow [2]. Consequently administration of systemic non-selective β-adrenergic agonists (*e.g.* isoprenaline) which successfully mimics sympathetic stimulation does not result in an increase in BAT activity [370].

11.2 Alternative imaging techniques in BAT detection and quantification

As the primary function of BAT is non-shivering thermogenesis, temperature presents an alternative route for identifying BAT.

Infrared thermography has been used to measure BAT in humans in a pilot study of 87 human adults [371]. This showed highest temperatures within the supraclavicular fossae, in which BAT is most prevalent. After exposure to cold, skin temperature within the supraclavicular fossae showed a smaller decrease (0.9°C) than other skin sites (2°C) although further work is required to determine whether this reflects changes in blood flow or true thermogenesis within BAT [371, 372].

Recently real-time 3D microwave imaging based methods have been used to successfully monitor subcutaneous heat deposition in breast-mimicking phantoms during microwave ablation therapy [373]. Although sub-centimetre spatial resolution was reported, with a sensitivity of 0.5°C, the technique was only found to be effective over hyperthermia and ablation temperature ranges, which are all higher than healthy tissue. It would be worth exploring whether this technique could allow dynamic *in vivo* monitoring of BAT following stimulation.

These methods, which use temperature increase as a surrogate marker for BAT, may not be identifying true brown or beige adipose tissue. Although BAT is recognised as the primary effector organ for non-shivering thermogenesis, this is not exclusively the case, for example non-shivering thermogenesis has been described in the Tasmanian bettong (*Bettongia gaimardi*) which is not attributable to BAT [374]. Although these techniques may provide indirect quantification of BAT activity they do not enable quantification of BAT volume.

11.3 The future of MR in BAT detection and quantification

The mainstay of non-invasive BAT imaging has been PET/CT, although this has several practical and ethical limitations including the administration of expensive short-lived radiotracers into several subjects, potentially on several occasions. A drive towards developing alternative means of identifying BAT has focussed on MR, which may able to detect BAT regardless of its state of activation [189]. MR studies have largely focussed on using chemical shift MR techniques to identify differences in fat fraction as a means of differentiating BAT and WAT (with BAT fat fraction being lower than that of WAT). Chemical shift techniques may be combined with a spectral pre-saturation inversion recovery (DUAL-SPIR) pulse to suppress fat signal [243]. Due to the high water content of BAT, MR signal persists even with fat saturation and could be used to mask out WAT in a similar manner to that described by Chen *et al.* [261], thereby potentially increasing accuracy. This technique has shown better correlation with histological findings than either ^{18}F-FDG PET/CT or chemical shift MR.

Initial hopes that fat fraction would allow the identification of anatomical BAT deposits have been undermined by the discovery that fat fraction varies within BAT, reflecting its functional status.

Contrast between BAT and WAT may be enhanced by increasing field strength, or by administering agents to amplify signal from the tissue of interest. One such technique uses hyperpolarised gas (typically noble gases *e.g.* ^{129}Xe) as a contrast agent. The hyperpolarised gas dissolves avidly in blood and shows a large chemical shift. As a result this can enhance signal to noise ratio even at low field strengths. Hyperpolarised ^{13}C has also been used to identify activated BAT in rodents [375]. Activated BAT is characterised by increased levels of oxidative phosphorylation and pyruvate metabolism. The incorporation of hyperpolarised ^{13}C into pyruvate and its metabolites allows their spatial distribution to be visualised using a dynamic chemical-shift-specific ^{13}C-imaging MR sequence [376].

The thermogenic ability of BAT may be targeted using MR. Proton resonance frequency (PRF) based techniques have been used for the non-invasive measurement of temperature changes *in vivo* during thermal ablation therapies [377]. The temperatures experienced during such therapies are likely much higher than that generated by BAT, and therefore these techniques may be insensitive to the small changes in temperature generated by BAT.

Gifford *et al.* [238] showed that MR temperature mapping may be used at physiological temperatures to identify activated BAT in adult humans *in vivo*. A temperature change of between 2.1°C and 6.2°C was reported in cold activated BAT (16°C), compared to -1.6°C to 4.1°C in inactive BAT at thermoneutrality (24°C).

BAT is highly vascular due to the need to transport nutrients and dissipate the heat generated by non-shivering thermogenesis. BAT perfusion has been shown to more than double following cold exposure [125, 378]. Basal oxygen consumption within BAT has been shown to be approximately 300% higher than subcutaneous WAT [379]. Techniques that aim to differentiate BAT and WAT have been be developed to exploit differences in local perfusion and oxygen consumption, and is exemplified by the functional MR technique blood-oxygen-level dependent (BOLD) imaging [277]. This technique detects metabolic activity by measuring haemodynamic changes resulting from changes in oxygen demand, which requires a measurement pre- and post-stimulus. This would rely on differences in magnetic susceptibility between oxyhaemoglobin (in oxygenated blood) and deoxyhaemoglobin (in deoxygenated blood), which becomes more apparent with increased blood flow. This techniques has shown promise in BAT research, with an increase in MR signal strength by 10.7% ± 1.8% following a decrease in temperature from 22-24°C to 13-16°C – higher than the MR signal changes seen in typical functional MR brain studies. Unfortunately this technique is limited to *in vivo* imaging.

The incorporation of superparamagnetic iron oxide nanocrystals into the lipoprotein cores has been suggested [22] as novel MR tracers although this may be insufficiently sensitive to detect inactive BAT.

A novel technique using intermolecular zero-quantum coherence transitions (iZQC) has been used to differentiate BAT and WAT in rats [380], and potentially overcome the problem of partial volume (or volume averaging) artefact. Large differences in the water–methylene and the olefinic–methylene peak ratio in the iZQC spectrum of BAT and WAT have been reported. This technique has shown the methylene-olefinic iZQC signal to be strong both in BAT and WAT, but that the water-methylene iZQC signal is specific to BAT.

In the field of BAT research, a variety of imaging technique have been suggested, all of which have their limitations. Their accuracy may be improved by adopting a multi-parametric approach in which multiple sequences are combined, although this would necessitate highly accurate co-registration of images using both rigid and non-rigid registration to allow for multimodality and temporal variation.

Appendix A: Supplementary tables

Supplementary table 1: Binomial univariate logistic regression analysis of patients' first scans (n=2,685), showing predictors of ^{18}F-FDG BAT.

Characteristic	B (SE)	*P*-value	95% CI for odds ratio		
			Odds ratio	Lower	Upper
Age	-0.051 (0.005)	<0.001	0.950	0.940	0.960
Sex (M compared to F)	-1.451 (0.196)	<0.001	0.234	0.160	0.344
BMI (kg/m^2)	-0.094 (0.019)	<0.001	0.911	0.878	0.945
Lean body mass (kg)	-0.072 (0.010)	<0.001	0.931	0.913	0.949
Basal metabolic rate	-0.001 (0.000)	<0.001	0.999	0.998	0.999
Fasting serum glucose (mmol/l)	-0.293 (0.082)	<0.001	0.746	0.635	0.876
Injected ^{18}F-FDG dose (MBq)	0.000 (0.003)	0.967	1.000	0.995	1.005
Time of scan	0.000 (0.000)	0.006	1.000	1.000	1.000
Temperature on scan date (°C)					
Minimum	-0.064 (0.016)	<0.001	0.938	0.909	0.967
Mean	-0.068 (0.015)	<0.001	0.934	0.907	0.962
Maximum	-0.064 (0.013)	<0.001	0.938	0.914	0.963
Temperature on preceding day					
(°C)	-0.064 (0.016)	<0.001	0.938	0.909	0.967
Minimum	-0.069 (0.015)	<0.001	0.934	0.906	0.962
Mean	-0.059 (0.013)	<0.001	0.943	0.919	0.968
Maximum					
Preceding 3 days' temperature (°C)					
Minimum	-0,.065 (0.016)	<0.001	0.937	0.909	0.967
Mean	-0.076 (0.016)	<0.001	0.926	0.898	0.955
Maximum	-0.062 (0.013)	<0.001	0.939	0.915	0.964
Preceding week's temperature (°C)					
Minimum	-0.040 (0.015)	0.009	0.961	0.932	0.990
Mean	-0.072 (0.016)	<0.001	0.931	0.901	0.961
Maximum	-0.060 (0.014)	<0.001	0.941	0.916	0.967
Mean monthly temperature (°C)	-0.063 (0.017)	<0.001	0.939	0.908	0.971
Hours of sunlight on scan date	-0.074 (0.017)	<0.001	0.928	0.899	0.959
Total monthly hours of sunlight	-0.005 (0.002)	0.004	0.995	0.992	0.998

Supplementary table 2: Binomial multivariate logistic regression analysis (forced entry method) of patients' first scans (n=2,685), showing predictors of ^{18}F-FDG BAT.

Characteristic	B (SE)	P-value	95% CI for odds ratio		
			Odds ratio	Lower	Upper
Constant	6.010 (1.020)				
Age (years)	-0.046 (0.006)	<0.001	0.955	0.944	0.966
Sex (M compared to F)	-1.429 (0.205)	<0.001	0.240	0.160	0.358
BMI (kg/m^2)	-0.085 (0.018)	<0.001	0.919	0.887	0.952
Fasting serum glucose (mmol/l)	-0.168 (0.088)	0.057	0.845	0.711	1.005
Time of scan	0.000 (0.000)	<0.001	1.000	1.000	1.000
Temperature on scan date					
Minimum	-0.018 (0.081)	0.824	0.982	0.838	1.152
Mean	0.041 (0.070)	0.555	1.042	0.909	1.194
Maximum	-0.111 (0.065)	0.089	0.895	0.788	1.017
Temperature on preceding day					
Minimum	0.065 (0.055)	0.239	1.067	0.958	1.189
Mean	0.131 (0.169)	0.438	1.140	0.818	1.588
Maximum	0.036 (0.092)	0.696	1.036	0.866	1.241
Preceding 3 days' temperature					
Minimum	0.004 (0.069)	0.948	1.004	0.878	1.150
Mean	-0.359 (0.186)	0.054	0.698	0.485	1.006
Maximum	0.025 (0.088)	0.780	1.025	0.863	1.218
Preceding week's temperature					
Minimum	0.046 (0.030)	0.127	1.047	0.987	1.110
Mean	0.036 (0.118)	0.758	1.037	0.823	1.307
Maximum	-0.004 (0.071)	0.960	0.966	0.867	1.145
Mean monthly temperature	0.018 (0.057)	0.754	1.018	0.911	1.138
Hours of sunlight on scan date	0.023 (0.115)	0.841	1.023	0.817	1.282
Total monthly hours of sunlight	0.000 (0.003)	0.981	1.000	0.995	1.005

R^2 goodness of fit tests= 0.079 (Cox and Snell), 0.228 (Nagelkerke).

Supplementary table 3: Correlation matrix of ^{18}F-FDG BAT determinants.

	Age	Sex	Scan time	BM (mmol/L)	BMI	Min temp on scan date	Mean temp on scan date	Max temp on scan date	Preceding day's min temp	Preceding day's mean temp	Preceding day's max temp	Preceding 3-days' min temp (°C)	Preceding 3-days' mean temp (°C)	Preceding 3-days' max temp (°C)	Preceding week's min temp	Preceding week's mean temp	Preceding week's max temp	Mean monthly temp	Daily sunshine (hours)	Total monthly sunshine (h)
Age	1	.080	0.023	.240	0.018	0.011	-0.002	-0.005	-0.009	0.001	-0.007	0.013	0.002	-0.002	0.012	0.006	0.008	0.006	-0.01	-0.013
Sex	.080	1	0.002	0.02	0.033	0.005	-0.001	0.004	0.009	0.012	0.015	0.002	0.008	0.007	-0.002	-0.004	-0.004	-0.021	.036	0.007
Scan time	0.023	0.002	1	-.197	.039	-0.028	-0.032	-0.033	-0.025	-0.028	-0.025	-0.02	-0.026	-0.025	-0.001	-0.028	-0.028	-.042	.054	0.015
BM (mmol/L)	.240	0.02	-.197	1	.060	-0.005	-0.012	-0.011	-0.011	-0.016	-0.018	-0.022	-0.016	-0.02	-0.02	-0.012	-0.009	-0.009	-.035	-0.021

Total monthly sunshine (h)	Daily sunshine (hours)	Mean monthly temp	Preceding week's max temp	Preceding week's mean temp	Preceding week's min temp	Preceding 3-days' max temp	Preceding 3-days' mean temp	Preceding 3-days' min temp	Preceding day's max temp	Preceding day's mean temp	Preceding day's min temp	Max temp on scan date	Mean temp on scan date	Min temp on scan date	BMI	
-0.013	-0.01	0.006	0.008	0.006	0.012	-0.002	0.002	0.013	-0.007	0.001	-0.009	-0.005	-0.002	0.011	0.018	Age
0.007	.036*	-0.021	-0.004	-0.004	-0.002	0.007	0.008	0.002	0.015	0.012	0.009	0.004	-0.001	0.005	0.033	Sex
0.015	.054**	-.042*	-0.028	-0.028	-0.001	-0.025	-0.026	-0.02	-0.025	-0.028	-0.025	-0.033	-0.032	-0.028	.039	Scan time
-0.021	-.035*	-0.009	-0.009	-0.012	-0.02	-0.02	-0.016	-0.022	-0.018	-0.016	-0.011	-0.011	-0.012	-0.005	.060	BM (mmol/L)
-0.019	-0.028	-0.02	-0.022	-0.025	-0.025	-0.02	-0.013	-0.015	-0.011	-0.014	0.002	-0.019	-0.022	-0.015	1	BMI
.402**	.249**	.794**	.798**	.845**	.788**	.818**	.884**	.783**	.847**	.941	.834	.810	.853	1	-0.015	Min temp on scan date
.531**	.373**	.862**	.859**	.876**	.809**	.879**	.896**	.792**	.910**	.926	.790	.962	1	.853	-0.022	Mean temp on scan date
.612**	.419**	.870**	.873**	.871**	.788**	.896**	.896**	.777**	.923**	.915	.773	1	.962	.810	-0.019	Max temp on scan date
.398**	.178**	.799**	.816**	.866**	.829**	.844**	.914**	.896**	.823**	.859	1	.773	.790	.834	0.002	Preceding day's min temp
.523**	.368**	.867**	.891**	.916**	.829**	.926**	.959**	.829**	.965**	1	.859	.915	.926	.941	-0.014	Preceding day's mean temp
.597**	.453**	.877**	.910**	.910**	.809**	.953**	.948**	.813**	1	.965	.823	.923	.910	.847	-0.011	Preceding day's max temp
.411**	.179**	.833**	.848**	.908**	.913**	.856**	.907**	1	.813**	.829	.896	.777	.792	.783	-0.015	Preceding 3-days' min temp (°C)
.533**	.363**	.893**	.934**	.965**	.877**	.969**	1	.907**	.948**	.959	.914	.896	.896	.884	-0.013	Preceding 3-days' mean temp (°C)
.614**	.456**	.894**	.956**	.947**	.845**	1	.969**	.856**	.953**	.926	.844	.896	.879	.818	-0.02	Preceding 3-days' max temp (°C)
.416**	.226**	.864**	.862**	.923**	1	.845**	.877**	.913**	.809**	.829	.829	.788	.809	.788	-0.025	Preceding week's min temp
.527**	.372**	.916**	.964**	1	.923**	.947**	.965**	.908**	.910**	.916	.866	.871	.876	.845	-0.025	Preceding week's mean temp
.615**	.433**	.907**	1	.964**	.862**	.956**	.934**	.848**	.910**	.891	.816	.873	.859	.798	-0.022	Preceding week's max temp
.601**	.382**	1	.907**	.916**	.864**	.894**	.893**	.833**	.877**	.867	.799	.870	.862	.794	-0.02	Mean monthly temp
.547**	1	.382**	.433**	.372**	.226**	.456**	.363**	.179**	.453**	.368	.178	.419	.373	.249	-0.028	Daily sunshine (hours)
1	.547**	.601**	.615**	.527**	.416**	.614**	.533**	.411**	.597**	.523	.398	.612	.531	.402	-0.019	Total monthly sunshine (h)

Appendix B: Articles, abstracts and presentations arising from this work

Peer-reviewed articles

- Reddy, N.L., Jones T.A. *et al.*, *Identification of brown adipose tissue using MR imaging in a human adult with histological and immunohistochemical confirmation.* J Clin Endocrin Metab, 2014. **99**(1): E117-E121.

Abstracts

- Jones, T.A., *et al.*, *Visual identification of brown adipose tissue in adult humans using Dixon MRI.* Proc. Intl. Soc. Mag. Reson. Med., 2014. **22**: 2144.
- Jones T.A., Reddy N.L. *et al.*, *Unequivocal identification of brown adipose tissue in an adult human using MRI.* Clinical Radiology 2013. **68** (Suppl 1): S2.
- Wayte, S.C., Reddy, N.L., Jones. T.A. *et al.*, *Identification of brown adipose tissue using Dixon imaging in a human adult with histological confirmation.* Proc. Intl. Soc. Mag. Reson. Med., 2013. **21**: p. 4052.
- Reddy, N.L., Jones. T.A. *et al.*, *Brown adipose tissue identification in an adult human using IDEAL MRI.* Endocrine Abstracts., 2013. **31**: P221.
- Reddy, N.L., Jones. T.A. *et al.*, *Unequivocal identification of brown adipose tissue in an adult human using Magnetic Resonance Imaging.* Proc. Physiol. Soc., 2012. **29**: C11 and PC11.

Presentations and posters

- Jones, T.A., *et al.*, *Visual identification of brown adipose tissue in adult humans using Dixon MRI.* Poster presentation at ISMRM, Milan, 10-16th May 2014.
- Jones T.A., *Tissue characterisation: brown fat and myositis*. Oral presentation at the West Midlands Association of Radiologists Autumn Scientific meeting, Coventry, 26th September 2013.
- Wayte, S.C., Reddy, N.L., Jones. T.A. *et al.*, *Identification of brown adipose tissue using Dixon imaging in a human adult with histological confirmation.* Poster presentation at ISMRM, Salt Lake City 2013.
- Jones T.A., Reddy, N. L. *et al.*, *Unequivocal identification of brown adipose tissue in an adult human using MRI.* Poster presentation at the Royal College of

Radiologists Clinical Radiology Annual Scientific Meeting, London, September 2013.

- Reddy, N.L., Jones. T.A. *et al*., *Identification of brown adipose tissue using MR imaging in a human adult with histological and imunohistochemical confirmation.* American Diabetes Association 73rd Scientific Sessions, Chicago, 21-25th June 2013.
- Reddy, N.L., Jones. T.A. *et al*., *Brown adipose tissue identification in an adult human using IDEAL MRI.* Oral presentation and poster at the Society for Endocrinology/British Endocrine Society annual meeting, Harrogate, 18-21th March 2013.
- Jones T.A., Reddy, N. L. *et al*., *Unequivocal identification of brown adipose tissue in an adult human using MRI*. Poster presentation at the West Midlands Association of Radiologists Spring Scientific meeting, Stoke-on-Trent, 16th April 2013.
- Reddy, N.L., Jones. T.A. *et al*., *Unequivocal identification of brown adipose tissue in an adult human using Magnetic Resonance Imaging.* Oral presentation and poster at the Physiological Society annual meeting, London 2012.

Other media

- Basset, M. *Use of MR to Identify Brown Fat Could Fuel Obesity Therapies*. RSNA News, 2014, **24** (12): 7-8.
- *Key milestone for brown fat research with a ground-breaking MRI scan.* University of Warwick website. URL: http://www2.warwick.ac.uk/newsandevents/pressreleases/key_milestone_for/.

References

1. Saarela, S., et al., *Is the "mammalian" brown fat-specific mitochondrial uncoupling protein present in adipose tissues of birds?* Comp Biochem Physiol B, 1991. **100**(1): p. 45-9.
2. Cannon, B. and J. Nedergaard, *Brown adipose tissue: function and physiological significance.* Physiol Rev, 2004. **84**(1): p. 277-359.
3. Saely, C.H., K. Geiger, and H. Drexel, *Brown versus white adipose tissue: a mini-review.* Gerontology, 2012. **58**(1): p. 15-23.
4. Ronti, T., G. Lupatelli, and E. Mannarino, *The endocrine function of adipose tissue: an update.* Clin Endocrinol (Oxf), 2006. **64**: p. 355-65.
5. Enerback, S., *Human brown adipose tissue.* Cell Metab, 2010. **11**(4): p. 248-52.
6. Gesner, K., *Conradi Gesneri medici Tigurini historiae animalium lib. I. de quadrupedibus viviparis*. 1551: Tiguri: apud Christ. Froschoverum.
7. Weber, W.A., *Brown adipose tissue and nuclear medicine imaging.* J Nucl Med, 2004. **45**(7): p. 1101-3.
8. Hatai, S., *On the presence in human embryos of an interscapular gland corresponding to the so-called hibernating gland in lower animals.* Anatomy Anzeiger, 1905. **xxi**: p. 369-373.
9. Bonnot, E., *The interscapular gland.* Journal of anatomy and physiology, 1908. **43**(Pt 1): p. 43.
10. Merkel, F., *Topographische Anatomie*. 1899: Braunschweig.
11. Charpy, A., *Traité d'anatomie humaine*, Poirier-Charpy, Editor. 1902: Paris.
12. Smith, R.E., *Thermogenic activity of the hubernating gland in the cold-acclimated rat.* Physiologist, 1961. **4**: p. 113.
13. Kolesnikov, V.V., O.V. Brandler, and B.B. Badmaev, *Folk use of marmots in Mongolia.* Ethnobiology, Ecology & Evolution, 2009. **21**: p. 285-7.
14. Klingenspor, M. and T. Fromme, *Brown adipose tissue*. Adipose Tissue Biology, ed. M.E. Symonds. 2012, New York: Springer. 39-69.
15. Del Mar Gonzalez-Barroso, M., D. Ricquier, and A.M. Cassard-Doulcier, *The human uncoupling protein-1 gene (UCP1): present status and perspectives in obesity research.* Obes Rev, 2000. **1**(2): p. 61-72.
16. Claessens-van Ooijen, A.M., et al., *Heat production and body temperature during cooling and rewarming in overweight and lean men.* Obesity (Silver Spring), 2006. **14**(11): p. 1914-20.
17. Power, G., *Biology of temperature: the mammalian fetus.* J Dev Physiol, 1989. **12**: p. 295-304.
18. Puchalski, W., et al., *Organ blood flow and brown adipose tissue oxygen consumption during noradrenaline-induced nonshivering thermogenesis in the Djungarian hamster.* J Exp Zool, 1987. **242**(3): p. 263-71.
19. Foster, D.O. and M.L. Frydman, *Nonshivering thermogenesis in the rat. II. Measurements of blood flow with microspheres point to brown adipose tissue as the dominant site of the calorigenesis induced by noradrenaline.* Can J Physiol Pharmacol, 1978. **56**(1): p. 110-22.
20. Rothwell, N.J. and M.J. Stock, *Luxuskonsumption, diet-induced thermogenesis and brown fat: the case in favour.* Clin Sci (Lond), 1983. **64**(1): p. 19-23.
21. Rothwell, N.J. and M.J. Stock, *A role for brown adipose tissue in diet-induced thermogenesis.* Nature, 1979. **281**(5726): p. 31-5.
22. Bartelt, A., et al., *Brown adipose tissue activity controls triglyceride clearance.* Nat Med, 2011. **17**(2): p. 200-5.

23. Himms-Hagen, J., *Obesity may be due to a malfunctioning of brown fat.* Can Med Assoc J, 1979. **121**(10): p. 1361-4.
24. Nedergaard, J. and B. Cannon, *The changed metabolic world with human brown adipose tissue: therapeutic visions.* Cell Metab, 2010. **11**(4): p. 268-72.
25. Almind, K., et al., *Ectopic brown adipose tissue in muscle provides a mechanism for differences in risk of metabolic syndrome in mice.* Proc Natl Acad Sci U S A, 2007. **104**(7): p. 2366-71.
26. Bartelt, A. and J. Heeren, *The holy grail of metabolic disease: brown adipose tissue.* Current Opinion in Lipidology, 2012.
27. Astrup, A., et al., *Ephedrine-induced thermogenesis in man: no role for interscapular brown adipose tissue.* Clin Sci (Lond), 1984. **66**(2): p. 179-86.
28. Cunningham, S., et al., *The characterization and energetic potential of brown adipose tissue in man.* Clin Sci (Lond), 1985. **69**(3): p. 343-8.
29. Kozak, L.P., *Brown fat and the myth of diet-induced thermogenesis.* Cell Metab, 2010. **11**(4): p. 263-7.
30. Lean, M.E., *Brown adipose tissue in humans.* Proc Nutr Soc, 1989. **48**(2): p. 243-56.
31. Dawkins, M.J. and J.W. Scopes, *Non-shivering thermogenesis and brown adipose tissue in the human new-born infant.* Nature, 1965. **206**(980): p. 201-2.
32. Lean, M.E. and G. Jennings, *Brown adipose tissue activity in pyrexial cases of cot death.* J Clin Pathol, 1989. **42**(11): p. 1153-6.
33. Merklin, R.J., *Growth and distribution of human fetal brown fat.* Anat Rec, 1974. **178**(3): p. 637-45.
34. Lean, M.E., et al., *Brown adipose tissue uncoupling protein content in human infants, children and adults.* Clin Sci (Lond), 1986. **71**(3): p. 291-7.
35. Gesta, S., Y.H. Tseng, and C.R. Kahn, *Developmental origin of fat: tracking obesity to its source.* Cell, 2007. **131**(2): p. 242-256.
36. Zingaretti, M.C., et al., *The presence of UCP1 demonstrates that metabolically active adipose tissue in the neck of adult humans truly represents brown adipose tissue.* FASEB J, 2009. **23**(9): p. 3113-20.
37. Heaton, J.M., *The distribution of brown adipose tissue in the human.* J Anat, 1972. **112**(Pt 1): p. 35-9.
38. Cypess, A.M., et al., *Identification and importance of brown adipose tissue in adult humans.* N Engl J Med, 2009. **360**(15): p. 1509-17.
39. Huttunen, P., J. Hirvonen, and V. Kinnula, *The occurrence of brown adipose tissue in outdoor workers.* Eur J Appl Physiol Occup Physiol, 1981. **46**(4): p. 339-45.
40. English, J., S. Patel, and M. Flanagan, *Association of pheochromocytomas with brown fat tumours.* Radiology, 1973. **1973**(107).
41. Fukuchi, K., et al., *Radionuclide imaging metabolic activity of brown adipose tissue in a patient with pheochromocytoma.* Exp Clin Endocrinol Diabetes, 2004. **112**(10): p. 601-3.
42. Saito, M., et al., *High incidence of metabolically active brown adipose tissue in healthy adult humans: effects of cold exposure and adiposity.* Diabetes, 2009. **58**(7): p. 1526-31.
43. van Marken Lichtenbelt, W.D., et al., *Cold-activated brown adipose tissue in healthy men.* N Engl J Med, 2009. **360**(15): p. 1500-8.
44. Virtanen, K.A., et al., *Functional brown adipose tissue in healthy adults.* N Engl J Med, 2009. **360**(15): p. 1518-25.
45. Lowell, B.B. and B.M. Spiegelman, *Towards a molecular understanding of adaptive thermogenesis.* Nature, 2000. **404**(6778): p. 652-60.
46. Jastroch, M., et al., *Marsupial uncoupling protein 1 sheds light on the evolution of mammalian nonshivering thermogenesis.* Physiol Genomics, 2008. **32**(2): p. 161-9.
47. Enerbäck, S., *The origins of brown adipose tissue.* N Engl J Med, 2009. **360**(19): p. 2021-3.

48. Atit, R., et al., *β-catenin activation is necessary and sufficient to specify the dorsal dermal fate in the mouse.* Dev Biol, 2006. **296**(1): p. 164-176.
49. Tang, W., et al., *White fat progenitor cells reside in the adipose vasculature.* Science, 2008. **322**(5901): p. 583-6.
50. Seale, P., et al., *PRDM16 controls a brown fat/skeletal muscle switch.* Nature, 2008. **454**(7207): p. 961-7.
51. Timmons, J.A., et al., *Myogenic gene expression signature establishes that brown and white adipocytes originate from distinct cell lineages.* Proceedings of the National Academy of Sciences, 2007. **104**(11): p. 4401-4406.
52. Seale, P., et al., *Transcriptional control of brown fat determination by PRDM16.* Cell Metab, 2007. **6**(1): p. 38-54.
53. Tseng, Y.H., et al., *New role of bone morphogenetic protein 7 in brown adipogenesis and energy expenditure.* Nature, 2008. **454**(7207): p. 1000-4.
54. Cinti, S., *Adipocyte differentiation and transdifferentiation: plasticity of the adipose organ.* J Endocrinol Invest, 2002. **25**(10): p. 823-35.
55. Guerra, C., et al., *Emergence of brown adipocytes in white fat in mice is under genetic control. Effects on body weight and adiposity.* J Clin Invest, 1998. **102**(2): p. 412-20.
56. Jespersen, Naja Z., et al., *A Classical Brown Adipose Tissue mRNA Signature Partly Overlaps with Brite in the Supraclavicular Region of Adult Humans.* Cell Metabolism, 2013. **17**(5): p. 798-805.
57. Wu, J., et al., *Beige adipocytes are a distinct type of thermogenic fat cell in mouse and human.* Cell, 2012. **150**(2): p. 366-76.
58. Christian, M. and M.G. Parker, *The engineering of brown fat.* J Mol Cell Biol, 2010. **2**(1): p. 23-5.
59. Schulz, T.J., et al., *Identification of inducible brown adipocyte progenitors residing in skeletal muscle and white fat.* Proc Natl Acad Sci U S A, 2011. **108**(1): p. 143-8.
60. Petrovic, N., et al., *Chronic peroxisome proliferator-activated receptor gamma (PPARgamma) activation of epididymally derived white adipocyte cultures reveals a population of thermogenically competent, UCP1-containing adipocytes molecularly distinct from classic brown adipocytes.* J Biol Chem, 2010. **285**(10): p. 7153-64.
61. Koppen, A. and E. Kalkhoven, *Brown vs white adipocytes: The PPARγ coregulator story.* FEBS Lett, 2010. **584**(15): p. 3250-3259.
62. Barbatelli, G., et al., *The emergence of cold-induced brown adipocytes in mouse white fat depots is determined predominantly by white to brown adipocyte transdifferentiation.* Am J Physiol Endocrinol Metab, 2010. **298**(6): p. E1244-53.
63. Sharp, L.Z., et al., *Human BAT possesses molecular signatures that resemble beige/brite cells.* PLoS ONE 7, 2012: p. e49452.
64. Walden, T.B., et al., *Recruited vs. nonrecruited molecular signatures of brown, "brite," and white adipose tissues.* Am J Physiol Endocrinol Metab, 2012. **302**(1): p. E19-31.
65. Cannon, B. and J. Nedergaard, *Cell biology: Neither brown nor white.* Nature, 2012. **488**(7411): p. 286-287.
66. Aherne, W. and D. Hull, *Brown adipose tissue and heat production in the newborn infant.* J Pathol Bacteriol, 1966. **91**(1): p. 223-34.
67. Cinti, S., *The role of brown adipose tissue in human obesity.* Nutr Metab Cardiovasc Dis, 2006. **16**(8): p. 569-74.
68. Cinti, S., *Transdifferentiation properties of adipocytes in the adipose organ.* Am J Physiol Endocrinol Metab, 2009. **297**(5): p. E977-86.
69. Mannella, C.A., *Structure and dynamics of the mitochondrial inner membrane cristae.* Biochim Biophys Acta, 2006. **1763**(5-6): p. 542-8.
70. Cousin, B., et al., *Occurrence of brown adipocytes in rat white adipose tissue: molecular and morphological characterization.* J Cell Sci, 1992. **103 (Pt 4)**: p. 931-42.
71. Hausberger, F.X. and M.M. Widelitz, *Distribution of labeled erythrocytes in adipose tissue and muscle in the rat.* Am J Physiol, 1963. **204**(4): p. 649-52.

72. Cinti, S., *Anatomy of the adipose organ.* Eat Weight Disord, 2000. **5**(3): p. 132-142.
73. Foster, D.O. and M.L. Frydman, *Tissue distribution of cold-induced thermogenesis in conscious warm- or cold-acclimated rats reevaluated from changes in tissue blood flow: the dominant role of brown adipose tissue in the replacement of shivering by nonshivering thermogenesis.* Can J Physiol Pharmacol, 1979. **57**(3): p. 257-70.
74. Zhao, J., B. Cannon, and J. Nedergaard, *Thermogenesis is beta3- but not beta1-adrenergically mediated in rat brown fat cells, even after cold acclimation.* Am J Physiol, 1998. **275**(6 Pt 2): p. R2002-11.
75. Giordano, A., et al., *Presence and distribution of cholinergic nerves in rat mediastinal brown adipose tissue.* J Histochem Cytochem, 2004. **52**(7): p. 923-30.
76. Rolfe, D., et al., *Contribution of mitochondrial proton leak to respiration rate in working skeletal muscle and liver to SMR.* Am J Physiol, 1999. **276**(3 part 1): p. C692-699.
77. Nicholls, D.G. and R.M. Locke, *Thermogenic mechanisms in brown fat.* Physiol Rev, 1984. **64**(1): p. 1-64.
78. Nedergaard, J., et al., *UCP1: the only protein able to mediate adaptive non-shivering thermogenesis and metabolic inefficiency.* Biochim Biophys Acta, 2001. **1504**(1): p. 82-106.
79. Afong, M., et al., *Immunological studies of the uncoupling protein of brown adipose tissue.* Can J Biochem Cell Biol, 1985. **63**(2): p. 96-101.
80. Silva, J. and P. Larsen, *Adrenergic activation of triidothyronine production in brown adipose tissue.* Nature, 1983. **305**: p. 712-3.
81. Cannon, B. and J. Nedergaard, *Thyroid hormones: igniting brown fat via the brain.* Nat Med, 2010. **16**(9): p. 965-7.
82. Celi, F.S., *Brown adipose tissue--when it pays to be inefficient.* N Engl J Med, 2009. **360**(15): p. 1553-6.
83. Shimizu, Y., H. Nikami, and M. Saito, *Sympathetic activation of glucose utilization in brown adipose tissue in rats.* J Biochem, 1991. **110**(5): p. 688-92.
84. Shimizu, Y., et al., *Increased expression of glucose transporter GLUT-4 in brown adipose tissue of fasted rats after cold exposure.* Am J Physiol, 1993. **264**(6 Pt 1): p. E890-5.
85. Cerri, M. and S.F. Morrison, *Activation of lateral hypothalamic neurons stimulates brown adipose tissue thermogenesis.* Neuroscience, 2005. **135**(2): p. 627-38.
86. Fueger, B.J., et al., *Impact of animal handling on the results of 18F-FDG PET studies in mice.* J Nucl Med, 2006. **47**(6): p. 999-1006.
87. Trayhurn, P., *Uncoupling protein in brown adipose tissue: molecular differentiation of the adipose tissues.* Biochem Soc Trans, 1996. **24**(2): p. 402-6.
88. Berg, F., U. Gustafson, and L. Andersson, *The uncoupling protein 1 gene (UCP1) is disrupted in the pig lineage: a genetic explanation for poor thermoregulation in piglets.* PLoS Genet, 2006. **2**(8): p. e129.
89. Xue, B., et al., *Genetic variability affects the development of brown adipocytes in white fat but not in interscapular brown fat.* J Lipid Res, 2007. **48**(1): p. 41-51.
90. Tiraby, C., et al., *Acquirement of brown fat cell features by human white adipocytes.* J Biol Chem, 2003. **278**(35): p. 33370-6.
91. Ohno, H., et al., *PPARγ agonists Induce a White-to-Brown Fat Conversion through Stabilization of PRDM16 Protein.* Cell Metabolism, 2012. **15**(3): p. 395-404.
92. Frontini, A., et al., *White-to-brown transdifferentiation of omental adipocytes in patients affected by pheochromocytoma.* Biochimica et Biophysica Acta (BBA) - Molecular and Cell Biology of Lipids, 2013. **1831**(5): p. 950-959.
93. Nisoli, E., et al., *Tumor necrosis factor-a induces apoptosis in rat brown adipocytes.* Cell Death Differ, 1997. **4**: p. 771-778.
94. Hotamisligil, G.S., *Mechanisms of TNF-alpha-induced insulin resistance.* Exp Clin Endocrinol Diabetes, 1999. **107**(2): p. 119-25.
95. Tews, D. and M. Wabitsch, *Renaissance of brown adipose tissue.* Horm Res Paediatr, 2011. **75**(4): p. 231-9.

96. Jacobsson, A., B. Cannon, and J. Nedergaard, *Physiological activation of brown adipose tissue destabilizes thermogenin mRNA.* FEBS Lett, 1987. **224**(2): p. 353-6.
97. Freeman, K.B., et al., *Effects of exposure temperature on brown adipose tissue uncoupling protein mRNA levels.* Biochem Cell Biol, 1989. **67**(2-3): p. 147-51.
98. Meyer, C.W., et al., *Adaptive thermogenesis and thermal conductance in wild-type and UCP1-KO mice.* Am J Physiol Regul Integr Comp Physiol, 2010. **299**(5): p. R1396-406.
99. Mineo, P.M., et al., *Chronic cold acclimation increases thermogenic capacity, non-shivering thermogenesis and muscle citrate synthase activity in both wild-type and brown adipose tissue deficient mice.* Comp Biochem Physiol A Mol Integr Physiol, 2012. **161**(4): p. 395-400.
100. Enerbäck, S., et al., *Mice lacking mitochondrial uncoupling protein are cold-sensitive but not obese.* Nature, 1997. **387**(6628): p. 90-94.
101. Nedergaard, J., T. Bengtsson, and B. Cannon, *Unexpected evidence for active brown adipose tissue in adult humans.* Am J Physiol Endocrinol Metab, 2007. **293**(2): p. E444-52.
102. Zaror-Behrens, G. and J. Himms-Hagen, *Cold-stimulated sympathetic activity in brown adipose tissue of obese (ob/ob) mice.* Am J Physiol, 1983. **244**(4): p. E361-6.
103. Moura, M.A., et al., *Effect of cold acclimation on brown adipose tissue fatty acid synthesis in rats adapted to a high-protein, carbohydrate-free diet.* Metabolism, 2001. **50**(12): p. 1493-8.
104. Yacoe, M.E., *Changes in mitochondrial components of hamster brown adipose tissue in response to cold acclimation.* Biochem J, 1981. **194**(2): p. 653-6.
105. Lee, P., et al., *High prevalence of brown adipose tissue in adult humans.* J Clin Endocrinol Metab, 2011. **96**(8): p. 2450-5.
106. Addae, J.I., et al., *Activation of thermogenesis of brown fat in rats by baclofen.* Neuropharmacology, 1986. **25**(6): p. 627-31.
107. Norman, D.C., D. Grahn, and T.T. Yoshikawa, *Fever and aging.* J Am Geriatr Soc, 1985. **33**(12): p. 859-63.
108. McDonald, R.B. and B.A. Horwitz, *Brown adipose tissue thermogenesis during aging and senescence.* J Bioenerg Biomembr, 1999. **31**(5): p. 507-16.
109. Scarpace, P.J., et al., *Impaired febrile response with age: role of thermogenesis in brown adipose tissue.* Proc Soc Exp Biol Med, 1992. **200**(3): p. 353-8.
110. Florez-Duquet, M. and R.B. McDonald, *Cold-induced thermoregulation and biological aging.* Physiol Rev, 1998. **78**(2): p. 339-58.
111. Scarpace, P.J., et al., *Thermoregulation with age: role of thermogenesis and uncoupling protein expression in brown adipose tissue.* Proc Soc Exp Biol Med, 1994. **205**(2): p. 154-61.
112. Ueno, N., et al., *Effect of age on brown adipose tissue activity in the obese (ob/ob) mouse.* Mech Ageing Dev, 1998. **100**(1): p. 67-76.
113. Yoneshiro, T., et al., *Age-related decrease in cold-activated brown adipose tissue and accumulation of body fat in healthy humans.* Obesity (Silver Spring), 2011. **19**(9): p. 1755-60.
114. Scarpace, P.J., J. Dove, and M. Matheny, *Effects of age on beta adrenergic subtype activation of adenylyl cyclase in brown adipose tissue.* Proc Soc Exp Biol Med, 1996. **213**(3): p. 262-7.
115. McDonald, R.B., et al., *Effect of age and gender on thermoregulation.* Am J Physiol, 1989. **257**(4 Pt 2): p. R700-4.
116. Timmons, J.A. and B.K. Pedersen, *The importance of brown adipose tissue.* N Engl J Med, 2009. **361**(4): p. 415-6; author reply 418-21.
117. Himms-Hagen, J., *Thermogenesis in brown adipose tissue as an energy buffer. Implications for obesity.* N Engl J Med, 1984. **311**(24): p. 1549-58.

118. Santos, G.C., et al., *Accumulation of brown adipose tissue and nutritional status. A prospective study of 366 consecutive autopsies.* Arch Pathol Lab Med, 1992. **116**(11): p. 1152-4.
119. Feldman, H., et al., *UCP1 ablation induces obesity and abolishes diet-induced thermogenesis in mice exempt from thermal stress by living at thermoneutrality.* Cell Metab, 2009. **9**(2): p. 203-209.
120. Xiao, X.Q., et al., *Excess weight gain during the early postnatal period is associated with permanent reprogramming of brown adipose tissue adaptive thermogenesis.* Endocrinology, 2007. **148**(9): p. 4150-9.
121. Lowell, B.B., et al., *Development of obesity in transgenic mice after genetic ablation of brown adipose tissue.* Nature, 1993. **366**(6457): p. 740-2.
122. World Health Organization, *2008-2013 Action Plan for the Global Strategy for the Prevention and Control of Noncommunicable Diseases*. 2008, World Health Organization: Geneva, Switzerland.
123. World Health Organization, *Obesity and Overweight, Fact sheet No 311*. 2012.
124. Reddy, N., *Novel insights in imaging and function of human brown adipose tissue*, in *Department of Metabolic Medicine*. 2014, University of Warwick.
125. Orava, J., et al., *Different metabolic responses of human brown adipose tissue to activation by cold and insulin.* Cell Metab, 2011. **14**(2): p. 272-9.
126. Muzik, O., et al., *^{15}O PET measurement of blood flow and oxygen consumption in cold-activated human brown fat.* J Nucl Med, 2013. **54**(4): p. 523-31.
127. Au-Yong, I.T., et al., *Brown adipose tissue and seasonal variation in humans.* Diabetes, 2009. **58**(11): p. 2583-7.
128. Cheng, W.Y., Z.H. Zhu, and M. Ouyang, *[Patterns and characteristics of brown adipose tissue uptake of 18F-FDG positron emission tomography/computed tomography imaging].* Zhongguo Yi Xue Ke Xue Yuan Xue Bao (Acta Acad Med Sin), 2009. **31**(3): p. 370-373.
129. Cohade, C., K. Mourtzikos, and R. Wahl, *"USA-Fat": Prevalence Is Related to Ambient Outdoor Temperature—Evaluation with 18F-FDG PET/CT.* J Nucl Med, 2003. **44**(8): p. 1267-1270.
130. Cronin, C.G., et al., *Brown fat at PET/CT: correlation with patient characteristics.* Radiology, 2012. **263**(3): p. 836-42.
131. Hany, T.F., et al., *Brown adipose tissue: a factor to consider in symmetrical tracer uptake in the neck and upper chest region.* Eur J Nucl Med Mol Imaging, 2002. **29**(10): p. 1393-8.
132. Jacene, H.A., et al., *The relationship between patients' serum glucose levels and metabolically active brown adipose tissue detected by PET/CT.* Mol Imaging Biol, 2011. **13**(6): p. 1278-83.
133. Ouellet, V., et al., *Outdoor temperature, age, sex, body mass index, and diabetic status determine the prevalence, mass, and glucose-uptake activity of 18F-FDG-detected BAT in humans.* J Clin Endocrinol Metab, 2011. **96**(1): p. 192-9.
134. Pace, L., et al., *Determinants of physiologic 18F-FDG uptake in brown adipose tissue in sequential PET/CT examinations.* Mol Imaging Biol, 2011. **13**(5): p. 1029-35.
135. Truong, M.T., et al., *Focal FDG uptake in mediastinal brown fat mimicking malignancy: a potential pitfall resolved on PET/CT.* AJR Am J Roentgenol, 2004. **183**(4): p. 1127-32.
136. Mei, L.T., *Prevalence and factors associated with brown adipose tissue detected by 18F-FDG PET/CT in Hong Kong Chinese*. 2012, University of Hong Kong.
137. Lin, E.C. and A. Alavi, *PET and PET/CT: A Clinical Guide*. 2nd ed. PET and PET/CT: A Clinical Guide. 2009, New York: Thieme.
138. Mamede, M., et al., *[18F]FDG uptake and PCNA, Glut-1, and Hexokinase-II expressions in cancers and inflammatory lesions of the lung.* Neoplasia, 2005. **7**(4): p. 369-79.
139. Watanabe, J., et al., *Significance of increase in glucose 6-phosphatase activity in brown adipose cells of cold-exposed and starved mice.* Anat Rec, 1987. **219**(1): p. 39-44.

140. Kapoor, V., B.M. McCook, and F.S. Torok, *An introduction to PET-CT imaging.* Radiographics, 2004. **24**(2): p. 523-43.

141. Kelloff, G.J., et al., *Progress and promise of FDG-PET imaging for cancer patient management and oncologic drug development.* Clin Cancer Res, 2005. **11**(8): p. 2785-808.

142. Allisy-Roberts, P. and J. Williams, *Chapter 8 Gamma Imaging*, in *Farr's Physics for Medical Imaging*. 2008, Saunders Elsevier: London. p. 121-145.

143. Votaw, J.R., *The AAPM/RSNA physics tutorial for residents. Physics of PET.* Radiographics, 1995. **15**(5): p. 1179-1190.

144. Kinahan, P.E., et al., *Attenuation correction for a combined 3D PET/CT scanner.* Med Phys, 1998. **25**(10): p. 2046-53.

145. Hounsfield, G.N., *Computerized transverse axial scanning (tomography): Part I. Description of system.* Br J Radiol, 1973. **46**: p. 1016-1022.

146. Cierniak, R., *Some Words About the History of Computed Tomography*. X-Ray Computed Tomography in Biomedical Engineering. 2011, London: Springer-Verlag.

147. Allisy-Roberts, P. and J. Williams, *Chapter 7 Computed Tomography*, in *Farr's Physics for Medical Imaging*. 2008, Saunders Elsevier: London. p. 103-119.

148. Cook, G.J., E.A. Wegner, and I. Fogelman, *Pitfalls and artifacts in 18FDG PET and PET/CT oncologic imaging.* Semin Nucl Med, 2004. **34**(2): p. 122-33.

149. Shankar, L.K., et al., *Consensus recommendations for the use of ^{18}F-FDG PET as an indicator of therapeutic response in patients in National Cancer Institute trials.* J Nucl Med, 2006. **47**(6): p. 1059-1066.

150. Kinahan, P.E., et al., *PET/CT Assessment of Response to Therapy: Tumor Change Measurement, Truth Data, and Error.* Transl Oncol, 2009. **2**(4): p. 223-30.

151. Tateishi, U., et al., *Glut-1 expression and enhanced glucose metabolism are associated with tumour grade in bone and soft tissue sarcomas: a prospective evaluation by [18F]fluorodeoxyglucose positron emission tomography.* Eur J Nucl Med Mol Imaging, 2006. **33**(6): p. 683-91.

152. Gu, J., et al., *Correlation of GLUT-1 overexpression, tumor size, and depth of invasion with 18F-2-fluoro-2-deoxy-D-glucose uptake by positron emission tomography in colorectal cancer.* Dig Dis Sci, 2006. **51**(12): p. 2198-205.

153. Tohma, T., et al., *Relationship between glucose transporter, hexokinase and FDG-PET in esophageal cancer.* Hepatogastroenterology, 2005. **52**(62): p. 486-90.

154. Gambhir, S.S., et al., *A tabulated summary of the FDG PET literature.* J Nucl Med, 2001. **42**(5 Suppl): p. 1S-93S.

155. Allman, K.C., *Noninvasive assessment myocardial viability: current status and future directions.* J Nucl Cardiol, 2013. **20**(4): p. 618-37; quiz 638-9.

156. Schindler, S.E., et al., *Advances in diagnostic testing for Alzheimer disease.* Mo Med, 2013. **110**(5): p. 401-5.

157. Meller, J., C.O. Sahlmann, and A.K. Scheel, *18F-FDG PET and PET/CT in fever of unknown origin.* J Nucl Med, 2007. **48**(1): p. 35-45.

158. Sobic-Saranovic, D., V. Artiko, and V. Obradovic, *FDG PET imaging in sarcoidosis.* Semin Nucl Med, 2013. **43**(6): p. 404-11.

159. Ito, K., et al., *Evaluation of Wegener's granulomatosis using 18F-fluorodeoxyglucose positron emission tomography/computed tomography.* Ann Nucl Med, 2013. **27**(3): p. 209-16.

160. Karunanithi, S., et al., *(18)F-FDG PET/CT for diagnosis and treatment response evaluation in large vessel vasculitis.* Eur J Nucl Med Mol Imaging, 2014. **41**(3): p. 586-7.

161. Treglia, G., et al., *Diagnostic performance of Fluorine-18-Fluorodeoxyglucose positron emission tomography in patients with chronic inflammatory bowel disease: a systematic review and a meta-analysis.* J Crohns Colitis, 2013. **7**(5): p. 345-54.

162. Engel, H., et al., *Whole-body PET: physiological and artifactual fluorodeoxyglucose accumulations.* J Nucl Med, 1996. **37**(3): p. 441-6.

163. Strauss, L.G. and P.S. Conti, *The applications of PET in clinical oncology.* J Nucl Med, 1991. **32**(4): p. 623-48; discussion 649-50.
164. Weber, W.A., *Assessing tumor response to therapy.* J Nucl Med, 2009. **50 Suppl 1**(Suppl 1): p. 1S-10S.
165. Weber, W.A., *Positron emission tomography as an imaging biomarker.* J Clin Oncol, 2006. **24**(20): p. 3282-92.
166. Nguyen, N.C., et al., *Is there a common SUV threshold in oncological FDG PET/CT, at least for some common indications? A retrospective study.* Acta Oncol, 2011. **50**(5): p. 670-677.
167. Sugawara, Y., et al., *Reevaluation of the Standardised Uptake Value for FDG: Variations with Body Weight and Methods for Correction* Radiology, 1999. **213**(2): p. 521-5.
168. Zasadny, K.R. and L.M. Wahl, *Standardized uptake values of normal tissues at PET with 2-[fluorine-18]-fluoro-2-deoxy-D-glucose: variations with body weight and a method for correction.* Radiology, 1993. **189**(3): p. 847-850.
169. Hamberg, L.M., et al., *The dose uptake ratio as an index of glucose metabolism: useful parameter or oversimplification?* J Nuc Med, 1994. **35**(8): p. 1308-1312.
170. Fukui, M.B., T.M. Blodgett, and C.C. Meltzer, *PET/CT imaging in recurrent head and neck cancer.* Semin Ultrasound CT MR, 2003. **24**(3): p. 157-63.
171. Soret, M., S.L. Bacharach, and I. Buvat, *Partial-volume effect in PET tumor imaging.* J Nucl Med, 2007. **48**(6): p. 932-45.
172. Erdi, Y.E., et al., *The CT motion quantitation [sic] of lung lesions and its impact on PET-measured SUVs.* J Nucl Med, 2004. **45**(8): p. 1287-92.
173. Brix, G., et al., *Radiation exposure of patients undergoing whole-body dual-modality 18F-FDG PET/CT examinations.* J Nucl Med, 2005. **46**(4): p. 608-13.
174. NHS Choices. *PET scan - Risks*. 3 June 2011 2 December 2011]; Available from: http://www.nhs.uk/Conditions/PET-scan/Pages/Risks.aspx.
175. Watson, S.J., et al., *HPA-RPD-001 - Ionising Radiation Exposure of the UK Population: 2005 Review*. 2005, Health Protection Agency: Didcot, Oxfordshire,UK.
176. van der Molen, A.J., et al., *A national survey on radiation dose in CT in The Netherlands.* Insights Imaging, 2013. **4**(3): p. 383-90.
177. Barrington, S.F. and M.N. Maisey, *Skeletal muscle uptake of fluorine-18-FDG: effect of oral diazepam.* J Nucl Med, 1996. **37**(7): p. 1127-9.
178. Tatsumi, M., et al., *Intense ^{18}F-FDG uptake in brown fat can be reduced pharmacologically.* J Nucl Med, 2004. **45**(7): p. 1189-93.
179. Basu, S. and B.P. Tiwari, *Asymmetric 18F-FDG Uptake in the Infradiaphragmatic Brown Adipose Tissue (BAT) Mimicking Adrenal Metastasis: A Relatively Rare Site of Brown Fat and a Potential Source for False Positive FDG-PET Study.* J Radiol Case Rep, 2009. **3**(10): p. 19-22.
180. Paidisetty, S. and T.M. Blodgett, *Brown fat: atypical locations and appearances encountered in PET/CT.* AJR Am J Roentgenol, 2009. **193**(2): p. 359-66.
181. Bogsrud, T.V. and V. Lowe, *Normal variants and pitfalls in whole body PET imaging with 18F-FDG.* Appl Radiol, 2006. **35**: p. 16-30.
182. Williams, G. and G.M. Kolodny, *Method for decreasing uptake of 18F-FDG by hypermetabolic brown adipose tissue on PET.* AJR Am J Roentgenol, 2008. **190**(5): p. 1406-9.
183. Parysow, O., et al., *Low-dose oral propranolol could reduce brown adipose tissue F-18 FDG uptake in patients undergoing PET scans.* Clin Nucl Med, 2007. **32**(5): p. 351-7.
184. Rosenbaum, S.J., et al., *False-positive FDG PET uptake--the role of PET/CT.* Eur Radiol, 2006. **16**(5): p. 1054-65.
185. Cohade, C., et al., *Uptake in supraclavicular area fat ("USA-fat"): description on ^{18}F-FDG PET/CT.* J Nuc Med, 2003. **44**(2): p. 170-176.

186. Yeung, H.W.D., et al., *Patterns of 18F-FDG uptake in adipose tissue and muscle: a potential source of false-positives for PET.* Journal of Nuclear Medicine, 2003. **44**(11): p. 1789-1796.

187. Lee, P., et al., *A critical appraisal of the prevalence and metabolic significance of brown adipose tissue in adult humans.* Am J Physiol Endocrinol Metab, 2010. **299**(4): p. E601-6.

188. Reddy, N.L., et al., *Identification of brown adipose tissue using MR imaging in a human adult with histological and immunohistochemical confirmation.* J Clin Endocrin Metab, 2014. **99**(1): p. E117-E121.

189. Nedergaard, J., T. Bengtsson, and B. Cannon, *Three years with adult human brown adipose tissue.* Ann N Y Acad Sci, 2010. **1212**(1): p. E20-36.

190. Park, J.Y., et al., *The Prevalence and Characteristics of Brown Adipose Tissue in an ^{18}F-FDG Study of Koreans.* Nucl Med Mol Imaging, 2010. **44**(3): p. 207-212.

191. Rousseau, C., et al., *Brown fat in breast cancer patients: analysis of serial (18)F-FDG PET/CT scans.* Eur J Nucl Med Mol Imaging, 2006. **33**(7): p. 785-91.

192. Garcia, C.A., et al., *Reduction of brown fat 2-deoxy-2-[F-18]fluoro-D-glucose uptake by controlling environmental temperature prior to positron emission tomography scan.* Mol Imaging Biol, 2006. **8**(1): p. 24-9.

193. Fang, N., et al., *Preliminary PET/CT study of ^{18}F-FDG Uptake in Cervical and Supraclavicular Brown Adipose Tissue.* Chin J Clin Oncol, 2008. **5**: p. 349-353.

194. Kim, S., et al., *Temporal relation between temperature change and FDG uptake in brown adipose tissue.* Eur J Nucl Med Mol Imaging, 2008. **35**(5): p. 984-9.

195. Stefan, N., C. Pfannenberg, and H.U. Haring, *The importance of brown adipose tissue.* N Engl J Med, 2009. **361**(4): p. 416-7; author reply 418-21.

196. Akkas, B.E., et al., *FDG uptake in brown adipose tissue-a brief report on brown fat with FDG uptake mechanisms and quantitative analysis using dual-time-point FDG PET/CT.* Revista Espanola de Medicina Nuclear, 2011. **30**(1): p. 14-8.

197. Huang, Y.-C., et al., *Review Analysis of the Association between the Prevalence of Activated Brown Adipose Tissue and Outdoor Temperature.* The Scientific World Journal, 2012. **Article ID 793039**.

198. Perkins, A.C., et al., *Prevalence and pattern of brown adipose tissue distribution of 18F-FDG in patients undergoing PET-CT in a subtropical climatic zone.* Nucl Med Commun, 2013. **34**(2): p. 168-74.

199. Pfannenberg, C., et al., *Impact of age on the relationships of brown adipose tissue with sex and adiposity in humans.* Diabetes, 2010. **59**(7): p. 1789-93.

200. Zukotynski, K.A., et al., *Seasonal variation in the effect of constant ambient temperature of 24 degrees C in reducing FDG uptake by brown adipose tissue in children.* Eur J Nucl Med Mol Imaging, 2010. **37**(10): p. 1854-60.

201. Hadi, M., et al., *Brown fat imaging with (18)F-6-fluorodopamine PET/CT, (18)F-FDG PET/CT, and (123)I-MIBG SPECT: a study of patients being evaluated for pheochromocytoma.* J Nucl Med, 2007. **48**(7): p. 1077-83.

202. Garcia, C., et al., *Effective reduction of brown fat FDG uptake by controlling environmental temperature prior to PET scan: an expanded case series.* Mol Imaging Biol, 2010. **12**(6): p. 652-6.

203. Huang, Y.-C., et al., *The relationship between brown adipose tissue activity and neoplastic status: an 18F-FDG PET/CT study in the tropics.* Lipids Health Dis, 2011. **10**: p. 238.

204. Persichetti, A., et al., *Prevalence, Mass, and Glucose-Uptake Activity of 18F-FDG-Detected Brown Adipose Tissue in Humans Living in a Temperate Zone of Italy.* PLoS ONE, 2013. **8**(5): p. e63391.

205. Shellock, F.G., M.S. Riedinger, and M.C. Fishbein, *Brown adipose tissue in cancer patients: possible cause of cancer-induced cachexia.* J Cancer Res Clin Oncol, 1986. **111**(1): p. 82-5.

206. Skillen, A., G.M. Currie, and J.M. Wheat, *Thermal Control of Brown Adipose Tissue in ^{18}F-FDG PET.* J Nucl Med Technol, 2012.

207. World Health Organization. *BMI classification*. Global Database on Body Mass Index 2006 [cited 6 November 2013; Available from: http://apps.who.int/bmi/index.jsp?introPage=intro_3.html.

208. World Health Organization, *Definition and diagnosis of diabetes mellitus and intermediate hyperglycaemia: report of a WHO/IDF consultation*. 2006, World Health Organization: Geneva, Switzerland.

209. The Health and Social Care Information Centre, *Statistics on Obesity, Physical Activity and Diet: England, 2013*. 2013, NHS.

210. Field, A., *Regression*, in *Discovering Statistics using SPSS*. 2011, Sage: London. p. 297-263.

211. Tobin, J., *Estimation of relationships for limited dependent variables.* Econometrica, 1958. **26**: p. 24-36.

212. Freelon, D.G., *ReCal: Intercoder reliability calculation as a web service.* International Journal of Internet Science, 2010. **5**(1): p. 20-33.

213. Landis, J.R. and G.G. Koch, *The measurement of observer agreement for categorical data.* Biometrics, 1977. **33**(1): p. 159-74.

214. Dunn, K.W., M.M. Kamocka, and J.H. McDonald, *A practical guide to evaluating colocalization in biological microscopy.* Am J Physiol Cell Physiol, 2011. **300**(4): p. C723-42.

215. Lachmanovich, E., et al., *Co-localization analysis of complex formation among membrane proteins by computerized fluorescence microscopy: application to immunofluorescence co-patching studies.* J Microsc, 2003. **212**: p. 122-131.

216. Lynch, R., et al., *Metabolic modulation of hexokinase association with mitochondria in living smooth muscle cells.* Am J Physiol Cell Physiol, 1996. **270**: p. C488-C499.

217. van Steensel, B., et al., *Partial colocalization of glucocorticoid and mineralocorticoid receptors in discrete compartments in nuclei of rat hippocampus neurons.* J Cell Sci, 1996. **109**(4): p. 787-792.

218. Bolte, S. and F. Cordelières, *A guided tour into subcellular colocalization analysis in light microscopy.* J Microsc, 2006. **224**(3): p. 213-232.

219. Manders, E., et al., *Dynamics of 3-dimensional replication patterns during the S-phase, analyzed by double-labeling of DNA and confocal microscopy.* J Cell Sci, 1992. **103**: p. 857-862.

220. Manders, E., F. Verbeek, and J. Aten, *Measurement of co-localization of objects in dual-colour confocal images.* J Microsc, 1993. **169**(3): p. 375-382.

221. Costes, S.V., et al., *Automatic and quantitative measurement of protein-protein colocalization in live cells.* Biophysical journal, 2004. **86**(6): p. 3993-4003.

222. Ramirez, O., et al., *Confined displacement algorithm determines true and random colocalization in fluorescence microscopy.* J Microsc, 2010. **239**(3): p. 173-83.

223. Fay, F., et al., *Quantitative Digital analysis of Diffuse and Concentrated Nuclear Distribution of Nascent Transcripts, SC35 and Poly(A)*1.* Exp Cell Res, 1997. **23**(1): p. 27-37.

224. Rasband, W.S., *ImageJ*. 1997-2004, National Institutes of Health, Bethesda, Maryland, USA, http://rsb.info.nih.gov/ij/.

225. Schindelin, J., et al., *Fiji: an open-source platform for biological-image analysis.* Nat Methods, 2012. **9**(7): p. 676-82.

226. Cordelières, F.P. and S. Bolte, *JACoP - Just another colocalization plugin*. 2010.

227. Allisy-Roberts, P. and J. Williams, *Chapter 10 - Magnetic resonance imaging*, in *Farr's Physics for Medical Imaging*. 2008, Saunders Elsevier: London. p. 169-195.

228. Pooley, R.A., *Fundamental Physics of MR Imaging.* Radiographics, 2005. **25**(4): p. 1087-1099.

229. Hendrick, R.E., *The AAPM/RSNA physics tutorial for residents. Basic physics of MR imaging: an introduction.* Radiographics, 1994. **14**(4): p. 829-46; quiz 847-8.
230. Bitar, R., et al., *MR Pulse Sequences: What Every Radiologist Wants to Know but Is Afraid to Ask.* Radiographics, 2006. **26**: p. 513-537.
231. Dixon, W.T., *Simple proton spectroscopic imaging.* Radiology, 1984. **153**(1): p. 189-94.
232. Machann, J., et al., *In Vivo Proton NMR Studies in Skeletal Musculature*, in *Annual Reports on NMR Spectroscopy*. 2003, Academic Press. p. 1-74.
233. Reeder, S.B., et al., *Iterative decomposition of water and fat with echo asymmetry and least-squares estimation (IDEAL): application with fast spin-echo imaging.* Magn Reson Med, 2005. **54**(3): p. 636-44.
234. GE Healthcare, *IDEAL IQ Software Option 5 10(k) Premarket Notification Submission*, in *FDA*, G. HEalthcare, Editor. 2011.
235. Fauhl, C., F. Reniero, and C. Guillou, *1H NMR as a tool for the analysis of mixtures of virgin olive oil with oils of different botanical origin.* Magn Reson Chem, 2000. **38**: p. 436.
236. Bydder, M., et al., *Relaxation effects in the quantification of fat using gradient echo imaging.* Magn Reson Imaging, 2008. **26**(3): p. 347-359.
237. Westphalen, A.C., et al., *Liver fat: effect of hepatic iron deposition on evaluation with opposed-phase MR imaging.* Radiology, 2007. **242**(2): p. 450-5.
238. Gifford, A., et al., *Temperature mapping in Human Brown Adipose Tissue Using Fat-Water MRI with Explicit Fitting of Water Peak Location.* Proc. Intl. Soc. Mag. Reson. Med, 2014. **22**: p. 2354.
239. Yoneshiro, T., et al., *Brown adipose tissue, whole-body energy expenditure, and thermogenesis in healthy adult men.* Obesity (Silver Spring), 2011. **19**(1): p. 13-6.
240. Huang, B., M.W. Law, and P.L. Khong, *Whole-body PET/CT scanning: estimation of radiation dose and cancer risk.* Radiology, 2009. **251**(1): p. 166-74.
241. Hu, H.H., et al., *Identification of brown adipose tissue in mice with fat-water IDEAL-MRI.* J Magn Reson Imaging, 2010. **31**(5): p. 1195-202.
242. *The Ionising Radiation (Medical Exposure) Regulations*. 2000, HMSO: London.
243. Holstila, M., et al., *Measurement of brown adipose tissue mass using a novel dual-echo magnetic resonance imaging approach: A validation study.* Metabolism, 2013. **62**(8): p. 1189-1198.
244. Hamilton, G., et al., *MR properties of brown and white adipose tissues.* J Magn Reson Imaging, 2011. **34**(2): p. 468-73.
245. Sbarbati, A., et al., *Chemical shift imaging at 4.7 tesla of brown adipose tissue.* J Lipid Res, 1997. **38**(2): p. 343-7.
246. Poon, C.S., et al., *Fat/water quantitation and differential relaxation time measurement using chemical shift imaging technique.* Magn. Reson. Imaging, 1989. **7**: p. 369-382.
247. Menschik, Z., *Histochemical comparison of brown and white adipose tissue in guinea pigs.* Anat Rec, 1953. **116**(4): p. 439-55.
248. Peng, X.-G., et al., *Comparison of brown and white adipose tissue fat fractions in ob, seipin, and Fsp27 gene knockout mice by chemical shift-selective imaging and 1H-MR spectroscopy*. Vol. 304. 2013. E160-E167.
249. Hines, C.D.G., et al., *T1 independent, T2* corrected chemical shift based fat–water separation with multi-peak fat spectral modeling is an accurate and precise measure of hepatic steatosis.* J Magn Reson Imaging, 2011. **33**(4): p. 873-881.
250. Valaparla, S.K., et al., *Evaluation of vastus lateralis muscle fat fraction measured by two-point Dixon water-fat Imaging and 1H-MRS.* Proc. Intl. Soc. Mag. Reson. Med, 2014. **22**: p. 1221.
251. Müller, H.-P., et al., *Quantification of human body fat tissue percentage by MRI.* NMR in Biomedicine, 2011. **24**(1): p. 17-24.
252. Reeder, S.B., et al., *Quantitative assessment of liver fat with magnetic resonance imaging and spectroscopy.* J Magn Res Imag, 2011. **34**(4): p. 729-749.

253. Hu, H.H., et al., *Variations in T2* and fat content of murine brown and white adipose tissues by chemical-shift MRI.* Magn Reson Imaging, 2012.

254. Yokoo, T., et al., *Effects of fat spectral model parameters on hepatic fat quantification by multi-echo gradient-echo magnetic resonance imaging.* Proc. Intl. Soc. Mag. Reson. Med, 2009. **17**(2134).

255. Lunati, E., et al., *In vivo quantitative lipidic map of brown adipose tissue by chemical shift imaging at 4.7 Tesla.* J Lipid Res, 1999. **40**(8): p. 1395-400.

256. Smith, D.L., et al., *Measurement of interscapular brown adipose tissue of mice in differentially housed temperatures by chemical-shift–encoded water–fat MRI.* Journal of Magnetic Resonance Imaging, 2013: p. n/a-n/a.

257. Brunner, A., et al., *14 T NMR and 7 T MRI in vitro investigation of cold stimulation of abdominal WAT, inguinal WAT and BAT.* Proc. Intl. Soc. Mag. Reson. Med, 2014. **22**: p. 1674.

258. Rasmussen, J.M., et al., *Brown Adipose Tissue Quantification in Human Neonates Using Water-Fat Separated MRI.* PLoS One, 2013. **8**(10): p. e77907.

259. Vasanawala, S.S., et al., *Estimation of liver T(2) in transfusion-related iron overload in patients with weighted least squares T(2) IDEAL.* Magn Reson Med, 2012. **67**(1): p. 183-90.

260. Kennan, R.P., J. Zhong, and J.C. Gore, *Intravascular susceptibility contrast mechanisms in tissues.* Magn Reson Med, 1994. **31**(1): p. 9-21.

261. Chen, Y.I., et al., *Anatomical and Functional Assessment of Brown Adipose Tissue by Magnetic Resonance Imaging.* Obesity, 2012.

262. Wood, J.C., et al., *MRI R2 and R2* mapping accurately estimates hepatic iron concentration in transfusion-dependent thalassemia and sickle cell disease patients.* Blood, 2005. **106**(4): p. 1460-5.

263. Hu, H.C.H., et al., *Unequivocal identification of brown adipose tissue in a human infant.* Journal of Magnetic Resonance Imaging, 2012. **35**(4): p. 938-942.

264. Hu, H.H., et al., *Characterization of human brown adipose tissue by chemical-shift water-fat MRI.* AJR Am J Roentgenol, 2013. **200**(1): p. 177-83.

265. Hu, H.H., et al., *Comparing Brown Adipose Tissue in Infants and Teenagers by Chemical-Shift Water-Fat MRI.* Proc. Intl. Soc. Mag. Reson. Med, 2013. **21**: p. 0403.

266. Hu, H.H., et al., *Comparison of brown and white adipose tissues in infants and children with chemical-shift-encoded water-fat MRI.* J Magn Reson Imaging, 2013. **38**(4): p. 885-96.

267. van Rooijen, B.D., et al., *Imaging Cold-Activated Brown Adipose Tissue Using Dynamic T2*-Weighted Magnetic Resonance Imaging and 2-Deoxy-2-[18F]fluoro-D-glucose Positron Emission Tomography.* Investigative Radiology, 2013. **48**(10): p. 708-714.

268. Lundström, E., et al., *Water fat separated MRI during cooling-reheating for the stimation of brown fat amount and activity.* Proc. Intl. Soc. Mag. Reson. Med, 2014. **22**: p. 3605.

269. Hu, H.H., et al., *Brown Adipose Tissue with Low Fat Content in Newborns with Hypothermia.* Proc. Intl. Soc. Mag. Reson. Med, 2014. **22**: p. 4272.

270. Rylander, E., H. Pribylova, and J. Lind, *A thermographic study of infants exposed to cold.* Acta Paediatr Scand, 1972. **61**(1): p. 42-8.

271. Dundamadappa, S.K., et al., *Imaging of brown fat associated with adrenal pheochromocytoma.* Acta Radiol, 2007. **48**(4): p. 468-72.

272. Carter, B.W. and W.G. Schucany, *Brown adipose tissue in a newborn.* Proc (Bayl Univ Med Cent), 2008. **21**(3): p. 328-30.

273. Lidell, M.E., et al., *Evidence for two types of brown adipose tissue in humans.* Nat Med, 2013. **19**(5): p. 631-4.

274. Hu, H.H., et al., *Variations in T2* as a potential indicator of human brown adipose tissue.* Proc. Intl. Soc. Mag. Reson. Med, 2012. **20**: p. 1268.

275. Gifford, A., et al., *Prelimenary Identification of Brown Adipose Tissue in Adult Humans Using Fat-Water MRI.* Proc. Intl. Soc. Mag. Reson. Med, 2012. **20**: p. 1269.
276. Jones, T.A., et al., *Visual identification of brown adipose tissue in adult humans using Dixon MR.* Proc. Intl. Soc. Mag. Reson. Med, 2014. **22**: p. 2144.
277. Chen, Y.C., et al., *Measurement of human brown adipose tissue volume and activity using anatomic MR imaging and functional MR imaging.* J Nucl Med, 2013. **54**(9): p. 1584-7.
278. Abràmoff, M.D., P.J. Magalhaes, and S.J. Ram, *Image Processing with ImageJ.* Biophotonics International, 2004. **11**(7): p. 36-42.
279. Schmidt, K., *MRI Analysis Calculator*. 2002, HypX Laboratory, Brigham & Women's Hospital, Harvard University.
280. Lundström, E., et al., *Water-fat imaging of supraclavicular brown and white adipose tissue at 1.5T: Iniital results in healthy volunteers.* Proc. Intl. Soc. Mag. Reson. Med, 2013. **21**: p. 4050.
281. Pinchon, M., L. Pasquet, and N. Bonnet, *A posteriori shading correction 514*. 2005.
282. Cordelières, F.P., *The 3D object counter plugin a.k.a. 3D-OC*. 2009, Institut Cure, Orsay: France.
283. Freelon, D., *ReCal OIR: Ordinal, Interval, and Ratio Intercoder Reliability as a Web Service.* Int J Internet Science, 2013. **8**(1): p. 10-16.
284. Ramirez, O., et al. *Confined Displacement Algorithm Determines True and Random Colocalization in Fluorescence Microscopy*. 203 18 July 2013 [cited 2013 8 January 2014]; Available from: imagejdocu.tudor.lu/doku.php?id=plugin:analysis:confined_displacement_determines true_and_random_colocalization_:start.
285. Carpten, J.D., et al., *HRPT2, encoding parafibromin, is mutated in hyperparathyroidism-jaw tumor syndrome.* Nat Genet, 2002. **32**(4): p. 676-80.
286. Eng, J., *Receiver operating characteristic analysis: a primer.* Acad Radiol, 2005. **12**(7): p. 909-16.
287. Youden, W.J., *Index for rating diagnostic tests.* Cancer, 1950. **3**(1): p. 32-5.
288. Schisterman, E.F., et al., *Optimal cut-point and its corresponding Youden Index to discriminate individuals using pooled blood samples.* Epidemiology, 2005. **16**: p. 73–81.
289. Ravussin, E. and L.P. Kozak, *Have we entered the brown adipose tissue renaissance?* Obes Rev, 2009. **10**(3): p. 265-8.
290. Astrup, A., et al., *Contribution of BAT and skeletal muscle to thermogenesis induced by ephedrine in man.* Am J Physiol, 1985. **248**(5 Pt 1): p. E507-15.
291. M., F.H., et al., *UCP1 ablation induces obesity and abolishes diet-induced thermogenesis in mice exempt from thermal stress by living at thermoneutrality.* Cell Metab, 2009. **9**(2): p. 203-209.
292. Ojha, S., et al., *Brown adipose tissue: a new human organ?* Expert Review of Endocrinology & Metabolism, 2013. **8**(2): p. 123-125.
293. Mei, L.T., *Prevalence and factors associated with brown adipose tissue detected in 18F-FDG PET/CT in Hong Kong Chinese*. 2012, The University of Hong Kong: Hong Kong.
294. Evans, K.D., T.A. Tulloss, and N. Hall, *18FDG uptake in brown fat: potential for false positives.* Radiol Technol, 2007. **78**(5): p. 361-6.
295. Admiraal, W.M., et al., *Cold-induced activity of brown adipose tissue in young lean men of South-Asian and European origin.* Diabetologia, 2013: p. 1-7.
296. Rohles Jr, F.J., *Thermal sensations of sedentary man in moderate temperatures.* Human Factors, 1971. **13**: p. 553-560.
297. Chiba, S., et al., *Evaluation of brown adipose tissue using positron emission tomography, computerised tomography and histochemical studies in association with body mass index, visceral fat accumulation and insulin resistance.* Obes Rev, 2006. **7**(Suppl 2): p. 87 (abstract).

298. Kalra, S., M. Mercuri, and S.S. Anand, *Measures of body fat in South Asian adults.* Nutr Diabetes, 2013. **3**(5): p. e69.

299. Morgan, D.J. and K.M. Bray, *Lean body mass as a predictor of drug dosage: implications for drug therapy.* Clin Pharmakinet, 1994. **26**(4): p. 292-307.

300. Carneheim, C., B. Cannon, and J. Nedergaard, *Rare fatty acids in brown fat are substrates for thermogenesis during arousal from hibernation.* Am J Physiol, 1989. **256**(1 Pt 2): p. R146-54.

301. Grimpo, K., et al., *Brown adipose tissue dynamics in wild-type and UCP1-knockout mice: in vivo insights with magnetic resonance.* Journal of Lipid Research, 2014. **55**(3): p. 398-409.

302. Baba, S., et al., *CT Hounsfield units of brown adipose tissue increase with activation: preclinical and clinical studies.* J Nucl Med, 2010. **51**(2): p. 246-50.

303. Hu, H.H., et al., *Differential computed tomographic attenuation of metabolically active and inactive adipose tissues: preliminary findings.* J Comput Assist Tomogr, 2011. **35**(1): p. 65-71.

304. Mitchell, J.R., et al., *Regulation of expression of the lipoprotein lipase gene in brown adipose tissue.* Am J Physiol, 1992. **263**(3 Pt 1): p. E500-6.

305. Carneheim, C., J. Nedergaard, and B. Cannon, *Cold-induced beta-adrenergic recruitment of lipoprotein lipase in brown fat is due to increased transcription.* Am J Physiol, 1988. **254**(2 Pt 1): p. E155-61.

306. Shabalina, I.G., et al., *Within brown-fat cells, UCP1-mediated fatty acid-induced uncoupling is independent of fatty acid metabolism.* Biochim Biophys Acta, 2008. **1777**(7-8): p. 642-50.

307. Shabalina, I.G., et al., *Native UCP1 displays simple competetive kinetics between the regulators purine nucleotides and fatty acids.* J Biol Chem, 2004. **279**: p. 38236-38248.

308. Klingenspor, M., et al., *Short photoperiod and cold activate brown fat lipoprotein lipase in the Djungarian hamster.* Am J Physiol, 1989. **257**(5 Pt 2): p. R1123-7.

309. Wiesinger, H., G. Heldmaier, and A. Buchberger, *Effect of photoperiod and acclimation temperature on nonshivering thermogenesis and GDP-binding of brown fat mitochondria in the Djungarian hamster Phodopus s. sungorus.* Pflugers Arch, 1989. **413**(6): p. 667-72.

310. Demas, G.E., et al., *Photoperiodic regulation of gene expression in brown and white adipose tissue of Siberian hamsters (Phodopus sungorus).* Am J Physiol Regul Integr Comp Physiol, 2002. **282**(1): p. R114-21.

311. Campbell, C.S., J. Tabor, and J.D. Davis, *Small effect of brown adipose tissue and major effect of photoperiod on body weight in hamsters (Mesocricetus auratus).* Physiol Behav, 1983. **30**(3): p. 349-52.

312. McElroy, J.F. and G.N. Wade, *Short photoperiod stimulates brown adipose tissue growth and thermogenesis but not norepinephrine turnover in Syrian hamsters.* Physiol Behav, 1986. **37**(2): p. 307-11.

313. Redlin, U., B. Nuesslein, and I. Schmidt, *Circadian changes of brown adipose tissue thermogenesis in juvenile rats.* Am J Physiol, 1992. **262**(3 Pt 2): p. R504-8.

314. Steger, R.W., et al., *Effects of short photoperiod on the ability of golden hamster pituitaries to secrete prolactin and gonadotropins in vitro.* Biol Reprod, 1983. **29**(4): p. 872-8.

315. Pearce, S., et al., *Prolactin, the prolactin receptor and uncoupling protein abundance and function in adipose tissue during development in young sheep.* J Endocrinol, 2005. **184**(2): p. 351-9.

316. Chan, E. and R. Swaminathan, *Role of prolactin in lactation-induced changes in brown adipose tissue.* Am J Physiol, 1990. **258**(1 Pt 2): p. R51-6.

317. Kott, K.S., et al., *Hyperprolactinemia prevents short photoperiod-induced changes in brown fat.* Am J Physiol, 1989. **256**(1 Pt 2): p. R174-80.

318. Vigas, M., J. Celko, and J. Koska, *Role of body temperature in exercise-induced growth hormone and prolactin release in non-trained and physically fit subjects.* Endocr Regul, 2000. **34**(4): p. 175-80.
319. Tan, D.X., et al., *Significance and application of melatonin in the regulation of brown adipose tissue metabolism: relation to human obesity.* Obes Rev, 2011. **12**(3): p. 167-88.
320. van der Veen, D.R., et al., *A diurnal rhythm in glucose uptake in brown adipose tissue revealed by in vivo PET-FDG imaging.* Obesity (Silver Spring), 2012. **20**(7): p. 1527-9.
321. Fukushima, M., J. Lupien, and G.A. Bray, *Interaction of light and corticosterone on food intake and brown adipose tissue of the rat.* Am J Physiol, 1985. **249**(6 Pt 2): p. R753-7.
322. Le Gouic, S., et al., *Characterization of a melatonin binding site in Siberian hamster brown adipose tissue.* Eur J Pharmacol, 1997. **339**(2-3): p. 271-8.
323. Reiter, R.J., et al., *Pineal melatonin rhythm: reduction in aging Syrian hamsters.* Science, 1980. **210**(4476): p. 1372-3.
324. Reiter, R., et al., *Age-associated reduction in nocturnal pineal melatonin levels in female rats.* Endocrinology, 1981. **109**: p. 1295-1297.
325. Viswanathan, M. and J.C. George, *Pinealectomy has no effect on diet-induced thermogenesis and brown adipose tissue proliferation in rats.* J Pineal Res, 1984. **1**(1): p. 69-74.
326. Perez, E., et al., *cAMP accumulation in the hypothalamus, cerebral cortex, pineal gland and brown fat across the wake-sleep cycle of the rat exposed to different ambient temperatures.* Brain Res, 1995. **684**(1): p. 56-60.
327. Paulsrud, J.R. and R.L. Dryer, *Circum-annual changes in triglyceride fatty acids of bat brown adipose tissue.* Lipids, 1968. **3**(4): p. 340-5.
328. Przelecka, A., *Seasonal changes in ultrastructure of brown adipose tissue in the common shrew (Sorex araneus l.).* Cell Tissue Res, 1981. **214**(3): p. 623-32.
329. Feist, D.D., *Increased beta-adrenergic receptors in brown fat of winter-acclimatized Alaskan voles.* Am J Physiol, 1983. **245**(3): p. R357-63.
330. Trayhurn, P., et al., *Effect of warm or cold exposure on GDP binding and uncoupling protein in rat brown fat.* Am J Physiol, 1987. **252**(2 Pt 1): p. E237-43.
331. Kortner, G., et al., *Rapid changes in metabolic cold defense and GDP binding to brown adipose tissue mitochondria of rat pups.* Am J Physiol, 1993. **264**(5 Pt 2): p. R1017-23.
332. Garcia, C.A., et al., *Benzodiazepine-resistant "brown fat" pattern in positron emission tomography: two case reports of resolution with temperature control.* Mol Imaging Biol, 2004. **6**(6): p. 368-72.
333. Christensen, C.R., P.B. Clark, and K.A. Morton, *Reversal of hypermetabolic brown adipose tissue in F-18 FDG PET imaging.* Clin Nucl Med, 2006. **31**(4): p. 193-6.
334. Zukotynski, K.A., et al., *Constant ambient temperature of 24 degrees C significantly reduces FDG uptake by brown adipose tissue in children scanned during the winter.* Eur J Nucl Med Mol Imaging, 2009. **36**(4): p. 602-6.
335. Ouellet, V., et al., *Brown adipose tissue oxidative metabolism contributes to energy expenditure during acute cold exposure in humans.* J Clin Invest, 2012. **122**(2): p. 545.
336. Virtanen, K.A., W.D. van Marken Lichtenbelt, and P. Nuutila, *Brown adipose tissue functions in humans.* Biochim Biophys Acta, 2013. **1831**(5): p. 1004-8.
337. Clarke, J.R., et al., *Atypical brown fat distribution in young males demonstrated on PET/CT.* Clin Nucl Med, 2007. **32**(9): p. 679-82.
338. Quevedo, S., et al., *Sex-associated differences in cold-induced UCP1 synthesis in rodent brown adipose tissue.* Pflugers Arch, 1998. **436**(5): p. 689-95.
339. Gilsanz, V., et al., *The Depiction of Brown Adipose Tissue Is Related to Disease Status in Pediatric Patients With Lymphoma.* American Journal of Roentgenology, 2012. **198**(4): p. 909-913.

340. Wahl, R., et al., *Repeatability of test-retest measurements of brown adipose tissue presence, metabolic activity, and volumes in humans.* J Nucl Med, 2014. **55**(Supplement 1): p. 233.

341. Inokuma, K., et al., *Uncoupling protein 1 is necessary for norepinephrine-induced glucose utilization in brown adipose tissue.* Diabetes, 2005. **54**(5): p. 1385-91.

342. Marette, A. and L.J. Bukowiecki, *Noradrenaline stimulates glucose transport in rat brown adipocytes by activating thermogenesis. Evidence that fatty acid activation of mitochondrial respiration enhances glucose transport.* Biochem J, 1991. **277**: p. 119-124.

343. Lockhart, C.M., et al., *Quantifying and reducing the effect of calibration error on variability of PET/CT standardized uptake value measurements.* J Nucl Med, 2011. **52**(2): p. 218-24.

344. Nahmias, C. and L.M. Wahl, *Reproducibility of standardized uptake value measurements determined by 18F-FDG PET in malignant tumors.* J Nucl Med, 2008. **49**(11): p. 1804-8.

345. Burger, I.A., et al., *Repeatability of FDG quantification in tumor imaging: averaged SUVs are superior to SUVmax.* Nucl Med Biol, 2012. **39**(5): p. 666-70.

346. Upadhye, T., A. Gandhi, and S. Basu, *Evaluation of ^{18}F-FDG Uptake Pattern in Brown Adipose Tissue Over Extended Time Period as Assessed by Multiple Time Point ^{18}F-FDG-PET.* Nuc Med Mol Imaging, 2012. **47**(2): p. 89-97.

347. Wehrli, N.E., et al., *Determination of age-related changes in structure and function of skin, adipose tissue, and skeletal muscle with computed tomography, magnetic resonance imaging, and positron emission tomography.* Seminars in Nuclear Medicine, 2007. **37**(3): p. 195-205.

348. Petrovic, N., et al., *Thermogenically competent noradrenergic recruitment in brown preadipocytes by a PPARgamma agonist.* Am J Physiol Endocrinol Metab, 2008. **295**: p. E287-E296.

349. Sbarbati, A., et al., *Contrast-enhanced MRI of brown adipose tissue after pharmacological stimulation.* Magn Reson Med, 2006. **55**(4): p. 715-8.

350. Zancanaro, C., et al., *Magnetic resonance spectroscopy investigations of brown adipose tissue and isolated brown adipocytes.* J Lipid Res, 1994. **35**(12): p. 2191-9.

351. Ohlson, K.B., et al., *Thermogenesis inhibition in brown adipocytes is a specific property of volatile anesthetics.* Anesthesiology, 2003. **98**(2): p. 437-8.

352. Lundbom, J., et al., *Deep subcutaneous adipose tissue is more saturated than superficial subcutaneous adipose tissue.* Int J Obes, 2013. **37**(4): p. 620-622.

353. Canese, R., et al., *In vivo MRI/MRS characterization of Brown and White Adipose Tissues in mice: plasticitiy due to High Fat Diet and pharmacological treatments.* Proc. Intl. Soc. Mag. Reson. Med, 2013. **21**: p. 4051.

354. Cinti, S., et al., *Morphologic techniques for the study of brown adipose tissue and white adipose tissue.* Methods Mol Biol, 2001. **155**: p. 21-51.

355. van Rooijen, B.D., et al., *Imaging Cold-Activated Brown Adipose Tissue Using Dynamic T2*-Weighted Magnetic Resonance Imaging and 2-Deoxy-2-[18F]fluoro-D-glucose Positron Emission Tomography.* Invest Radiol, 2013. **48**(10): p. 708-714.

356. Soher, B.J., et al., *Noninvasive temperature mapping with MRI using chemical shift water-fat separation.* Magn. Reson. Med., 2010. **63**(5): p. 1238-1246.

357. Baba, S., et al., *Effect of nicotine and ephedrine on the accumulation of 18F-FDG in brown adipose tissue.* J Nucl Med, 2007. **48**(6): p. 981-6.

358. Liu, C.-Y., et al., *Fat quantification with IDEAL gradient echo imaging: Correction of bias from T1 and noise.* Magnetic Resonance in Medicine, 2007. **58**(2): p. 354-364.

359. Szczepaniak, L.S., et al., *Bulk magnetic susceptibility effects on the assessment of intra- and extramyocellular lipids in vivo.* Magn Reson Med, 2002. **47**(3): p. 607-10.

360. Hey, S., et al., *Temperature sensitivity of the triglyceride fat spectral model for Dixon based fat fraction quantification.* Proc. Intl. Soc. Mag. Reson. Med, 2014. **22**: p. 2130.

361. Hu, H.H., et al., *ISMRM workshop on fat-water separation: Insights, applications and progress in MRI.* Magnetic Resonance in Medicine, 2012. **68**(2): p. 378-388.
362. Yoo, Y.H., et al., *Fat-signal fraction quantification of paravertebral muscle using T2*-corrected multi-echo Dixon technique.* Proc. Intl. Soc. Mag. Reson. Med, 2014. **22**: p. 1226.
363. Bley, T.A., et al., *Fat and water magnetic resonance imaging.* J Magn Reson Imaging, 2010. **31**(1): p. 4-18.
364. Yu, H., et al., *Multiecho water-fat separation and simultaneous R2* estimation with multifrequency fat spectrum modeling.* Magn Reson Med, 2008. **60**(5): p. 1122-34.
365. Zhuo, J. and R.P. Gullapalli, *AAPM/RSNA physics tutorial for residents: MR artifacts, safety, and quality control.* Radiographics, 2006. **26**(1): p. 275-97.
366. Bailes, D.R., et al., *Respiratory ordered phase encoding (ROPE): a method for reducing respiratory motion artifacts in MR imaging.* J Comput Assist Tomogr, 1985. **9**(4): p. 835-838.
367. Hu, H.H., et al., *Quantification of Absolute Fat Mass by Magnetic Resonance Imaging: a Validation Study against Chemical Analysis.* Int J Body Compos Res, 2011. **9**(3): p. 111-122.
368. Kang, G.H., et al., *Reproducibility of MRI-determined proton density fat fraction across two different MR scanner platforms.* J Magn Reson Imaging, 2011. **34**(4): p. 928-34.
369. Madar, I., et al., *F-18-Fluorobenzyl Triphenyl Phosphonium: A Noninvasive Sensor of Brown Adipose Tissue Thermogenesis.* Journal of Nuclear Medicine, 2011. **52**(5): p. 808-814.
370. Vosselman, M.J., et al., *Systemic β-adrenergic stimulation of thermogenesis is not accompanied by brown adipose tissue activity in humans.* Diabetes, 2012. **61**(12): p. 3106-13.
371. Lee, P., K.K. Ho, and J.R. Greenfield, *Hot fat in a cool man: infrared thermography and brown adipose tissue.* Diabetes Obes Metab, 2011. **13**(1): p. 92-3.
372. Tam, C.S., V. Lecoultre, and E. Ravussin, *Brown Adipose Tissue: Mechanisms and Potential Therapeutic Targets.* Circulation, 2012. **125**: p. 2782-2791.
373. Haynes, M., J. Stang, and M. Moghaddam, *Real-time Microwave Imaging of Differential Temperature for Thermal Therapy Monitoring.* IEEE Trans Biomed Eng, 2014. **61**(6): p. 1787-97.
374. Rose, R.W., et al., *Nonshivering thermogenesis in a marsupial (the tasmanian bettong Bettongia gaimardi) is not attributable to brown adipose tissue.* Physiol Biochem Zool, 1999. **72**(6): p. 699-704.
375. Lau, A.Z., et al., *Noninvasive identification and assessment of functional brown adipose tissue in rodents using hyperpolarized 13C imaging.* Int J Obes, 2013.
376. Lau, A.Z., A.P. Chen, and C.H. Cunningham, *Integrated Bloch-Siegert B1 mapping and multislice imaging of hyperpolarized 13C pyruvate and bicarbonate in the heart.* Magn Reson Med, 2012. **67**(1): p. 62-71.
377. McDannold, N., *Quantitative MRI-based temperature mapping based on the proton resonant frequency shift: review of validation studies.* Int J Hyperthermia, 2005. **21**(6): p. 533-46.
378. Heim, T. and D. Hull, *The blood flow and oxygen consumption of brown adipose tissue in the new-born rabbit.* J Physiol, 1966. **186**(1): p. 42-55.
379. Vijgen, G.H., et al., *Increased Oxygen Consumption in Human Adipose Tissue from the "Brown Adipose Tissue" Region.* J Clin Endocrin Metab, 2013. **98**(7): p. E1230-4.
380. Branca, R.T. and W.S. Warren, *In vivo brown adipose tissue detection and characterization using water-lipid intermolecular zero-quantum coherences.* Magn Reson Med, 2011. **65**(2): p. 313-9.